The Effect of Interaction on Boundary-Layer Separation and Breakdown

by

Kevin W. Cassel

Presented to the Graduate and Research Committee

of Lehigh University

in Candidacy for the Degree of

Doctor of Philosophy

in

Mechanical Engineering

Lehigh University

December, 1993

19980115 174

REPORT DOCUMENTATION PAGE		*Form Approved* OMB No. 0704-0188

Public reporting burden for this collection of information is estimated to average 1 hour per response, including the time for reviewing instructions, searching existing data sources, gathering and maintaining the data needed, and completing and reviewing the collection of information. Send comments regarding this burden estimate or any other aspect of this collection of information, including suggestions for reducing this burden, to Washington Headquarters Services, Directorate for information Operations and Reports, 1215 Jefferson Davis Highway, Suite 1204, Arlington, VA 22202-4302, and to the Office of management and Budget, Paperwork Reduction Project (0704-0188) Washington, DC 20503.

1. AGENCY USE ONLY (Leave Blank)	2. REPORT DATE December 1993	3. REPORT TYPE AND DATES COVERED Final

4. TITLE AND SUBTITLE The Effect of Interaction on Boundary-Layer Separation and Breakdown	5. FUNDING NUMBERS

6. AUTHORS
Kevin W. Cassel

7. PERFORMING ORGANIZATION NAME(S) AND ADDRESS(ES) Lehigh University	AFRL-SR-BL-TR-98- ◯ ◯◯ ⑥

9. SPONSORING/MONITORING AGENCY NAME(S) AND ADDRESS(ES) AFOSR/NI 110 Duncan Avenue, Room B-115 Bolling Air Force Base, DC 20332-8080	10. SPONSORING/MONITORING AGENCY REPORT NUMBER

11. SUPPLEMENTARY NOTES

12a. DISTRIBUTION AVAILABILITY STATEMENT Approved for Public Release	12b. DISTRIBUTION CODE

13. ABSTRACT *(Maximum 200 words)*
See attached.

DTIC QUALITY INSPECTED 2

14. SUBJECT TERMS	15. NUMBER OF PAGES
	16. PRICE CODE

17. SECURITY CLASSIFICATION OF REPORT Unclassified	18. SECURITY CLASSIFICATION OF THIS PAGE Unclassified	19. SECURITY CLASSIFICATION OF ABSTRACT Unclassified	20. LIMITATION OF ABSTRACT UL

Standard Form 298 (Rev. 2-89)
Prescribed by ANSI Std. 239.18
Designed using WordPerfect 6.1, AFOSR/XPP, Oct 96

Approved and recommended for acceptance as a dissertation in partial fulfillment of the requirements for the degree of Doctor of Philosophy.

Dec 13, 1993
Date

Dr. J. D. A. Walker, Professor,
Department of Mechanical Engineering
    and Mechanics
(Dissertation Advisor and Chairman
    of the Special Committee)
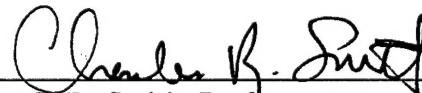
Dr. C. R. Smith, Professor,
Department of Mechanical Engineering
    and Mechanics
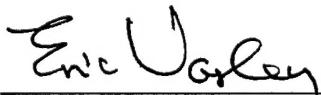
Dr. E. Varley, Professor,
Department of Mechanical Engineering
    and Mechanics

Dr. A. Liakopoulos, Associate Professor,
Department of Mechanical Engineering
    and Mechanics
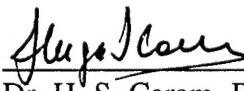
Dr. H. S. Caram, Professor,
Department of Chemical Engineering

ii

Acknowledgements

I would like to express special appreciation to my wife Adrienne D. Cassel for her encouragement and support over the last four years and to my son Ryan for reminding me each day that there are more important titles one can obtain in life than "Dr."

The Effect of Interaction on Boundary-Layer Separation and Breakdown

List of Figures

ix

Abstract

It is common in boundary-layer flow at high Reynolds numbers involving separation for an interaction to be provoked between the viscous boundary layer and the inviscid external flow. The effect that this viscous-inviscid interaction has on both steady and unsteady boundary-layer separation is investigated. In part I the unsteady boundary-layer separation process is considered in the context of two-dimensional incompressible flow. In regions of adverse streamwise pressure gradient along solid surfaces, it is common for the boundary layer to erupt away from the surface in a narrow streamwise region. Classical non-interacting boundary-layer solutions of such flows breakdown within a finite time, but the thickening boundary layer induces an interaction with the outer inviscid flow during the first interactive stage in order to relieve the singularity. Numerical solutions were obtained of the first interactive stage formulated in Lagrangian coordinates. These results show that the viscous-inviscid interaction causes the flow to become unstable, resulting in a breakdown of the first interactive stage. The instability is of a high-frequency inviscid type and is shown to be characterized by large complex wavespeeds.

In part II separation of a hypersonic boundary layer flowing over a compression ramp is considered, both with and without wall cooling. For small ramp angles, the flow in the vicinity of the corner is governed by the triple-deck structure which accounts for the viscous-inviscid interaction. The flow over the compression ramp exhibits separation in the corner for ramp angles above a critical value. Numerical solutions have been obtained for the hypersonic triple deck and show that for larger ramp angles the flow becomes unstable in the form of a stationary wave packet which forms near the corner. Wall cooling was found to have a significant effect upon both the location of separation and the extent of the recirculating-flow region, and it is shown to stabilize or destabilize the instability at high ramp angles depending upon the average Mach number across the boundary layer.

1

1. Introduction

1.1 Viscous-Inviscid Interaction

A general mathematical model for fluid flow is provided by the Navier-Stokes equations which are the mathematical statement of conservation of mass and momentum and describe a balance between inertial, pressure and viscous forces within a fluid. These equations apply for a wide variety of flow situations; however, analytical solutions are rare and very difficult to obtain due to the highly non-linear nature of the equations. In recent times increasingly powerful computer systems have facilitated numerical solutions of the Navier-Stokes equations in many flow environments; however, there are numerous unresolved questions in fluid mechanics which cannot currently be addressed using such direct numerical simulations. In particular, it has become evident through asymptotic analyses that many important flow features in high Reynolds number Re flows occur over length and time scales which are too small to be resolved solely by numerical solutions of the Navier-Stokes equations and this situation is likely to persist for the foreseeable future. Prior to the advent of the modern computer age, a common theoretical approach was to the consider appropriately simplified subsets of the full Navier-Stokes equations which were more amenable to solution. This approach was eventually formalized and is now known as asymptotic analysis, wherein solutions in each subregion of the flow field are found and then systematically matched together. Even if computational resources at some point in the distant future allow for accurate solutions of the Navier-Stokes equations for general flow environments and especially at high flow speeds, significant physical insight into specific flow features can be gained through knowledge of the predominant physics in each region of the flow. This is best obtained through an isolation of the dominant terms in the governing equations within each region of the flow through asymptotic techniques.

2

In the early development of theoretical fluid mechanics, it was often assumed that the effects of friction, *i.e.* viscosity, were negligible. Therefore, the terms in the Navier-Stokes equations which describe the effects of viscous forces were neglected giving rise to the inviscid Euler equations of ideal fluid theory. While this assumption appeared valid for many of the common fluids (such as air and water) that have very small viscosity, the ideal fluid theory was found to be incapable of accounting for certain observed phenomena. For example, inviscid theory predicts that a solid body moving through a uniform stream of fluid does not experience drag forces; this is called d'Alembert's paradox since it clearly violates experimental observation. Such discrepancies, as well as a number of situations involving non-uniqueness, perplexed theoreticians for many years.

For flow near solid walls, some of the difficulties were resolved by Prandtl (1904) who argued that, while the Euler equations govern over a majority of the flow field, they are not uniformly valid, and viscous effects must become important in a thin layer along the surfaces. This boundary layer is necessary in order to adjust the tangential surface velocity from the slip value predicted by inviscid theory to relative rest at the surface; the steep velocity gradients within this layer result in viscous forces that are of the same order as the inertial forces. Prandtl's classical boundary-layer equations have been the basis of innumerable investigations, and these are responsible for much of our current understanding of high Reynolds number fluid flows involving solid surfaces. The basic assumption of the boundary-layer equations is that the layer remains thin and it emerges that the thickness is $O(Re^{-1/2})$ as $Re \rightarrow \infty$. This leads to two consequences for the boundary-layer flow, namely that the variation in pressure gradient normal to the surface is small, and that the velocity normal to the surface is small. Since the boundary layer is thin, it is expected to have little effect on the external inviscid flow. Mathematically, the boundary-layer equations consist of a second-order partial differential equation of parabolic type; these equations can, in principle, be solved by marching a solution downstream from a known velocity profile subject to the no-slip condition at the surface and a pressure gradient prescribed from an inviscid

3

solution.

When the pressure gradient imposed across the boundary layer is adverse (*i.e.* the pressure is increasing in the flow direction), the low momentum fluid within the boundary layer is susceptible to developing regions of reversed flow which may cause the boundary layer to separate from the surface. Separation is a dominant feature in many flows and can have a significant affect upon lift and drag, as well as overall performance of systems involving fluid flow. In Prandtl's (1904) physical picture of separation for flow past fixed wall, the boundary layer was assumed to leave the surface at a point where the skin friction vanished. Early attempts to integrate the boundary-layer equations (Howarth, 1938), however, encountered difficulties as a solution was computed downstream toward a point where the skin friction vanished. Goldstein (1948) showed that this difficulty was due to a singularity which forms at the separation point (*i.e.* a point of zero wall shear in steady flows) in all cases where the inviscid pressure or external velocity is prescribed. It was later shown that an inverse method, in which the wall shear stress or boundary-layer displacement thickness is prescribed rather than the pressure gradient, could be used to advance a solution through small-scale separation regions for which the boundary layer remains thin with a thickness which is $O(Re^{-1/2})$.

Whereas the Goldstein singularity occurs in steady flows at a separation point defined by vanishing wall shear, a more general separation criterion is required in unsteady flows and flows with moving surfaces (see Williams, 1977). Sears and Telionis (1975) introduced the MRS model of unsteady separation which is named for Moore (1958), Rott (1956) and Sears (1956). This criterion, which is discussed in more detail in §2.2, indicates that unsteady separation occurs when the shear stress and velocity vanish simultaneously at a point within the boundary layer in a singular manner in a frame of reference moving with the separation point. This unsteady separation singularity was first demonstrated in a numerical calculation by Van Dommelen and Shen (1980) who considered the flow over the impulsively-started circular cylinder. This and other examples involving the unsteady separation

4

singularity will be discussed in §2.4, and the analytical form of the singular solution will be given in §2.5. Both the steady Goldstein singularity and the unsteady Van Dommelen singularity suggest outflows at the outer edge of the boundary layer which eventually are locally greater than $O(Re^{-1/2})$.

Boundary-layer theory corresponds to a first-order approximation to the Navier-Stokes equations in regions near solid surfaces and in the limit of small viscosity (large Re). In the classical interactive strategy (Smith, 1982), the displacement effect of the boundary layer is considered to provoke a viscous-inviscid interaction in the form of a second-order correction to the external flow field. When the boundary layer remains thin and attached at high Reynolds numbers, the interaction has only a small influence upon the external flow. In such cases the classical interactive strategy may be used wherein solutions for the outer inviscid flow and the boundary-layer flow are obtained in a hierarchical process. First, a solution is determined for the inviscid flow around some given surface geometry. Then the boundary-layer solution is obtained using the inviscid mainstream velocity as a condition at the boundary-layer edge. The boundary layer displaces the external flow a distance which is $O(Re^{-1/2})$ and thereby effectively alters the surface shape; therefore, the inviscid flow solution must then be modified to take this effect into account. This new inviscid solution is then used to refine the boundary-layer solution, and the iteration continues until convergence to some desired accuracy is achieved. This strategy may be regarded as only weakly interactive since it does not allow for the simultaneous interaction between both regions of the flow. It is more accurately described as a hierarchical approach, because each iteration is identical to a classical boundary-layer calculation where the pressure gradient (or mainstream velocity) is prescribed. Therefore, steady calculations using this strategy fail when a point of separation is encountered since a Goldstein singularity is produced just as in the non-interactive case. One of the few examples where the classical interactive strategy is successful is the flow over a flat plate aligned parallel to a uniform mainstream. Most other flows involve bodies of finite thickness giving rise to regions of adverse pressure gradient and separation.
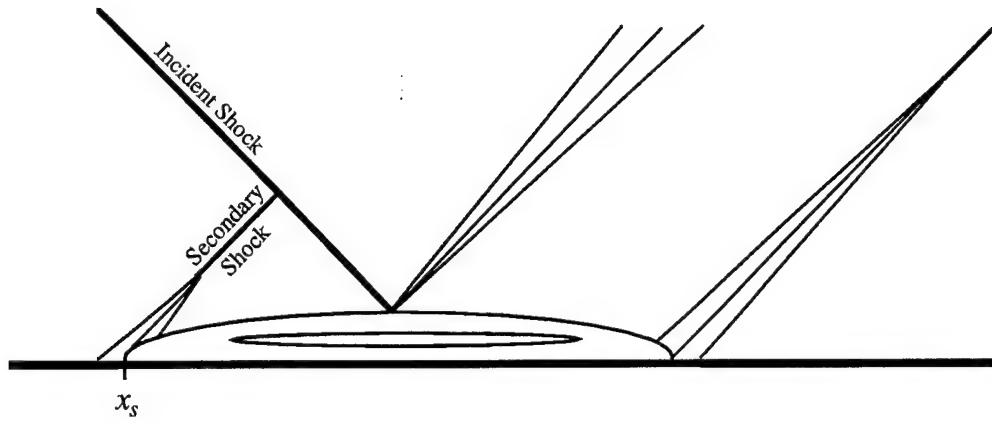
Figure 1.1 - Schematic of shock-induced boundary-layer separation in a supersonic flow.

One of the first examples in which it was realized that viscous-inviscid interaction must play a central role in the flow dynamics involves the impingement of a shock wave on a boundary layer in a supersonic stream. It was observed in several experimental studies of this flow (see, for example, Ackeret *et al.*, 1947 and Chapman *et al.*, 1957) that an incident shock wave causes the boundary-layer flow to separate from the surface upstream of the point of impingement of the primary shock, and a secondary shock forms near the separation point. This is illustrated schematically in figure 1.1. The impingement of a shock wave on a surface is an example of a compressive disturbance in which the disturbance induces a rise in the inviscid pressure distribution along the surface. A compressive disturbance may also be caused in supersonic flows by a surface that turns toward the flow. Chapman *et al.* (1957) carried out experiments for cases where separation was induced by such surface geometries (including steps and corners) which also exhibited separation upstream of the disturbance. The upstream influence observed in these examples was puzzling because the boundary-layer equations are parabolic and, therefore, do not permit upstream propagation of disturbances within the boundary layer. Likewise, the

6

supersonic mainstream can only transmit disturbances downstream. The first physical explanation for this upstream influence was given by Lighthill (1953a,b) who recognized that when a compressive disturbance of sufficient strength induces separation, the thickened boundary layer alters the external flow by inducing a pressure rise ahead of the separation point, and the resulting adverse pressure gradient then causes the flow to separate farther upstream. This is often called self-induced separation. The theoretical work of Lighthill (1953b) became the basis for the supersonic triple-deck theory of Stewartson and Williams (1969) and Neiland (1969) which provides a theoretical explanation for the upstream influence in supersonic self-induced separation.

It is interesting to note that for supersonic flows, the flow in the vicinity of the separation point does not depend upon the form or strength of the disturbance for sufficiently large compressive disturbances. This was observed in the experiments by Chapman *et al.* (1957) and was considered theoretically by Stewartson and Williams (1969). This phenomenon is called a free interaction because the flow near separation is 'free' from the direct influences of the downstream geometry and conditions. In the free-interaction region, the pressure rises from its upstream value, through a universal value at separation (regardless of the strength of the disturbance) to a constant plateau pressure in the separated region. Likewise, the wall shear has a characteristic behavior heading into the recirculating-flow region in which it falls from its upstream value to zero at the separation point.

Another classical interactive problem involves the steady flow in the vicinity of the trailing edge of a flat plate. This interaction does not involve separation but rather is provoked by an abrupt change in boundary conditions. The incompressible case was first considered by Stewartson (1969) and Messiter (1970). It had been known that the Blasius solution for the boundary-layer flow over a flat plate does not match smoothly to the near-wake solution (Goldstein, 1930) downstream of the trailing edge. The change in boundary condition is from the no-slip condition on the plate to a symmetry condition on the wake centerline. This causes an acceleration of the flow near the

7

symmetry line into the wake, leading to vertical motion toward the centerline and a decrease in displacement thickness. The apparent irregularities in the near-wake solution at the trailing edge may be regarded as resulting because the parabolic boundary-layer equations are unable to anticipate this acceleration. The solution is smoothed out in a three-layer or triple-deck structure centered at the trailing edge. For incompressible flows this structure was first discovered by Stewartson (1969) and Messiter (1970) and was subsequently found to apply to a variety of physical situations. The triple-deck structure consists of a thin sublayer adjacent to the wall, a middle deck which is essentially the continuation of the upstream boundary layer and an upper deck which rides over the boundary layer within the external-flow region. In subsonic flows, disturbances are propagated upstream in the upper deck. Triple-deck theory will be discussed in more detail in §1.3 with additional examples given where the structure occurs.

Triple-deck theory corresponds to a limit analysis ($Re \rightarrow \infty$) and has proven very useful in cases involving local interactions. However, triple-deck analysis often involves difficult analytical behaviors as well as challenging computational problems. An alternative approach is conventional interacting boundary-layer theory where a large but finite Reynolds number is assumed. In this approach the boundary-layer equations are solved subject to an interaction condition which accounts for second-order perturbations in the external flow provoked by the boundary layer. Interacting boundary-layer formulations differ from the classical interactive approach in that the boundary-layer and external-flow solutions are evaluated simultaneously rather than sequentially. In this way the Goldstein singularity, which occurs when the external pressure distribution is prescribed for the boundary layer, is avoided. Interacting boundary-layer theory will be discussed in §1.2.

Significant interaction between the viscous boundary layer and the outer inviscid flow may occur in a wide variety of flow situations. In many instances interaction is provoked by a relatively small-scale steady separation of the boundary layer; this can occur in flows about bluff bodies, in the vicinity of airfoil trailing edges

of finite thickness or at angle of attack, with surface injection, over surface humps and cavities, past corners and due to an incident shock wave. Unsteady boundary-layer separation, which often involves local eruptions of fluid away from the surface, may occur in the flow about impulsively-started bluff bodies and surfaces undergoing unsteady motion such as pitching airfoils. Unsteady separation also occurs in applications involving the convection of vortices in the vicinity of solid surfaces. Such vortices may arise due to flows encountering surface-mounted obstacles, vortex shedding from upstream surfaces and vortices found in turbulent boundary layers. Examples of unsteady boundary-layer separation are discussed in more detail in §2.1. In addition to separation-induced interactions, flows involving abrupt changes in boundary conditions, such as at a trailing edge or jump in surface temperature, often provoke an interaction in order to communicate the impending change to the upstream boundary layer.

This thesis is concerned with the effect of viscous-inviscid interaction on both steady and unsteady boundary-layer separation. Each type of separation will be considered in different flow environments. The first to be considered corresponds to unsteady separation of incompressible boundary layers and is described in part I (consisting of chapters 2, 3 and 4) of this thesis. In the examples involving unsteady separation mentioned above, it is common for a highly unsteady eruption to occur in regions of adverse streamwise pressure gradient along surfaces. The adverse pressure gradient causes the formation of a region of recirculating flow within the boundary layer which often is a precursor to an abrupt local ejection of near-wall fluid into the external flow. When flows of this nature are investigated within the framework of classical non-interactive boundary-layer theory, the unsteady solution terminates in a singularity characterized by dramatic local thickening of the boundary layer and strong outflows within a narrow streamwise region. This separation singularity is a consequence of the breakdown of the boundary-layer assumptions which require the boundary layer to remain thin. Numerical solutions of the classical boundary-layer equations which evolve toward this singularity are discussed in §2.4, and a detailed

description of the analytical form of the singularity is given in §2.5.

As the flow evolves toward the separation singularity, an interaction is provoked between the thickening viscous boundary layer and the outer inviscid flow. In two-dimensional incompressible flows this viscous-inviscid interaction is accounted for in the so called first interactive stage formulated by Elliott, Cowley and Smith (1983). This stage describes a generic unsteady separation structure in the limit of infinite Reynolds number that applies in most cases of unsteady separation, regardless of the global flow environment in which it occurs. The first interactive stage is discussed in detail in §3.2. In this investigation numerical solutions of the first interactive stage of unsteady separation were obtained in Lagrangian coordinates as described in chapter 3. The computation of unsteady eruptive flows in Lagrangian coordinates has distinct advantages over traditional Eulerian formulations (which are discussed in §2.3). The results obtained here show that the first interactive stage breaks down in the form of a high-frequency instability immediately upon the onset of interaction. The consequences of these results for the unsteady separation process are discussed in chapter 4.

The second flow environment considered in this thesis is at the opposite end of the flow speed spectrum and involves separation in a hypersonic boundary layer with and without wall cooling. This case is considered in part II (consisting of chapters 5, 6 and 7) of this thesis. The effect of wall cooling is of particular interest because cooling is often necessary in hypersonic flows in order to combat the high temperatures generated near the surface. The hypersonic triple-deck formulation for cold walls is given in chapter 5, and the algorithm used here to solve this flow is described in chapter 6. This algorithm was extended from that developed for supersonic flow by Ruban (1978) in order to incorporate cold wall effects; the method applies for general surface shapes within the triple-deck length scales.

Solutions were obtained here for the flow over the compression ramp with various ramp angles and levels of wall cooling. This simple geometry induces separation near the corner for ramp angles above a critical value and provides a

framework in which to investigate the effects of surface geometry and wall cooling on steady separation. The present results are the first to demonstrate that the flow over compression ramps at sufficiently high ramp angles becomes unstable and develops stationary wave packets. In addition, the results show that wall cooling has a significant effect upon both stability and separation. Wall cooling was found to stabilize or destabilize the flow depending on the average Mach number in the boundary layer approaching the corner. Cooling was also found to have a dramatic effect upon both the location and size of the recirculating-flow region and to limit the upstream or downstream propagation of disturbances.

1.2 Interacting Boundary-Layer Theory

Consider an incompressible flow having characteristic speed U_∞ past a solid body having a characteristic length L. The flow is characterized by the non-dimensional Reynolds number defined by

$$Re = \frac{\rho \, U_\infty L}{\mu},$$ (1.1)

where ρ and μ are the density and viscosity of the fluid, respectively. Cartesian coordinates x and y (non-dimensionalized with respect to L) are defined in directions along and normal to the surface, respectively; velocity components u and v (non-dimensionalized with respect to U_∞) are defined in the corresponding directions. In addition, let t be the time coordinate and p the dynamic pressure non-dimensionalized with respect to L/U_∞^2 and $\rho \, U_\infty^2$, respectively.

Classical, or non-interacting, boundary-layer theory assumes that a given flow may be subdivided into two flow regimes namely, an external inviscid region consisting of the majority of the flow field and a thin boundary layer adjacent to the solid surface in which viscous effects are important. The flow in the external region is

11

governed by the Euler equations subject to a condition of zero normal velocity at the surface ($v = 0$ at $y = 0$), and the solution to these equations then produces a slip velocity along the surface

$$u \to U_e(x,t) \quad \text{as } y \to 0. \tag{1.2}$$

To satisfy the no-slip condition ($u = 0$ at $y = 0$) at the surface, a thin boundary layer (having a thickness $O(Re^{-1/2})$) is required in order to adjust the streamwise velocity from U_e to relative rest. Within the boundary layer, scaled variables are defined by

$$y = Re^{-1/2} Y, \quad v = Re^{-1/2} V, \tag{1.3a,b}$$

such that Y and V are $O(1)$. The flow within this thin layer is governed by the boundary-layer equations given by

$$\frac{\partial u}{\partial t} + u \frac{\partial u}{\partial x} + V \frac{\partial u}{\partial Y} = -\frac{\partial p}{\partial x} + \frac{\partial^2 u}{\partial Y^2}, \quad \frac{\partial p}{\partial Y} = 0, \tag{1.4a,b}$$

$$\frac{\partial u}{\partial x} + \frac{\partial V}{\partial Y} = 0. \tag{1.4c}$$

The boundary-layer equations are an exact subset of the Navier-Stokes equations in the limit $Re \to \infty$. Equation (1.4b) simply asserts that the surface pressure distribution from the inviscid solution is impressed across the boundary layer; therefore, $p = p(x,t)$ in the boundary layer. The boundary conditions for (1.4) are then

$$u = V = 0 \quad \text{at } Y = 0, \tag{1.5a}$$

$$\lim_{Y \to \infty} u(x,Y,t) = U_e(x,t). \tag{1.5b}$$

12

The solution in the external region is generally obtained independently of the boundary layer, and the boundary-layer flow is driven by the prescribed streamwise pressure gradient obtained from the external flow solution. Applying equation (1.4a) at the boundary-layer edge, the streamwise pressure gradient may be related to the inviscid slip velocity through

$$-\frac{\partial p}{\partial x} = \frac{\partial U_e}{\partial t} + U_e \frac{\partial U_e}{\partial x}.$$ (1.6)

Solutions for which an unsteady separation singularity develops in the classical boundary-layer equations will be discussed in §2.4. This non-interactive singularity develops as a consequence of imposing the external pressure field on the boundary layer for an indefinite period of time. The presence of an adverse streamwise pressure gradient eventually triggers a sequence of events that causes a dramatic local growth in the boundary layer eventually provoking an interaction with the outer inviscid flow. One method of treating these types of flows is conventional interacting boundary-layer theory which assumes a large but finite Reynolds number and accounts for the small $O(Re^{-1/2})$ perturbations induced by the boundary layer on the external flow. Taking these perturbations into account supplements the classical non-interacting boundary-layer equations (1.4) with an interaction condition which may be obtained from the analysis described in Appendix B for incompressible flow and is

$$U_e(x,t) = U_{e0}(x,t) + Re^{-1/2} \frac{1}{\pi} \int_{-\infty}^{\infty} \frac{\partial}{\partial s} [U_e(s,t)\, \delta^*(s,t)] \frac{ds}{x-s}.$$ (1.7)

Here, $U_{e0}(x,t)$ is the leading-order inviscid slip velocity associated with the non-interacting case, and $\delta^*(x,t)$ is the scaled dimensionless displacement thickness defined by

$$\delta^*(x,t) = \int_0^\infty \left[1 - \frac{u(x,Y,t)}{U_e(x,t)} \right] dY. \qquad (1.8)$$

The second term in the interaction condition (1.7) must remain small in comparison to U_{e0} in order for the approach to remain valid; this term is due to the perturbations induced by the boundary layer on the external flow and is a Cauchy principal-value integral. Equation (1.7), therefore, defines a Cauchy principal-value integro-differential equation which relates the mainstream pressure (see equation 1.6) to the displacement thickness of the boundary layer thus permitting mutual interaction between the boundary layer and the external inviscid flow.

Steady interacting boundary-layer theory has been used extensively and with good success (see, for example, Burggraf, Rizzetta, Werle and Vatsa, 1979); in particular, the approach has been shown to relieve the Goldstein (1948) singularity which occurs at a point of zero surface shear stress in steady non-interacting boundary-layer flows provided the boundary-layer calculation is executed in a specific manner. More recently, interacting boundary-layer theory has been applied to unsteady separating flows, but the results have proven controversial. The impulsively-started circular cylinder has been considered by Henkes and Veldman (1987) and the vortex-induced boundary layer by Chuang and Conlisk (1989) and Peridier, Smith and Walker (1991b). Riley and Vasantha (1989) considered both of these model problems. The contradictory results obtained in these studies will be discussed in §2.6, as they relate to the unsteady boundary-layer separation process.

1.3 Limit Analyses of Interaction Problems

An alternative to the interacting boundary-layer theory discussed in the previous section is to consider a limit analysis ($Re \to \infty$) of the viscous-inviscid interaction problem; in this approach the relevant flow regions are identified (along with the pertinent scales) as functions of the Reynolds number and the governing equations

14

determined through an asymptotic analysis. Two such theories are the focus of the present investigation: the first interactive stage of unsteady incompressible boundary-layer separation and the hypersonic boundary-layer separation on a cold wall. The first interactive stage was first described in association with the onset of unsteady incompressible boundary-layer separation, although the structure probably applies (in modified form) to compressible boundary layers. This analysis will be discussed in part I of this thesis.

Triple-deck theory applies to the hypersonic cold wall problem, as well as to a surprising number of diverse problems involving relatively small-scale viscous-inviscid interactions. The triple-deck structure was first discovered as a result of a search for a theoretical explanation of the experimental findings of Liepmann (1946), Ackeret, Feldmann and Rott (1947), Chapman, Kuehn and Larson (1957) and others; these authors found that a shock wave in supersonic flow impinging on a boundary layer may induce separation within the boundary layer but upstream of the shock. This so called "self-induced" separation problem cannot be explained solely in terms of the parabolic boundary-layer equations which do not permit the upstream propagation of disturbances; therefore, in the context of classical theory the boundary layer is unaware of the presence of the shock wave upstream of the point of impingement. Chapman *et al.* (1957) speculated correctly that the physical mechanism for the upstream influence was a mutual interaction between the displacement thickness of the boundary layer and the pressure gradient in the outer inviscid flow. The theoretical work of Lighthill (1953) then provided the framework for the development of the subsequent supersonic triple-deck theory of Stewartson and Williams (1969) and Neiland (1969).

The analogous incompressible triple deck was formulated simultaneously for the problem at the trailing edge of a flat plate by Stewartson (1969) and Messiter (1970). As the flow over a flat plate (described by the Blasius boundary-layer solution) encounters the trailing edge, the solution must merge downstream into the Goldstein (1930) near-wake solution. However, the transition is apparently not smooth and contains irregularities, with infinite streamwise gradients and normal velocity being

15

predicted at the trailing edge. These irregularities are a result of the abrupt change in boundary conditions from the no-slip condition along the flat plate to the symmetry condition downstream in the wake. Again, the problem is associated with the fact that the solution of the parabolic boundary-layer equations is unaware of the approaching trailing edge; thus, the solution cannot adjust for the impending acceleration of the flow within the wake. The difficulty is resolved by introducing a triple-deck structure centered on the trailing edge. This short interaction region allows for the effects of the upstream influence (in the upper deck) and provides a smooth transition from the Blasius solution upstream to the Goldstein near-wake solution.

In subsequent years, triple-deck theory has been applied to many seemingly diverse problems in both steady and unsteady flow and throughout the subsonic and supersonic flow regimes. A common feature in all these problems, however, is some surface or mainstream disturbance which provokes a viscous-inviscid interaction in a local region above the boundary layer where upstream influence is facilitated. Some examples are small surface features such as humps, indentations, ramps or abrupt changes in surface conditions such as weak surface injection or a jump in surface temperature. The triple deck structure also applies in the vicinity of the separation point for steady large-scale separating flows. These situations and other triple-deck problems have been reviewed by Neiland (1974, 1981), Stewartson (1974, 1981), Lagerstrom (1975), Messiter (1979, 1983), Adamson and Messiter (1980) and Smith (1982). Historically, the primary focus has been on the two-dimensional triple deck, but the analogous structure exists in three-dimensions and has been considered by Smith, Sykes and Brighton (1977), Smith (1982) and Duck and Burggraf (1986).

Despite the wide variety of situations in which it occurs, the triple-deck structure is surprisingly generic. The interaction region is centered at the disturbance and has streamwise extent $O(Re^{-3/8})$; it consists of three layers as shown schematically in figure 1.2. A thin viscous sublayer (region I) having a thickness $O(Re^{-5/8})$ occurs adjacent to the surface in which the flow is governed by the incompressible boundary-layer equations but with unknown pressure gradient. The balance of the boundary layer

16

III

Upper Deck

$O(Re^{-3/8})$

II

Main Deck

$O(Re^{-1/2})$

**Boundary
Layer**

I

Viscous Sublayer

$O(Re^{-5/8})$

$O(Re^{-3/8})$
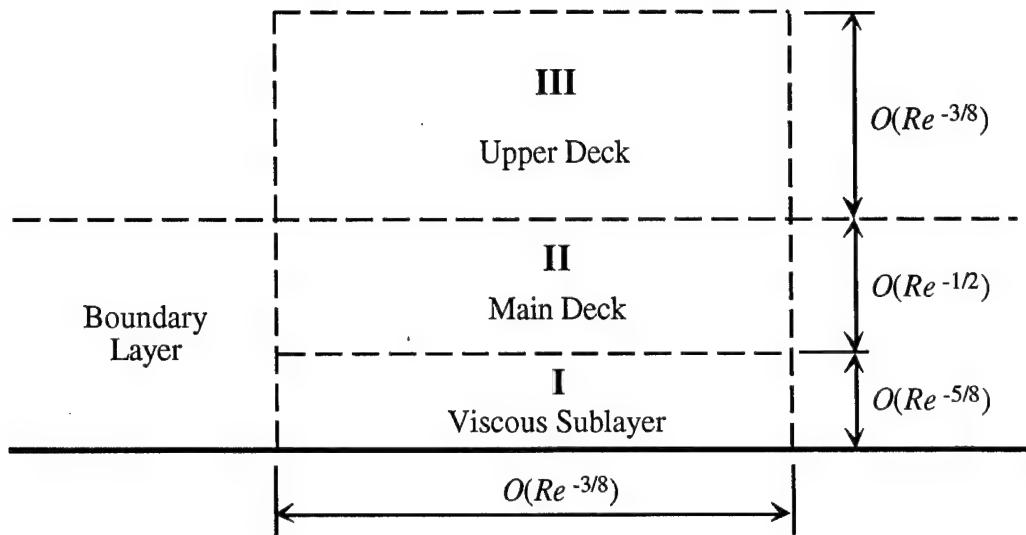
Figure 1.2 - Schematic of the general triple-deck structure.

(region II) is referred to as the main deck and essentially is a continuation of the upstream boundary layer. This layer has a thickness $O(Re^{-1/2})$ and serves to communicate the affects of the interaction between the viscous sublayer and the upper deck. Finally, the upper deck (region III) is the local portion of the outer inviscid flow which is altered by interaction with the viscous sublayer. The solution in this upper layer provides an interaction condition that couples the induced pressure in the external flow with the displacement effect of the viscous sublayer. The form of this condition depends on whether the flow is subsonic or supersonic. It is through this viscous-inviscid interaction that upstream influence is permitted within the boundary layer. While at first sight the triple-deck structure appears rather complex, the equations which comprise the triple-deck formulation are simply the incompressible boundary-layer equations in the viscous sublayer subject to an interaction condition. The complete triple-deck formulation is as follows:

17

$$\frac{\partial u}{\partial t} + u \frac{\partial u}{\partial x} + v \frac{\partial u}{\partial y} = -\frac{\partial p}{\partial x} + \frac{\partial^2 u}{\partial y^2}, \qquad \frac{\partial p}{\partial y} = 0, \tag{1.9b}$$

$$\frac{\partial u}{\partial x} + \frac{\partial v}{\partial y} = 0, \tag{1.9c}$$

$$u = v = 0 \quad \text{at } y = 0, \tag{1.9d}$$

$$u \to y + \cdots \quad \text{as } x \to -\infty, \tag{1.9e}$$

$$u \to y + A(x,t) + \cdots \quad \text{as } y \to \infty, \tag{1.9f}$$

where u and v are the velocities in the streamwise x and the normal y directions, respectively, t is time and $p(x,t)$ is the pressure distribution across the triple deck. All variables are scaled to be $O(1)$ within the viscous sublayer. The interaction conditions are

$$p(x,t) = \frac{1}{\pi} \int_{-\infty}^{\infty} \frac{\partial A}{\partial s} \frac{ds}{x-s}, \tag{1.10a}$$

for subsonic flow and

$$p(x,t) = -\frac{\partial A}{\partial x}, \tag{1.10b}$$

for supersonic flow. Here, $A(x,t)$ represents the displacement thickness of the viscous sublayer. The triple-deck formulation (1.9-1.10) applies to numerous situations which differ only in small modifications to the boundary conditions.

One question which arises here is whether a limit approach with large Reynolds number is appropriate for the investigation of laminar flows, in light of the fact that

18

transition to turbulent flow generally occurs at high Reynolds numbers. A second question concerns whether the triple deck and interacting boundary-layer theory (discussed in the previous section) are consistent in the limit $Re \rightarrow \infty$. The latter question was studied by Burggraf *et al.* (1979) who considered supersonic flow over a compression ramp. They computed the flow using both interacting boundary-layer theory and triple-deck theory and found that the triple-deck results closely represented the limiting form of the interacting boundary-layer results. For the case considered, agreement was extremely close for Reynolds numbers greater than about 10^8. In addition, good agreement was found between experiment and the interacting boundary-layer results at lower Reynolds number. In another study Jobe and Burggraf (1974) produced numerical solutions for the incompressible triple deck near the trailing edge of a flat plate and found reasonable agreement with experimental results for Reynolds numbers as low as 10. Therefore, not only does triple-deck theory provide asymptotic solutions for high Reynolds number flows, it often gives reasonably accurate results for Reynolds numbers below the critical value at which the flow becomes turbulent. Perhaps more importantly, limit structures, such as the triple deck, give the dominant length and time scales of particular flow features. Any attempts to obtain purely numerical solutions of flows involving these features (for example, using the full Navier-Stokes equations) must take these scales into consideration when choosing numerical grids.

In part II of this thesis, the hypersonic triple deck will be considered with and without wall cooling. Numerical solutions of the hypersonic triple deck are obtained for the flow over the compression ramp in order to determine the effects of wall cooling on the separation which normally takes place in the corner. The presence of a cold wall diminishes the displacement effect of the lower deck until eventually that associated with the main and lower decks are comparable. The formulation differs from classical triple-deck theory in that an additional term appears in the interaction condition (1.10b).

19

PART I

Unsteady Breakdown of Incompressible Boundary Layers
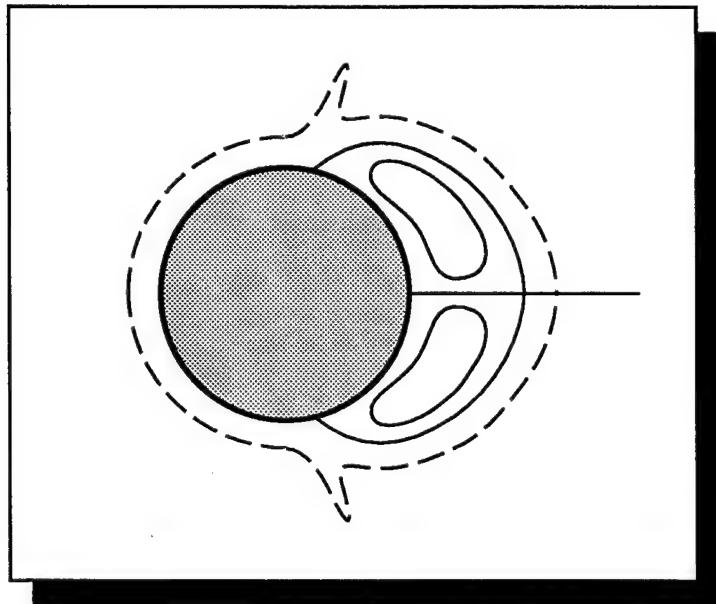
2. Unsteady Boundary-Layer Separation

2.1 Introduction

Because flow past a rigid body must come to relative rest at the surface, the fluid within the boundary layer experiences a momentum deficit and is susceptible to the onset of reversed flow in regions of adverse external pressure gradient. It is common in certain unsteady high Reynolds number flows (where such conditions exist) for boundary-layer fluid to be eventually ejected away from the surface in a local eruption into the outer flow. The adverse pressure gradient which initiates this unsteady boundary-layer eruption may be due to the surface geometry or some external flow feature such as a vortex convecting above the surface. Unsteady eruptions have been observed in a number of technologically important applications and some representative examples are discussed here.

In the impulsive motion of bluff bodies through a fluid, localized eruptions of near-wall fluid are often observed. The eruptive process is generally initiated by the formation of recirculating flow near the surface where the mainstream pressure gradient is adverse. As this recirculation region grows, a narrow zone of strong outflow is observed to form within the boundary layer at sufficiently high Reynolds number, and this ultimately provokes an interaction with the outer inviscid flow. One extensively studied example is the impulsively-started circular cylinder (see, for example, Bouard and Coutanceau, 1980 and Ta Phuoc Loc and Bouard, 1985). Soon after the impulsive start two symmetric reversed-flow regions develop near the rear stagnation point. As time progresses, these regions grow both in streamwise and lateral extent; secondary eddies are often observed to form subsequently near the point of separation. For large times it is known that periodic vortex shedding occurs from the upper and lower surfaces of the cylinder; however, the exact sequence of events connecting the development at small time to observed features at large times are not well understood for high Reynolds number flows. Theoretical studies of the

21

impulsively-started circular cylinder will be discussed in §2.4 in which it is argued that the flow near the upstream separation point ultimately focuses toward a sharp eruption. This highly unsteady event occurs within a very narrow streamwise zone and culminates in an abrupt ejection of fluid away from the surface.

Although at first glance it might appear that vortices near solid surfaces would induce motions very different from that of unsteady bluff body flows, it emerges that the resulting boundary-layer flow also exhibits unsteady eruptions. Vortices may be shed from upstream surfaces (such as airfoil tips), in the dynamic stall of a pitching airfoil or from other objects which protrude into the flow. Three-dimensional flows encountering surface-mounted obstacles, such as wing/body junctures, also produce vortices which interact with the surface. On a much smaller scale, turbulent boundary layers contain complex vortical structures known as hairpin vortices which convect along the surface (Smith *et al.*, 1991). In each of these examples, the adverse pressure gradient induced by the vortex on the surface generates unsteady eruptive events which are surprisingly similar considering the differences of their various origins. These vortex-induced eruptions are reviewed by Doligalski, Smith and Walker (1994), and model problems have been considered numerically by Doligalski and Walker (1984), who considered a convected rectilinear vortex, Ersoy and Walker (1985, 1986), who considered counter-rotating vortex pairs, and Walker *et al.* (1987), who considered vortex rings experimentally and theoretically. In all model problems, a spike was found to form eventually in the boundary-layer displacement thickness in an event indicative of an unsteady boundary-layer eruption.

A three-dimensional example of vortex-induced eruptions occurs near the base of surface-mounted obstacles as in Baker (1979) and Doligalski *et al.* (1994). As a flow encounters a large three-dimensional obstacle on the surface, adverse pressure gradients in both the streamwise and cross-stream directions cause the vorticity within the boundary layer to become concentrated into discrete vortices near the juncture. These vortices, often called 'necklace' or 'horseshoe' vortices, wrap around the obstacle and extend downstream. For high Reynolds numbers, a series of several

22

horseshoe vortices can develop. An unsteady eruption, essentially similar to the two-dimensional case, can be induced by the portions of the vortex just upstream of the obstacle and also along the streamwise legs extending downstream once the Reynolds number is sufficiently high. After an eruption occurs, the ejected boundary-layer vorticity is observed to wrap around the primary vortex adjacent to the obstacle causing it to convect toward the obstruction and diminish in strength. Another vortex is then observed to form upstream, and the process repeats in a periodic fashion.

Perhaps the most widely applicable example of vortex-induced unsteady eruptions occurs on a much smaller scale within transitional and turbulent boundary layers. Turbulent boundary layers generally consist of two regions: (1) a thin inner wall layer adjacent to the surface, where viscous effects are important, and (2) an outer layer comprising the bulk of the boundary layer where the flow is predominantly inviscid but highly rotational. Vortex structures are common within the outer layer, and in recent years much research has been focused on the hairpin vortex which is believed to be the central element in the generation and maintenance of turbulence in wall-bounded flows. For recent reviews of this process see Falco (1991), Grass *et al.* (1991), Robinson (1991) and Smith *et al.* (1991). It has been shown experimentally that hairpin vortices can be generated by small disturbances on the surface, as well as by fluid injection at the surface (Acarlar and Smith, 1987a,b); the subsequent evolution of the hairpin vortex has been documented experimentally by these authors as well as computationally by Hon and Walker (1991). As a hairpin convects above the surface, the rotational motion of its legs, which are oriented in the streamwise direction, causes the formation of low-speed streaks within the wall layer that extend in the streamwise direction. As the hairpin convects downstream, it moves closer to the wall and eventually provokes an interaction with the viscous wall layer. Local adverse streamwise and lateral pressure gradients are induced on the surface in the regions between the legs and behind the vortex head. In these regions, therefore, three-dimensional unsteady eruptions occur along crescent-shaped ridges (see Van Dommelen and Cowley, 1990 and Smith *et al.*, 1991) injecting highly rotational fluid

23

into the outer region of the boundary layer. These plumes of vorticity then roll over and form new hairpin vortices setting up a regenerative process in which the turbulence is initially generated and subsequently sustained through the introduction of new vorticity from the wall layer into the outer region.

Finally, an interesting example of unsteady separation which exhibits eruptions induced by both the geometry and the interaction of vortices with the surface flow is the dynamic stall process at high Reynolds numbers. This stall process occurs when an airfoil is pitched up rapidly in applications involving maneuverable aircraft as well as on the blades of rotorcraft. As an airfoil is pitched up, an increasingly adverse pressure gradient forms on the upper surface of the airfoil, and a recirculation zone forms downstream of the leading edge. Similar to the flow about an impulsively-started circular cylinder, an unsteady eruption subsequently occurs on the upstream side of this region sending a plume of near-wall vorticity into the external flow. This eruptive spire then rolls up to form the primary stall vortex. As the primary stall vortex convects downstream along the surface, a second eruption of the near-wall flow is induced near midchord. The eruptive plume then rolls over the primary vortex in a strong viscous-inviscid interaction. For the duration of the dynamic stall event, when the primary vortex remains close to the surface, dramatic increases in lift can be realised. However, stall occurs when the vortex detaches from the upper surface of the airfoil and convects into the wake causing a significant decrease in lift and a strong pitching moment on the airfoil. In some situations, such as rapid flight maneuvers, the first portion of this type of event may be desirable in order to enhance lift and performance. On the other hand, the strong pitching moment associated with stall can have a serious negative impact on the performance of rotorcraft. Stall is also not desirable in turbomachinery where the objective is to maintain smooth attached flow over the blades. For more detailed discussions of dynamic stall see McCroskey (1982) and Doligalski *et al.* (1994).

There are many applications in which unsteady boundary-layer separation is a prominent flow feature, but two model problems illustrate many of the generic features of the phenomenon and have been the subject of extensive theoretical study; these are

24

the impulsively-started circular cylinder and the rectilinear vortex above a plane wall. Many numerical studies of the impulsive start of circular cylinders (see, for example, Collins and Dennis, 1973 and Cebeci, 1982, 1986) accurately predicted the flow for small times and compared well with experimental investigations (Bouard and Coutenceau, 1980). However, significant numerical difficulties were experienced by all authors in extending the boundary-layer calculations significantly beyond a stage where recirculation developed in the boundary layer. Similar difficulties were encountered at large times by Walker (1978) (see also Doligalski and Walker, 1984) when computing the boundary-layer evolution induced by a two-dimensional vortex. A common feature in all of these studies was the formation of a growing reversed-flow region. Eventually, the formation of a region of narrow streamwise extent in the upstream portion of the recirculation zone was observed where dramatic increases in boundary-layer thickness and displacement velocity occurred just prior to failure of the numerical algorithm.

This apparent difficulty was resolved subsequently by Van Dommelen and Shen (1980, 1982). These authors obtained numerical solutions of the boundary-layer equations in Lagrangian coordinates, wherein the trajectories of the fluid particles are determined; this was in contrast to all of the previous studies where traditional Eulerian coordinates were utilized. The Lagrangian formulation of the classical boundary-layer equations will be discussed in §2.3; it emerges that fluid motion in the streamwise direction in this description (governed by the momentum equation) is decoupled from that normal to the surface (governed by the continuity equation). Van Dommelen and Shen (1980, 1982) pointed out that the streamwise momentum equation does not contain the quantities (y and v) which become large as an eruption initiates, and the Lagrangian solution remains regular even after the occurrence of a singularity in the continuity equation. An additional advantage of Lagrangian coordinates is that it permits an unambiguous criterion for the occurrence of a singularity in the boundary-layer solution. Van Dommelen and Shen (1980, 1982) performed a numerical calculation for the impulsively-started circular cylinder and found that the boundary-

layer solution does develop a singularity at a finite time in which the displacement thickness and normal velocity at the outer edge of the boundary layer become unbounded. A computation in Lagrangian variables was also carried out by Peridier *et al.* (1991a) for the vortex-induced separation problem. Here again the boundary layer evolved toward a sharp eruption resulting in a singularity of the same form as Van Dommelen and Shen (1982) for the impulsively-started circular cylinder. These classical boundary-layer results will be discussed in §2.4.

The analytical form of this terminal boundary-layer structure for two-dimensional incompressible flows was determined by Van Dommelen and Shen (1982) and Elliott *et al.* (1983), and a detailed discussion will be given in §2.5. This structure describes the formation of a sharp spike in the boundary-layer thickness in a region which progressively narrows in the streamwise direction to zero thickness as the solution evolves toward a singularity at $t = t_s$. In the process the boundary layer bifurcates into two essentially passive shear layers above and below an intermediate vorticity-depleted region which thickens normal to the surface as the time of the singularity is approached. An important characteristic of this terminal state is that the structure is ultimately independent of the specific form of the external adverse pressure gradient which originally initiated the eruptive process. Consequently, the structure is believed to be generic and to apply to most cases of unsteady boundary-layer eruptions in two-dimensional incompressible flow at high Reynolds numbers.

Of course singularities do not exist in real fluid flows, and when they occur in a mathematical model, they represent the consequences of neglecting certain physical mechanisms which must come into play as a singularity develops. Classical non-interacting boundary-layer theory describes the evolution of a thin layer adjacent to the surface driven by an inviscid pressure gradient that is generally imposed in a calculation for an indefinite period of time. However, the terminal boundary-layer solution describes a locally and rapidly thickening boundary layer which at some point must begin to alter the outer flow initiating interaction between the viscous boundary layer

and the inviscid external flow. This viscous-inviscid interaction may be dealt with in two ways namely: (1) a continuation of a limit analysis for infinite Reynolds number or (2) conventional interacting boundary-layer theory.

In the latter technique, a large but finite value of the Reynolds number is assumed, and the boundary-layer equations are solved as usual except that the pressure (or external velocity), rather than being prescribed, is coupled with the displacement thickness (or displacement velocity) through an interaction condition containing a Cauchy principal-value integral. This approach has been used by Henkes and Veldman (1987), Chuang and Conlisk (1989), Riley and Vasantha (1989) and Peridier *et al.* (1991b) to compute the boundary layers on an impulsively-started circular cylinder and along a wall induced by the passage of a vortex. The results have been somewhat contradictory, but most suggest that some type of breakdown occurs in this formulation as well. Henkes and Veldman (1987) indicate a delay in the onset of breakdown when interaction is taken into account (as compared to the limit problem $Re \to \infty$). On the other hand, Riley and Vasantha's (1989) calculations apparently did not reveal any singular behavior. The results of these studies may be suspect for large times because Eulerian coordinates and first-order methods were used for solving the Cauchy integral. On the other hand, Peridier *et al.* (1991b), utilizing Lagrangian coordinates, found that interacting boundary-layer theory actually gave rise to a singularity at an earlier time than computed without interaction. Chuang and Conlisk (1989) also experienced breakdown for a similar vortex-induced separation problem using Eulerian coordinates. Both of these investigations utilized second-order accurate schemes for the Cauchy integral. The calculations of Peridier *et al.* (1991b) also corroborate the scalings found by Elliott, Cowley and Smith (1983) for the first interactive stage to be discussed in §3.2. In addition, Smith (1988b) concluded on theoretical grounds that the unsteady interacting boundary-layer formulation could breakdown at a finite time and determined the resulting singular structure; the numerical results of Peridier *et al.* (1991b) are in broad agreement with this structure. In §2.6 interacting boundary-layer results will be discussed in more detail.

27

The alternative approach is to consider a limit analysis ($Re \rightarrow \infty$) to discern the appropriate flow regions and their scalings that must develop just prior to the time of the singularity in the non-interactive case. Such a limit analysis has been carried out by Elliott *et al.* (1983) for two-dimensional incompressible flows; this is called the first interactive stage and a detailed description will be given in chapter 3. The flow regions delineated in the terminal boundary-layer structure evolve during this stage subject to an interaction condition relating the external pressure (which is imposed across the separating boundary layer) and the growing displacement thickness. While the two bounding shear layers associated with the terminal solution remain passive, the flow in the intermediate region is altered by the effects of interaction. A numerical solution of the first interactive stage of unsteady boundary-layer separation was considered in this thesis. Due to the recent success of numerical calculations based on Lagrangian coordinates (Van Dommelen and Shen, 1980 and Peridier *et al.,* 1991a,b), a solution was sought using the Lagrangian formulation for the first interactive stage. The region of primary interest is the intermediate layer which is governed by an inviscid streamwise momentum equation. Interaction is accounted for by a Cauchy principal-value integral relating the pressure distribution in the outer inviscid flow to the displacement thickness of the growing boundary layer. The detailed numerical procedures and results will be described in chapter 3.

2.2 Definition of Unsteady Separation

For steady boundary-layer flows past fixed walls, separation has traditionally been defined as implying the existence of a region of reversed flow attached to the surface with the point of separation being characterized by vanishing of the wall shear stress. This definition, however, is not sufficiently general for application to all cases of separation. In particular, flows involving moving surfaces may develop points of zero wall shear and even regions of reversed flow but without any dramatic effect on the boundary layer (see Sears and Telionis, 1971, 1975). In such situations the

28

classical criterion for separation, namely vanishing of the wall shear, is often not consistent with general concepts of boundary-layer separation that imply a significant local alteration of the external flow. This led Sears and Telionis (1971, 1975) to propose that separation should be defined in all cases as occurring with the development of a singularity in classical (non-interactive) boundary-layer solutions. The evolution of a singularity normally signifies that the assumption of a thin non-interactive boundary layer is violated. Sears and Telionis (1975) argued that separation occurs when a boundary layer breaks away from the surface and is no longer confined to an $O(Re^{-1/2})$ layer adjacent to the surface. Such an event signals a breakdown of the boundary-layer assumptions. Although modern terminology varies somewhat, most authors currently use the terms 'separation,' 'breakdown' or 'breakaway' synonymously with the onset of a singularity in a boundary-layer solution. In steady flows this takes the form of a Goldstein (1948) singularity at a point of zero wall shear. In unsteady flows this singularity has only recently been identified by Van Dommelen and Shen (1980) and will be discussed in detail in sections 2.4 and 2.5.

While this modern definition of separation is clear, a precise criterion for the occurrence of the separation singularity is necessary. This criterion has come to be known as the MRS model named for Moore (1958), Rott (1956) and Sears (1956). The MRS model identifies conditions which must be satisfied at a two-dimensional separation point where the boundary-layer solution becomes singular. In general, this point may be located away from the surface. Let the location of the separation point be (x_s, y_s) where the streamwise velocity is u_s; the MRS model specifies two necessary conditions that must apply at separation. First, the separation point must move with the local flow speed (MRS I)

$$u_s = u(x_s, y_s), \qquad\qquad (2.1a)$$

where u is the streamwise velocity. Secondly, the separation point must be located at a point of zero shear (MRS II); that is,

29

$$\frac{\partial u}{\partial y} = 0 \quad \text{at} \quad x = x_s, y = y_s, \tag{2.1b}$$

or equivalently, the separation point must be located somewhere along a line of zero vorticity $(\omega = -\partial u/\partial y)$. It should be noted that a zero vorticity line exists in any flow containing a region of recirculation. Van Dommelen (1991) argues that because the flow is effectively inviscid in the outer region of the boundary layer, the vorticity of each fluid particle must remain constant; therefore, the zero vorticity line is also a material line. Thus, if there are initial differences in velocity of adjacent fluid particles along this line, a streamwise compression must take place; by continuity this compression requires a corresponding expansion in the normal direction.

Observe that for steady flow over stationary surfaces the separation point remains fixed, and here the MRS criterion reduces to the classical definition of separation, *viz.*

$$\frac{\partial u}{\partial y} = 0 \quad \text{at} \quad u = 0. \tag{2.2}$$

Van Dommelen (1981) referred to this type of separation as 'non-slipping separation,' because the point of separation is not moving with respect to the wall. He also identified two possible types of unsteady separation for $u_s \neq 0$. If the separation point is moving upstream with respect to the surface, Van Dommelen (1981) referred to it as 'upstream-slipping separation;' conversely, cases where the separation point is moving downstream with respect to the surface are called 'downstream-slipping separation.' Upstream-slipping separation has been observed in many problems including the impulsively-started circular cylinder and vortex-induced separation. The case of downstream-slipping separation, on the other hand, occurs much less frequently if at all. Indeed, in a recent study by Degani and Walker (1994), no cases of downstream-slipping separation were observed for either the boundary layer induced by a vortex or

30

the translating and rotating circular cylinder; this latter problem had been conjectured to contain both upstream- and downstream-slipping separation because the upper and lower surfaces of the rotating cylinder move in opposite directions with respect to the mainstream flow.

2.3 Lagrangian Methods

Traditionally, solutions to the boundary-layer equations have been sought in Eulerian coordinates as given by equations (1.4). In this description of fluid motion, flow quantities are evaluated at fixed points in space as functions of time (for an unsteady flow). However, in unsteady eruptive flows of the type considered here, conventional Eulerian methods generally fail as the flow focuses into a narrow streamwise region containing large updrafts. Alternatively, the boundary-layer equations may be formulated in Lagrangian variables (Van Dommelen, 1981) in which the trajectories and flow quantities are evaluated for a large number of individual fluid particles. As discussed in a recent review by Cowley, Van Dommelen and Lam (1990), this description of fluid motion has significant advantages over an Eulerian formulation in problems involving unsteady separation at high Reynolds numbers.

In Lagrangian coordinates, the independent variables are time t and the initial (at time t_0) spatial locations ξ and η of the fluid particles in the streamwise and normal directions, respectively. The dependent variables are the current fluid particle positions $x(\xi,\eta,t)$, $y(\xi,\eta,t)$ in the streamwise and normal direction with corresponding streamwise $u(\xi,\eta,t)$ and normal $v(\xi,\eta,t)$ velocities. In order to transform from Eulerian to Lagrangian coordinates, the following transformation laws are used (see, for example, Van Dommelen, 1981 and Peridier and Walker, 1989):

$$\frac{\partial}{\partial x} = \frac{\partial y}{\partial \eta}\frac{\partial}{\partial \xi} - \frac{\partial y}{\partial \xi}\frac{\partial}{\partial \eta}, \quad \frac{\partial}{\partial y} = -\frac{\partial x}{\partial \eta}\frac{\partial}{\partial \xi} + \frac{\partial x}{\partial \xi}\frac{\partial}{\partial \eta}. \tag{2.3a,b}$$

The momentum equation (1.4a) then becomes

31

$$\frac{\partial u}{\partial t} = -\frac{\partial p}{\partial x} + \left(\frac{\partial x}{\partial \xi}\frac{\partial}{\partial \eta} - \frac{\partial x}{\partial \eta}\frac{\partial}{\partial \xi}\right)^2 u, \quad \frac{\partial x}{\partial t} = u, \qquad (2.4a,b)$$

where the convective terms on the left-hand side (given by the substantial derivative in Eulerian coordinates) simply represent the acceleration of a fluid particle and are, therefore, greatly simplified in the Lagrangian formulation. At the same time, the viscous term becomes considerably more complicated The boundary-layer equations (2.4) are solved subject to the boundary conditions

$$u = 0 \quad \text{at} \quad \eta = 0, \qquad (2.5a)$$

$$u \to U_e(x,t) \quad \text{as} \quad \eta \to \infty, \qquad (2.5b)$$

where $U_e(x,t)$ is the external streamwise velocity. The initial conditions are

$$u = u_0(\xi,\eta) \quad \text{at} \quad t = t_0, \qquad (2.6a)$$

$$x = \xi, y = \eta \quad \text{at} \quad t = t_0. \qquad (2.6b)$$

Examination of the boundary-layer equations (2.4) reveals that the flow in the streamwise direction, given by $x(\xi,\eta,t)$ and $u(\xi,\eta,t)$, has apparently been decoupled from that in the normal direction. It is evident that at separation, the normal particle positions $y(\xi,\eta,t)$ and velocities $v(\xi,\eta,t)$ become large (Cowley *et al.*, 1990); on the other hand, the streamwise particle positions $x(\xi,\eta,t)$ and velocities $u(\xi,\eta,t)$ remain regular even at separation. Since the formulation in Eulerian coordinates (1.4) involves the normal velocity, numerical calculations normally encounter severe difficulties and generally fail as the boundary layer starts to separate from the wall.

While it is not necessary to evaluate y or v in order to advance the solution of equation (2.4) in time, the normal particle positions $y(\xi,\eta,t)$ and velocities $v(\xi,\eta,t)$

may be computed at any stage during the calculation from an integration of the continuity equation. The continuity equation in Lagrangian coordinates becomes (Van Dommelen, 1981)

$$-\frac{\partial x}{\partial \eta}\frac{\partial y}{\partial \xi} + \frac{\partial x}{\partial \xi}\frac{\partial y}{\partial \eta} = 1. \tag{2.7}$$

This relation is the mathematical statement that the Jacobian of the transformation is one and implies that the volume of individual fluid particles is conserved. Since the streamwise particle position distribution $x(\xi,\eta,t)$ is known from a solution of equation (2.4), the continuity equation (2.7) may be regarded as a first-order linear equation for the unknown normal particle positions $y(\xi,\eta,t)$. Solutions of the continuity equation are obtained along characteristic curves which are lines of constant x having the equations

$$\frac{d\xi}{-\partial x/\partial \eta} = \frac{d\eta}{\partial x/\partial \xi} = dy. \tag{2.8}$$

When these characteristics of constant x are plotted against the initial particle locations (ξ,η) at a given time, they represent the initial locations of a line of fluid particles which are located along the vertical line $x = $ constant at the current time. Defining (ξ_0,η_0) to be some point along a characteristic at which the normal distance $y(\xi_0,\eta_0,t)$ is taken to be zero (generally at the wall), the normal distance of a fluid particle initially located at (ξ,η) may be expressed from (2.8) as

$$y(\xi,\eta,t) = \int_{(\xi_0,\eta_0)}^{(\xi,\eta)} \frac{ds}{\sqrt{(\partial x/\partial \xi)^2 + (\partial x/\partial \eta)^2}}. \tag{2.9}$$

From the integral (2.9) it is evident that a fluid particle would be located an infinite

33

distance from the wall if a stationary point develops in the $x(\xi,\eta,t)$ field; that is

$$\frac{\partial x}{\partial \xi} = \frac{\partial x}{\partial \eta} = 0 \quad \text{at} \quad \xi = \xi_s, \ \eta = \eta_s, \ t = t_s. \tag{2.10}$$

These conditions for a stationary point in $x(\xi,\eta,t)$ mean physically that two adjacent particles initially located an infinitesimal distance $d\xi$ apart have reached the same x position $(\partial x/\partial \xi = 0)$ but without experiencing any rotation $(\partial x/\partial \eta = 0)$. Cowley, Van Dommelen and Lam (1990) described this process in terms of a fluid particle which has been compressed in the streamwise direction to zero lateral thickness. Continuity then requires the fluid particle to expand rapidly in the normal direction. However, the boundary-layer equations do not contain normal pressure gradient or viscous diffusion effects which would, in principle, act to restrain the normal expansion. Therefore, a singularity develops, and fluid particles are forced to grow an infinite distance away from the surface (on the boundary-layer scale) toward the external flow. The condition (2.10), therefore, provides a criterion for the development of a singularity within the boundary-layer equations at (ξ_s,η_s,t_s). This unambiguous criterion is another significant advantage of the Lagrangian formulation. In the Eulerian formulation there is no clear condition for the evolution of a singularity, and in any case the singularity is not reachable using the Eulerian approach in light of the severe numerical difficulties encountered as the singularity is approached. The asymptotic structure of unsteady separation in two-dimensional incompressible flows in terms of Lagrangian coordinates has been considered by Van Dommelen and Shen (1982) and for three-dimensional compressible flows by Van Dommelen and Cowley (1990) and Cowley *et al.* (1991).

34

2.4 Classical Boundary-Layer Results

The complex flow involved in unsteady boundary-layer separation generally prohibits closed-form analytical solutions from being obtained, and the bulk of the theoretical studies have been based on numerical solutions. As discussed in §2.1, many unsteady separation studies have been associated with either bluff body or vortex-induced flows. A common feature of both environments is the development of a region of adverse streamwise pressure gradient over portions of the surface in which the unsteady separation process is eventually initiated. Two model problems have been studied extensively, namely the impulsively-started circular cylinder and the rectilinear vortex above a plane wall. The dynamics for each of these model problems and the theoretical investigations related to each will be discussed.

The impulsively-started circular cylinder has been the subject of study for many years due to its simple geometry and the fact that the flow features are representative of more complex bluff body flows. When a circular cylinder is impulsively started from rest, a thin boundary layer forms on the surface of the cylinder; this layer is initially completely attached and exhibits no reversed flow. The inviscid flow solution gives the external velocity along the surface as $U_e(x) = 2 \sin(x)$, where x measures radians along the surface from the origin at the front stagnation point. Consequently, the mainstream decelerates from $x = \pi/2$ toward a rear stagnation point at $x = \pi$, and an adverse pressure gradient $(\partial p/\partial x > 0)$ is imposed along the rear portion of the cylinder. This eventually causes the flow near the rear stagnation point to reverse direction and form a small recirculating region attached to the cylinder surface. Defining t to be the dimensionless time with respect to a/U_0, where a is the radius of the cylinder and U_0 is its speed, the onset of reversed flow was found from series expansions in time (see, for example, Cowley, 1983) to occur at $t = 0.32$. Such time-series solutions are normally valid only for small times, and numerical methods are required to extend the solution to larger times. Early attempts at such computations by Collins and Dennis (1973), Bar-Lev and Yang (1975) and Cebeci (1979) were carried out in Eulerian coordinates and

35

were successful in advancing the solution well beyond the onset of reversed flow. After the wall shear first vanishes near the rear stagnation point, the separation point (in the classical sense) moves rapidly upstream as the reversed flow region grows. Eventually, the movement of the separation point slows at approximately 110° from the front stagnation point, and then the recirculating zone starts to expand significantly in the direction normal to the cylinder. These aforementioned studies were able to compute the flow up until this stage with varying degrees of success, but all of them experienced severe numerical difficulties which in hindsight were suggestive of an impending singularity in the boundary-layer equations.

At the time, it was generally believed that the difficulties were due to inadequate numerical algorithms. However, Van Dommelen and Shen (1980) and Van Dommelen (1981) finally showed that the problems were associated with the use of Eulerian coordinates, and by formulating the boundary-layer equations in Lagrangian coordinates (as discussed in §2.3), they were able to compute the flow up until a singularity clearly developed at a finite time $t_s = 1.5$ after the impulsive start. The impulsively-started circular cylinder was shown to exhibit upstream-slipping separation having $u_s = -K$, where $K = 0.26$. The results of Van Dommelen and Shen (1980) showed that the boundary-layer solution in the vicinity of the separation point just prior to the singularity contracted rapidly in the streamwise direction and developed explosive growth away from the wall. Velocity and vorticity profiles from their results at the streamwise location corresponding to separation show that the velocity becomes nearly constant $u \approx -K$ ($\omega \approx 0$) over the bulk of the boundary layer with shear layers that develop above and below the central region.

The evolution of the boundary-layer flow induced by a two-dimensional vortex in an otherwise stagnant fluid above an infinite plane wall proceeds in a similar fashion. The first numerical solutions of this problem were provided by Walker (1978) and were obtained using conventional Eulerian coordinates. In the case of the impulsively-started circular cylinder, the adverse pressure gradient is due to the body geometry, while in this case it is caused by the presence of the vortex convecting above the

surface. Non-dimensionalizing the time by a/V_c, where a is the height of the vortex above the wall, and V_c is the self-induced vortex velocity, a recirculating eddy was found to develop within the boundary layer at $t = 0.28$. Unlike the circular cylinder, however, the eddy is not attached to the surface but forms away from the surface. The eddy subsequently grows in both streamwise and normal extent causing substantial growth locally in the displacement thickness. The calculations of Walker (1978) could not be continued with good accuracy beyond about $t = 0.75$. Upon demonstration of the advantages of the use of Lagrangian coordinates for these types of flows by Van Dommelen and Shen (1980), the problem was revisited by Peridier, Smith and Walker (1991a) (see also Peridier and Walker, 1989) who solved the boundary-layer equations in Lagrangian variables. This work extended the calculation until $t = 0.989$ at which time a singularity formed. Instantaneous streamlines are shown from their results in figure 2.1 for two different times in a frame of reference moving with the vortex; here the vortex center is at $x = 0$, and the vortex is located above the boundary layer. Figure 2.1a shows the streamlines in the boundary layer at $t = 0.45$ which is a time after the recirculating eddy had previously formed between approximately $x = 0$ and $x = 1$. The eddy subsequently grows, particularly in the normal direction, until the occurrence of a singularity (see figure 2.1b) at which time the streamlines just to the left of the eddy focus into a narrow streamwise band in the onset of an eruption from the surface. The resulting temporal evolution of the displacement thickness of the boundary layer is shown in figure 2.2. Again, the flow in the vicinity of separation is seen to collapse to zero thickness in the streamwise direction and expand rapidly away from the surface as the singularity is approached. The velocity of the separation point was negative, and apparently this is another example of upstream-slipping separation. Just as in the case of the impulsively-started circular cylinder (Van Dommelen and Shen, 1980), the results of Peridier *et al.* (1991a) reveal a region of nearly constant velocity surrounding the separation point which is sandwiched between two shear layers above and below. Although the two singularities described here arise in rather different flow environments, it has been shown by Van Dommelen and Shen (1982) and Elliott,
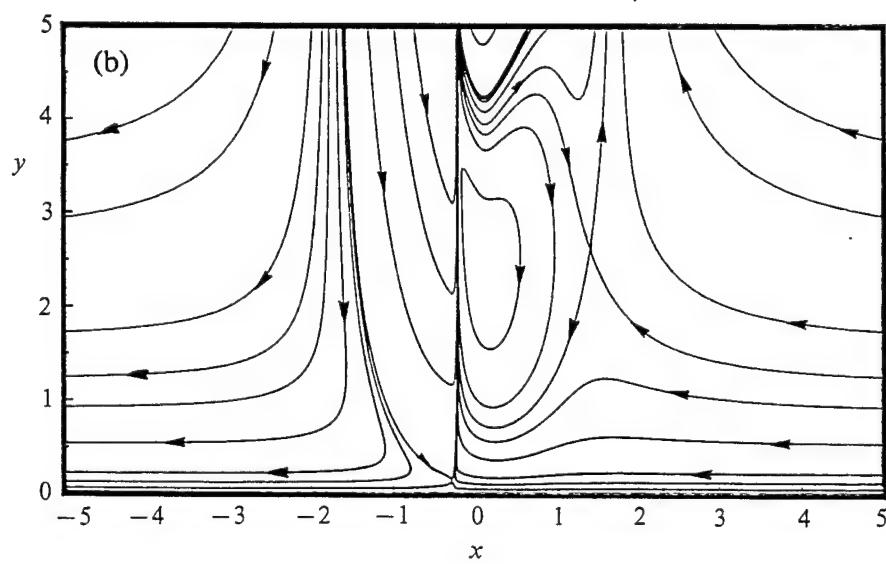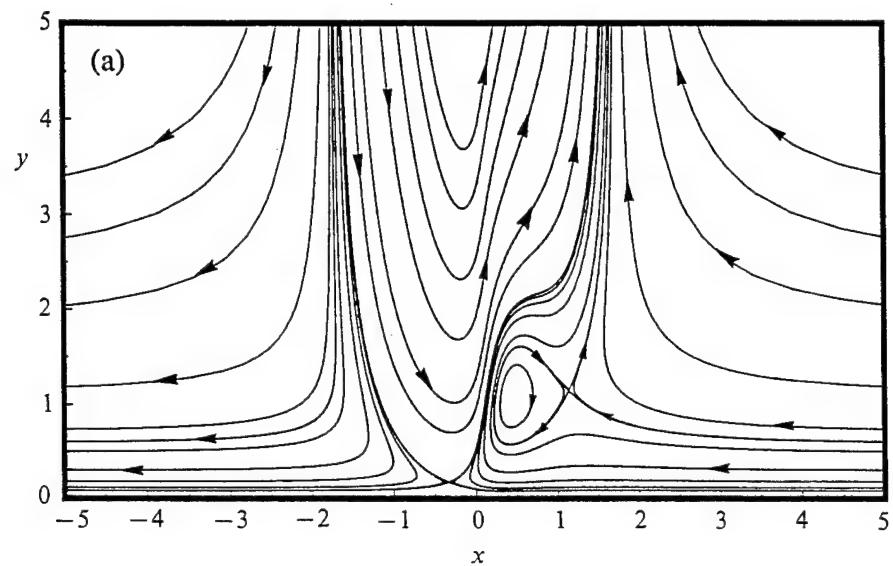
Figure 2.1 - Instantaneous streamlines for vortex-induced separation in
frame of reference moving with vortex located at $x = 0$;
(a) $t = 0.45$; (b) $t = t_s = 0.989$. (Reproduced from Peridier,
Smith and Walker, 1991a).

38
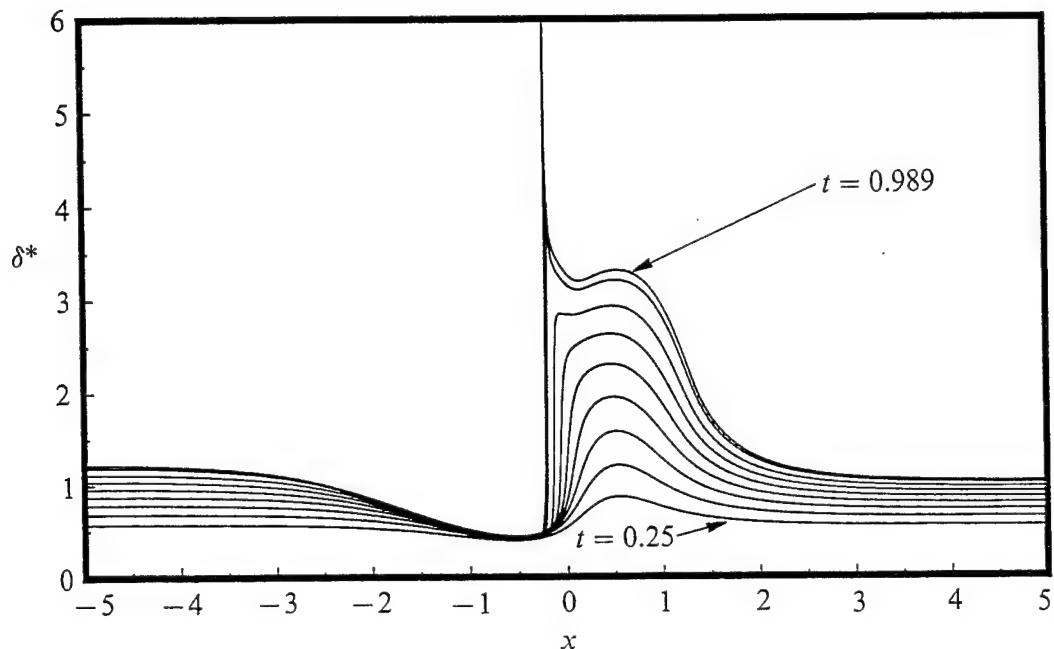
Figure 2.2 - Temporal development of displacement thickness for vortex-induced separation. (Reproduced from Peridier, Smith and Walker, 1991a)

Cowley and Smith (1983) that the form of the singularity itself is probably generic and applies to most cases of unsteady separation, regardless of the flow environment in which it arises. This work is discussed in the next section.

Recently, Degani and Walker (1994) have investigated two other model problems: the translating and rotating circular cylinder and a vortex convected in a uniform flow above a plane wall. Previous investigations of each of these problems were carried out by Ece *et al.* (1984) and Doligalski and Walker (1984), respectively, both using the Eulerian formulation. Using Lagrangian coordinates, Degani and Walker (1994) showed that in both problems the onset of the unsteady separation singularity is delayed, and eventually suppressed, with increasing wall speed. Interestingly, the critical wall speed at which separation was suppressed was found to be just less than the maximum external velocity in both model problems. In all cases considered by Degani and Walker (1994), separation was found to be of the upstream-slipping type.

2.5 Terminal Boundary-Layer Solution

2.5.1 Form of the Terminal Singularity

The numerical results of Van Dommelen and Shen (1980) showed that a singularity can occur in the boundary-layer equations within a finite time, and this prompted Van Dommelen and Shen (1982) and Elliott *et al.* (1983) to seek a local analytical description of the separation singularity which is referred to here as the terminal boundary-layer structure or, equivalently, as the non-interactive singularity. Van Dommelen and Shen (1982) argued that the streamwise particle position field in Lagrangian coordinates should remain regular up to the time of separation; they then constructed a local Taylor series expansion for the momentum equation near the point of separation and represented the solution of the continuity equation (which becomes

40

singular) as an asymptotic series (see also Cowley, Van Dommelen and Lam 1990). Alternatively, Elliott *et al.* (1983) obtained the same structure in Eulerian coordinates. A detailed description of the terminal solution is given here because it constitutes the initial condition for the first interactive stage to be considered in the next chapter.

Taking x and y to be the streamwise and normal coordinates and u and v to be the velocities in their respective directions, scaled boundary-layer variables are defined,

$$Y = Re^{1/2}y, \quad V = Re^{1/2}v, \tag{2.11}$$

so that Y and V are $O(1)$ within the boundary layer. The streamfunction is defined by

$$u = \frac{\partial \psi}{\partial Y}, \quad V = -\frac{\partial \psi}{\partial x}, \tag{2.12}$$

such that the continuity equation is satisfied. In terms of the scaled variables, the unsteady incompressible boundary-layer equations are

$$\frac{\partial u}{\partial t} + u\frac{\partial u}{\partial x} - \frac{\partial \psi}{\partial x}\frac{\partial u}{\partial Y} = -\frac{\partial p}{\partial x} + \frac{\partial^2 u}{\partial Y^2}, \quad u = \frac{\partial \psi}{\partial Y}, \tag{2.13a,b}$$

where $p(x,t)$ is the mainstream pressure distribution determined from an inviscid solution.

Assuming that a singularity develops in the solution of the boundary-layer equations at t_s, a temporal similarity solution is sought as $t \to t_s$ in the immediate vicinity of the moving separation point. At $t = t_s$ the separation point is located at x_s and for upstream-slipping separation is assumed to be drifting with constant velocity $-K$ where $K > 0$. In accordance with the numerical solutions of the boundary-layer equations by Van Dommelen and Shen (1980, 1982) (see also Peridier *et al.*, 1991a),

41

it is evident that the boundary layer is thickening rapidly in a region which is thinning in the streamwise direction just prior to separation. Therefore, consider the following scaled variables which describe the motion in a moving region which progressively thins and eventually arrives at the separation location at $x = x_s$ as $t \to t_s$:

$$x = x_s + K(t_s - t) + (t_s - t)^M \tilde{X}, \quad M > 0, \tag{2.14a}$$

$$Y = (t_s - t)^{-N} \tilde{Y}, \quad N > 0, \tag{2.14b}$$

$$u = -K + (t_s - t)^L \tilde{U}(\tilde{X}, \tilde{Y}) + \cdots, \quad L > 0, \tag{2.14c}$$

where $\tilde{X}$, $\tilde{Y}$ and $\tilde{U}$ are $O(1)$ in the region of interest and L, M and N are to be determined. These variables describe a moving coordinate system which drifts upstream with constant velocity $-K$ with the origin arriving at the separation point x_s at time t_s. Since $\partial x / \partial t = u$ it follows from (2.14a) and (2.14c) that

$$L = M - 1, \quad M > 1. \tag{2.15}$$

An expression for the streamfunction may be obtained by integrating equation (2.13b) using equations (2.14b,c) to give

$$\psi = -K(t_s - t)^{-N} \tilde{Y} + (t_s - t)^{M-N-1} \tilde{\Psi}, \quad \tilde{U} = \frac{\partial \tilde{\Psi}}{\partial \tilde{Y}}. \tag{2.16}$$

Substitution of the transformations (2.14) and (2.16), with the relationship between L and M from equation (2.15), into the boundary-layer equations (2.13) shows that the magnitudes of the unsteady, inertial, pressure gradient and viscous terms are $O(t_s - t)^{M-2}$, $O(t_s - t)^{M-2}$, $O(t_s - t)^0$ and $O(t_s - t)^{2N+M-1}$, respectively. Therefore, as $t \to t_s$ the viscous term is negligible with respect to the pressure gradient term, and

42

the principal balance is inviscid. Furthermore, a balance between the unsteady convection terms and the pressure gradient is only possible if $M = 2$; however, solutions where $1 < M < 2$ represent a larger streamwise scale and would dominate if they exist. It will subsequently be assumed that $1 < M < 2$, and such solutions will be shown to occur. In this case the boundary-layer equations become

$$- (M-1)\, \tilde{U} + M\tilde{X}\frac{\partial \tilde{U}}{\partial \tilde{X}} - N\tilde{Y}\frac{\partial \tilde{U}}{\partial \tilde{Y}} + \tilde{U}\frac{\partial \tilde{U}}{\partial \tilde{X}} - \frac{\partial \tilde{\Psi}}{\partial \tilde{X}}\frac{\partial \tilde{U}}{\partial \tilde{Y}} = 0, \quad \tilde{U} = \frac{\partial \tilde{\Psi}}{\partial \tilde{Y}}, \quad (2.17\text{a,b})$$

constituting a first-order nonlinear equation for $\tilde{U}(\tilde{X},\tilde{Y})$ which is independent of the mainstream pressure gradient. Generally, the presence of an adverse external pressure gradient initiates the eruptive process; however, the singular flow structure which results is generic, and the terminal solution apparently "forgets" the initiating pressure gradient. Solutions to equations (2.17) were originally given by Elliott *et al.* (1983); an alternative method of solution is given in appendix A where it is shown that

$$\frac{\partial \tilde{U}}{\partial \tilde{Y}} = \pm \frac{|\tilde{U}|^{1+N/(M-1)}}{G(\phi)}, \quad \phi = \frac{|\tilde{U}|^{M/(M-1)}}{|\tilde{U}+\tilde{X}|}, \quad (2.18\text{a,b})$$

where G is a strictly positive function. Integration of equation (2.18a) for fixed $\tilde{X}$ gives

$$\tilde{Y} - \tilde{Y_0}(\tilde{X}) = \text{sgn}(\tau) \int_{\tilde{U_0}(\tilde{X})}^{\tilde{U}} G(\phi) \,\big| \,\tilde{U}\,\big|^{-[1+N/(M-1)]}\, \mathrm{d}\tilde{U}. \quad (2.19)$$

Here, $\tilde{Y_0}(\tilde{X})$ is the location where $\tau = 0$ and where the velocity $\tilde{U}$ is a minimum denoted by $\tilde{U_0}(\tilde{X})$. It then remains to determine the unknown functions $\tilde{U_0}(\tilde{X})$, $\tilde{Y_0}(\tilde{X})$ and $G(\phi)$ as well as the scales M and N on x and Y, respectively.

Because $\tilde{Y_0}(\tilde{X})$ defines a line of zero shear, and because $\tilde{U_0}(\tilde{X})$ is in general

43

non-zero, equation (2.18a) requires that $G(\phi) \to \infty$ for values of ϕ such that

$$\phi \to \phi_0 = \frac{|\tilde{U}_0|^{M/(M-1)}}{|\tilde{U}_0 + \tilde{X}|} > 0 \qquad (2.20)$$

along the reference line. For given values of ϕ_0, (2.20) defines an equation for $\tilde{U}_0$ in terms of $\tilde{X}$, but different branches are possible depending on the signs of $\tilde{U}_0$ and $\tilde{U}_0 + \tilde{X}$. However, in order for $\tilde{U}_0(\tilde{X})$ to be a single-valued function of $\tilde{X}$, only the following branches are possible

$$\tilde{U}_0^{M/(M-1)} + \phi_0 (\tilde{U}_0 + \tilde{X}) = 0 \quad \text{for } \tilde{U}_0 > 0, \ \tilde{U}_0 + \tilde{X} < 0, \qquad (2.21a)$$

$$(- \tilde{U}_0)^{M/(M-1)} - \phi_0 (\tilde{U}_0 + \tilde{X}) = 0 \quad \text{for } \tilde{U}_0 < 0, \ \tilde{U}_0 + \tilde{X} > 0. \qquad (2.21b)$$

Recalling that $M > 1$, and recognizing from equations (2.21) that

$$\tilde{U}_0 \sim - \tilde{X} \quad \text{as} \quad \tilde{X} \to 0, \qquad (2.22)$$

the exponent $M/(M - 1)$ must be an integer greater than one; this is because the alternative is not acceptable implying an infinite derivative of $\tilde{U}_0(\tilde{X})$ at $\tilde{X} = 0$. Furthermore, $M/(M - 1)$ must be odd in order to have a unique $\tilde{U}_0(\tilde{X})$ for each $\tilde{X}$, and thus equations (2.21a,b) may be written as the single equation

$$\tilde{U}_0^{M/(M-1)} + \phi_0 (\tilde{U}_0 + \tilde{X}) = 0, \quad \phi_0 > 0. \qquad (2.23)$$

Therefore, the choices for the scale on x are narrowed to

$$M = \frac{3}{2}, \frac{5}{4}, \frac{7}{6}, \cdots \qquad (2.24)$$

44

which all lie in the range $1 < M < 2$ as assumed.

As noted previously, the function G must be such that $G(\phi) \rightarrow \infty$ as $\phi \rightarrow \phi_0$ suggesting that

$$G \sim \frac{G_1}{(\phi - \phi_0)^{q_1}} \quad \text{as} \quad \phi \rightarrow \phi_0, \tag{2.25}$$

where G_1 and q_1 are constants to be found. To determine q_1 the Taylor series expansions of ϕ and $\tilde{U}$ are written for points close to the reference line and fixed $\tilde{X}$ as

$$\phi - \phi_0 = (\tilde{U} - \tilde{U}_0) \left. \frac{\partial \phi}{\partial \tilde{U}} \right|_{\tilde{U}_0} + \cdots, \tag{2.26}$$

$$\tilde{U} - \tilde{U}_0 = (\tilde{Y} - \tilde{Y}_0) \left. \frac{\partial \tilde{U}}{\partial \tilde{Y}} \right|_{\tilde{Y}_0} + \frac{(\tilde{Y} - \tilde{Y}_0)^2}{2} \left. \frac{\partial^2 \tilde{U}}{\partial \tilde{Y}^2} \right|_{\tilde{Y}_0} + \cdots. \tag{2.27}$$

Substituting the expansion (2.26) for ϕ into equation (2.25), and observing the form of the shear stress from the leading-order term of (2.27), equation (2.18a) indicates that

$$\tilde{Y} - \tilde{Y}_0 \sim (\tilde{U} - \tilde{U}_0)^{1 - q_1} + \cdots \quad \text{as} \quad \tilde{Y} \rightarrow \tilde{Y}_0. \tag{2.28}$$

Because the shear stress is zero along the reference line, substitution of equation (2.28) into the expansion (2.27) for $\tilde{U}$ requires the exponent to be $q_1 = 1/2$. It can also be shown from considerations of the solution near the top and bottom of the domain, which will be discussed in the next section, that $G(\infty)$ must be finite and nonzero. These conditions on $G(\phi)$ along with the regularity condition of Van Dommelen (1981) lead to the simplest choice acceptable for $G(\phi)$

$$G(\phi) = \Lambda\left(\frac{\phi}{\phi - \phi_0}\right)^{1/2}, \tag{2.29}$$

where Λ is an arbitrary constant.

Finally, it remains to determine N, the scale on Y. Begin by expanding the integral in equation (2.18b) (referred to here as I) about the reference line velocity $\tilde{U} = \tilde{U}_0(\tilde{X})$ and substituting the expression (2.25) for $G(\phi)$ near the reference line to give

$$\tilde{Y} - \tilde{Y}_0 = \left(\tilde{U} - \tilde{U}_0\right)\frac{\partial I}{\partial \tilde{U}}\bigg|_{\tilde{U}_0} + \cdots = \pm\left(\tilde{U} - \tilde{U}_0\right)|\tilde{U}_0|^{-[1+N/(M-1)]}\frac{G_1}{(\phi - \phi_0)^{1/2}} + \cdots. \tag{2.30}$$

In order to substitute the expansion (2.26) for ϕ, the derivative of ϕ with respect to $\tilde{U}$ must be evaluated at $\tilde{U} = \tilde{U}_0(\tilde{X})$. Differentiating (2.19), taking care to deal with the absolute values, it is found that

$$\frac{\partial \phi}{\partial \tilde{U}} = \frac{\left(M\tilde{X} + \tilde{U}\right)|\tilde{U}|^{M/(M-1)}}{(M-1)\,\tilde{U}\,|\tilde{U} + \tilde{X}|\left(\tilde{U} + \tilde{X}\right)}. \tag{2.31}$$

Evaluating equation (2.31) at $\tilde{U} = \tilde{U}_0(\tilde{X})$, recalling that $M/(M-1)$ is an odd integer and using the expression for $\tilde{U}_0 + \tilde{X}$ from equation (2.23), the expansion (2.26) for ϕ becomes

$$\phi - \phi_0 = -\left(\tilde{U} - \tilde{U}_0\right)\phi_0^2\,\tilde{U}_0^{\frac{1-2M}{M-1}}\frac{\left(M\,\tilde{X} + \tilde{U}_0\right)}{M-1} + \cdots. \tag{2.32}$$

Substitution of this expansion into (2.30) gives

$$\tilde{Y} - \tilde{Y}_0 = \pm\frac{G_1}{\phi_0}(M-1)^{1/2}\left(\frac{\tilde{U} - \tilde{U}_0}{M\tilde{X} + \tilde{U}_0}\right)^{1/2}|\tilde{U}_0|^{-[1+N/(M-1)]}\,\tilde{U}_0^{\frac{2M-1}{2(M-1)}} + \cdots. \tag{2.33}$$

46

If this expression is rewritten in terms of $\tilde{U} - \tilde{U}_0$, and using the behavior of $\tilde{U}_0$ as $\tilde{X} \to 0$ given by equation (2.22), the expansion for $\tilde{U}$ may be written as

$$\tilde{U} - \tilde{U}_0 = \frac{\phi_0^2}{G_1^2} \tilde{X} |\tilde{X}|^{\frac{2N-1}{M-1}} (\tilde{Y} - \tilde{Y}_0)^2 + \cdots, \quad \tilde{X} \to 0. \tag{2.34}$$

Consequently, in order to avoid singularities at $\tilde{X} = 0$, the exponent must be such that

$$\frac{2N-1}{M-1} = -1, 0, 1, 2, ..., \tag{2.35}$$

and thus there are an infinite number of possibilities for the scales M and N. However, it is the lowest order singularity, the one with the slowest growth rate (smallest N), which is of interest. It follows from equations (2.24) and (2.35) that

$$M = \frac{3}{2}, \quad N = \frac{1}{4}. \tag{2.36}$$

Having determined the scales (2.36) and the function $G(\phi)$, it is possible to return to the terminal-state transformations and the solution of the terminal boundary-layer equation. The constants ϕ_0 and Λ appearing in equation (2.29) may be scaled out by redefining the transformation in equations (2.14a,b,c) according to

$$x = x_s + K (t_s - t) + (t_s - t)^{3/2} \phi_0^{1/2} \tilde{X}, \tag{2.37a}$$

$$Y = (t_s - t)^{-1/4} \Lambda \phi_0^{-1/4} \tilde{Y}, \tag{2.37b}$$

$$u = -K + (t_s - t)^{1/2} \phi_0^{1/2} \tilde{U}(\tilde{X}, \tilde{Y}) + \cdots. \tag{2.37c}$$

Having chosen the form of $G(\phi)$ given by equation (2.29), this along with equation (2.19) for ϕ, may be substituted into the solution (2.18a) or (2.18b) of the terminal

47

boundary-layer equation. Recalling the appropriate signs from (2.21a,b) for the quantities within the absolute values, the solution becomes

$$\tau = \frac{\partial \tilde{U}}{\partial \tilde{Y}} = \pm \left(\tilde{U}^3 + \tilde{U} + \tilde{X} \right)^{1/2}, \qquad (2.38a)$$

or in integral form

$$\tilde{Y} - \tilde{Y}_0 = \text{sgn}(\tau) \int_{\tilde{U}_0}^{\tilde{U}} \frac{d\tilde{U}}{\left(\tilde{U}^3 + \tilde{U} + \tilde{X} \right)^{1/2}}. \qquad (2.38b)$$

At this point in the development of the terminal boundary-layer solution, it is instructive to discuss the significance of the reference line height $\tilde{Y}_0(\tilde{X})$ and the streamwise velocity $\tilde{U}_0(\tilde{X})$ along this line. Until now $\tilde{Y}_0(\tilde{X})$ has been defined as the height at each $\tilde{X}$ at which a minimum in the streamwise velocity profile occurs, corresponding to a line of zero shear. Because the minimum for each velocity profile occurs along this line, the shear stress must be positive $(\partial \tilde{U}/\partial \tilde{Y} > 0)$ above the reference line $(\tilde{Y} > \tilde{Y}_0(\tilde{X}))$ and negative $(\partial \tilde{U}/\partial \tilde{Y} < 0)$ below it $(\tilde{Y} < \tilde{Y}_0(\tilde{X}))$. Therefore, integration of equation (2.38b) from the reference line velocity $\tilde{U}_0(\tilde{X})$ to some value of $\tilde{U}$ results in two values of $\tilde{Y}$ which are equidistant from the reference line, and as a result the curve $\tilde{Y}_0(\tilde{X})$ is the center line of the inviscid region, about which the flow is symmetric. The solution then applies in the range $0 \le \tilde{Y}_0(\tilde{X}) \le 2\tilde{Y}_0(\tilde{X})$. However, the solution in the inviscid region is not uniformly valid since it cannot satisfy either the no-slip condition at the wall or the matching condition to the mainstream for large $\tilde{Y}$. Note that the transformation for the streamwise velocity (2.37c) suggests that $\tilde{U}$ must become very large as $\tilde{Y} \to 0$ and $\tilde{Y} \to 2\tilde{Y}_0(\tilde{X})$ to overcome the small factor $(t_s - t)^{1/2}$ and adjust the drift velocity $- K$ to the no-slip condition and the mainstream velocity, respectively. Because $\tilde{U} \to \infty$ as $\tilde{Y} \to 0$ and $\tilde{Y} \to 2\tilde{Y}_0(\tilde{X})$, in both cases the solution (2.38b) provides

that

$$\tilde{Y}_0(\tilde{X}) = \int_{\tilde{U}_0}^{\infty} \frac{d\tilde{U}}{\left(\tilde{U}^3 + \tilde{U} + \tilde{X}\right)^{1/2}}, \tag{2.39}$$

which is the equation defining the central line. In addition, because the shear stress is zero along the central line, equation (2.38a) requires the streamwise velocity along the central line to satisfy

$$\tilde{U}_0^3 + \tilde{U}_0 + \tilde{X} = 0. \tag{2.40}$$

The solution to this cubic equation is (see Abramowitz and Stegun, 1964)

$$\tilde{U}_0(\tilde{X}) = \left[-\frac{\tilde{X}}{2} + \left(\frac{1}{27} + \frac{\tilde{X}^2}{4}\right)^{1/2}\right]^{1/3} + \left[-\frac{\tilde{X}}{2} - \left(\frac{1}{27} + \frac{\tilde{X}^2}{4}\right)^{1/2}\right]^{1/3}. \tag{2.41}$$

Observe that the behavior of this equation as $\tilde{X} \to 0$ agrees with the result (2.22).

Integrals, such as (2.38b) and (2.39), involving the inverse of the square root of a cubic polynomial may be rewritten in terms of elliptic integrals. For the current case, the polynomial has only one real root $\tilde{U} = \tilde{U}_0(\tilde{X})$ in which case Abramowitz and Stegun (1964) indicate the transformation

$$\cos\theta = \frac{\tilde{U} - \tilde{U}_0 - \lambda^2}{\tilde{U} - \tilde{U}_0 + \lambda^2}, \tag{2.42}$$

where

$$\lambda^2 = \left(3\,\tilde{U}_0^2 + 1\right)^{1/2}. \tag{2.43}$$

49

Substitution of (2.42) into the equation for the central line (2.39) gives

$$\tilde{Y}_0(\tilde{X}) = \frac{1}{\lambda} \int_0^\pi \frac{d\theta}{\left(1 - m \sin^2\theta\right)^{1/2}} = \frac{2}{\lambda} F\left(\frac{\pi}{2}\Big| m\right) = \frac{2}{\lambda} K(m), \tag{2.44}$$

where F is the incomplete elliptic integral of the first kind, K is the complete elliptic integral of the first kind and

$$m = \sin^2\alpha = \frac{1}{2} - \frac{3\tilde{U}_0}{4\lambda^2}. \tag{2.45}$$

Similarly, the equation for the velocity distribution (2.38b) may be transformed to

$$\tilde{Y} - \tilde{Y}_0(\tilde{X}) = \frac{1}{\lambda} \int_\theta^\pi \frac{dz}{\left(1 - m \sin^2 z\right)^{1/2}} = \begin{cases} \tilde{Y}_0(\tilde{X}) - \frac{1}{\lambda} F(\theta| m), & 0 < \theta < \frac{\pi}{2} \\ -\frac{1}{\lambda} F(\theta - \pi| m), & \frac{\pi}{2} < \theta < \pi \end{cases}. \tag{2.46}$$

Thus, the terminal boundary-layer solution has been reduced to equation (2.46) with (2.42), (2.43) and (2.45) for the streamwise velocity distribution $\tilde{U}$. The domain is bisected by the curve $\tilde{Y}_0(\tilde{X})$ given by equation (2.44) along which the velocity $\tilde{U}_0(\tilde{X})$ is given by (2.41).

2.5.2 Properties of the Terminal Solution

The above solution describes the flow in the immediate vicinity of the separation point as $t \to t_s$ in a reference frame moving with the fluid particle that becomes laterally compressed to zero thickness as $t \to t_s$; this is the physical nature of the singularity in the solution which occurs somewhere off the surface along a line of zero vorticity, according to the MRS conditions. The theoretical picture that ensues is illustrated in figure 2.3, where the streamwise scale of the eruptive spike (see figure 2.2
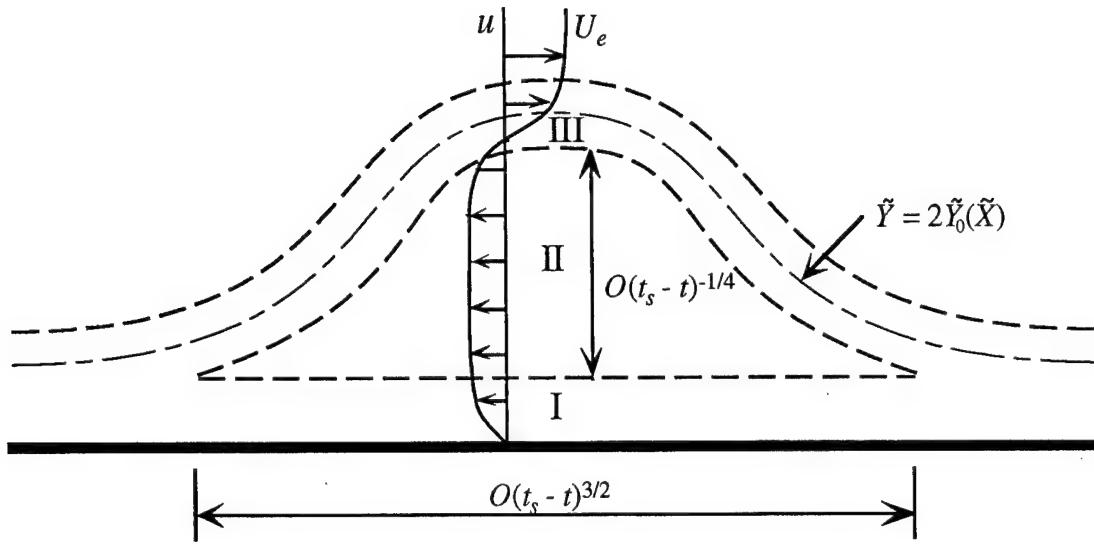
Figure 2.3 - Schematic of the terminal boundary-layer structure near x_s (not to scale).

for example) has been greatly exaggerated for illustrative purposes. As the boundary layer evolves toward the terminal state, it bifurcates into two shear layers (regions I and III) above and below the central inviscid region (region II). A typical velocity profile across the boundary layer is shown in the figure indicating that the velocity is nearly constant across the central region and is adjusted across the shear layers to the mainstream and wall velocities. Due to the nature of the velocity distribution, region II is sometimes referred to as a vorticity-depleted or dead-water region which is reflected in the expansion (2.37c) for the velocity near x_s. While the shear layers remain passive and thin of $O(Re^{-1/2})$ as $t \to t_s$, the dead-water zone contracts in the streamwise direction proportional to $(t_s - t)^{3/2}$ and expands proportional to $(t_s - t)^{-1/4}$ in the normal direction. It should be remembered that this structure is completely contained within the initially thin boundary layer. As the singularity develops, a displacement thickness spike forms and fluid particles in the upper part of the boundary layer will ultimately be located an infinite distance from the wall on the boundary-layer scale. However, this phenomena

51

appears as a small sharp spike in the boundary layer on the physical scale.

Keeping this overall picture in mind, focus returns to the central region (region II) which drives the boundary layer into the singularity. The most significant characteristic of the terminal solution in region II is that the structure is independent of the pressure gradient in the external mainstream. Although an adverse pressure gradient is an essential precursor to an unsteady boundary-layer eruption, the boundary layer evolves into a generic singular state which is believed to be common to most cases of eruption of two-dimensional unsteady incompressible boundary layers.

It is worthwhile to consider in more detail the velocity distributions throughout the dead-water zone. The streamwise velocity is determined from a numerical solution of equation (2.46) with (2.42), (2.43) and (2.45), which is discussed in §3.3. Velocity profiles from such a solution are shown in figure 2.4 at a few $\tilde{X}$ locations. As mentioned previously, the velocity becomes very large at the top and bottom of the domain in order to match to the shear layers (regions I and III). Near the central line $\tilde{Y}_0(\tilde{X})$ the velocity is positive for $\tilde{X} < 0$ and negative for $\tilde{X} > 0$. Therefore, the flow is focusing toward the point $(\tilde{X}, \tilde{Y}) = (0, \tilde{Y}_0(0))$ which is the eventual separation point. By continuity, the boundary layer must thicken near $\tilde{X} = 0$. As $|\tilde{X}| \to \infty$, the streamwise velocity along the central line from (2.42) is

$$\tilde{U}_0(\tilde{X}) \sim -\tilde{X}^{1/3} \quad \text{as} \quad |\tilde{X}| \to \infty \tag{2.47}$$

and becomes very large in order to overcome the small factor $(t_s - t)^{1/2}$ in the transformation and thereby adjust u from $-K$ to match the conventional boundary layer upstream and downstream of the spike. In equation (2.39) $\tilde{U}$ may be neglected compared to $\tilde{U}^3$ to leading order, and at upstream and downstream infinity a similarity solution is easily found which is of the form

$$\tilde{U} = U(\eta)|\tilde{X}|^{1/3}, \tag{2.48}$$
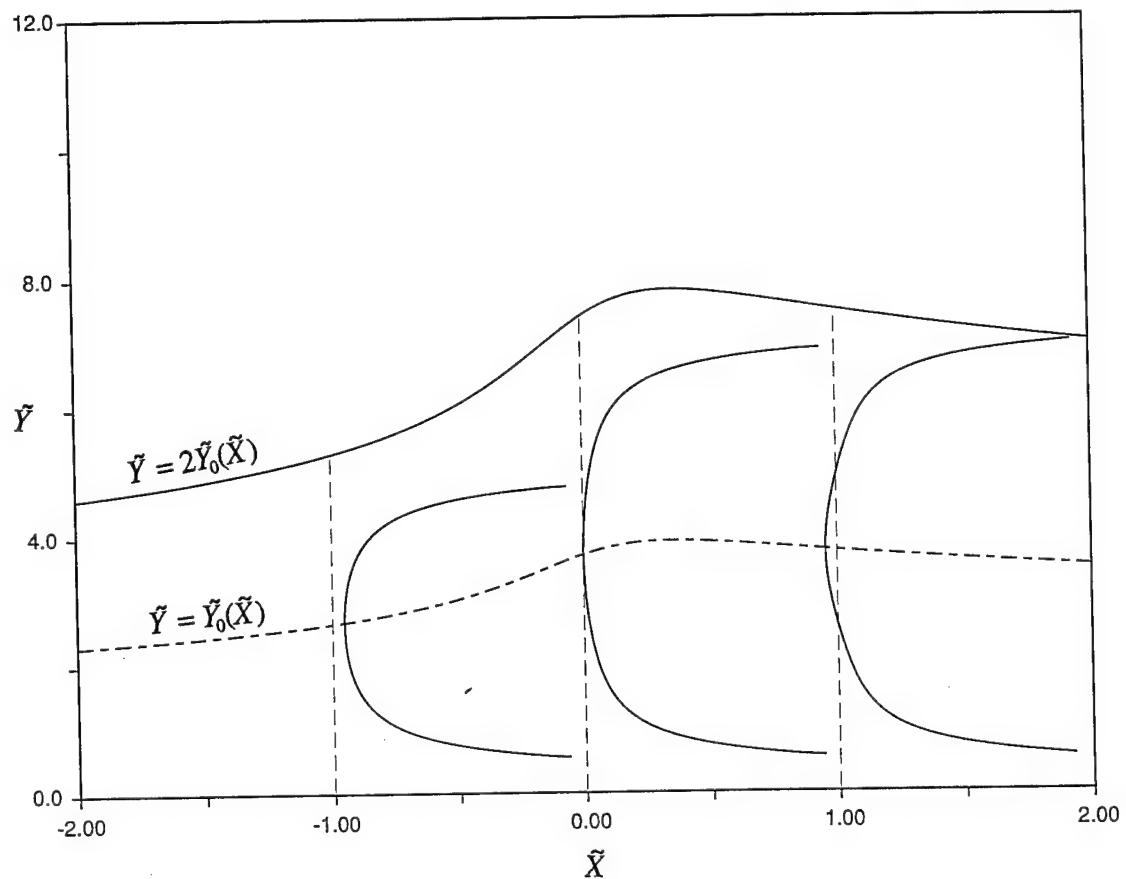
Figure 2.4 - Velocity profiles for the terminal boundary-layer solution.

53

where η is a similarity variable defined by

$$\eta = \tilde{Y}\,|\tilde{X}|^{1/6}. \tag{2.49}$$

The function $U(\eta)$ is determined from a solution of

$$\eta - \eta_0 = \begin{cases} \eta_0 - \dfrac{1}{3^{1/4}}\,F(\theta^*\,|\,m^*), & 0 < \theta^* < \dfrac{\pi}{2} \\[2mm] -\dfrac{1}{3^{1/4}}\,F(\theta^* - \pi\,|\,m^*), & \dfrac{\pi}{2} < \theta^* < \pi \end{cases}, \tag{2.50a}$$

where θ^* and η_0 are defined by

$$\cos\theta^* = \frac{U(\eta) + b - \sqrt{3}}{U(\eta) + b + \sqrt{3}}, \tag{2.50b}$$

$$\eta_0 = \frac{2}{3^{1/4}}\,K(m^*), \tag{2.50c}$$

and the constants b and m^* depend on whether $\tilde{X} \to \infty$ or $\tilde{X} \to -\infty$ in the following way

$$m^* = \begin{cases} \sin^2\!\left(\dfrac{5\pi}{12}\right), & \tilde{X} \to \infty \\[2mm] \sin^2\!\left(\dfrac{\pi}{12}\right), & \tilde{X} \to -\infty \end{cases}, \tag{2.50d}$$

$$b = \begin{cases} +1, & \tilde{X} \to \infty \\ -1, & \tilde{X} \to -\infty \end{cases}. \tag{2.50e}$$

The form of the velocity as $\tilde{Y} \to 0$ and $\tilde{Y} \to 2\tilde{Y}_0(\tilde{X})$ is also of interest. From the solutions of the terminal boundary-layer equation in integral form (2.38b) and the central line height (2.40), the solution above the central line may be written as

54

$$2\tilde{Y}_0 - \tilde{Y} = \int_0^{\infty} \frac{d\tilde{U}}{\left(\tilde{U}^3 + \tilde{U} + \tilde{X}\right)^{1/2}}, \qquad \tilde{Y} > \tilde{Y}_0(\tilde{X}) \tag{2.51a}$$

and below the central line as

$$\tilde{Y} = \int_0^{\infty} \frac{d\tilde{U}}{\left(\tilde{U}^3 + \tilde{U} + \tilde{X}\right)^{1/2}}, \qquad \tilde{Y} < \tilde{Y}_0(\tilde{X}). \tag{2.51b}$$

Recalling that $\tilde{U} \to \infty$ as $\tilde{Y} \to 0, 2\tilde{Y}_0(\tilde{X})$, the integrands in (2.51a,b) are proportional to $\tilde{U}^{-3/2}$. Thus, integration provides the form of the velocity required to match the shear layers above and below the central region to be

$$\tilde{U} \sim \frac{4}{\left(\tilde{Y} - 2\tilde{Y}_0\right)^2} \qquad \text{as} \quad \tilde{Y} \to 2\tilde{Y}_0(\tilde{X}), \tag{2.52a}$$

$$\tilde{U} \sim \frac{4}{\tilde{Y}^2} \qquad\qquad \text{as} \quad \tilde{Y} \to 0. \tag{2.52b}$$

These are the matching conditions to the shear layers above and below region II. Consequently, the central region is characterized by unbounded perturbation streamwise velocities on all four sides.

At this point it is worthwhile to discuss numerical confirmation of the terminal boundary-layer solution. To date boundary-layer computations have been carried out up to the time of the terminal singularity for two model problems. The impulsively-started circular cylinder was investigated by Van Dommelen and Shen (1982), and a vortex-induced boundary layer was studied by Peridier *et al.* (1991a). In both cases an eruptive singularity occurred within a finite time which was characterized by the formation of a sharp spike in the displacement thickness (see, for example, figure 2.2).

55

The numerical results for times just prior to $t = t_s$ corroborate the analytically obtained structure described above in both cases. Constant vorticity contours reveal the formation of a zero vorticity line (which is required by the MRS conditions for separation) and an eventual concentration of constant vorticity contours comprising the upper shear layer (region III). Velocity profiles near the separation point also reveal the upper and lower shear layers surrounding the vorticity-depleted region where the velocity is nearly constant. A minimum in the velocity is also evident within the dead-water zone. In addition to these qualitative features, Peridier *et al.* (1991a) used a least-squares curve fit to determine the growth rate of the maximum in displacement thickness just prior to the singularity. They found the growth rate to be $N = 0.253 \pm 0.003$, which is in good agreement with the analytically determined value $N = 1/4$. The fact that these different flows evolve toward the same terminal state supports the expectation that the terminal boundary-layer solution is generic and is independent of the pressure gradient, which initiated the unsteady separation process.

2.6 Interacting Boundary-Layer Results

The primary question that arises from the preceding discussion of unsteady separation concerns the effect that the eventual interaction with the external inviscid flow has on the erupting boundary layer as the singularity is approached. Such a viscous-inviscid interaction must become important at some time prior to the non-interactive singularity time t_s in order to prevent actual formation of the singularity. Due to previous success realized in relieving the Goldstein singularity for steady boundary-layer flows, interacting boundary-layer (IBL) theory would seem to be a natural framework in which to interrogate this issue. Indeed, IBL theory was the basis for some of the first studies of the effect of viscous-inviscid interaction on unsteady separation. In this approach, discussed in §1.2, a large but finite value of the Reynolds number is assumed, and the boundary-layer equations are solved as usual except that the pressure, rather than being prescribed as in classical boundary-layer theory, is

coupled with the displacement thickness of the boundary layer through an interaction condition. For incompressible flows this condition involves a Cauchy principal-value integral of the normal velocity or displacement thickness induced by the boundary layer.

There have only been a few studies of unsteady separation using interacting boundary-layer theory to date, and the results have been somewhat contradictory. The first such study was carried out by Henkes and Veldman (1987) for the impulsively-started circular cylinder. They concluded on the basis of their results obtained in Eulerian coordinates that the influence of viscous-inviscid interaction at least delays the onset of the singularity. Their numerical results, however, exhibit large oscillations in the calculated results (particularly displacement thickness) for times prior to the corresponding non-interactive singularity time; relatively coarse meshes were used, and their results do not seem to be grid independent at least for larger times. A similar conclusion was arrived at by Chuang and Conlisk (1989) who considered the boundary layer induced by a rectilinear vortex convected in a uniform flow above a wall. These authors also used Eulerian coordinates and were able to extend the numerical calculations farther in time than for a non-interactive Eulerian calculation; one important result of this study was the recognition that first-order methods for the evaluation of the Cauchy integral seem to be inadequate as the interaction develops. It should be noted that the conclusion of Chuang and Conlisk (1989) that there is a delay in the onset of breakdown was based on the authors' ability to carry the interactive calculations further in time than their non-interactive Eulerian calculation with the same basic algorithm. However, it was not possible to extend the calculations beyond the time when the non-interactive solution obtained in Lagrangian coordinates becomes singular. On the other hand, the interactive calculations of Riley and Vasantha (1989) were continued well beyond the times of the non-interactive singularity, and they did not seem to encounter any breakdown at all. All of the above mentioned studies utilized the conventional Eulerian formulation of the boundary-layer problem, and some used numerical algorithms of relatively low accuracy which may have acted to smooth out the small-

scale separation process. For these reasons the results of these studies are potentially suspect for large times and are certainly inconclusive in terms of clearly defining the effect of viscous-inviscid interaction on the unsteady separation process.

The first investigation to carry out an interactive calculation in Lagrangian coordinates was performed by Peridier, Smith and Walker (1991b) who considered the boundary layer induced by a rectilinear vortex above an infinite plane wall in an otherwise stagnant fluid; in contrast to the previous studies, these interacting boundary-layer calculations clearly terminated in a singularity at times prior to the non-interactive singularity time. This hastening of breakdown was increasingly pronounced as the Reynolds number was decreased. As would be expected, the flow development closely paralleled that of the non-interactive case (see Peridier *et al.,* 1991a) until times at which a strong interaction develops. The interaction was found to have an influence on the secondary eddy observed in the non-interactive case (see figure 2.1); at moderate Reynolds numbers the secondary eddy split into two co-rotating eddies, and a tertiary eddy was observed to form just upstream of the eruptive spike. As the Reynolds number is decreased, the size of the secondary eddy is reduced, while the tertiary eddy becomes increasingly prominent and causes an additional secondary spike to form in the displacement thickness. Although the development of the eruption that occurs was found to be qualitatively similar to that of the non-interactive case, the streamwise extent of the spike, while still small, thickens with decreasing Reynolds number. In addition, as the Reynolds number is reduced, the wall shear and pressure distributions develop severe local distortions as the singularity is approached, and the mainstream speed departs increasingly from the steady solution associated with the infinite Reynolds number case.

The possibility of an unsteady interactive singularity occurring within a finite time has been considered by Smith (1988b). This analytical study is a generalization of a special case considered by Brotherton-Ratcliffe and Smith (1987), and the analysis applies to two- and three-dimensional flows in both the subsonic and supersonic regimes which are considered within the framework of either conventional unsteady

interacting boundary-layer theory (see §1.2) or triple-deck theory (see §1.3). A 'moderate' and a 'severe' type break-up were found, but only the moderate type will be discussed here as it is believed to be the most common. A singularity was assumed to develop in the interactive formulation at time $t = t_s$ and streamwise location $x = x_s$, and the singular structure moves downstream with speed c (Smith, 1988b). The streamwise variable describing a local region near the singularity is

$$x - x_s = - c\,(t_s - t) + (t_s - t)^{3/2}\,\xi, \tag{2.52}$$

where ξ is $O(1)$. The structure as $t \to t_s^-$ is similar schematically to that of the terminal boundary-layer structure shown in figure 2.3; however, instead of a flat profile in the central inviscid zone, the profile is generally rotational. The normal extent of the main, or intermediate, zone is $O(Re^{-1/2})$ and those of the viscous wall layer and upper critical layer bounding the inviscid region are $O(Re^{-1/2}\,(t_s - t)^{3/4})$ and $O(Re^{-1/2}\,(t_s - t)^{1/4})$, respectively. A critical layer occurs where the streamwise velocity u is exactly balanced by the assumed speed of the singularity. As the singularity forms, the pressure distribution near x_s develops a local distortion of the form

$$p - p_0 = O\big((x - x_s)^{1/3}\big) \quad \text{as} \quad x \to x_s, \tag{2.53}$$

where p_0 is a constant. The break-up causes the maximum values in pressure gradient, normal velocity and wall shear stress to become singular in a manner having the following forms

$$\left.\frac{dp}{dx}\right|_{max} \sim \frac{c_1}{t_s - t}, \quad v_{max} \sim \frac{c_2}{t_s - t}, \quad \tau_{w max} \sim \frac{c_3}{(t_s - t)^{1/4}}, \tag{2.54}$$

as $t \to t_s$. The numerical results of Peridier $et\ al.$ (1991b) were in broad agreement with equations (2.54). It emerges from the analysis of Smith (1988b) that the leading-order criterion for this break-up is

$$\int_0^\infty \frac{dY}{[u(Y) - c]^2} = 0, \qquad\qquad (2.55)$$

where the integration is carried out across the boundary layer and $u(Y)$ is the profile at $x = x_s$. It is believed that this unsteady interactive singularity may be relieved through the action of normal pressure gradient effects (Smith, 1988b and Hoyle, Smith and Walker, 1991) which are not accounted for in either interacting boundary-layer theory nor the triple deck. The relationship between this new interactive singularity and the terminal singularity of the non-interactive boundary-layer problem is unfortunately not known at present.

3. The First Interactive Stage

3.1 Introduction

The terminal boundary-layer solution derived in §2.5 describes the local flow structure as an eruption develops and a singularity subsequently forms in the classical (non-interactive) boundary-layer formulation. The onset of the eruption can be initiated by a variety of mainstream pressure distributions which contain a region of adverse streamwise pressure gradient; however, the terminal structure is independent, to leading order, of the particular form of the initiating pressure gradient. Consequently, the terminal solution is believed to describe a generic structure which is expected to form whenever a two-dimensional incompressible boundary layer exhibits eruptive behavior, at least in the case of upstream-slipping separation (see Van Dommelen, 1981). Because of this, the subsequent stages of development determined through limit analyses are expected to apply to a variety of situations corresponding to different geometries and/or mainstream conditions.

Realistic solutions of the Navier-Stokes equations cannot contain singularities; therefore, the occurrence of a singularity in a reduced set of equations indicates that terms in the Navier-Stokes equations which were originally neglected are becoming significant as a new physical process begins to develop. In the problem under consideration, the terminal boundary-layer structure describes a rapid growth and eventual singularity in the displacement thickness indicating that the classical boundary-layer equations (which assume an attached thin boundary layer) must fail to correctly describe the situation at some stage. As a result, the problem must be reformulated in a local region near the developing spike for times in advance of the formation of the singularity. The next stage, called the first interactive stage, accounts for the inevitable viscous-inviscid interaction which must take place as the boundary layer progressively starts to leave the surface. This stage has been formulated by Elliott, Cowley and

61

Smith (1983) in traditional Eulerian coordinates, and a description of the problem follows in §3.2.1. Unfortunately, there are severe numerical difficulties that are encountered in trying to solve the Eulerian problem. On the other hand, success has been achieved recently in the calculation of eruptive boundary-layer flows utilizing Lagrangian coordinates (see Van Dommelen and Shen, 1980 and Peridier *et al.*, 1991a,b). The problem for the first interactive stage is reformulated in terms of Lagrangian variables in §3.2.2. It will be shown that the evolution of the first interactive stage is governed by the inviscid streamwise momentum equation subject to a viscous-inviscid interaction condition. This interaction condition is a Cauchy principal-value integral relating the pressure distribution in the outer inviscid flow to the displacement thickness of the thickening boundary layer. Determination of the displacement thickness requires integration of the continuity equation (which in Lagrangian coordinates is a first-order linear partial differential equation) along characteristic curves describing lines of constant streamwise particle positions. The numerical procedures used for the present calculations are discussed in §3.3 followed by a discussion of the results in §3.4 and §3.5.

3.2 Formulation of the First Interactive Stage

3.2.1 Eulerian Formulation

For an attached laminar boundary layer, the normal velocity induces perturbations in the outer inviscid flow; for a boundary layer having a thickness $\delta = O(Re^{-1/2})$, these perturbations are generally small as discussed in appendix B (*cf.* equations (B.3)). As shown in equations (B.5) and (B.6), the motion induced at the boundary-layer edge is closely related to the boundary-layer displacement thickness. As the displacement thickness grows and evolves toward a singularity, an interaction must eventually develop between the thickening viscous boundary layer and the outer inviscid flow. Here, the task is to ascertain the time scale over which this interaction

first occurs just prior to the formation of this singularity. Recall from §2.5 that as $t \to t_s$, the unsteady convective terms in the streamwise momentum equation are $O[(t_s - t)^{-1/2}]$ and dominate the pressure gradient term, which is $O(1)$, and the viscous terms, which are $O(t_s - t)$. Here, the time scale is sought for which the pressure gradient first balances the convection terms and interaction effects therefore become important. To this end, the mainstream pressure at the surface is expanded according to

$$p = p_0 + Re^{-1/2} p_1 + \cdots, \tag{3.1}$$

where in general p_0 is the leading-order inviscid pressure, and p_1 is the pressure perturbation in the external flow induced by the boundary layer. Since the streamwise extent of the developing eruption is very narrow, the leading term in the expansion (3.1) may be taken to be a constant corresponding to the local value at $x = 0$; here, separation is assumed to occur at time t_s at $x = 0$. A general formulation for the induced pressure gradient is given in appendix B. Since the interaction is localized near $x = 0$, $U_e(x)$ may be replaced in equation (B.18) by the local value $U_e(0)$, and it follows that

$$\frac{\partial p}{\partial x} = O\left(Re^{-1/2} \frac{\partial^2 \delta^*}{\partial x^2}, Re^{-1/2} \frac{\partial^2 \delta^*}{\partial x \partial t}\right), \tag{3.2}$$

where only the most highly differentiated terms on the right side of equation (B.18) have been retained. It is readily inferred from the discussion in §2.5 and figure 2.3 that the dominant contribution to displacement thickness δ^* is associated with the expanding central region and

$$\delta^* = O\left[(t_s - t)^{-1/4} \tilde{Y}_0(\tilde{X})\right]. \tag{3.3}$$

It then follows from equations (2.37), (3.2) and (3.3) that

63

$$\frac{\partial p}{\partial x} = O\left[Re^{-1/2}(t_s - t)^{-13/4}\right], \tag{3.4}$$

as $t \to t_s$. Consequently, a balance with the convective terms, which are $O[(t_s - t)^{-1/2}]$, occurs when

$$(t_s - t) = O(Re^{-2/11}). \tag{3.5}$$

Therefore, interaction does not become significant until a very short time before a singularity forms in the solution of the non-interactive problem. Events that occur on this short time scale are referred to as taking place in the first interactive stage and evidently must occur rapidly in order to prevent formation of the singularity.

During the first interactive stage the upper and lower shear layers remain essentially passive having a thickness $O(Re^{-1/2})$, while the pressure distribution induced by the interaction begins to alter the flow in the intermediate region II (*cf.* figure 2.3) between the shear layers. It follows from equations (2.37a) and (3.5) that the streamwise extent of the interactive zone in this stage is $O(Re^{-3/11})$; in addition, since $y = Re^{-1/2} Y$ it follows from equation (2.37b) that the normal extent of the intermediate region II expands to become $O(Re^{-5/11})$. These considerations suggest the following definitions of new independent variables for the central region II in the first interactive stage:

$$x - x_s = K(t_s - t) + Re^{-3/11} \phi_0^{1/2} \bar{x}_I, \quad y = Re^{-5/11} \Lambda \phi_0^{-1/4} \bar{Y}_I, \quad t - t_s = Re^{-2/11} \bar{t}_I, \tag{3.6a,b,c}$$

where the factors of ϕ_0 and Λ (associated with the terminal solution) are inserted for convenience in equations (3.6) to be consistent with the variables in the previous stage defined in equations (2.37). It also follows from equations (2.37c) and (3.5) that the streamwise velocity and pressure during the first interactive stage have the following expansions

64

$$u = -K + Re^{-1/11}\,\phi_0^{1/2}\,\bar{u}_I(\bar{x}_I,\bar{Y}_I,\bar{t}_I), \qquad p = p_s + Re^{-2/11}\,\phi_0\,\bar{p}_I(\bar{x}_I,\bar{Y}_I,\bar{t}_I), \qquad (3.7a,b)$$

where again the factors involving the constant ϕ_0 in the terminal solution are inserted for convenience; here, p_s denotes the mainstream pressure evaluated as $x \to x_s$. The streamwise and time scales (3.6a,c) were first proposed by Elliot *et al.* (1983) and seem to have been confirmed by Peridier *et al.* (1991b) in their numerical solutions for the vortex-induced separation problem. Substitution of the scaled variables (3.6) and (3.7) into the Navier-Stokes equations yields the governing equations in region II for the infinite Reynolds number limit:

$$\frac{\partial \bar{u}_I}{\partial \bar{t}_I} + \bar{u}_I \frac{\partial \bar{u}_I}{\partial \bar{x}_I} - \frac{\partial \bar{\psi}_I}{\partial \bar{x}_I}\frac{\partial \bar{u}_I}{\partial \bar{Y}_I} = -\frac{\partial \bar{p}_I}{\partial \bar{x}_I}, \qquad \bar{u}_I = \frac{\partial \bar{\psi}_I}{\partial \bar{Y}_I}, \qquad (3.8a,b)$$

$$\frac{\partial \bar{p}_I}{\partial \bar{Y}_I} = 0, \qquad (3.9)$$

where $\bar{\psi}_I$ is a perturbation streamfunction. These equations describe the evolution of the flow in the thickening central region II (shown in figure 3.1) between $\bar{Y}_I = 0$ and the upper shear layer at $\bar{Y}_I = \bar{\beta}_I(\bar{x}_I,\bar{t}_I)$ which is to be found as part of the solution of the first interactive stage. Note that the problem in the central region is non-linear and inviscid.

The solution of equations (3.8) and (3.9) on the interactive time scale must match as $\bar{t}_I \to -\infty$ to the terminal boundary-layer solution as $t \to t_s^-$. Relating the interactive variables defined by equations (3.6a,b,c) and (3.7a) with the variables (2.37a,b,c) for the terminal solution yields the following:

$$\bar{x}_I = (-\bar{t}_I)^{3/2}\,\tilde{X}, \qquad \bar{Y}_I = (-\bar{t}_I)^{-1/4}\,\tilde{Y}, \qquad \bar{u}_I(\bar{x}_I,\bar{Y}_I,\bar{t}_I) = (-\bar{t}_I)^{1/2}\,\tilde{U}(\tilde{X},\tilde{Y}). \quad (3.10a,b,c)$$

These equations serve to relate the solution in the first interactive stage to that of the terminal boundary-layer solution and provide initial conditions for large negative $\bar{t}_I$. Note that for fixed values of $\tilde{X}$ and $\tilde{Y}$, $\bar{x}_I$ increases and $\bar{Y}_I$ decreases as $\bar{t}_I \to -\infty$

65
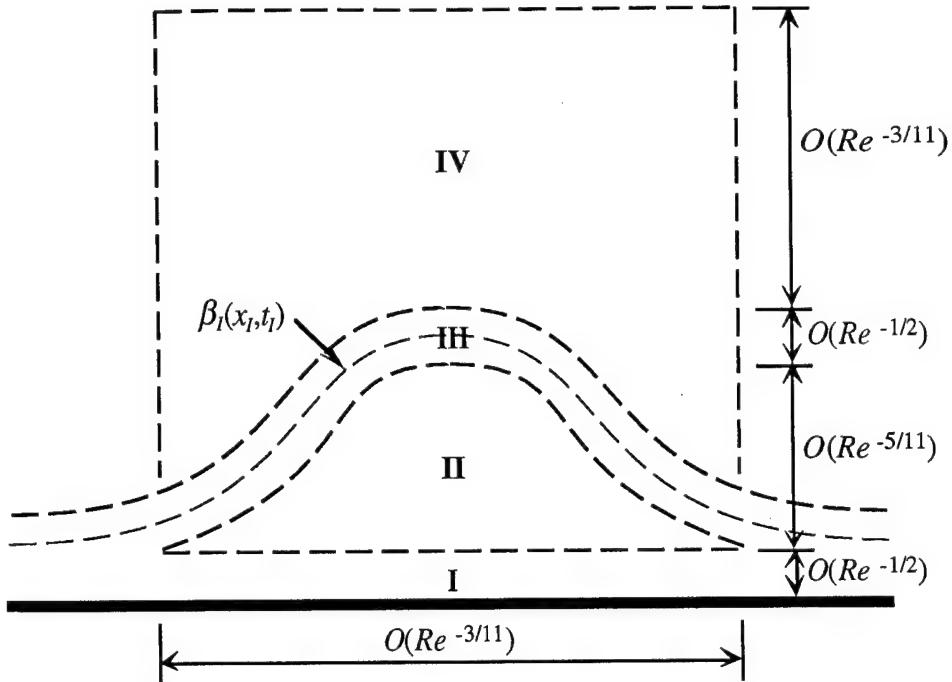
Figure 3.1 - Schematic of the first interactive stage of unsteady boundary-
layer separation.

indicating that region II broadens in the streamwise direction and shrinks in the normal direction as time is decreased. Likewise, the perturbation velocity $\bar{u}_I$ increases as $\bar{t}_I \to -\infty$ (relative to $\tilde{U}$) except as $|\tilde{X}|$ or $|\bar{x}_I| \to \infty$, where there is a steady similarity solution. As $\bar{t}_I \to -\infty$, the initial condition for the equation of the upper shear layer is given by

$$\bar{Y}_I = \bar{\beta}_I(\bar{x}_I, \bar{t}_I) = (-\bar{t}_I)^{-1/4} 2 \tilde{Y}_0(\tilde{X}). \tag{3.11}$$

The matching conditions to the upper and lower shear layers (regions I and III, respectively, in figure 3.1) were given in equations (2.52) and in view of equations (3.10b) and (3.10c) become

66

$$\bar{u}_I \sim \frac{4}{(\bar{Y}_I - \bar{\beta}_I)^2} \qquad \text{as} \quad \bar{Y}_I \to \bar{\beta}_I, \tag{3.12a}$$

$$\bar{u}_I \sim \frac{4}{\bar{Y}_I^2} \qquad \text{as} \quad \bar{Y}_I \to 0. \tag{3.12b}$$

Because the perturbation velocities are very large near the upper and lower shear layers, it proves very challenging to devise an effective numerical solution method for equations (3.8) and (3.9).

The pressure gradient appears in equation (3.8a); therefore, to complete the formulation it is necessary to find a method to evaluate the streamwise pressure gradient impressed by the outer inviscid flow due to the interactive effects. It is evident from equations (3.6a) and (3.6b) that the slope of the upper shear layer $\bar{Y}_I = \bar{\beta}_I$ is $O(Re^{-2/11})$; consequently, perturbations $O(Re^{-2/11})$ in the pressure and normal velocity are induced in a local interaction region having dimensions $O(Re^{-3/11})$ by $O(Re^{-3/11})$; this is indicated as region IV in figure 3.1. The solution in region IV leads to the pressure-displacement relation

$$\bar{p}_I(\bar{x}_I, \bar{t}_I) = -\frac{1}{\pi} \int_{-\infty}^{+\infty} \frac{\partial \bar{\beta}_I(s, \bar{t}_I)}{\partial s} \frac{ds}{\bar{x}_I - s}, \tag{3.13}$$

which is derived in Appendix B and involves a Cauchy principal-value integral. As indicated in equation (3.13), the growing region II leads to an increase in $\bar{\beta}_I$ which in turn influences the pressure and hence the flow in region II. The expected outcome of this interaction is that the singularity present in the terminal boundary-layer solution will be relieved.

In principle, a numerical solution of the system (3.8) and (3.9) could be initiated at some large negative time t_{I0} using equations (3.10) evaluated at $t_I = t_{I0}$ as initial conditions (in terms of the terminal solution). However, it is convenient to scale the initial time out of most of the problem formulation through the following

67

transformations:

$$\bar{x}_I = (-t_{I0})^{3/2} x_I, \qquad \bar{Y}_I = (-t_{I0})^{-1/4} Y_I, \qquad \bar{t}_I = (-t_{I0}) t_I, \qquad (3.14a,b,c)$$

$$\bar{u}_I = (-t_{I0})^{1/2} u_I, \qquad \bar{\psi}_I = (-t_{I0})^{1/4} \psi_I, \qquad \bar{p}_I = (-t_{I0}) p_I. \qquad (3.14d,e,f)$$

The momentum equations (3.8) and (3.9) remain unchanged and become

$$\frac{\partial u_I}{\partial t_I} + u_I \frac{\partial u_I}{\partial x_I} - \frac{\partial \psi_I}{\partial x_I} \frac{\partial u_I}{\partial Y_I} = - \frac{\partial p_I}{\partial x_I}, \qquad u_I = \frac{\partial \psi_I}{\partial Y_I}, \qquad (3.15a,b)$$

$$\frac{\partial p_I}{\partial Y_I} = 0. \qquad (3.16)$$

In addition, the boundary conditions (3.12) at the upper and lower shear layers also remain unchanged with

$$u_I \sim \frac{4}{(Y_I - \beta_I)^2} \qquad \text{as } Y_I \rightarrow \beta_I, \qquad (3.17a)$$

$$u_I \sim \frac{4}{Y_I^2} \qquad \text{as } Y_I \rightarrow 0, \qquad (3.17b)$$

while the initial condition (3.10), which applies at $t_I = -1$, is simply the terminal boundary-layer solution and

$$\left. \begin{array}{l} x_I = \tilde{X}, \quad Y_I = \tilde{Y} \\ u_I(x_I, Y_I) = \tilde{U}(\tilde{X}, \tilde{Y}) \\ \beta_I(x_I) = 2\,\tilde{Y}_0(\tilde{X}) \end{array} \right\} \quad \text{at } t_I = -1. \qquad (3.18)$$

The starting time t_{I0} for the integrations only appears in this formulation in the

pressure-displacement relation (3.13) which becomes

$$p_I(x_I,t_I) = -\frac{(-t_{I0})^{-11/4}}{\pi} \int_{-\infty}^{\infty} \frac{\partial \beta_I(s,t_I)}{\partial s} \frac{ds}{x_I - s}. \qquad (3.19)$$

In principle, solutions should be obtained for a range of values t_{I0} which are large and negative; evidently, the slope of the upper shear layer must grow significantly in order to overcome the small factor $(-t_{I0})^{-11/4}$ so that the pressure p_I becomes sensibly large. Equations (3.15) through (3.19) describe the formulation of the first interactive stage in terms of conventional Eulerian coordinates.

3.2.2 Lagrangian Formulation

Because of the large perturbation velocities indicated in equations (3.17) near the top and bottom of region II as well as the fact that a focusing of the solution in the streamwise direction is expected, a solution of the system (3.15) through (3.19) does not appear to be feasible in the conventional Eulerian formulation. However, as discussed in §2.3, a Lagrangian formulation is conducive to these types of flow because the streamwise momentum equation does not involve the quantities which eventually become singular. In addition, the criterion for the formation of a singularity is unambiguous in Lagrangian coordinates.

In a Lagrangian formulation the fluid particle positions (x_I,Y_I) and their corresponding velocity components (u_I,v_I) are evaluated as functions of their initial locations (ξ,η) and time t_I; thus, the dependent variables are

$$x_I = x_I(\xi,\eta,t_I), \quad Y_I = Y_I(\xi,\eta,t_I), \quad u_I = u_I(\xi,\eta,t_I), \quad v_I = v_I(\xi,\eta,t_I), \quad (3.20\text{a,b,c,d})$$

with x_I and u_I being the principal independent variables in the boundary-layer

69

equations. The left hand side of equation (3.15) is the substantial derivative of the streamwise velocity representing streamwise acceleration of the fluid particles; therefore, it is a Lagrangian time derivative of the streamwise velocity which itself is a Lagrangian derivative in time of the streamwise particle position. Therefore, the system (3.15) governing the flow in region II is

$$\frac{\partial u_I}{\partial t_I} = -\frac{\partial p_I}{\partial x_I}, \qquad \frac{\partial x_I}{\partial t_I} = u_I, \qquad\qquad\qquad (3.21\text{a,b})$$

in Lagrangian coordinates. Note that the pressure gradient of a fluid particle in equation (3.21a) must be expressed in terms of the instant particle position distribution x_I at any t as opposed to the initial location ξ. The lateral momentum equation (3.16) merely indicates that the pressure is only a function of the streamwise particle position and time. In Lagrangian coordinates the initial conditions consist of specifying the initial particle locations with the initial velocities given from the terminal boundary-layer solution in equation (3.18); consequently,

$$\left.\begin{array}{l} x_I = \xi, \quad Y_I = \eta \\ u_I = \tilde{U}(\xi, \eta) \end{array}\right\} \quad \text{at} \quad t_I = -1. \qquad\qquad (3.22)$$

The matching conditions (3.17) show that the motion must become parallel as the bounding shear layers at the edges of region II are approached; thus, in these regions $Y_I = \eta$ for all t_I, and it follows that

$$u_I \sim \frac{4}{[\eta - \beta_0(\xi)]^2} \qquad \text{as} \quad \eta \to \beta_0(\xi), \qquad\qquad (3.23\text{a})$$

$$u_I \sim \frac{4}{\eta^2} \qquad\qquad \text{as} \quad \eta \to 0, \qquad\qquad\qquad (3.23\text{b})$$

70

where $\beta_0(\xi) = 2\,\tilde{Y}_0(\tilde{X})$ defines the initial height of the upper shear layer in terms of that associated with the terminal solution.

The solution of the momentum equation (3.21) subject to the initial conditions (3.22) and the boundary conditions (3.23) will provide the streamwise particle positions $x_I(\xi,\eta,t_I)$ and their velocities $u_I(\xi,\eta,t_I)$ as functions of initial position and scaled time t_I. In order to obtain the pressure gradient, which appears in equation (3.21a), the pressure must be evaluated using the interaction condition, and this requires a knowledge of the location of the upper shear layer β_I as a function of (x_I,t_I). The determination of $\beta_I(x_I,t_I)$ at a given time necessitates a solution of the continuity equation. In Lagrangian coordinates the continuity equation states that the Jacobian of the particle positions with respect to their initial locations is equal to unity; thus,

$$-\frac{\partial x_I}{\partial \eta}\frac{\partial Y_I}{\partial \xi} + \frac{\partial x_I}{\partial \xi}\frac{\partial Y_I}{\partial \eta} = 1. \tag{3.24}$$

Assume that at a given time the streamwise particle positions $x_I(\xi,\eta,t_I)$ are known from an integration of the momentum equation (3.21). The continuity equation (3.24) is a first-order linear equation for the normal positions $Y_I(\xi,\eta,t_I)$ of the particles. The solution of the continuity equation can be found by integrating along the characteristic curves of equation (3.24) defined by

$$\frac{d\xi}{-\partial x_I/\partial \eta} = \frac{d\eta}{dx_I/\partial \xi} = dY_I, \tag{3.25}$$

from a location where the particle positions are known. Each characteristic is a curve of constant x_I which when plotted in the (ξ,η) plane represents the initial positions of a set of fluid particles which at the current time are located along the vertical line $x_I =$ constant. The current values of Y_I for particles which initially started out distributed along the line $Y_I = \eta = \beta_0(\xi)$ at $t_I = -1$ defines the current height of region II, i.e. $Y_I = \beta_I(x_I,t_I)$, and permits the evaluation of pressure from the interaction condition

71

(3.19).

Although the Lagrangian formulation is complete, the large velocities indicated by (3.23) at the upper and lower edges of region II give rise to considerable numerical difficulties in solving the problem as presently formulated. The large variations in velocity (and subsequently particle position) implied by conditions (3.23) near the top and bottom of the domain would necessitate very small time steps in a numerical solution of the momentum equation (3.21). These potential problems can be alleviated by instead calculating the velocity perturbation about the terminal-solution velocity. To this end, the streamwise velocity is written in the form

$$u_l(\xi,\eta,t_l) = \tilde{U}(\xi,\eta) + U_l(\xi,\eta,t_l),$$
(3.26)

where the perturbation function U_l vanishes at $t_l = -1$, viz.

$$U_l(\xi,\eta,t_l) = 0 \quad \text{at} \quad t_l = -1$$
(3.27)

for all (ξ,η). Then from integration of equation (3.21b), the streamwise particle position distribution may be expressed as

$$x_l(\xi,\eta,t_l) = (t_l + 1)\,\tilde{U}(\xi,\eta) + X_l(\xi,\eta,t_l),$$
(3.28)

where to satisfy the initial condition (3.22)

$$X_l(\xi,\eta,t_l) = \xi \quad \text{at} \quad t_l = -1.$$
(3.29)

Substitution of equation (3.26) and (3.28) into the momentum equation (3.21) gives

72

$$\frac{\partial U_I}{\partial t_I} = -\frac{\partial p_I}{\partial X_I}, \qquad \frac{\partial X_I}{\partial t_I} = U_I. \tag{3.30a,b}$$

Thus, the momentum equation for the perturbation quantities does not contain the terminal-state velocity distribution explicitly, and $\tilde{U}$ in equation (3.26) satisfies the unbounded velocity conditions (3.23) at the edges of region II, where the perturbation function U_I is bounded and independent of η. The initial pressure distribution is influenced by the terminal solution but at any stage is a function of x_I and t_I obtained from equation (3.19). Also observe that the initial conditions (3.27) and (3.29) for U_I and X_I are all independent of η; consequently, this implies that the perturbations U_I and X_I are one-dimensional unsteady distributions, *viz.*

$$U_I = U_I(\xi, t_I), \qquad X_I = X_I(\xi, t_I). \tag{3.31a,b}$$

Substitution of equation (3.28) into equation (3.24) taking account of equations (3.31) shows that the continuity equation becomes

$$-(t_I+1)\frac{\partial \tilde{U}}{\partial \eta}\frac{\partial Y_I}{\partial \xi} + \left[(t_I+1)\frac{\partial \tilde{U}}{\partial \xi} + \frac{\partial X_I}{\partial \xi}\right]\frac{\partial Y_I}{\partial \eta} = 1. \tag{3.32}$$

It is evident that the interaction affects the computation of the characteristics of equation (3.32) through the particle position perturbation $X_I(\xi, t_I)$, while the remaining terms in the coefficients are associated with the terminal boundary-layer solution. It is also clear that there is symmetry in the constant x_I characteristics. Recall that the terminal-state velocity $\tilde{U}(\xi, \eta)$ is symmetric about the central line $\tilde{Y} = \tilde{Y}_0(\tilde{X})$ that bisects the central region, and also that the particle position perturbation X_I does not depend on η. Therefore, the coefficient of the first term in equation (3.32) (which is associated with the streamwise component of any step along a characteristic) is anti-symmetric about $\eta = \beta_0(\xi)/2 = \tilde{Y}_0(\tilde{X})$ which bisects region II. On the other hand, the second coefficient

in equation (3.32) (which is associated with the normal component of any step along a characteristic) is symmetric about the central curve. As a result, the characteristics are all symmetric about $\eta = \beta_0(\xi)/2 = \breve{Y}_0(\breve{X})$.

3.2.3 Singularity Conditions

In conventional Eulerian formulations it is not possible to accurately evaluate the flow development as a focusing irregularity starts to occur. On the other hand, Lagrangian methods provide a clear criterion for the formation of a singularity. From the equations (3.25) of the characteristics associated with the continuity equation (3.24), the following expression for the vertical position of a fluid particle initially located at (ξ,η) is obtained

$$Y_I(\xi,\eta,t_I) - Y_{I0} = \int_{(\xi_0,\eta_0)}^{(\xi,\eta)} \frac{ds}{\sqrt{(\partial x_I/\partial \xi)^2 + (\partial x_I/\partial \eta)^2}}, \qquad (3.33)$$

where the integral is along the constant x_I characteristic passing through the point (ξ,η) and originating at (ξ_0,η_0) where $Y_I = Y_{I0}$. A singularity occurs when a particle at an initial position (ξ,η) is eventually located at an infinite normal distance from the surface. From equation (3.33) it is evident that this occurs when a stationary point in the x_I field develops at some location (ξ_s,η_s) at some time t_s. The criterion for infinite shear layer growth (on the boundary-layer scale) is

$$\frac{\partial x_I}{\partial \xi} = \frac{\partial x_I}{\partial \eta} = 0 \quad \text{at} \quad \xi = \xi_s, \ \eta = \eta_s, \ t_I = t_{Is}. \qquad (3.34)$$

Therefore, a singularity develops at a point where the coefficients of the continuity equation become zero. In the problem under consideration here, the first coefficient of

74

equation (3.32) is zero (for $t_I > -1$) along the central line due to the symmetric form of the streamwise terminal-state velocity. Note that this is consistent with the MRS model for unsteady separation (see §2.2) which indicates that if a separation singularity forms, it must occur somewhere along the zero vorticity line given by $\partial u_I / \partial Y_I = 0$. If the first interactive stage terminates in a singularity, therefore, it must occur when the second coefficient in equation (3.32) becomes zero at a point along the central line, $\eta = \beta_0(\xi)/2$, *viz.*

$$(t_I + 1)\frac{\partial \tilde{U}}{\partial \xi} + \frac{\partial X_I}{\partial \xi} = 0 \qquad (3.35)$$

at some ξ_s where $\eta_s = \beta_0(\xi_s)/2$. Note that this coefficient is equal to one everywhere at the start of the integration at $t_I = -1$.

3.2.4 Transformation to a Finite Domain

In order to obtain a numerical solution of the first interactive stage within the intermediate zone (region II), it is convenient to transform the region into a finite rectangular domain. The streamwise coordinate, which is defined on the range $(-\infty,\infty)$, can be transformed to the finite range $(-1,1)$ by the transformation

$$\hat{\xi} = \frac{2}{\pi}\arctan\!\left(\frac{\xi}{a}\right). \qquad (3.36)$$

Here, a is a stretching parameter that affects the concentration of points near $\xi=0$; for a uniform mesh in $\hat{\xi}$, a relatively larger number of mesh points is clustered near $\xi=0$ for smaller values of a. The transformation (3.36) maps upstream infinity to $\hat{\xi}=-1$ and downstream infinity to $\hat{\xi}=1$ with the domain still centered at $\hat{\xi}=0$. Similarly, the streamwise particle position perturbation can be transformed to the range $(-1,1)$ using

75

$$\hat{X}_I = \frac{2}{\pi} \arctan\left(\frac{X_I}{a}\right). \tag{3.37}$$

The normal coordinate is defined in the range $(0, \beta_0(\hat{\xi}))$ in region II, and it is convenient to apply the scaling

$$\hat{\eta} = \frac{2 \eta}{\beta_0(\hat{\xi})}, \tag{3.38}$$

so that $\hat{\eta}$ is defined over the range $(0,2)$. The lower extent of the domain is $\hat{\eta} = 0$, and the upper extent is then $\hat{\eta} = 2$, while $\hat{\eta} = 1$ corresponds to the central line $\eta = \beta_0(\xi)/2 = \tilde{Y}_0(\tilde{X})$ about which the flow is symmetric.

Application of the transformations (3.36) through (3.38) to the momentum equation (3.30) results in the equations

$$\frac{\partial U_I}{\partial t_I} = -\frac{\Gamma(\hat{X}_I)}{a} \frac{\partial p_I}{\partial \hat{X}_I}, \qquad \frac{\partial \hat{X}_I}{\partial t_I} = \frac{\Gamma(\hat{X}_I)}{a} U_I, \tag{3.39a,b}$$

and the continuity equation (3.32) becomes

$$-(t_I + 1)\frac{\partial \tilde{U}}{\partial \hat{\eta}} \frac{\partial Y_I}{\partial \hat{\xi}} + \left[(t_I + 1)\frac{\partial \tilde{U}}{\partial \hat{\xi}} + \frac{a}{\Gamma(\hat{X}_I)} \frac{\partial \hat{X}_I}{\partial \hat{\xi}}\right] \frac{\partial Y_I}{\partial \hat{\eta}} = \frac{a}{2} \frac{\beta_0(\hat{\xi})}{\Gamma(\hat{\xi})}. \tag{3.40}$$

In equations (3.39) and (3.40), the function Γ is defined by

$$\Gamma(z) = \frac{1}{\pi}\left[1 + \cos(\pi z)\right]. \tag{3.41}$$

The initial conditions (3.22) are now

76

$$\left.\begin{array}{l} \hat{X}_I = \hat{\xi} \quad Y_I = \dfrac{\beta_0(\hat{\xi})}{2}\hat{\eta} \\[2mm] U_I(\hat{\xi},t_I) = 0 \end{array}\right\} \quad \text{at} \quad t_I = -1, \qquad\qquad (3.42)$$

and the boundary conditions (3.23), which are necessary in order to match to the shear layers above and below region II, are

$$u_I \sim \frac{16}{\beta_0^2(\hat{\xi})\,(\hat{\eta}-2)^2} \qquad \text{as} \quad \hat{\eta} \to 2, \qquad\qquad (3.43a)$$

$$u_I \sim \frac{16}{\beta_0^2(\hat{\xi})\,\hat{\eta}^2} \qquad \text{as} \quad \hat{\eta} \to 0. \qquad\qquad (3.43b)$$

The effect of the streamwise transformation (3.36) on the interaction condition (3.19) is considered in §3.3.4 where the numerical algorithm for solution of the Cauchy integral is described.

3.3 Numerical Methods

3.3.1 General Considerations

The first interactive stage of unsteady boundary-layer separation in Lagrangian coordinates is governed by the inviscid momentum equation (3.39) with the initial conditions (3.42), the continuity equation (3.40) and the interaction condition (3.19). The boundary conditions (3.43) are inherently satisfied by the initial velocity distribution $\tilde{U}(\hat{\xi},\hat{\eta})$ from the terminal solution, and thus do not need to be applied directly in the numerical solution to the momentum equation for the unsteady one-dimensional perturbation $U_I(\hat{\xi},t_I)$. The general solution procedure at each time step is as follows. The solution of the one-dimensional momentum equation (3.39) provides the

velocity perturbation $U_l(\hat{\xi},t_l)$ and particle position perturbation $\hat{X}_l(\hat{\xi},t_l)$ at each time. The distribution $\hat{X}_l(\hat{\xi},t_l)$ is necessary, along with the terminal-state velocity $\tilde{U}(\hat{\xi},\hat{\eta})$, in order to solve the continuity equation (3.40) for the normal particle positions $Y_l(\hat{\xi},\hat{\eta},t_l)$ and the upper boundary $\beta_l(\hat{x}_l,t_l)$ of region II. The Cauchy integral (3.19) of the equation of the upper boundary then gives the pressure distribution $p_l(\hat{X}_l,t_l)$ which is required for the solution of the momentum equation.

In solutions of the non-interactive boundary-layer equations in Lagrangian coordinates, the momentum equation is solved independently of the continuity equation; however, in interactive calculations the solutions of the momentum and continuity equations are strongly coupled. Integration of the continuity equation (3.40) is accomplished on a two-dimensional mesh which must be defined in the ξ and η directions. The integration of the momentum equation is carried out on a one-dimensional mesh in the ξ direction. However, the position of the upper shear layer may be calculated from the continuity equation for any desired $\hat{\xi}$ location, and in principle the one-dimensional mesh for $U_l(\hat{\xi},t_l)$, $\hat{X}_l(\hat{\xi},t_l)$, $p_l(\hat{X}_l,t_l)$ and $\beta_l(\hat{x}_l,t_l)$ may be defined independently of the two-dimensional mesh associated with the continuity equation. This enables the discretizations to be chosen according to the specific requirements of each. In fact, since the pressure gradient must be evaluated at the current x_l particle positions rather than mesh locations, a different mesh distribution in ξ could be used for U_l and $\hat{X}_l$ than that used for p_l and β_l. However, this is generally not advantageous because these functions are highly interdependent and basically require the same degree of resolution. Recall that the terminal solution $\tilde{U}$ and the characteristics of the continuity equation (lines of constant x_l) are symmetric about the central line $\hat{\eta} = 1$. Therefore, the two-dimensional mesh associated with the continuity equation need only be defined over the lower half of the domain, *i.e.* for $-1 \le \hat{\xi} \le 1$ and $0 \le \hat{\eta} \le 1$. Subdividing each of the $\hat{\xi}$ and $\hat{\eta}$ intervals into a total of $I_0 - 1$ and $J_0 - 1$ equal subintervals, respectively, the mesh locations $(\hat{\xi}_i,\hat{\eta}_j)$ were defined for $i = 1,...,I_0$ and $j = 1,...,J_0$. The streamwise interval for the one-dimensional functions $U_l(\hat{\xi},t_l)$, $\hat{X}_l(\hat{\xi},t_l)$, $p_l(\hat{X}_l,t_l)$ and $\beta_l(\hat{x}_l,t_l)$ was subdivided into a total of $K_0 - 1$ equal subintervals

78

with the mesh locations $\hat{\xi}_k$ where $k = 1,...,K_0$. While different values of I_0 and K_0 were tried, it was found that the choice $I_0 = K_0$ was most appropriate as it provides the same resolution for the one- and two-dimensional meshes. In the following development, known quantities from the previous time step are denoted by an asterisk.

3.3.2 Momentum Equation

In order to integrate the inviscid momentum equation (3.39) forward in time, the pressure gradient from the previous time step, denoted by $(\partial p_I / \partial \hat{X}_I)_k^*$, was assumed known. Time was advanced in steps of Δt_I so that $t_I = t_I^* + \Delta t_I$. The first-order equations (3.39a,b) for U_I and $\hat{X}_I$ were then solved using a predictor-corrector algorithm. The values of $U_I(\hat{\xi}_k, t_I)$ and $\hat{X}_I(\hat{\xi}_k, t_I)$ at the current time step were estimated using the following difference formulae (which are first-order accurate in Δt_I)

$$U_{Ip}(\hat{\xi}_k, t_I) = U_I(\hat{\xi}_k, t_I^*) - \frac{\Gamma\left[\hat{X}_I(\hat{\xi}_k, t_I^*)\right]}{a} \left(\frac{\partial p_I}{\partial \hat{X}_I}\right)_k^* \Delta t_I, \qquad (3.44a)$$

$$\hat{X}_{Ip}(\hat{\xi}_k, t_I) = \hat{X}_I(\hat{\xi}_k, t_I^*) + \frac{\Gamma\left[\hat{X}_I(\hat{\xi}_k, t_I^*)\right]}{a} U_{Ip}(\hat{\xi}_k, t_I) \Delta t_I, \qquad (3.44b)$$

for $k = 1,...,K_0$. With these estimates for $U_{Ip}(\hat{\xi}_k, t_I)$ and $\hat{X}_{Ip}(\hat{\xi}_k, t_I)$, the pressure gradient $(\partial p_I / \partial \hat{X}_I)_{pk}$ was estimated at the current time step using an algorithm that will subsequently be described. The distributions of $U_I(\hat{\xi}_k, t_I)$ and $\hat{X}_I(\hat{\xi}_k, t_I)$ at the current time step were refined using the following second-order accurate formulae

$$U_I(\hat{\xi}_k, t_I) = U_I(\hat{\xi}_k, t_I^*) - \frac{\Gamma\left[\hat{X}_{Ip}(\hat{\xi}_k, t_I)\right]}{2a} \left[\left(\frac{\partial p_I}{\partial \hat{X}_I}\right)_k^* + \left(\frac{\partial p_I}{\partial \hat{X}_I}\right)_{pk}\right] \Delta t_I, \qquad (3.45a)$$

$$\hat{X}_I(\hat{\xi}_k, t_I) = \hat{X}_I(\hat{\xi}_k, t_I^*) + \frac{\Gamma\left[\hat{X}_{Ip}(\hat{\xi}_k, t_I)\right]}{2a} \left[U_{Ip}(\hat{\xi}_k, t_I) + U_I(\hat{\xi}_k, t_I)\right] \Delta t_I, \qquad (3.45b)$$

79

for $k = 1,...,K_0$. Observe that in equations (3.44a) and (3.45a), the pressure gradient must be evaluated at the current particle position location $\hat{X}_l$ as opposed to the initial location $\hat{\xi}$. Therefore, to determine $(\partial p_l / \partial \hat{X}_l)_k$ the pressure gradient with respect to the initial location $\hat{\xi}$, $i.e.$ $(\partial p_l / \partial \hat{\xi})_k$ with $k = 1,...,K_0$, was evaluated using central differences at mesh locations $\hat{\xi} = \hat{X}_l(\hat{\xi}_k, t_l)$. In order to advance the solution of the momentum equation to the next time step (also from the predictor to the corrector), the pressure distribution must be determined at the current time. This is accomplished through a calculation along the characteristics of the continuity equation to obtain the current equation of the upper shear layer $\beta_l(\hat{\xi}_k, t_l)$ which is used in the interaction condition defining the pressure distribution. These two steps are discussed in the next two sections.

3.3.3 Equation of the Upper Shear Layer

Inspection of the continuity equation (3.40) reveals that the effect of interaction is represented by the particle position perturbation $\hat{X}_l(\hat{\xi}, t_l)$, while the remainder of the terms represent the continuation in time of the terminal solution. In order to evaluate the coefficients of the continuity equation, the terminal-state velocity distribution $\tilde{U}(\hat{\xi}, \hat{\eta})$ must be known, as well as the initial displacement thickness $\beta_0(\hat{\xi}) = 2 \tilde{Y}_0(\hat{\xi})$. Determination of $\beta_0(\hat{\xi})$ from equation (2.44) requires the evaluation of complete elliptic integrals, while the calculation of equation (2.46) with (2.42), (2.43) and (2.45) for the terminal-state velocity $\tilde{U}(\hat{\xi}, \hat{\eta})$ involves evaluation of incomplete elliptic integrals. The necessary elliptic integrals were evaluated using the descending Landen transformation described in Abramowitz and Stegun (1964). To compute the terminal-state velocity distribution $\tilde{U}(\hat{\xi}_i, \hat{\eta}_j)$ on the mesh, an implicit procedure was required. For a given point in the mesh $(\hat{\xi}_i, \hat{\eta}_j)$, the central line velocity $\tilde{U}_0(\hat{\xi}_i)$ was determined using equation (2.41), and λ and m were obtained from equations (2.43) and (2.45). For a specified value of $\tilde{Y} = \eta$ in equation (2.46) the value of θ was found using a root finding technique such that equation (2.46) was satisfied; $\tilde{U}(\hat{\xi}_i, \hat{\eta}_j)$ was subsequently

80

determined from equation (2.42). In this manner $\tilde{U}(\hat{\xi}_i,\hat{\eta}_j)$ was evaluated on a two-dimensional mesh defined for $i = 1,...,J_0$, $j = 1,...,J_0$.

A knowledge of the terminal-state velocity and the particle position perturbation permits an integration of the continuity equation at any given t_l. Recall that the continuity equation in Lagrangian coordinates is a first-order linear equation which is of the form

$$P(\hat{\xi},\hat{\eta},t_l)\frac{\partial Y_l}{\partial \hat{\xi}} + Q(\hat{\xi},\hat{\eta},t_l)\frac{\partial Y_l}{\partial \hat{\eta}} = R(\hat{\xi},\hat{\eta},t_l). \tag{3.46a}$$

In the present case (see equation 3.40), the coefficients are

$$P(\hat{\xi},\hat{\eta},t_l) = -(t_l + 1)\frac{\partial \tilde{U}}{\partial \hat{\eta}}, \tag{3.46b}$$

$$Q(\hat{\xi},\hat{\eta},t_l) = (t_l + 1)\frac{\partial \tilde{U}}{\partial \hat{\xi}} + \frac{a}{\Gamma(\hat{X}_l)}\frac{\partial \hat{X}_l}{\partial \hat{\xi}}, \tag{3.46c}$$

$$R(\hat{\xi},\hat{\eta},t_l) = \frac{a}{2}\frac{\beta_0(\hat{\xi})}{\Gamma(\hat{\xi})}. \tag{3.46d}$$

Observe that the coefficient $R = R(\hat{\xi})$ and the derivatives of $\tilde{U}$ (the terminal-state velocity) in equations (3.46b) and (3.46c) do not change with time and were evaluated once and for all using central differences prior to an unsteady calculation. The second term in equation (3.46c) is a function of $\hat{\xi}$ only and reflects the effects of the unsteady interaction. The coefficients in equations (3.46b,c,d) were computed at each time step for each point in the two-dimensional mesh according to

$$P(\hat{\xi}_i, \hat{\eta}_j, t_l) = -(t_l + 1)\left(\frac{\partial \tilde{U}}{\partial \hat{\eta}}\right)_{i,j}, \tag{3.47a}$$

$$Q(\hat{\xi}_i, \hat{\eta}_j, t_l) = (t_l + 1)\left(\frac{\partial \tilde{U}}{\partial \hat{\xi}}\right)_{i\,j} + \frac{a}{\Gamma[\hat{X}_l(\hat{\xi}_i, t_l)]}\left(\frac{\partial \hat{X}_l}{\partial \hat{\xi}}\right)_i, \tag{3.47b}$$

$$R(\hat{\xi}_i) = \frac{a}{2}\frac{\beta_0(\hat{\xi}_i)}{\Gamma(\hat{\xi}_i)}, \tag{3.47c}$$

for $i = 1,\dots,J_0$, $j = 1,\dots,J_0$.

The solution to the continuity equation (3.46a) is obtained by integration along characteristics which are curves of constant x_l. The equations of these characteristics are

$$\frac{d\hat{\xi}}{P} = \frac{d\hat{\eta}}{Q} = \frac{dY_l}{R} = ds, \tag{3.48}$$

where s is a variable along a characteristic. The integration can be carried out along the characteristics in order to determine the normal position $Y_l(\hat{\xi}, \hat{\eta}, t_l)$ of any fluid particle; however, the equation of the upper shear layer, which is given by $\beta_l(\hat{\xi}, t_l) = Y_l(\hat{\xi}, 2, t_l)$, is of particular interest. In a typical boundary-layer calculation (see, for example, Peridier *et al.*, 1991a), integration along the characteristics is initiated at the surface where $x = \xi$ and $y = 0$ for all time; that is, in view of the no-slip condition, particles which are initially on the wall must remain there. In the present problem, however, the integration cannot be initiated at $\hat{\eta} = 0$ because of the unbounded streamwise velocity condition (3.43b) as the lower shear layer is approached for $\hat{\eta} \to 0$. Therefore, integration along the characteristics must begin at a more convenient location. To this end, consider integration of the last of equations (3.48) ($dY_l = R(\hat{\xi})\,ds$) along a characteristic. Since the right side is independent of Y_l, it is not necessary to know the value of Y_l at $s = 0$, and integration of the equation may begin anywhere and, in effect,

82
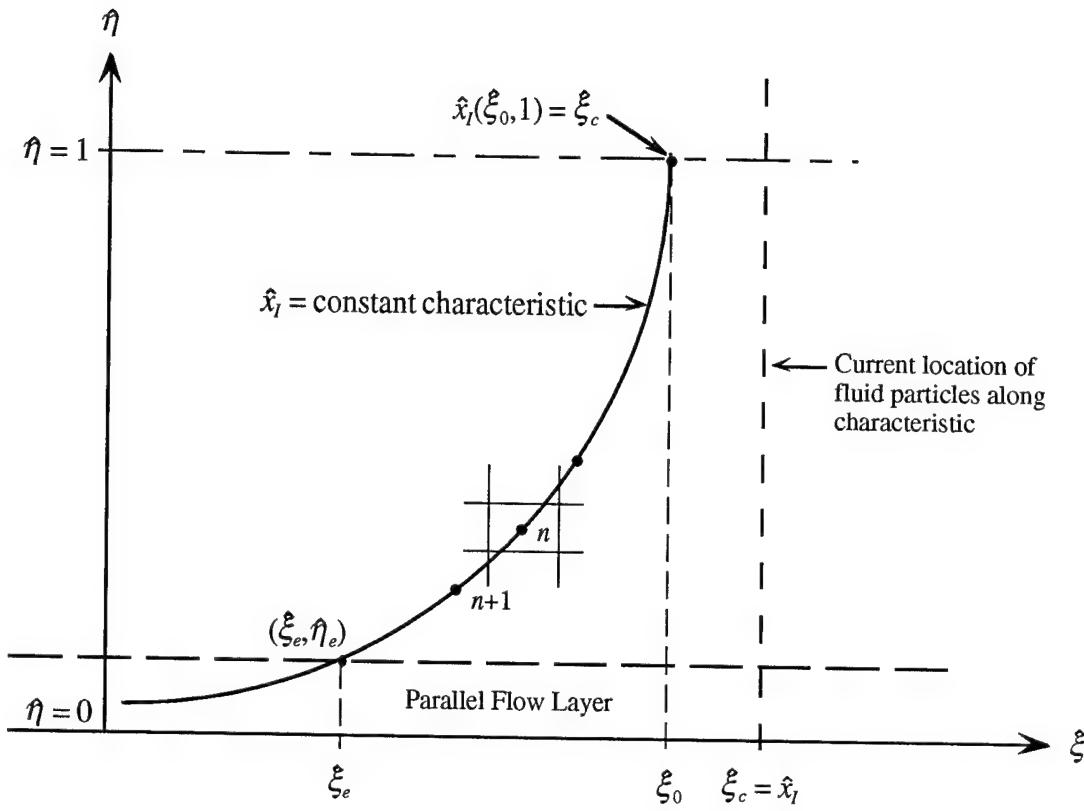
Figure 3.2 - Schematic of characteristic integration.

produces the change in Y_I between any two points. In the present method, the integrations were initiated at the point where each characteristic intersects the central line $\hat{\eta} = 1$. In addition, recall from the matching conditions (3.43) at the top and bottom of the domain that the flow becomes steady and parallel at the shear layers which bound region II, *i.e.* $u = u(\eta)$, as $\hat{\eta} \to 0$ and $\hat{\eta} \to 2$. In this study integrations were carried out along the characteristics from the central line ($\hat{\eta} = 1$) downward toward the parallel flow layer that develops as $\hat{\eta} \to 0$. The path of this integration is illustrated schematically in figure 3.2. In order to compute the displacement thickness at some point $x_I = \xi_c$, which in the finite domain is $\hat{\xi}_c$ as may be calculated from equation

(3.36), it is necessary to determine where a fluid particle, which at time t_I is located at $x_I = \xi_c$, started out at time $t_I = -1$. Denote this initial position by ξ_0 or in the finite domain as $\hat{\xi}_0$. For the illustrative situation shown in figure 3.2, the fluid particle now at $x_I = \xi_c$, or equivalently from equation (3.36) at

$$\hat{x}_I = \frac{2}{\pi} \arctan\left(\frac{\xi_c}{a}\right) = \hat{\xi}_c, \tag{3.49}$$

is assumed to have experienced a drift to the right along the central line in the time interval from $t_I = -1$ to t_I. Thus, from equation (3.28) with the transformation (3.37), the point $\hat{\xi}_0$ is determined from the relation

$$x_I(\hat{\xi}_0, 1, t_I) = (t_I + 1)\, \hat{U}(\hat{\xi}_0, 1) + a\, \tan\left[\frac{\pi}{2}\, \hat{X}_I(\hat{\xi}_0, t_I)\right] = \xi_c. \tag{3.50}$$

For a given $\hat{\xi}_c$ at time t_I, the appropriate value of $\hat{\xi}_0$ can by evaluated iteratively using second-order accurate interpolation formulae. Therefore, the initial conditions for integration along a characteristic are

$$\hat{\xi} = \hat{\xi}_0, \quad \hat{\eta} = 1, \quad Y_I = 0 \quad \text{at} \quad s = 0. \tag{3.51}$$

The characteristics have the general shape indicated in figure 3.2 and bend to the left as they approach the lower shear layer. Because of the high velocities near the lower shear layer, all characteristics emanate from the lower left corner at $\hat{\xi} = -1$ and $\hat{\eta} = 0$. Similarly, all characteristics in the upper portion of the shear layer bend to the left above $\hat{\eta} = 1$ and end up in the upper left corner at $\hat{\xi} = -1$ and $\hat{\eta} = 2$.

Integration of the characteristic equation (3.48) was carried out in the $(\hat{\xi}, \hat{\eta})$ plane using a predictor-corrector algorithm to step along the characteristics. Assume that the integration along the characteristic has reached the nth point denoted by $(\hat{\xi}^n, \hat{\eta}^n)$ and $Y_I = Y_I^n$; the coordinates of the next point $(\hat{\xi}^{n+1}, \hat{\eta}^{n+1})$, where $Y_I = Y_I^{n+1}$, are to be evaluated next. First, the coefficients P^n, Q^n and R^n of the continuity equation in

84

equations (3.47) at the nth point must be computed. This was accomplished using bilinear interpolation between the four mesh points surrounding the point $(\hat{\xi}^n, \hat{\eta}^n)$ (see Abramowitz and Stegun, 1964). The next step along the characteristic was evaluated from the following relation

$$\Delta s = \frac{\theta \, \Delta \hat{\xi}}{\sqrt{(P^n)^2 + (Q^n)^2}},$$

(3.52)

where $0 < \theta < 1$ and a typical value of θ used was $\theta = 0.25$. This formula restricts the step along the characteristic so that the arc length involved is some fraction of the mesh spacing $\Delta \hat{\xi}$; this gives rise to very small steps in s near $\hat{\eta} = 0$ where the coefficients P and Q become large. The location and normal distance of the $(n+1)$ point were then predicted using

$$\hat{\xi}_p^{n+1} = \hat{\xi}^n - P^n \, \Delta s,$$

(3.53a)

$$\hat{\eta}_p^{n+1} = \hat{\eta}^n - Q^n \, \Delta s,$$

(3.53b)

$$Y_{Ip}^{n+1} = Y_I^n + R^n \, \Delta s,$$

(3.53c)

where the negative signs in (3.53a,b) appear because the integration was carried out backward along the characteristic starting from the central line $\hat{\eta} = 1$ and moving toward the bottom shear layer at $\hat{\eta} = 0$. The coefficients P^{n+1}, Q^{n+1} and R^{n+1} were then evaluated at the point $(\hat{\xi}_p^{n+1}, \hat{\eta}_p^{n+1})$ through interpolation, and the corrector algorithm was implemented using

85

$$\hat{\xi}^{n+1} = \hat{\xi}^n - \frac{1}{2}(P^n + P^{n+1})\,\Delta s, \tag{3.54a}$$

$$\hat{\eta}^{n+1} = \hat{\eta}^n - \frac{1}{2}(Q^n + Q^{n+1})\,\Delta s, \tag{3.54b}$$

$$Y_I^{n+1} = Y_I^n + \frac{1}{2}(R^n + R^{n+1})\,\Delta s. \tag{3.54c}$$

Each integration proceeds along the characteristic successively in this way until the vicinity of the parallel flow layer is reached as $\hat{\eta} \to 0$. The level at which the characteristic integration is terminated must be carefully chosen; it must be near enough to $\hat{\eta} = 0$ so that the flow is essentially plane parallel but still sufficiently large so that substantial computational errors do not arise from attempting to integrate too far through this high velocity region where as illustrated in figure 3.2, the characteristics continue far upstream gradually asymptoting to $\hat{\eta} = 0$. A typical value of η_e used in the present integrations was $\eta_e = 0.7$. Once the parallel flow region is reached, the contribution to the normal distance Y_I from the remainder of the characteristic is simply the initial normal coordinate η_e of the point since $Y_I = \eta_e$ for locations in the parallel flow layer. Then because region II is symmetric about the central line, the current distance of the upper shear layer from the wall at $\hat{x}_I = \hat{\xi}_c$ is given by

$$\beta_I(\hat{\xi}_c, t_I) = 2\,(Y_{Ie} + \eta_e). \tag{3.55}$$

Here, Y_{Ie} is the value of Y_I obtained in the integration along the characteristic from $\hat{\eta} = 1$ to $\hat{\eta} = \hat{\eta}_e$. The characteristic integration was executed for each point along the mesh $\hat{\xi} = \hat{\xi}_k$, where $k = 1,\dots,K_0$, to obtain the equation of the upper shear layer at the current time.

As a check on this method of characteristic integration, the interpolation required at each point $(\hat{\xi}^n, \hat{\eta}^n)$ along a characteristic was replaced by a semi-analytical determination of the parts of the coefficients P^n and Q^n which are based on the terminal

solution (see equations (3.46b,c)). These terms require the gradients of the streamwise velocity $\tilde{U}$ from the terminal solution with respect to $\hat{\xi}$ and $\hat{\eta}$. The term $\partial \tilde{U}/\partial \hat{\eta}$ was evaluated using equation (2.38a) where $\tilde{U}(\hat{\xi}^n, \hat{\eta}^n)$ was determined directly from the terminal solution (equations (2.41)-(2.46)) rather than from interpolation between grid points. An analytical expression for $\partial \tilde{U}/\partial \hat{\xi}$ is difficult to obtain, but the derivative can be determined using a central-difference approximation if $\tilde{U}$ is found (from the terminal solution) for points $(\hat{\xi}^n - \Delta\hat{\xi}, \hat{\eta}^n)$ and $(\hat{\xi}^n + \Delta\hat{\xi}, \hat{\eta}^n)$ for a small $\Delta\hat{\xi}$. This method requires many evaluations of the streamwise velocity $\tilde{U}$ at each time step using the implicit procedure described at the beginning of §3.3.3 and is, therefore, very time consuming. Although it was found to be more accurate, this procedure yields the same results described in §3.4.

3.3.4 Interaction Condition

A central feature of the first interactive stage is the interaction condition (3.19) which relates the pressure to the growing distance of the upper shear layer from the wall. Equation (3.19) is a Cauchy principal-value integral, and an accurate numerical method to evaluate this integral is critical to the success of the overall scheme. In many previous interacting boundary-layer studies (see, for example, Henkes and Veldman, 1987 and Riley and Vasantha, 1989) first-order accurate methods in $\Delta\xi$ have been used to compute the Cauchy integral; this may be one reason for the contradictory results obtained in some of these investigations. Peridier *et al.* (1991b) describe a second-order accurate scheme for computing Cauchy integrals on a uniform mesh. Here, this algorithm is extended to include the possibility of a nonuniform mesh.

Consider a general Cauchy integral

$$C(x) = \frac{1}{\pi} \int_{-\infty}^{\infty} \frac{F(s)}{x-s} \, ds, \qquad\qquad (3.56)$$

and assume that the asymptotic behavior of $F(x)$ is known for $|x| \to \infty$. The

interaction condition is calculated at fixed t_I, and thus the time dependence will be omitted in the following analysis; in addition, the subscript I will be omitted from x through the remainder of this section. In the present study (*cf.* equation (3.19)),

$$F(x) = -(-t_{I0})^{-11/4} \frac{\partial \beta_I(x)}{\partial x}, \qquad (3.57)$$

where $\beta_I(x)$ is the normal distance of the upper shear layer at the current time. The calculation of the integral (3.56) is considered here for a typical point x_m in the mesh. The integral is divided into two parts

$$C(x_m) = S(x_m) + L(x_m), \qquad (3.58a)$$

where the main part of the integral is

$$S_m = S(x_m) = \frac{1}{\pi} \int_{-R}^{R} \frac{F(s)}{x_m - s}\, ds, \qquad (3.58b)$$

and R is some large fixed value of x. The contribution from the asymptotic tails is

$$L_m = L(x_m) = \frac{1}{\pi} \left\{ \int_{-\infty}^{-R} \frac{F(s)}{x_m - s}\, ds + \int_{R}^{\infty} \frac{F(s)}{x_m - s}\, ds \right\}. \qquad (3.58c)$$

As with the rest of the formulation of the first interactive stage, a finite-domain transformation similar to equation (3.36) is defined so that $\hat{s}$ and $\hat{x}$ are defined in the range $(-1,1)$. This interval is divided into M segments that are not necessarily of equal length except for the last interval on each end which both have the same length with $\Delta \hat{x}_1 = \Delta \hat{x}_M$. The mesh structure is illustrated in figure 3.3. The constant R is chosen so that the asymptotic tails are taken over the last half intervals in the finite-domain mesh; therefore,

88
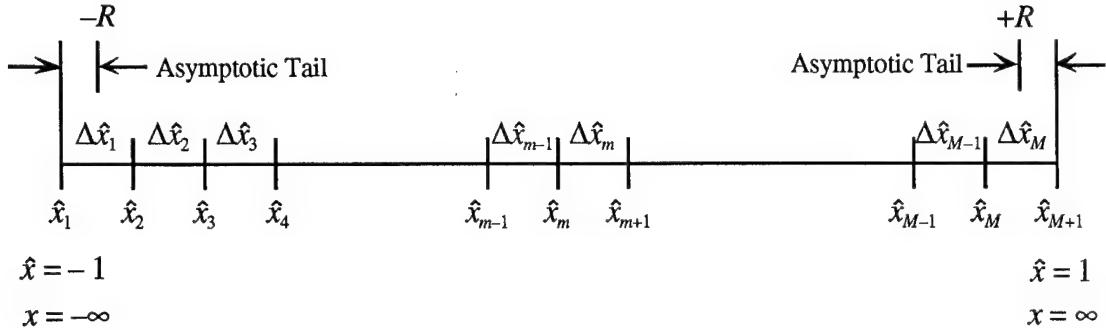
Figure 3.3 - Mesh definitions for Cauchy integral algorithm.

$$R = a \tan\left\{\frac{\pi}{2}\left(1 - \frac{1}{2}\,\Delta\hat{x}_e\right)\right\}, \tag{3.59}$$

where $\Delta\hat{x}_e = \Delta\hat{x}_1 = \Delta\hat{x}_M$.

First, the main part (3.58b) of the Cauchy integral will be considered. Applying the transformation (3.36) to s and x, equation (3.58b) becomes

$$S_m = S(\hat{x}_m) = \frac{1}{2}\cos\left(\frac{\pi\,\hat{x}_m}{2}\right)\int_{-R}^{R}\frac{H(\hat{s})}{\sin\left[\frac{\pi}{2}\,(\hat{x}_m - \hat{s})\right]}\,d\hat{s}, \tag{3.60a}$$

where

$$H(\hat{x}) = \frac{F(\hat{x})}{\cos\left(\frac{\pi\,\hat{x}}{2}\right)} = -\frac{2\,(-t_{I0})^{-11/4}}{\pi\,a}\cos\left(\frac{\pi\,\hat{x}}{2}\right)\frac{\partial\beta_I(\hat{x})}{\partial\hat{x}}. \tag{3.60b}$$

The integral (3.60a) is divided into integrals around each mesh point and summed

89

$$S_m = S(\hat{x}_m) = \frac{1}{2} \cos\left(\frac{\pi \hat{x}_m}{2}\right) \sum_{n=2}^{M} \int_{\hat{x}_n - \frac{\Delta \hat{x}_{n-1}}{2}}^{\hat{x}_n + \frac{\Delta \hat{x}_n}{2}} \frac{H(\hat{s})}{\sin\left[\frac{\pi}{2}(\hat{x}_m - \hat{s})\right]} \, d\hat{s}, \qquad (3.61)$$

where each integral is from the midpoint between $\hat{x}_{n-1}$ and $\hat{x}_n$ to the midpoint between $\hat{x}_n$ and $\hat{x}_{n+1}$. Expanding the function $H(\hat{x})$ in a Taylor series about $\hat{x}_n$ gives

$$H(\hat{x}) = H(\hat{x}_n) + (\hat{x} - \hat{x}_n) \frac{dH}{d\hat{x}}\bigg|_{\hat{x}_n} + \cdots = H_n + (\hat{x} - \hat{x}_n) H_n' + \cdots , \qquad (3.62)$$

where the prime denotes differentiation with respect to $\hat{x}$. Substituting this expansion into the integral, equation (3.61) can be approximated as

$$S_m = S(\hat{x}_m) = \frac{1}{2} \cos\left(\frac{\pi \hat{x}_m}{2}\right) \sum_{n=2}^{M} \left\{ A_{mn} H_n + B_{mn} H_n' \right\}, \qquad (3.63)$$

where

$$A_{mn} = \int_{\hat{x}_n - \frac{\Delta \hat{x}_{n-1}}{2}}^{\hat{x}_n + \frac{\Delta \hat{x}_n}{2}} \frac{d\hat{s}}{\sin\left[\frac{\pi}{2}(\hat{x}_m - \hat{s})\right]}, \qquad (3.64)$$

$$B_{mn} = \int_{\hat{x}_n - \frac{\Delta \hat{x}_{n-1}}{2}}^{\hat{x}_n + \frac{\Delta \hat{x}_n}{2}} \frac{\hat{s} - \hat{x}_n}{\sin\left[\frac{\pi}{2}(\hat{x}_m - \hat{s})\right]} \, d\hat{s}. \qquad (3.65)$$

The integral (3.64) for A_{mn} may be evaluated in closed form to give

90

$$A_{mn} = -\frac{1}{\pi} \log \left\{ \frac{\sin(r_{mn} + a_n) - \sin b_n}{\sin(r_{mn} + a_n) + \sin b_n} \right\}^2, \tag{3.66}$$

where

$$r_{mn} = \frac{\pi}{2} (\hat{x}_m - \hat{x}_n), \tag{3.67a}$$

$$a_n = \frac{\pi}{8} (\Delta\hat{x}_{n-1} - \Delta\hat{x}_n), \tag{3.67b}$$

$$b_n = \frac{\pi}{8} (\Delta\hat{x}_{n-1} + \Delta\hat{x}_n). \tag{3.67c}$$

The integral (3.65) for B_{mn} cannot be evaluated in a convenient closed form; instead, let

$$\mu = \frac{\hat{s} - \hat{x}_n}{\Delta\hat{x}_{n-1}}, \tag{3.68}$$

so that the integral (3.65) becomes

$$B_{mn} = (\Delta\hat{x}_{n-1})^2 \int_{-1/2}^{\frac{\Delta\hat{x}_n}{2\,\Delta\hat{x}_{n-1}}} \frac{\mu\,d\mu}{\sin(r_{mn} - \varepsilon\,\mu)}, \tag{3.69}$$

where $\varepsilon = \pi\,\Delta\hat{x}_{n-1}/2$. The denominator of the integrand in (3.69) can be rewritten and approximated for small ε as

$$\sin(r_{mn} - \varepsilon\,\mu) = \sin r_{mn} - \varepsilon \cos r_{mn}\,\mu + O(\varepsilon^2). \tag{3.70}$$

Substitution of the expansion (3.70) into (3.69) produces integrals which can be evaluated in closed form to give

91

$$B_{mn} = -\frac{(\Delta\hat{x}_{n-1})^2}{\varepsilon \cos r_{mn}} \left\{ \frac{1}{2}\left(\frac{\Delta\hat{x}_n}{\Delta\hat{x}_{n-1}} + 1\right) \right.$$
$$\left. + \frac{\sin r_{mn}}{\varepsilon \cos r_{mn}} \log\left| \frac{2\sin r_{mn} - \varepsilon\,(\Delta\hat{x}_n/\Delta\hat{x}_{n-1})\cos r_{mn}}{2\sin r_{mn} + \varepsilon\cos r_{mn}} \right| \right\}. \qquad (3.71a)$$

When r_{mn} is large, this expression may be simplified by rewriting the logarithmic term and expanding to obtain

$$B_{mn} = \frac{(\Delta\hat{x}_{n-1})^2}{8\sin r_{mn}} \left\{ \left(\frac{\Delta\hat{x}_n}{\Delta\hat{x}_{n-1}}\right)^2 - 1 + \frac{\varepsilon\cos r_{mn}}{3\sin r_{mn}}\left[\left(\frac{\Delta\hat{x}_n}{\Delta\hat{x}_{n-1}}\right)^3 + 1\right] \right\}. \qquad (3.71b)$$

In practice, equation (3.71a) was found to be most effective for $|r_{mn}| < 0.6$ and equation (3.71b) for $|r_{mn}| > 0.6$. If the mesh is uniform, *i.e.* $\Delta\hat{x}_{n-1} = \Delta\hat{x}_n = \Delta\hat{x}$, the expressions (3.66) and (3.71) reduce to

$$A_{mn} = -\frac{1}{\pi}\log\left\{ \frac{\sin r_{mn} - \sin\left(\frac{\pi\,\Delta\hat{x}}{4}\right)}{\sin r_{mn} + \sin\left(\frac{\pi\,\Delta\hat{x}}{4}\right)} \right\}^2, \qquad (3.72a)$$

$$B_{mn} = \begin{cases} -\dfrac{(\Delta\hat{x})^2}{\varepsilon\cos r_{mn}}\left\{1 + \dfrac{\sin r_{mn}}{\varepsilon\cos r_{mn}}\log\left|\dfrac{2\sin r_{mn} - \varepsilon\cos r_{mn}}{2\sin r_{mn} + \varepsilon\cos r_{mn}}\right|\right\}, & |r_{mn}| < 0.6 \\[2ex] \dfrac{\pi}{24}(\Delta\hat{x})^3\,\dfrac{\cos r_{mn}}{\sin^2 r_{mn}}, & |r_{mn}| > 0.6 \end{cases}, \qquad (3.72b)$$

which are the same as those obtained by Peridier *et al.* (1991b).

It is evident from the form of the dependence on r_{mn} in equations (3.72) that the matrices of coefficients A_{mn} and B_{mn} are such that each element along a diagonal contains the same value if the mesh is uniform. Therefore, only $(2M-1)$ values must be stored for each of A_{mn} and B_{mn} rather than M^2 values as for the nonuniform mesh case. For either the uniform or nonuniform case, if the mesh does not change with

time, the coefficients A_{mn} and B_{mn} must only be calculated once, whereas they must be calculated at every time step if the mesh changes with time as in a time dependent adaptive meshing scheme. Therefore, use of a time dependent mesh involves a considerable increase in computational time. One such scheme was tried in the present investigation in which the displacement thickness at a given time was computed at the current streamwise locations of a predefined set of fluid particles along the central line. In this way, the resolution was enhanced in regions where the flow focused into a narrow streamwise region. While this method did provide some increase in resolution as the flow evolved toward an eruption, the increase in accuracy was not sufficient to warrant the substantial increase in computational time. As a result, a uniform mesh without time dependence was used for the majority of the calculations.

Now, consider the contribution of the asymptotic tails to the Cauchy integral. In order to evaluate the integrals in equation (3.58c) for $|x| \to \infty$, the form of $\partial \beta_I / \partial x$ must be determined for large $|x|$. Substitution of (2.43), (2.45) and (2.47) into (2.44) give the following expressions for the displacement thickness at large x:

$$\beta_I \sim \begin{cases} -\dfrac{4\,K\left(\dfrac{5\,\pi}{12}\right)}{3^{1/4}\,x^{1/6}}, & x \to \infty \\[4mm] \dfrac{4\,K\left(\dfrac{\pi}{12}\right)}{3^{1/4}\,(-x)^{1/6}}, & x \to -\infty \end{cases}, \tag{3.73}$$

where K is the complete elliptic integral. Taking the derivative of (3.73) with respect to x and substituting into (3.57) and (3.58c), the contribution due to the asymptotic tails is

$$L_m = L(x_m) = \frac{2\,(-t_{I0})^{-11/4}}{3^{5/4}\,\pi}\left\{ K\left(\frac{\pi}{12}\right)\int_{-\infty}^{-R}\frac{ds}{(-s)^{7/6}\,(s-x_m)} - K\left(\frac{5\,\pi}{12}\right)\int_{R}^{\infty}\frac{ds}{s^{7/6}\,(s-x_m)} \right\}. \tag{3.74}$$

The integrals in equation (3.74) can be evaluated separately for $x_m \neq 0$, where the

93

substitution $s = x_m/\tau^6$ is helpful, and $x_m = 0$. The resulting expressions are

$$L_m = \begin{cases} \dfrac{1}{6} \dfrac{(-t_{I0})^{-11/4}}{3^{1/4}\,\pi\,|x_m|^{7/6}} \left\{ K\!\left(\dfrac{\pi}{12}\right) T_-(x_m) - K\!\left(\dfrac{5\,\pi}{12}\right) T_+(x_m) \right\}, & x_m \neq 0 \\[3mm] -\dfrac{4}{7} \dfrac{(-t_{I0})^{-11/4}}{3^{1/4}\,\pi\,R^{7/6}} \left\{ K\!\left(\dfrac{\pi}{12}\right) + K\!\left(\dfrac{5\,\pi}{12}\right) \right\}, & x_m = 0 \end{cases}, \qquad (3.75a)$$

where

$$T_-(x_m) = \begin{cases} -T_1(x_m), & x_m > 0 \\ T_2(x_m), & x_m < 0 \end{cases}, \qquad (3.75b)$$

$$T_+(x_m) = \begin{cases} T_2(x_m), & x_m > 0 \\ -T_1(x_m), & x_m < 0 \end{cases}, \qquad (3.75c)$$

and

$$T_1(x_m) = 24\ \gamma - \sqrt{3}\ \log\!\left\{\dfrac{\gamma^2 + \sqrt{3}\ \gamma + 1}{\gamma^2 - \sqrt{3}\ \gamma + 1}\right\}^2 - 8\ \tan^{-1}\gamma - 4\ \tan^{-1}\!\left\{\dfrac{\gamma}{1-\gamma^2}\right\}, \qquad (3.75d)$$

$$T_2(x_m) = 24\ \gamma + \log\!\left\{\dfrac{(1+\gamma^3)\,(1-\gamma)^3}{(1-\gamma^3)\,(1+\gamma)^3}\right\}^2 - 4\ \sqrt{3}\ \tan^{-1}\!\left\{\dfrac{\sqrt{3}\ \gamma}{1-\gamma^2}\right\}, \qquad (3.75e)$$

where $\gamma = \left|\dfrac{x_m}{R}\right|^{1/6}$.

3.4 Calculated Results

Before discussing the numerical solution of the full interactive case, the problem without the influence of interaction will be considered in order to test the algorithm described in the last section. In this calculation the pressure is not evaluated from equation (3.19), and the pressure gradient is set equal to zero in equation (3.30a).

94

Without the pressure gradient term, the solution, starting at some value $\bar{t}_I = t_{I0}$, should consist of the continuation of the terminal solution which ultimately must become singular at $t_I = 0$. Because the terminal solution is exact and known, the ability of the numerical algorithm to continue to track the solution all the way to the singularity gives confidence in the numerical method. For example, the variables defined in the first interactive stage given in equations (3.6a,b,c) and in equations (3.14a,b,c) are related to the terminal-state variables in equations (2.37a,b,c) by

$$\tilde{X} = (-t_I)^{-3/2} x_I, \tag{3.76a}$$

$$\beta_I(x_I,t_I) = (-t_I)^{-1/4} \beta_0(\tilde{X}). \tag{3.76b}$$

Equations (3.76) may be used to obtain an exact result for the equation of the upper shear layer for any streamwise location x_I and time t_I which then can be compared directly with the results of the numerical integration. Note that in equation (3.76b), $\beta_0(\tilde{X}) = 2\tilde{Y}_0(\tilde{X})$ is the initial displacement thickness given by the terminal solution. Calculations were carried out using the algorithm described in §3.3 using 401 points in the ξ direction. Since the pressure gradient is taken equal to zero in equation (3.30a), a value of t_{I0} need not be prescribed (since this only appears in equation (3.19)), and both the perturbations U_I and X_I in equations (3.30) remain unchanged for all t_I. Because of this behavior, all reasonable values of the time step will produce the same result, and basically the integration procedure corresponds to starting a calculation at some arbitrary location in time just prior to the formation of the singularity. The central question to be answered here is how well the numerical integration scheme for the continuity equation performs in producing distributions of $\beta_I(x_I,t_I)$ given exactly by equations (3.76). The displacement thickness from such a calculation at several times is shown in figure 3.4. The initial condition at $t_I = -1$ is the terminal solution; subsequently, the spike in displacement thickness narrows in the streamwise direction and expands away from the surface according to the scalings in (3.76) before becoming

95
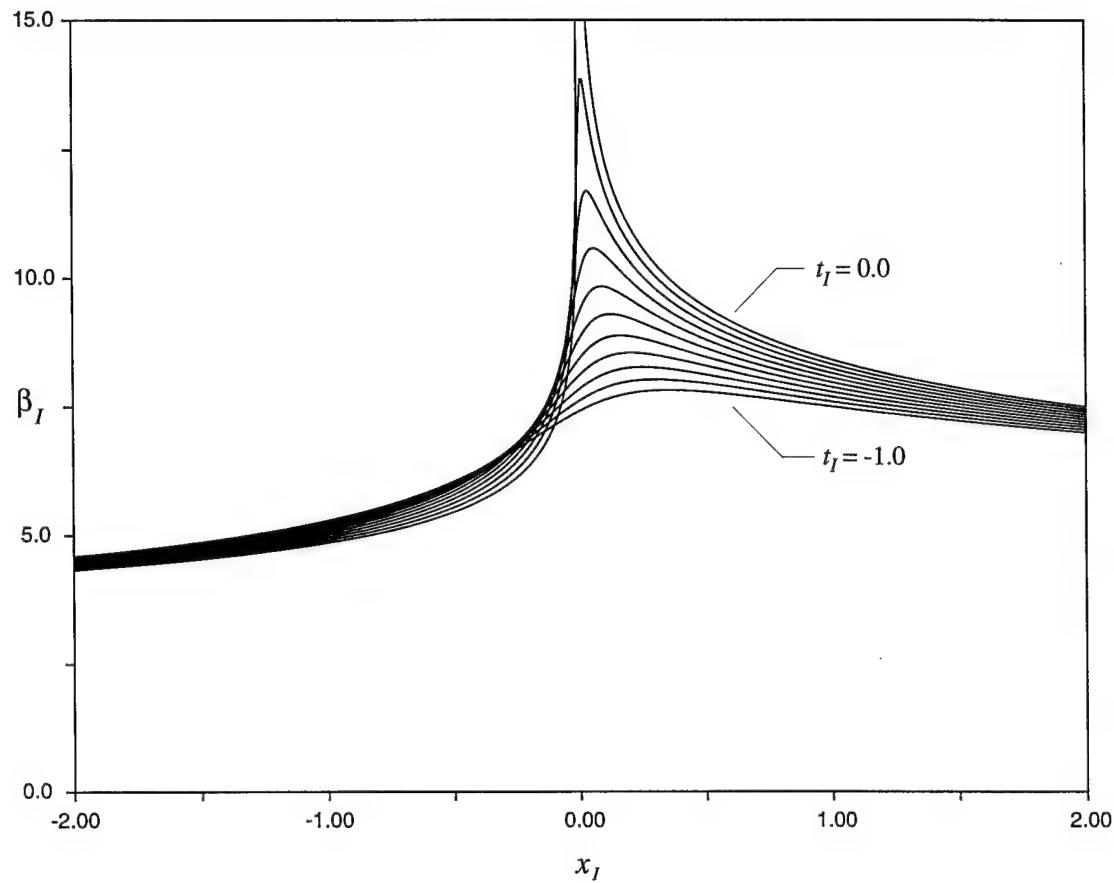
Figure 3.4 - Equation of the upper shear layer β_I for non-interactive case.

singular at $t_l = 0$. It may be noted that the integration scheme for the continuity equation reproduces the developing terminal solution very closely, and the computed and exact results are indistinguishable graphically. These calculations give confidence in the algorithm for integration of the continuity equation, and it is now possible to turn attention to the first interactive stage.

For the first interactive stage, the interest is on how the evolving terminal boundary-layer solution is altered by the influence of interaction. In order to obtain a numerical solution of the first interactive stage, the time at which the calculation is initiated t_{I0} and the time step Δt_I must be chosen. Many calculations were carried out with different values of both of these parameters, and it was found that $t_{I0} = -50$ was sufficient to capture the bulk of the interaction, and the solution did not change for time steps smaller that $\Delta t_I = 0.001$. All results shown were obtained using these values, and the effect of changes in these parameters on the numerical solution will be discussed further as the solution is described.

Based on the interactive boundary-layer calculations of Peridier *et al.* (1991b), it was expected in the initial stages of the investigation that the first interactive stage would terminate in a singularity at a time prior to that which occurs in the non-interactive case (*i.e.* the terminal solution). Indeed, for the mesh sizes used in the initial stages of the investigation, the singularity (as described in §3.2.3) always occurred at negative times (*i.e.* $t_{Is} < 0$). In these cases the form of the singularity was essentially similar to the terminal singularity that occurs without interaction as shown in figure 3.4 except that it occurred at an earlier time. For example, the singularity times for a few different meshes are given in table 3.1. These results appeared encouraging since the singularity time found by Peridier *et al.* (1991b) was approximately $\bar{t}_{Is} = -3.0$ (the exact value varied slightly with Reynolds number). As seen in table 3.1, however, it proved impossible to obtain a grid independent solution; as finer meshes were used, the singularity occurred at progressively earlier times.

As the mesh was refined further, an irregularity appeared in the solution, and

97

| Mesh	t_{ls}	$\bar{t}_{ls}$
$I_0 = K_0 = 101,\ J_0 = 51,\ a = 1.0$	-0.019	-0.950
$I_0 = K_0 = 201,\ J_0 = 101,\ a = 1.0$	-0.048	-2.400
$I_0 = K_0 = 401,\ J_0 = 201,\ a = 1.0$	-0.081	-4.050

Table 3.1 - Singularity times from calculations of the first interactive stage for various meshes.

results for a typical case are shown in figure 3.5 which were obtained using a mesh defined by $I_0 = K_0 = 801, J_0 = 401$ and $a = 1.0$. Before discussing the nature of the irregularity, some general features of the solution will be discussed. The effective displacement β_I, shown in figure 3.5a, evolves essentially as in the non-interactive case; the effect of the interaction is small globally. The pressure p_I induced by the growing displacement thickness is shown in figure 3.5b. Note that the magnitude is small due to the factor $(-t_{I0})^{-11/4}$ in the interaction condition (3.19). Figures 3.5c and 3.5d show the streamwise velocity perturbation and particle position perturbation, respectively. It is these perturbation variables which most clearly reveal the overall effects of the interaction. Recall from the description of the terminal solution (about which the flow is perturbed) that the streamwise velocity becomes progressively larger as the upper and lower extents of the region, as well as the upstream and downstream extents, are approached. Therefore, the one-dimensional velocity perturbation, which is small in magnitude, only alters the flow appreciably in the immediate vicinity of the center of the domain, near the point $(\hat{\xi}, \hat{\eta}) = (0,1)$, where the terminal-state velocity is small. Recall also that the velocity along the central line is positive upstream of $(\hat{\xi}, \hat{\eta}) = (0,1)$ and negative downstream of this point. With this in mind, the

98
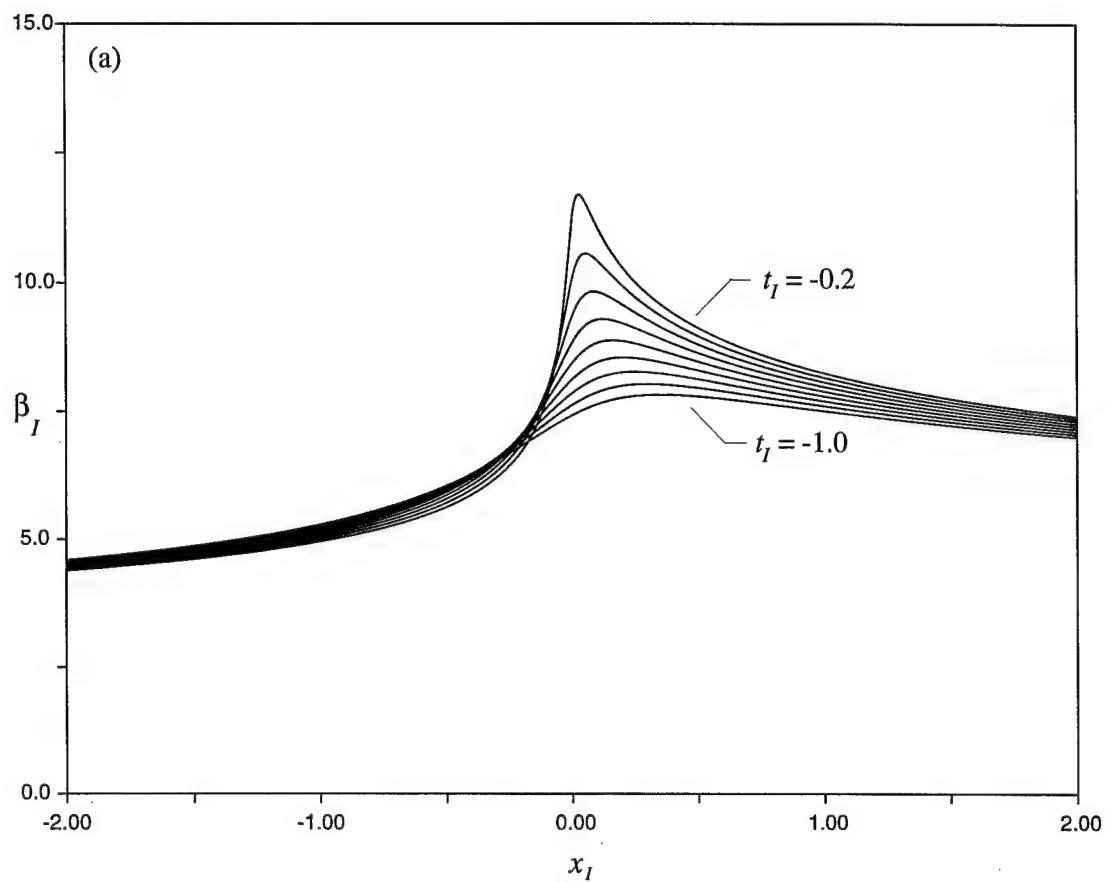
(a) Equation of the upper shear layer β_I.

Figure 3.5 - Interactive calculation with $a = 1.0$.
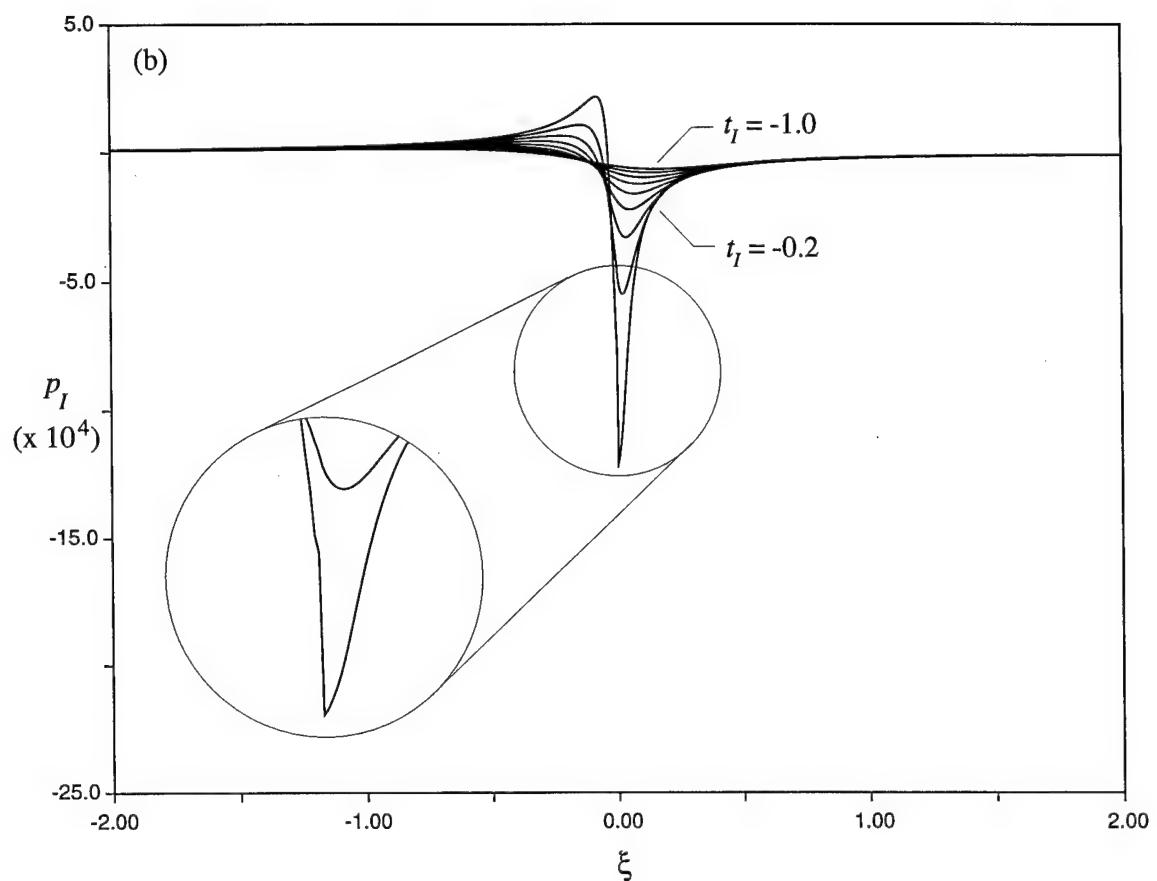
(b) Induced pressure p_I.

Figure 3.5 - Continued.
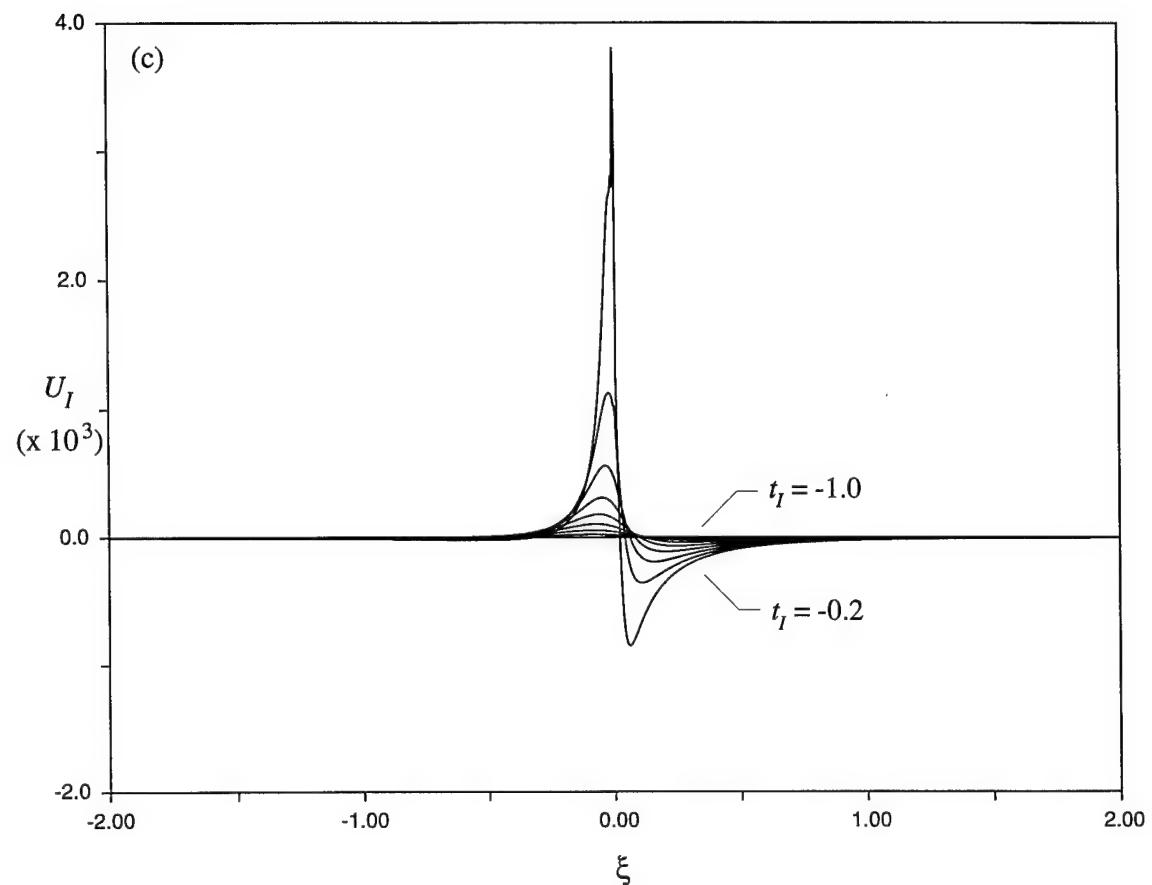
(c) Streamwise velocity perturbation U_I.

Figure 3.5 - Continued.

101
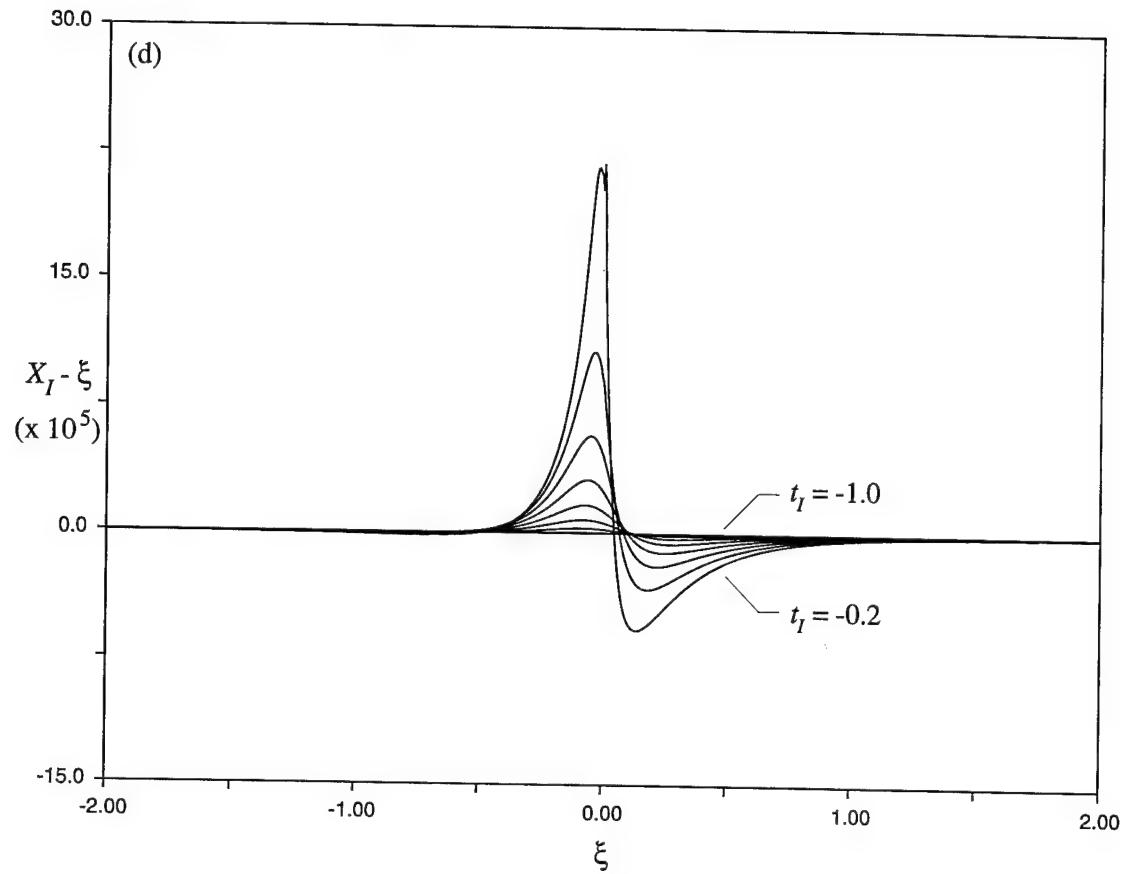
(d) Particle position perturbation $X_I - \xi$.

Figure 3.5 - Continued.

102

perturbation velocity (figure 3.5c) reveals an increasing positive perturbation just upstream of $\hat{\xi} \approx 0$ and a negative perturbation just downstream of this point. Thus, the interaction accelerates the focusing of the flow toward the eventual separation point; this suggests that the onset of the singularity would likewise be accelerated as was found in the coarse mesh results described above.

The irregularity exhibited in the latter stages of the case shown in figure 3.5 is in the form of a short length scale spike centered at $\hat{\xi} \approx 0$ which forms in the induced pressure, velocity perturbation and particle position perturbation distributions. The effect of concentrating more points near $\xi = 0$, by reducing the value of the streamwise stretching parameter a in the finite-domain transformation, is shown in figure 3.6. These results were obtained on the same mesh used to obtain the results shown in figure 3.5 except for the value of a; figure 3.6a shows results for $a = 0.5$, and figure 3.6b shows results for $a = 0.25$. Note that halving a approximately doubles the number of points in the vicinity of $\xi = 0$. Comparing the results for the induced pressure in figure 3.6a,b with the case shown in figure 3.5b, it becomes apparent that as more points are concentrated near $\xi = 0$, an instability is present which is manifest at earlier times for finer meshes. This type of behavior is reminiscent of the short wavelength instability found by Ryzhov and Smith (1984) in considering dynamic stall and by Tutty and Cowley (1986) for triple-deck type interactions. Such an instability does not permit grid independent solutions, because smaller step sizes in the mesh admit shorter wavelength, faster growing modes. This also accounts for the occurrence of the instability near $\xi = 0$ where the step sizes are smallest due to the transformation (3.36). The presence of an instability in the first interactive stage is considered further in §3.5.

The effects of the other solution parameters support the physical existence of a high-frequency instability in the first interactive stage. Increasing the number of points in the streamwise mesh K_0 has the same effect as reducing the stretching parameter; the smaller step sizes promote faster growth of the instability. In addition, the choice of

103
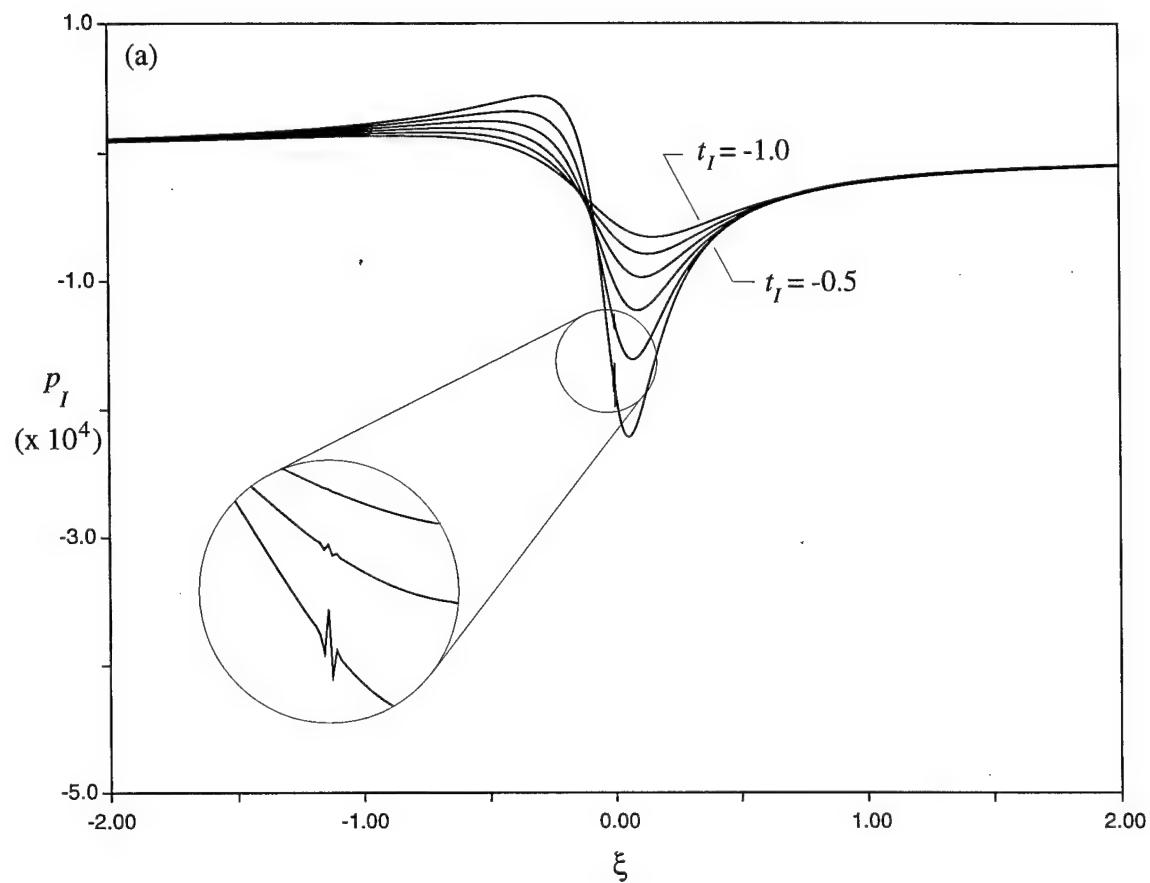
(a) $a = 0.5$.

Figure 3.6 - Induced pressure p_I from interactive calculations.

104
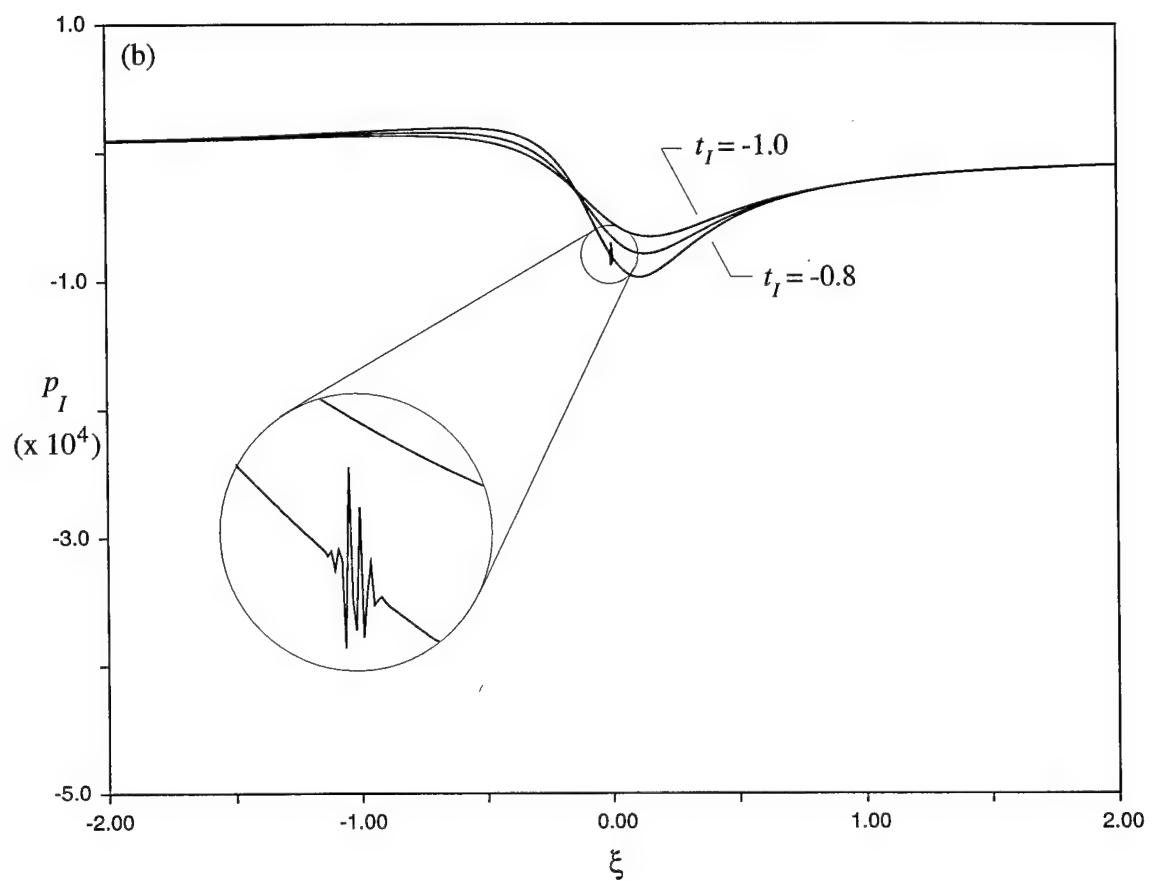
(b) $a = 0.25$.

Figure 3.6 - Continued.

an initial start time affects the spacial resolution. Choosing the initial time t_{I0} at which to start the interactive calculation involves a compromise between capturing the interaction and mesh resolution. In order to capture the bulk of the interaction, the magnitude of t_{I0} should be large; however, the transformation (3.14) indicates that increasing the magnitude of t_{I0} reduces the resolution of the physical mesh in the streamwise direction. It was possible to alleviate this difficulty through a remeshing procedure in which a calculation was performed successively over a series of time intervals with the results of the previous interval (scaled according to equations (3.14)) being the initial conditions for the next interval with smaller $|t_{I0}|$. Although this procedure captured more of the interaction, the effect on the instability was not noticeable, apparently because the instability is so highly mesh dependent. Of particular interest in numerical computations exhibiting instabilities is the effect of the time step Δt_I. Interestingly, reductions in the time step produced results which were indistinguishable from those shown here even after the instability was well developed. From a numerical point of view, this is perhaps the strongest evidence that the instability encountered here is physically contained in the formulation of the first interactive stage. However, a physical instability can only be distinguished from a numerical one through experimental or analytical means. Therefore, an analytical investigation of the instability is considered in the next section.

But first, it is of interest to consider the effect of suppressing the instability, whether numerical or physical, through a smoothing technique. This has routinely been done in calculations of vortex sheet motion (see, for example, Krasny, 1986 and Shelley, 1992) where numerical round-off error can have a catastrophic effect on the results; the smoothing was accomplished in these studies by application of a Fourier filter. After calculation of the discreet Fourier transform of the function, the Fourier coefficients with magnitude smaller than a prescribed value, which was set near the level of round-off of the computer, were set equal to zero. Alternatively, smoothing may be accomplished through convolution of the data function with a prescribed

106

response function (see, for example, Press *et al.* (1989)). This technique smooths out features in the data function which are smaller than the length scale of the response function. This was done here by convolution of the pressure distribution at each time step with the response function

$$r(\xi) = b \, e^{-d^2 \xi^2}, \tag{3.77}$$

where the constant b was chosen in order to preserve the original scale of the data function, and d determined the length scale of the response function. Reducing d increased the degree of smoothing, and solutions were sought which were independent of d. The convolution was carried out by (1) taking the fast Fourier transforms of the pressure distribution and response function, (2) multiplying the corresponding Fourier coefficients of these two function together and (3) computing the inverse transform of the resulting function.

An example of the effect of smoothing, with $d = 200.0$, on the pressure distribution is shown in figure 3.7. The mesh used for this case was $I_0 = K_0 = 1024$, $J_0 = 512$ and $a = 0.25$. Although the number of grid points has been increased compared with the case shown in figure 3.6b (the convolution algorithm required 2^n grid points), the instability is much less severe and the solution breaks down at a much later time. By decreasing d further, the instability is gradually suppressed until eventually there is no evidence of the instability for values less than about $d = 25.0$. The solution for cases in which the instability is completely suppressed then evolve toward a singularity, similar to the non-interactive case, as determined by §3.2.3 just as for the early coarse mesh results. However, it was not possible to determine a solution independent of the level of smoothing as specified by d, but the singularity always occurred at times prior to the non-interactive singularity ($t_{ls} < 0$); this is consistent with the interacting boundary-layer results of Peridier *et al.* (1991b) and the coarse mesh results described previously. While the effect of suppressing the instability through smoothing is interesting as it relates to a hypothetically disturbance free flow environment, the question remains as to the physical existence of the instability within the formulation of the first interactive stage; this is considered next.

107
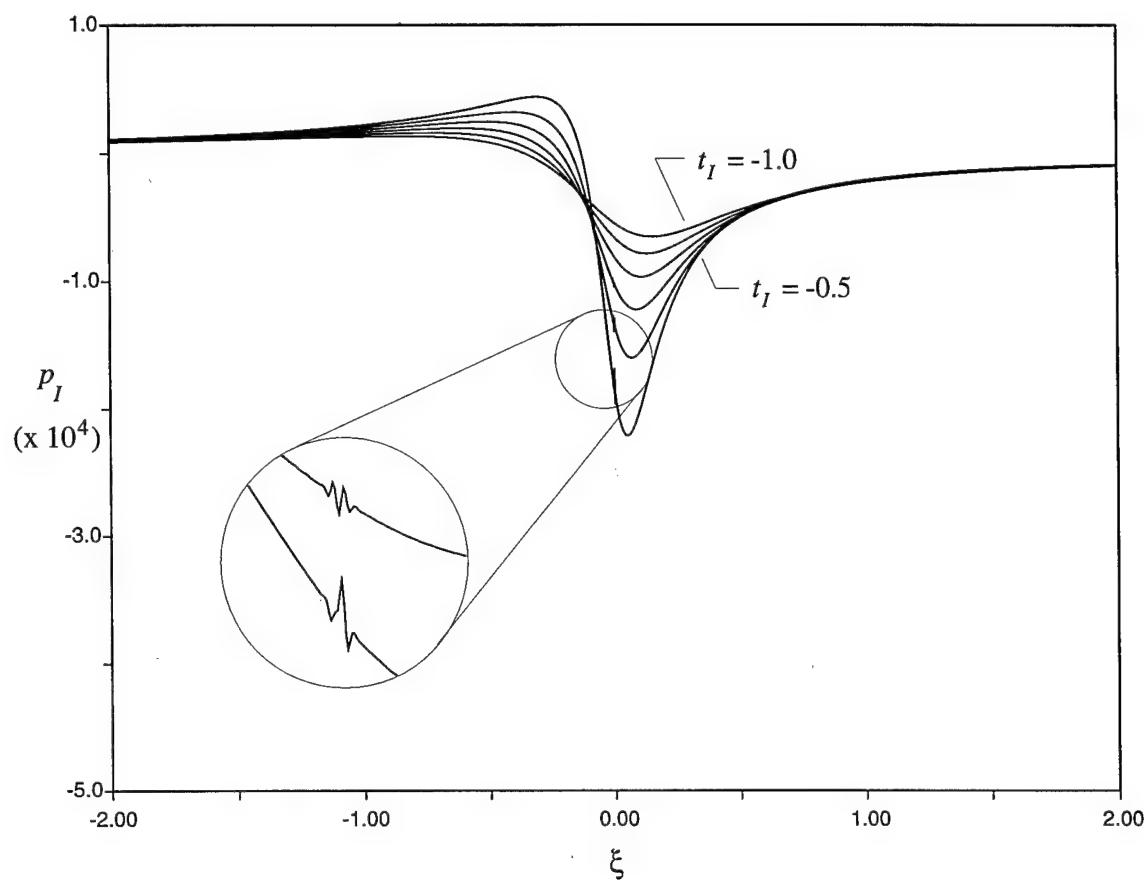
Figure 3.7 - Interactive calculation with smoothing: $d = 200$.

3.5 Stability Analysis

3.5.1 Linear Stability

The numerical results described in the previous section suggest the presence of a high-frequency instability within the first interactive stage. In order to investigate such a possibility, infinitesimal harmonic disturbances of amplitude $\varepsilon \ll 1$ areintroduced, and the linear stability of the developing exact solution in the first interactive stage (denoted by subscript zero) is considered (see a similar analysis given by Tutty and Cowley, 1986). Therefore, define

$$u_I = u_0(x_I,Y_I,t_I) + \varepsilon\ e^{i(\alpha x_I - \alpha c\, t_I)}\ u_1(x_I,Y_I,t_I) + \cdots, \qquad (3.78a)$$

$$\psi_I = \psi_0(x_I,Y_I,t_I) + \varepsilon\ e^{i(\alpha x_I - \alpha c\, t_I)}\ \psi_1(x_I,Y_I,t_I) + \cdots, \qquad (3.78b)$$

$$p_I = p_0(x_I,t_I) + \varepsilon\ e^{i(\alpha x_I - \alpha c\, t_I)}\ p_1(x_I,t_I) + \cdots, \qquad (3.78c)$$

$$\beta_I = \beta_0(x_I,t_I) + \varepsilon\ e^{i(\alpha x_I - \alpha c\, t_I)}\ \beta_1(x_I,t_I) + \cdots. \qquad (3.78d)$$

The wavenumber α is real and is assumed large ($\alpha \gg 1$) in accordance with the numerical results of the previous section, and $c = c_r + i\,c_i$ is the complex wavespeed. Consequently, the temporal stability of the first interactive stage is of interest here, and a disturbance is unstable if $c_i > 0$. Substituting the expressions (3.78) into the momentum equation (3.15a,b) and retaining the $O(\varepsilon\alpha)$ terms ($O(\varepsilon\alpha) > O(\varepsilon)$), the following equations are obtained

$$(u_0 - c)\,u_1 - \psi_1 \frac{\partial u_0}{\partial Y_I} = -\,p_1, \quad u_1 = \frac{\partial \psi_1}{\partial Y_I}. \qquad (3.79a,b)$$

109

Note that because α is large, equations (3.79) are the same as would be obtained if the flow were plane parallel and u_0, u_1, ψ_0 and ψ_1 were function of Y_I and β_0, β_1, p_0 and p_1 were constants. Substitution of (3.79b) into (3.79a) gives the first-order linear equation

$$\frac{\partial \psi_1}{\partial Y_I} - \frac{\partial u_0 / \partial Y_I}{u_0 - c} \psi_1 = -\frac{p_1}{u_0 - c},\tag{3.80}$$

which has the integrating factor $(u_0 - c)^{-1}$. Thus, the solution to (3.80) is

$$\psi_1 = - p_1 (u_0 - c) \int_0^{Y_I} \frac{dY_I}{(u_0 - c)^2},\tag{3.81}$$

where an arbitrary function of (x_I, t_I) must be zero to satisfy $\psi_1 = 0$ at $Y_I = 0$. Thus, the perturbation velocity from differentiation of equation (3.81) is

$$u_1 = \frac{\partial \psi_1}{\partial Y_I} = - p_1 \frac{\partial u_0}{\partial Y_I} \int_0^{Y_I} \frac{dY_I}{(u_0 - c)^2} - \frac{p_1}{u_0 - c}.\tag{3.82}$$

Substitution of the expansions (3.78a) and (3.78d) into the matching condition (3.17a) requires that for $\varepsilon \ll 1$

$$u_1 \sim \frac{8\,\beta_1}{(Y_I - \beta_0)^3} \quad \text{as} \quad Y_I \to \beta_0.\tag{3.83}$$

Evaluating the solution (3.82) as $Y_I \to \beta_0$, where the form of $\partial u_0 / \partial Y_I$ is determined as $Y_I \to \beta_0$ from the matching condition (3.17a), and substituting equation (3.83) gives

$$p_1 I_c = \beta_1,\tag{3.84a}$$

110

where

$$I_c = \int_0^{\beta_0} \frac{dY_l}{(u_0 - c)^2}. \qquad (3.84b)$$

Now considering the interaction condition (3.19), substitution of equations (3.78c) and (3.78d) gives

$$e^{i \alpha x_l} p_1 = - \frac{i \alpha (-t_{l0})^{-11/4}}{\pi} \int_{-\infty}^{\infty} \frac{\beta_1(s,t_l) e^{i \alpha s}}{x_l - s} \, ds. \qquad (3.85)$$

Letting $w = s - x_l$, equation (3.85) becomes

$$p_1 = \frac{i \alpha (-t_{l0})^{-11/4}}{\pi} \int_{-\infty}^{\infty} \frac{\beta_1(x_l + w,t_l) e^{i \alpha w}}{w} \, dw, \qquad (3.86)$$

and the integral may be evaluated using contour integration and is equal to $\pi i \beta_1(x_l,t_l)$. Hence, the interaction condition requires that

$$p_1 = - (-t_{l0})^{-11/4} \alpha \beta_1. \qquad (3.87)$$

Substituting this expression into equation (3.84a) gives the eigenvalue relation

$$(-t_{l0})^{-11/4} \alpha I_c = - 1, \qquad (3.88)$$

where I_c is defined by equation (3.84b). Because $\alpha \gg 1$ and is real, I_c must also be real but small and negative. In the present case $u_0(Y_l)$ is symmetric about $Y_l = \beta_0/2$; thus, applying the transformation $\hat{Y}_l = 2Y_l/\beta_0$ as before, the integral (3.84b) may be written

111

$$I_c = \beta_0 \int_0^1 \frac{d\hat{Y}_I}{(u_0 - c)^2}, \tag{3.89}$$

where again c is complex, $u_0(x_I, Y_I, t_I)$ is a typical velocity profile and $\beta_0(x_I, t_I)$ is the displacement thickness at the x_I location at which the velocity profile is considered.

3.5.2 Large c Instability

In order to determine if the flow is unstable, a solution is sought for the integral (3.89) using typical velocity profiles from a calculation of the first interactive stage to determine if there are values of the complex wavespeed c, with $c_i > 0$, for which I_c is small, real and negative. Because the integration range in equation (3.89) is finite, this suggests the following expansion

$$I_c = \frac{\beta_0}{c^2} + \cdots, \quad |c| \gg 1, \tag{3.90}$$

and thus for large c, the eigenvalue relation (3.88) gives

$$c_i = (-t_{I0})^{-11/8} (\beta_0 \, \alpha)^{1/2}, \tag{3.91}$$

and the flow would be highly unstable. Therefore, the growth rate for this case would be

$$\Omega = \alpha \, c_i = (-t_{I0})^{-11/8} (\beta_0 \, \alpha^3)^{1/2}, \tag{3.92}$$

which, apart from the constant $(-t_{I0})^{-11/8}$, is the same as the linear stability case of Brown, Cheng and Smith (1988) (see their equation 2.8). This case would dominate any unstable points having $c = O(1)$, if they exist, due to its faster growth rate. It must

112

be determined, however, whether the large u_0 behavior as $\hat{Y}_I \to 0$ effects the result (3.90) and thus the existence of the large c instability.

In order to confirm the viability of the large c instability, the integral (3.89) was evaluated numerically for typical velocity profiles $u_0(x_I,Y_I,t_I)$ and for a range of c. The algorithm used to compute the singular integral (3.89) is due to Tutty and Cowley (1986) and is described in appendix C. Although the first interactive stage is unsteady, the unsteady one-dimensional velocity perturbation, shown in equation (3.26) in the Lagrangian formulation, does not qualitatively change the velocity profiles from the initial condition (*i.e.* the terminal boundary-layer solution); it merely adds a constant offset to each profile. Alternatively, in the Eulerian formulation the initial condition for the first interactive stage at $t_I = -1$ is given in equation (3.18); it is from this terminal solution that the velocity profile develops in the first interactive stage. As a result, it is sufficient to consider typical velocity profiles from the terminal solution for the stability analysis. The integral (3.89) was evaluated over a range of c for velocity profiles at several streamwise locations. The results for each velocity profile were qualitatively the same; therefore, the results shown are for the velocity profile from the terminal boundary-layer solution at $x_I = 0$ (the center of the domain). Note that it is near $x_I = 0$ that the high-frequency oscillations were invariably observed in the calculations. Physically, this is believed to occur because the streamwise velocity on the central line is smallest at $x_I = 0$, and thus the effect of the pressure gradient induced by the interaction is largest there.

Figure 3.8a shows contours of constant $Im(I_c)$ on the complex c plane obtained by calculating the integral (3.89) for a large number of complex values of c. Note that since u_0 is very large as $\hat{Y}_I \to 0$, the integrand approaches zero rapidly near the bottom shear layer. Unstable points, if they exist, are located in the upper half-plane $(c_i > 0)$ along lines where I_c is real, *i.e.* $Im(I_c) = 0$; there is one such line in the upper half plane which is indicated by A in figure 3.8a. From the eigenvalue relation (3.88), a point along line A will be unstable if $I_c < 0$ and is small. Figure 3.8b shows the results of integrations of equation (3.89) for values of c along line A in figure 3.8a. Also

shown are the values of I_c predicted by the expansion (3.90) for large c. It is evident that there are no unstable points along line A for $c = O(1)$ since the magnitude of I_c is increasing as $c_i \to 0$. However, I_c is small and negative as c_i becomes larger, and the numerical results do converge to the large c prediction; this confirms the presence of the large c instability in the first interactive stage. It is significant to note that the instability is present at the very onset of interaction. Whereas instabilities are typically brought on by the development of an inflection point in a velocity profile; here, the primary features contributing to the instability are (1) the presence of interaction and (2) the existence of a shear layer within a finite distance of the wall. The large velocity behavior as $\hat{Y}_I \to 0$ and $\hat{Y}_I \to 2$ is not a significant feature of the instability. In contrast, the triple-deck cases considered by Tutty and Cowley (1986) require integration of equation (3.89) to be carried out across the semi-infinite range $(0,\infty)$ of the viscous sublayer, and the large c instability, therefore, is not possible.
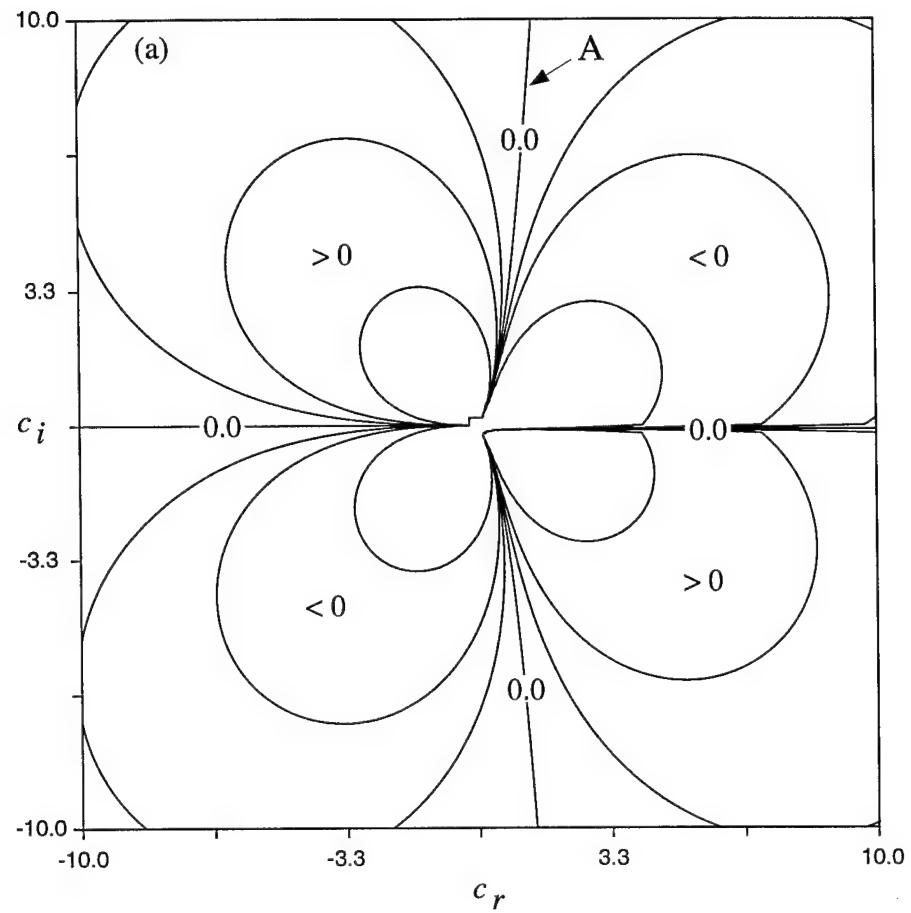
(a) Contours of constant $\text{Im}(I_c)$ on complex c plane.

Figure 3.8 - Numerical results for I_c.
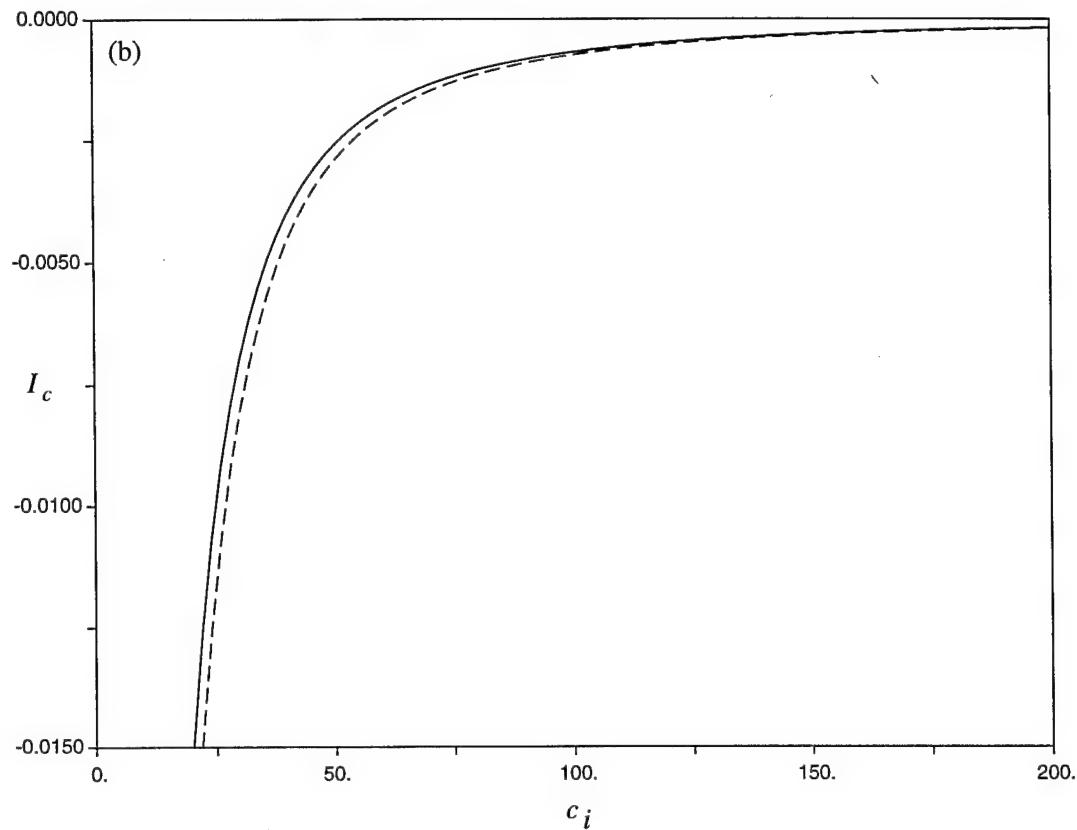
(b) Comparison of analytical (---------) and numerical (————)
results for I_c along line A in (a).

Figure 3.8 - Continued.

116

4. Conclusions

The numerical solution of the first interactive stage of unsteady boundary-layer separation has been obtained in Lagrangian coordinates. The first interactive stage has been found to contain a high-frequency inviscid instability which is manifest at the very onset of the viscous-inviscid interaction. The presence of the instability precludes a grid independent numerical solution from being obtained; as the grid is refined, the admittance of shorter wavelength, faster growing modes results in breakdown at progressively earlier times. Reductions in the time step yield results which are indistinguishable from those with larger time steps even after the instability has become prominent. The presence of the instability within the formulation of the first interactive stage was confirmed analytically by a linear stability analysis. The instability condition was evaluated for typical velocity profiles over a range of the complex wavespeed c, and it was found that the instability can occur for large c. It should be emphasized that since the instability criterion was met in the initial condition (*i.e.* the terminal boundary-layer solution) of the first interactive stage, the instability is present as soon as the interaction comes into effect.

These results would seem to significantly alter the physical picture of unsteady boundary-layer separation. Previously, it was thought that an eruptive boundary layer evolves toward the terminal boundary-layer structure of Van Dommelen and Shen (1982) and Elliott *et al.* (1983) until times just prior to this non-interactive singularity of $O(Re^{-2/11})$ when interaction with the outer inviscid flow becomes important. The flow on this time scale, corresponding to the first interactive stage, was then thought to evolve toward the interacting boundary-layer singularity of Smith (1988b) at a time prior to the non-interactive singularity as concluded by Peridier *et al.* (1991b). It is believed that the effects of normal pressure gradient must then be taken into account in order to relieve the interacting boundary-layer singularity (Hoyle, Smith and Walker, 1991).

The current results, however, indicate that the first interactive stage of unsteady boundary-layer separation is unstable. This suggests that as a boundary layer focuses toward an eruption, the flow in the vicinity of the separation point becomes unstable at the onset of interaction with the outer inviscid flow. Therefore, it is expected that this instability would also be possible within conventional unsteady interacting boundary-layer solutions as a significant viscous-inviscid interaction is first provoked by a developing eruption. However, it is not surprising that no such instability was observed in the numerical results of Peridier *et al.* (1991b), because the instability has short wavelengths in a structure with narrow streamwise extent embedded within the boundary layer. On the scale of the first interactive stage, the instability was only observed when very high resolution computations were performed. A conventional interacting boundary-layer calculation, therefore, would require resolution in the separation region which likely is well beyond most current computational resources. Instead, a condition analogous to equation (3.88) with (3.89) would need to be found and tested in order to determine if and when an instability occurred in an interacting boundary-layer calculation.

Because the present instability was found to exist at the very onset of interaction, the question arises as to whether an instability develops prior to viscous-inviscid interaction, *i.e.* in the framework of classical boundary-layer theory. It is possible that most calculations of unsteady boundary-layer separation carried out to date may not have sufficient resolution to pick up such an instability. The work of Cowley, Hocking and Tutty (1985) suggests that an instability may occur in the classical boundary-layer equations when a point of zero shear stress develops within the boundary layer. Recall that this is also an essential precursor to an unsteady separation event. The growth rate $O(\alpha^{1/2})$ of the Cowley-Hocking-Tutty instability is relatively small, however, and the amplification of small disturbances may not have sufficient time to become manifest in a numerical calculation when the boundary layer rapidly evolves toward a finite-time singularity. Note that the growth rate in the present interactive instability is much larger and is $O(\alpha^{3/2})$. More study is necessary in order

118

to determine the connection between the Cowley-Hocking-Tutty instability and unsteady separation.

It also is not clear how the present results relate to the interacting boundary-layer singularity found by Smith (1988b). Observing the similarity between the conditions for the occurrence of the instability (equation (3.88) with (3.89)) and the interacting boundary-layer singularity (equation (2.55)), it may be that as interactive effects become important, the boundary layer evolves immediately toward Smith's (1988b) interactive singularity just prior to becoming unstable. This seems unlikely, however, because the interactive singularity (see §2.6) involves a singularity in the pressure gradient which requires the action of interaction over a period of time in order to evolve from the smooth prescribed non-interactive pressure gradient. In contrast, the instability within the first interactive stage is present at the very onset of interaction, and it would seem, therefore, to preempt the interactive singularity. While the present work has elucidated some of the effects of viscous-inviscid interaction on unsteady flows, it has also raised additional questions with regard to the sequence of events leading up to unsteady boundary-layer eruptions in two-dimensional incompressible flows.

PART II

Hypersonic Boundary-Layer Separation
on a Cold Wall
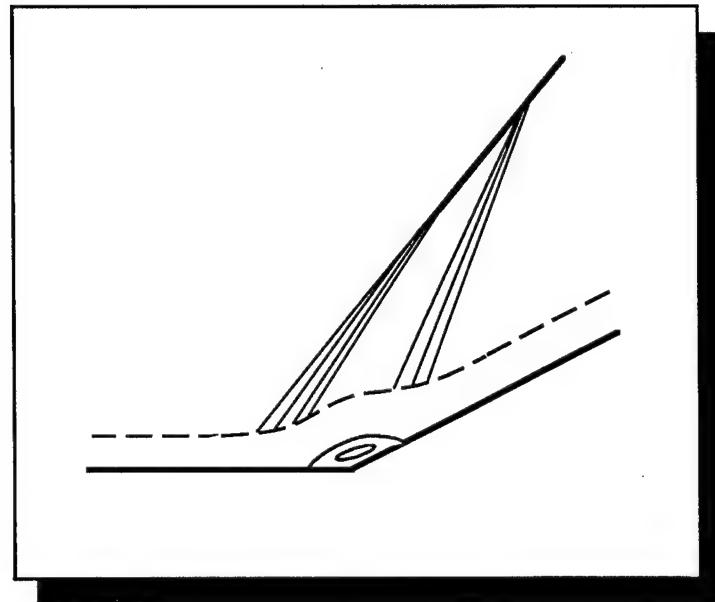
5. Triple-Deck Interaction Theory

5.1 Introduction

In part I the asymptotic structure was considered in the limit of high Reynolds number for unsteady separation of incompressible boundary layers. In part II the asymptotic structure of steady laminar separation for high-speed compressible flows will be considered. The classical triple-deck structure for subsonic and supersonic flows was discussed in §1.3; here, the triple deck for hypersonic flows will be considered both with and without wall cooling.

Before describing the hypersonic triple-deck theory, some general features of hypersonic flow (see, for example, Anderson, 1989) will be discussed. In practice, a flow is generally called hypersonic if the Mach number M is greater than about five or six. Some examples of hypersonic flight vehicles, therefore, are the space shuttle, the Apollo spacecraft and the proposed national aerospace plane which have attained (or are expected to achieve) Mach 25, Mach 36 and Mach 25, respectively, upon reentry into the earth's atmosphere. Unlike the abrupt change in flow characteristics that occurs in going from subsonic to supersonic flow at Mach 1, the transition to hypersonic flow is not clearly defined and is characterized by new physical effects which gradually become more important as the Mach number is increased. For example, recall from inviscid theory that as the Mach number increases, the angle of inclination of a shock wave (which might be generated at a sharp leading edge, for example) decreases. Therefore, hypersonic flow is often characterized by a very thin shock layer which is the region between the outer edge of the boundary layer on the downstream surface and the shock wave which was generated at some upstream surface.

While shock layers may be very thin, hypersonic boundary layers generally thicken in the downstream direction much more rapidly than their counterparts at slower speeds. This effect is due to the substantial viscous dissipation which takes place in a hypersonic boundary layer as the high speed flow is adjusted across the

boundary layer to relative rest at the surface. The increased dissipation results in significant increases in temperature within the boundary layer which in turn acts to increase the viscosity coefficient and decrease the density of the boundary-layer fluid. Both of these effects cause the boundary-layer thickness δ to grow rapidly according to $\delta \sim M_\infty^2 Re_x^{-1/2}$, where M_∞ is the freestream Mach number, and Re_x is the local Reynolds number along the surface (Stewartson, 1964). This rapid growth in boundary-layer thickness can provoke a global interaction with the outer inviscid flow and can in some cases eventually cause the boundary layer to merge with the leading-edge shock. This viscous interaction is said to be strong near the leading edge of a surface but becomes weak downstream if the boundary-layer thickness is small in comparison to the body thickness. A further discussion of this global viscous interaction has been given by Anderson (1989) and Mikhailov, Neiland and Sychev (1971), and a recent review of hypersonic viscous flow research has been given by Cheng (1993). The hypersonic triple deck, to be discussed subsequently, applies in regions of weak global viscous interaction where instead the interaction is localized and is due to some small scale feature along the surface. There are a variety of other important phenomena in hypersonic flow for which Anderson (1989) provides a good introduction and additional references.

The triple-deck formulation was extended to the case of hypersonic flow by Neiland (1973) and Brown, Cheng and Lee (1990) who considered the boundary layer on a cooled wall; a special case ($\gamma \rightarrow 1$) of hypersonic flow was also considered by Brown, Stewartson and Williams (1975). The consideration of cold wall effects is of particular interest for hypersonic flight vehicles which often require some means of surface protection from the high temperatures generated within a hypersonic boundary layer. Inclusion of the effects of wall cooling bring about three primary changes in the triple-deck formulation as compared to the classical triple deck discussed in chapter 1. As will become evident from the scalings described in §5.2, the first is an overall reduction in the length scales of the triple-deck structure as the surface is cooled. Secondly, because of the cold wall, the boundary layer upstream of the triple-deck
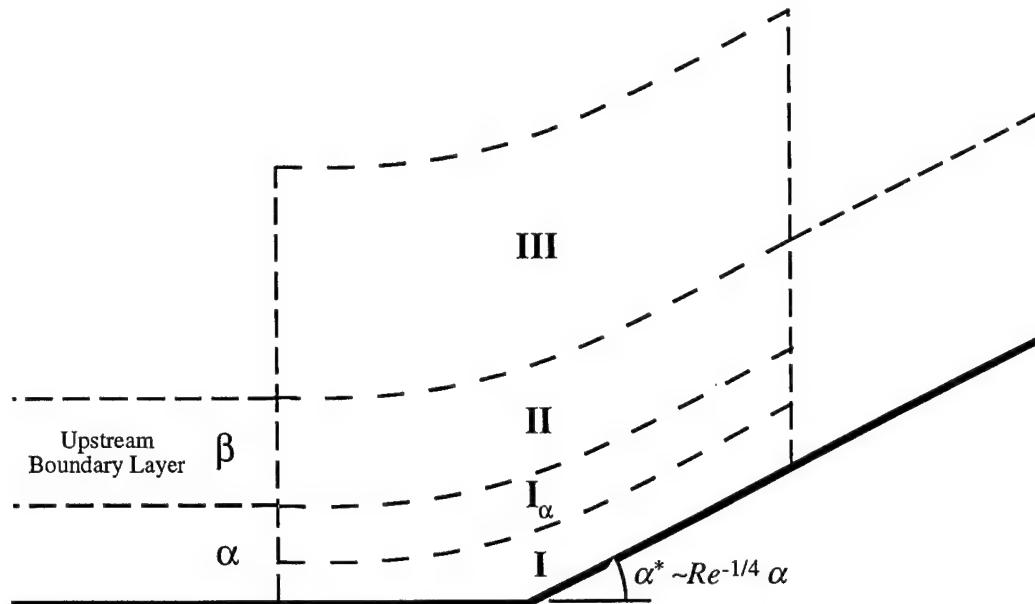
Figure 5.1 - Schematic of the triple-deck structure for hypersonic flow
over a cold wall near a compression ramp (not to scale).

region develops a double structure with a thin inner wall layer becoming necessary in order to adjust the temperature to that at the surface. As will be shown in §5.2, the thickness of this wall layer is greater than that of the viscous sublayer in the interaction region (see figure 5.1); therefore, an intermediate layer is introduced between the viscous sublayer (region I) and the main deck (region II) which is a continuation of the upstream inner wall layer into the interaction region. This intermediate region serves a similar purpose as the main deck in the classical triple deck; it communicates changes between the viscous sublayer and the main and upper decks but does not itself contribute to the displacement effect of the boundary layer. Thirdly, the most significant effect that wall cooling has on the triple-deck formulation is a reduction in the displacement thickness of the viscous sublayer and a corresponding rise in the contribution to the displacement thickness due to the main deck. Neiland (1973) found that this contribution to the displacement thickness due to the main deck is proportional

to the pressure rise induced by the boundary layer. If the average Mach number across the boundary layer just upstream of the interaction region is less than one, a pressure increase leads to boundary-layer thickening; if greater than one, a pressure increase leads to a decrease in boundary-layer thickness. The former case is referred to as subcritical and the latter supercritical because of the analogous behavior in subsonic and supersonic boundary layers, respectively. The cold wall effect on thickening of the main deck introduces an additional term in the interaction law which takes this into account. Further details are provided for the hypersonic triple deck in §5.2.

If the wall temperature is greater than that necessary for a balance between the contributions to the displacement thickness due to the viscous sublayer and the main deck, as is the case for a hypersonic boundary layer without wall cooling, the contribution to the displacement thickness from the main deck is negligibly small, and the formulation is the same as the classical triple deck given by Stewartson and Williams (1969) and Neiland (1969) for supersonic flow. Numerical solutions of this case have been considered by Rizzetta, Burggraf and Jenson (1978) and Ruban (1978) for a boundary layer encountering a compression ramp having various small ramp angles. Their results reveal that a separation region centered at the corner occurs for all ramp angles greater than a critical value. As the ramp angle is increased, the extent of the separation region grows, and a plateau is observed to form in the pressure distribution near separation. The compression ramp without wall cooling will be considered further in §6.4.1.

Conversely, for very low wall temperatures, lower than the balance discussed above, the contribution to the displacement thickness due to the viscous sublayer is negligible, and that due to the main deck dominates. This situation has been considered recently by Kerimbekov, Ruban and Walker (1993) for subcritical and supercritical boundary layers and by Zhikharev (1993) for subcritical boundary layers encountering a compression ramp; their results are discussed in more detail in §5.4.2. It was found for the limiting case of strong supercritical wall cooling that there are no disturbances upstream of the corner and separation occurs downstream on the ramp itself. This case

124

was found to exhibit marginal separation behavior similar to that which occurs near the leading edge of thin airfoils at a critical angle of attack (see Ruban, 1981, 1982 and Stewartson, Smith and Kaups, 1982). On the other hand, for strong subcritical wall cooling, separation can only occur upstream of the corner (Kerimbekov *et al.,* 1993); a Goldstein (1948) singularity was found to develop at a separation point in this case, but the singularity is found to be removable by the theory described by Smith and Daniels (1981).

In order to provide a bridge between these theories for moderate wall temperatures and strongly cooled walls, the triple-deck formulation for hypersonic boundary-layer flow on a cold wall will be considered in part II for wall temperature ranges where the contributions of the viscous sublayer and the main deck to the displacement thickness are of the same order. This range will be defined more precisely in subsequent sections. The remainder of chapter 5 will provide the theoretical background for this case. The general triple-deck formulation for hypersonic flow over a cold wall with a small surface disturbance will be discussed in detail in §5.2. The hypersonic triple deck will then be applied to the compression ramp geometry, as discussed in §5.3, for which two types of singularities have been identified; these are associated with large ramp angles and strong wall cooling and are discussed in §5.4. Subsequently, in chapter 6 a solution algorithm will be described for the hypersonic triple deck and numerical results given for cases with and without wall cooling.

5.2 Formulation for the Hypersonic Boundary Layer on a Cold Wall

The following development is a derivation of the two-dimensional hypersonic triple-deck formulation for a flat plate boundary layer encountering a small surface disturbance when the wall is cooled; this problem was first considered by Neiland (1973). The disturbance (such as a compression ramp) is located a distance L from the leading edge of the flat plate, and the flow is assumed steady except for possible

local unsteadiness which might be provoked by the surface disturbance. The fluid is taken to be a compressible ideal gas where the upstream flow is uniform and parallel to the plate with speed U_∞, pressure p_∞, density ρ_∞ and enthalpy h_∞. Throughout this section primes denote dimensional quantities. The specific heat ratio γ is considered constant, and the viscosity coefficient μ' is taken to depend only on the temperature subject to the power law

$$\frac{\mu'}{\mu_0} = \left(\frac{h'}{h_0}\right)^n,$$

(5.1)

where n is a positive constant, h' is the dimensional enthalpy, and μ_0 is the value of the viscosity coefficient evaluated at the stagnation temperature corresponding to $h' = h_0 = U_\infty^2$. The Reynolds number and upstream Mach number are defined by

$$Re_0 = \frac{\rho_\infty U_\infty L}{\mu_0}, \qquad M_\infty = U_\infty \left(\frac{\gamma p_\infty}{\rho_\infty}\right)^{-1/2},$$

(5.2a,b)

respectively. For hypersonic flow, Re_0 and M_∞ are large, but the hypersonic viscous interaction parameter χ will be assumed small, *viz.*

$$\chi = M_\infty^2 \, Re_0^{-1/2} \ll 1.$$

(5.3)

Physically, the disturbance is assumed to be located far downstream of the leading edge so that the global viscous interaction is weak (as discussed in the previous section) and has negligible effect upon the boundary-layer flow in the vicinity of the disturbance. Note that if the Reynolds number is defined in terms of the viscosity at the mainstream static temperature rather than the stagnation temperature, as done here, the hypersonic viscous interaction parameter is $\chi = M_\infty^3 \, Re_\infty^{-1/2}$ in place of equation (5.3) (see, for example, Brown *et al.*, 1990).
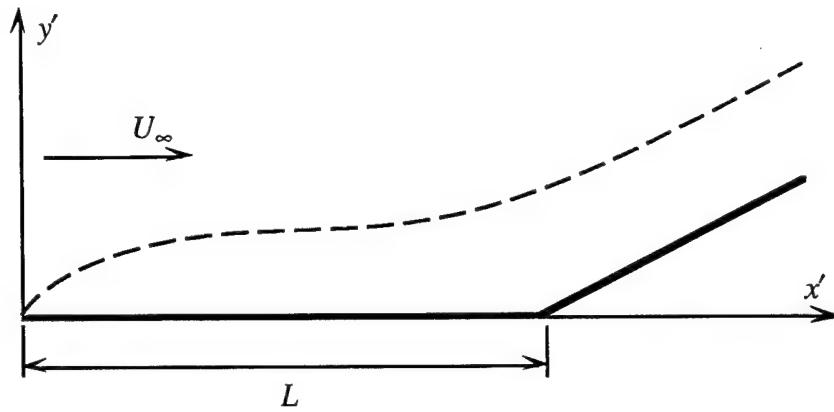
Figure 5.2 - Geometry and coordinate system for compression ramp.

5.2.1 The Upstream Boundary Layer

With origin at the leading edge of the flat plate, coordinates are chosen such that x' is the coordinate along the plate and y' is the coordinate normal to the plate as shown in figure 5.2. The velocity components $u'(x',y')$ and $v'(x',y')$ are in the respective x' and y' directions. Upstream of the disturbance, the steady boundary-layer flow on the flat plate is described in terms of the scaled independent variables

$$x' = L\,x, \quad y' = L\,M_\infty\,Re_0^{-1/2}\,Y, \tag{5.4a,b}$$

and the scaled dependent variables

$$u' = U_\infty\,U(X,Y) + \cdots, \qquad v' = U_\infty\,M_\infty\,Re_0^{-1/2}\,V(X,Y) + \cdots, \tag{5.4c,d}$$

$$h' = U_\infty^2\,H(X,Y) + \cdots, \qquad p' = p_\infty + p_\infty\,M_\infty^2\,Re_0^{-1/2}\,P(X,Y) + \cdots, \tag{5.4e,f}$$

$$\rho' = \rho_\infty\,M_\infty^{-2}\,R(X,Y) + \cdots, \qquad \mu' = \mu_0\,\mu(X,Y) + \cdots, \tag{5.4g,h}$$

127

where ρ' and p' are the density and pressure, respectively. Note that the freestream conditions are related to each other through the ideal gas law which gives $p_\infty = \rho_\infty U_\infty^2/M_\infty^2$. Substitution of equations (5.4) into the Navier-Stokes and energy equations gives

$$R\,U\,\frac{\partial U}{\partial X} + R\,V\,\frac{\partial U}{\partial Y} = \frac{\partial}{\partial Y}\left(\mu\,\frac{\partial U}{\partial Y}\right), \qquad \frac{\partial p}{\partial Y} = 0, \qquad (5.5\text{a,b})$$

$$R\,U\,\frac{\partial H}{\partial X} + R\,V\,\frac{\partial H}{\partial Y} = \frac{1}{Pr}\frac{\partial}{\partial Y}\left(\mu\,\frac{\partial H}{\partial Y}\right) + \mu\left(\frac{\partial U}{\partial Y}\right)^2, \qquad (5.5\text{c})$$

where Pr is the Prandtl number and is assumed constant. The continuity equation becomes

$$\frac{\partial(RU)}{\partial X} + \frac{\partial(RV)}{\partial Y} = 0. \qquad (5.5\text{d})$$

The viscosity law (5.1) and the ideal gas equation of state are

$$\mu = H^n, \qquad H = \frac{1}{(\gamma-1)\,R}, \qquad (5.6\text{a,b})$$

respectively. Because h_∞/U_∞^2 is $O(M_\infty^{-2})$ as $M_\infty \rightarrow \infty$, the conditions required for matching to the external flow are

$$U \rightarrow 1, \quad H \rightarrow 0 \quad \text{as} \quad Y \rightarrow \infty, \qquad (5.7)$$

while at the surface

$$U = V = 0, \quad H = g_w \quad \text{at} \quad Y = 0. \qquad (5.8)$$

128

Here, g_w is the temperature factor defined by $g_w = h_w'/U_\infty^2$; for a specified wall temperature distribution, g_w may in general be a function of X.

5.2.2 The Upstream Inner Wall Layer

When g_w is $O(1)$, the solution to (5.5)-(5.8) is uniformly valid throughout the boundary layer upstream of the obstacle, and the analysis would proceed to consideration of the interaction region. However, $g_w \ll 1$ for a cold wall, and H must then vanish to leading order at the surface; therefore, the conditions on the upstream boundary layer are

$$U = V = H = 0 \quad \text{at} \quad Y = 0. \tag{5.9}$$

In view of the viscous dissipation term in equation (5.5c), H is $O(1)$ in the boundary layer, but according to equations (5.8) and (5.9) H must vanish at the wall and as the mainstream is approached. This suggests that there is not a uniformly valid solution, and an additional layer is necessary within the upstream boundary layer adjacent to the surface in order to adjust the enthalpy H to g_w at the surface. From the viscosity law (5.6a), the solution to the upstream boundary-layer equations (5.5) along the surface are of the form

$$U \to a(X)\, Y^{\frac{1}{n+1}}, \quad H \to b(X)\, Y^{\frac{1}{n+1}}, \quad R \to \frac{Y^{-\frac{1}{n+1}}}{(\gamma-1)\,b(X)} \quad \text{as} \quad Y \to 0, \tag{5.10a,b,c}$$

where $a(X)$ and $b(X)$ are arbitrary functions. Therefore, $H \to 0$ and $R \to \infty$ as $Y \to 0$, and the solution is not valid all the way to the surface. According to equation (5.10b) H approaches zero at the wall, and in order to satisfy the last of conditions (5.8), a region with thickness $Y^{\frac{1}{n+1}} = O(g_w)$ is required near the wall. This thin region is denoted by α, as indicated in figure 5.1, while the rest of the upstream boundary layer

is referred to as region β. From the scalings (5.4) in region β and the form of the solution along the wall (5.10), the normal variable in the inner most region α is scaled according to

$$y' = L\, M_\infty\, g_w^{n+1}\, Re_0^{-1/2}\, \hat{Y}, \tag{5.11a}$$

with new dependent variables defined by

$$u' = U_\infty\, g_w\, \hat{U}(X,\hat{Y}) + \cdots, \qquad v' = U_\infty\, M_\infty\, g_w^{n+2}\, Re_0^{-1/2}\, \hat{V}(X,\hat{Y}) + \cdots, \tag{5.11b,c}$$

$$h' = U_\infty^2\, g_w\, \hat{H}(X,\hat{Y}) + \cdots, \qquad p' = p_\infty + p_\infty\, M_\infty^2\, Re_0^{-1/2}\, \hat{P}(X) + \cdots, \tag{5.11d,e}$$

$$\rho' = \rho_\infty\, M_\infty^{-2}\, g_w^{-1}\, \hat{R}(X,\hat{Y}) + \cdots, \qquad \mu' = \mu_0\, g_w^n\, \hat{\mu}(X,\hat{Y}) + \cdots. \tag{5.11f,g}$$

Substitution into the Navier-Stokes equations and the energy equation shows that the viscous and conduction terms are dominant, and the governing equations in region α are

$$\frac{\partial}{\partial\hat{Y}}\left(\hat{\mu}\,\frac{\partial\hat{U}}{\partial\hat{Y}}\right) = 0, \qquad \frac{\partial}{\partial\hat{Y}}\left(\hat{\mu}\,\frac{\partial\hat{H}}{\partial\hat{Y}}\right) = 0. \tag{5.12a,b}$$

The viscosity law (5.6a) and ideal gas equation (5.6b) become

$$\hat{\mu} = \hat{H}^n, \qquad \hat{H} = \frac{1}{(\gamma-1)\,\hat{R}}. \tag{5.13a,b}$$

In order to match with the solution in region β as $Y \to 0$, equation (5.10) requires

$$\hat{U} \to a(X)\,\hat{Y}^{\frac{1}{n+1}}, \quad \hat{H} \to b(X)\,\hat{Y}^{\frac{1}{n+1}} \quad \text{as} \quad \hat{Y} \to \infty, \tag{5.14}$$

130

and the boundary conditions along the surface are

$$\hat{U} = \hat{V} = 0, \quad \hat{H} = 1 \quad \text{at} \quad \hat{Y} = 0. \tag{5.15}$$

Integration of equations (5.12) subject to the conditions (5.14) and (5.15) gives the solution in the upstream inner wall layer and

$$\hat{U} = \frac{a(X)}{b(X)} \left\{ [b(X)]^{n+1} \, \hat{Y} + 1 \right\}^{\frac{1}{n+1}} - \frac{a(X)}{b(X)}, \tag{5.16a}$$

$$\hat{H} = \left\{ [b(X)]^{n+1} \, \hat{Y} + 1 \right\}^{\frac{1}{n+1}}. \tag{5.16b}$$

The form of this inner solution along the surface is then given by

$$\hat{U} \to \frac{1}{n+1} a(X) [b(X)]^n \, \hat{Y} + \cdots, \quad \hat{\mu} \to 1 + \cdots, \quad \hat{H} \to 1 + \cdots \quad \text{as} \quad \hat{Y} \to 0. \tag{5.17a,b,c}$$

5.2.3 Scalings of the Interaction Region

As the upstream boundary layer encounters the surface disturbance (*e.g.* a compression corner), a short streamwise region develops in which viscous-inviscid interaction becomes important. Within this region the flow is governed by a triple-deck structure which is modified slightly by the presence of the upstream inner wall layer. This structure is shown in figure 5.1 where the disturbance is shown as a compression ramp at a small angle of inclination. In this section the length scales of the viscous sublayer (region I) and the magnitudes of the flow variables therein are sought. It will be assumed, and subsequently verified, that the viscous sublayer is much thinner than the inner wall layer of the upstream boundary layer. Thus the interaction region I sees a linear velocity, according to equation (5.17a), far upstream Substitution of the scalings (5.11a,b) for the inner wall layer into the form of this inner solution along the surface (5.17a) gives an estimate of the order of magnitude of the streamwise velocity

131

component in region I,

$$u' \sim \frac{U_\infty}{L \, M_\infty \, g_w^n \, Re_0^{-1/2}} \, y',$$

(5.18)

relative to the thickness of the viscous sublayer y'. Here, the $\sim$ is used to imply that both sides are of comparable magnitude. It is expected that the pressure variation $\Delta p'$ in the outer inviscid flow (region III in figure 5.1) induced by the interaction is sufficient to provoke a nonlinear convective response in the viscous sublayer. Therefore, a balance of the nonlinear convection terms and the pressure gradient term in the streamwise momentum equation is expected; thus,

$$\rho' \, u' \, \frac{\partial u'}{\partial x'} \sim \frac{\partial p'}{\partial x'}.$$

(5.19)

Because the problem in the sublayer is assumed to be nonlinear, the variation in streamwise velocity $\Delta u'$ in region I is of the same order as u'. So from the scale of the density in the upstream wall layer in equation (5.11f), it follows from equation (5.19) that

$$\rho_\infty \, M_\infty^{-2} \, g_w^{-1} \, (u')^2 \sim \Delta p'.$$

(5.20)

The flow in region I is also viscous, and a balance with the convective terms requires

$$\rho' \, u' \, \frac{\partial u'}{\partial x'} \sim \frac{\partial}{\partial y'} \left(\mu' \, \frac{\partial u'}{\partial y'} \right),$$

(5.21)

in which case equation (5.11f,g) give a relation of the form

132

$$\rho_\infty M_\infty^{-2} \, g_w^{-1} \, \frac{(u')^2}{\Delta x'} \sim \mu_0 \, g_w^n \, \frac{u'}{(y')^2},$$ (5.22)

where $\Delta x'$ is the streamwise extent of the interaction region. In addition, it is easily shown from linearized compressible flow theory that the pressure induced in the outer inviscid flow is proportional to the slope of the streamlines just outside the boundary layer. A primary disturbance in the outer flow is assumed to be induced by the nonlinear response and the displacement effect of the viscous sublayer. This relationship is the Ackeret formula and gives

$$\Delta p' \sim \frac{\rho_\infty U_\infty^2}{M_\infty} \, \frac{y'}{\Delta x'}.$$ (5.23)

Equations (5.18), (5.20), (5.22) and (5.23) are four equations for the four unknowns $\Delta x'$, y', u' and $\Delta p'$ which when solved give

$$\Delta x' \sim L \, M_\infty^{3/2} \, g_w^{n+1/2} \, Re_0^{-3/8}, \qquad y' \sim L \, M_\infty^{3/2} \, g_w^{n+1/2} \, Re_0^{-5/8},$$ (5.24a,b)

$$u' \sim U_\infty \, M_\infty^{1/2} \, g_w^{1/2} \, Re_0^{-1/8}, \qquad \Delta p' \sim \rho_\infty \, U_\infty^2 \, M_\infty^{-1} \, Re_0^{-1/4}.$$ (5.24c,d)

It follows from the continuity equation that

$$v' \sim U_\infty \, M_\infty^{1/2} \, g_w^{1/2} \, Re_0^{-3/8}.$$ (5.24e)

The balance in equation (5.23), from considering the pressure induced by the displacement effect of the viscous sublayer, and the subsequent scalings (5.24) assume that the order of magnitude of the contribution to the displacement thickness due to the main deck (region II) is at most comparable to that due to the viscous sublayer (region I) For the case when there is not significant wall cooling, the contribution due to the

133

main deck is negligible compared to that due to the viscous sublayer. However, when the wall is cooled, the displacement effect due to the viscous region decreases, and eventually the contributions of regions I and II to the displacement thickness of the boundary layer become of comparable magnitude. Here, the magnitude of the temperature factor g_w required for this situation to occur will be determined, and in order to do this, the contribution due to the main deck must be considered. From the magnitudes of the flow variables required to match to the upstream boundary layer (5.4) in region β, the balance in equation (5.19) and the fact that $u' \sim U_\infty$ leads to the relationship

$$\Delta u' \sim U_\infty \frac{\Delta p'}{p_\infty}, \tag{5.25}$$

in region II instead of equation (5.20). Whereas the balance (5.21) in region I is viscous, the flow in region II is inviscid to leading order, and conservation of entropy requires

$$\frac{p'}{(\rho')^\gamma} = \text{constant} \tag{5.26}$$

along a streamline. Application of this law at two points along a streamline passing through region II indicates that

$$\Delta \rho' \sim \rho' \frac{\Delta p'}{p_\infty}. \tag{5.27}$$

Notice from the estimate for the magnitude of the pressure (5.24d) in the interaction region and the definition (5.3) of the hypersonic interaction parameter that $\Delta p'/p_\infty \sim \chi^{1/2}$. Since χ is assumed small in the region of the interaction, the perturbations in the flow variables, from (5.25) and (5.27), in region II are linear. In addition, taking d' to be the normal distance between two arbitrary streamlines in region II and $\Delta d'$ to be the variation in that distance, mass conservation ($\rho' u' d' = \text{constant}$) of the flow between

134

the streamlines gives the relation

$$\Delta d' \sim d' \frac{\Delta p'}{p_\infty}. \tag{5.28}$$

Just as for the variations in velocity and pressure, therefore, the variation in separation distance between streamlines in region II is small. But the interest here is on the case for which this variation is of the same order of magnitude as the displacement of streamlines due to the viscous sublayer (region I). In such cases, both regions I and II have comparable contributions to variations in the displacement thickness of the boundary layer. From the scale of the upstream boundary layer (5.4b), d' is $O(L\,M_\infty\,Re_0^{-1/2})$, and from equation (5.28) $\Delta d' = O(L\,M_\infty\,Re_0^{-1/2}\,\chi^{1/2})$ or $\Delta d' = O(L\,M_\infty^2\,Re_0^{-3/4})$ using equation (5.3). Therefore, $\Delta d'$ is $O(y')$, where y' is the scale of the viscous sublayer defined by equation (5.24b), when

$$g_w^{n+1/2} \sim M_\infty^{1/2}\,Re_0^{-1/8}, \tag{5.29}$$

which occurs for g_w small in the limit $Re_0 \to \infty$ with M_∞ fixed. Observe from comparison of the vertical scales for the viscous sublayer in equation (5.24b) and upstream inner wall layer in equation (5.11a) along with the balance (5.29) that the viscous sublayer (region I) is thinner, by a factor which is $O(g_w^n)$, than the upstream inner wall layer α; this verifies the assumption made previously in this section. Similarly, from equations (5.4b) and (5.24a) the streamwise extent of the interaction region is larger, by a factor which is $O(M_\infty)$, than the thickness of the upstream boundary layer.

5.2.4 The Viscous Sublayer

The scalings (5.24) determined in the previous section for the interaction region in the vicinity of the surface disturbance suggest the following scaled independent variables in region I:

$$t' = L \, U_\infty^{-1} \, M_\infty \, g_w^n \, Re_0^{-1/4} \, t^*, \tag{5.30a}$$

$$x' = L + L \, M_\infty^{3/2} \, g_w^{n+1/2} \, Re_0^{-3/8} \, x^*, \qquad y' = L \, M_\infty^{3/2} \, g_w^{n+1/2} \, Re_0^{-5/8} \, y^*, \tag{5.30b,c}$$

and expansions for the flow quantities

$$u' = U_\infty \, M_\infty^{1/2} \, g_w^{1/2} \, Re_0^{-1/8} \, u^*(x^*,y^*,t^*) + \cdots, \tag{5.30d}$$

$$v' = U_\infty \, M_\infty^{1/2} \, g_w^{1/2} \, Re_0^{-3/8} \, v^*(x^*,y^*,t^*) + \cdots, \tag{5.30e}$$

$$p' = p_\infty + \rho_\infty \, U_\infty^2 \, M_\infty^{-1} \, Re_0^{-1/4} \, p^*(x^*,y^*,t^*) + \cdots, \tag{5.30f}$$

$$h' = U_\infty^2 \, g_w \, h^*(x^*,y^*,t^*) + \cdots, \tag{5.30g}$$

$$\rho' = \rho_\infty \, M_\infty^{-2} \, g_w^{-1} \, \rho^*(x^*,y^*,t^*) + \cdots, \tag{5.30h}$$

$$\mu' = \mu_0 \, g_w^n \, \mu^*(x^*,y^*,t^*) + \cdots. \tag{5.30i}$$

Substitution of these scaled variables into the energy equation yields

$$\rho^* \left(\frac{\partial h^*}{\partial t^*} + u^* \frac{\partial h^*}{\partial x^*} + v^* \frac{\partial h^*}{\partial y^*} \right) = \frac{1}{Pr} \frac{\partial}{\partial y^*} \left(\mu^* \frac{\partial h^*}{\partial y^*} \right), \tag{5.31}$$

136

while the viscosity law and ideal gas equation become

$$\mu^* = (h^*)^n, \quad h^* = \frac{1}{(\gamma - 1)\rho^*}, \qquad (5.32\text{a,b})$$

respectively. Since the viscous sublayer is much thinner than the inner wall layer of the upstream boundary layer (region α in figure 5.1), the solution in region I must match to the condition (5.17c) as $x^* \to -\infty$ and specifically

$$h^* \to 1 \quad \text{as} \quad x^* \to -\infty. \qquad (5.33\text{a})$$

Because the interaction region is very short in the streamwise direction, the temperature of the wall may be considered constant through the interaction region; thus,

$$h^* = 1 \quad \text{at} \quad y^* = f^*(x^*, t^*), \qquad (5.33\text{b})$$

where $f^*(x^*, t^*)$ is the prescribed surface shape. From consideration of the asymptotic behaviour of h^* as $y^* \to \infty$, it can be shown that there is no variation of h^* near the outer edge of the viscous sublayer; therefore, in order to match to the upstream boundary layer (5.17c)

$$h^* \to 1 \quad \text{as} \quad y^* \to \infty. \qquad (5.33\text{c})$$

Hence, for an initial enthalpy distribution in region I of $h^* = 1$ for all (x^*, y^*), the solution to the energy equation (5.31) subject to the boundary conditions (5.33) is simply

$$h^*(x^*, y^*, t^*) = 1. \qquad (5.34\text{a})$$

It follows from the viscosity law (5.32a) and the ideal gas law (5.32b) that

$$\mu^*(x^*,y^*,t^*) = 1, \quad \rho^*(x^*,y^*,t^*) = \frac{1}{\gamma - 1}, \tag{5.34b,c}$$

respectively; therefore, the flow in the viscous sublayer is incompressible to leading order. With the result (5.34), substitution of equations (5.30) into the Navier-Stokes equations gives the following form of the incompressible boundary-layer equations

$$\frac{1}{\gamma - 1}\left(\frac{\partial u^*}{\partial t^*} + u^*\frac{\partial u^*}{\partial x^*} + v^*\frac{\partial u^*}{\partial y^*}\right) = -\frac{\partial p^*}{\partial x^*} + \frac{\partial^2 u^*}{\partial y^{*2}}, \quad \frac{\partial p^*}{\partial y^*} = 0, \tag{5.35a,b}$$

and the continuity equation becomes

$$\frac{\partial u^*}{\partial x^*} + \frac{\partial v^*}{\partial y^*} = 0. \tag{5.35c}$$

The no-slip and zero normal velocity conditions,

$$u^* = 0, \quad v^* = \frac{\partial f^*}{\partial t^*} \quad \text{at} \quad y^* = f^*(x^*,t^*), \tag{5.36}$$

apply at the surface. In order to match to the upstream flow (5.17a) in region α, the streamwise velocity must be of the form

$$u^* \to \lambda\, y^* + \cdots \quad \text{as} \quad x^* \to -\infty, \tag{5.37}$$

where $\lambda = a\, b^n/(n + 1)$. The constants a and b are the limiting values of $a(X)$ and $b(X)$ as $X \to 1$ which must be obtained from a solution of the upstream boundary layer. The solution to the first of equations (5.35) at the outer edge of the viscous sublayer can be shown to be of the form

$$u^* \to \lambda\, y^* + \lambda\, A^*(x^*,t^*) + \cdots \quad \text{as} \quad y^* \to \infty, \tag{5.38a}$$

138

where $A^*(x^*,t^*)$ is a displacement function which is unknown and to be found from a solution to the full triple-deck problem. Substitution of (5.38a) into the continuity equation (5.35c) then gives

$$v^* \rightarrow -\lambda \frac{\partial A^*}{\partial x^*} y^* + \cdots \quad \text{as} \quad y^* \rightarrow \infty. \tag{5.38b}$$

Thus, the flow within the viscous sublayer (region I) is governed by equations (5.35) with the conditions (5.36)-(5.38). Finally, note that the slope of the streamlines at the outer edge of region I follows from equations (5.38) and (5.30d,e) and is given by

$$\frac{v'}{u'} = -Re_0^{-1/4} \frac{\partial A^*}{\partial x^*}. \tag{5.39}$$

5.2.5 Region I_α

In more traditional triple-deck formulations, the upstream boundary-layer equations are uniformly valid across the entire boundary layer and there is no inner wall layer; therefore, the discussion at this juncture would now turn to consideration of the main deck. However, for the present case with wall cooling, the upstream inner wall layer α gives rise to an additional layer between regions I and II which will be called region I_α and which is essentially a continuation of the flow in the upstream inner wall layer. Because the viscous sublayer is very thin on the scale of the upstream inner wall layer, region I_α has the same thickness and shares the same normal coordinate $\hat{Y}$ as region α, given by equation (5.11a). Comparison with the normal variable in the sublayer y^* defined in equation (5.30c) gives the relationship

$$y^* = M_\infty^{-1/2} g_w^{1/2} Re_0^{1/8} \hat{Y} \tag{5.40}$$

between the two normal variables. Therefore, from the expansions in region I

(5.30d,e) and the relationship (5.40), matching to the conditions at the top of the viscous sublayer described by equation (5.38) requires the flow in region I_α to be of the form

$$\left.\begin{aligned}
u' &\to U_\infty\, g_w\, \lambda\, \hat{Y} + U_\infty\, M_\infty^{1/2}\, g_w^{1/2}\, Re_0^{-1/8}\, \lambda\, A^*(x^*,t^*) + \cdots\\
v' &\to -U_\infty\, g_w\, Re_0^{-1/4}\, \lambda\, \frac{\partial A^*}{\partial x^*}\, \hat{Y} + \cdots
\end{aligned}\right\} \quad \text{as } \hat{Y} \to 0. \qquad (5.41)$$

The time scale and streamwise length scale are the same for all layers within the interaction region; therefore, the matching conditions (5.41) suggest the following expansions for the flow variables in region I_α

$$u' = U_\infty\, g_w\, \hat{U}_0(\hat{Y}) + U_\infty\, M_\infty^{1/2}\, g_w^{1/2}\, Re_0^{-1/8}\, \hat{U}_1(x^*,\hat{Y},t^*) + \cdots, \qquad (5.42a)$$

$$v' = U_\infty\, g_w\, Re_0^{-1/4}\, \hat{V}_1(x^*,\hat{Y},t^*) + \cdots, \qquad (5.42b)$$

$$p' = p_\infty + \rho_\infty\, U_\infty^2\, M_\infty^{-1}\, Re_0^{-1/4}\, \hat{P}_1(x^*,\hat{Y},t^*) + \cdots, \qquad (5.42c)$$

$$h' = U_\infty^2\, g_w\, \hat{H}_0(\hat{Y}) + U_\infty^2\, M_\infty^{1/2}\, g_w^{1/2}\, Re_0^{-1/8}\, \hat{H}_1(x^*,\hat{Y},t^*) + \cdots, \qquad (5.42d)$$

$$\rho' = \rho_\infty\, M_\infty^{-2}\, g_w^{-1}\, \hat{R}_0(\hat{Y}) + \rho_\infty\, M_\infty^{-3/2}\, g_w^{-3/2}\, Re_0^{-1/8}\, \hat{R}_1(x^*,\hat{Y},t^*) + \cdots, \qquad (5.42e)$$

$$\mu' = \mu_0\, g_w^n\, \hat{\mu}_0(\hat{Y}) + \cdots. \qquad (5.42f)$$

Note that the leading-order terms for p', h', ρ' and μ' are of the same magnitude as in the viscous sublayer given by equations (5.30f-i). Comparison of the expansions (5.42a,b) with the conditions (5.41) gives

$$\hat{U}_0 \to \lambda \hat{Y} + \cdots, \quad \hat{U}_1 \to \lambda A^*(x^*,t^*) + \cdots, \quad \hat{V}_1 \to -\lambda \frac{\partial A^*}{\partial x^*} \hat{Y} + \cdots \quad \text{as} \quad \hat{Y} \to 0. \quad (5.43\text{a,b,c})$$

In addition, matching to the solution in region α given by equation (5.16) with the scalings (5.11) requires the leading-order solution in region I_α to be

$$\hat{U}_0(\hat{Y}) = \frac{a}{b}\left[b^{n+1}\hat{Y} + 1\right]^{\frac{1}{n+1}} - \frac{a}{b}, \qquad (5.44\text{a})$$

$$\hat{H}_0(\hat{Y}) = \left[b^{n+1}\hat{Y} + 1\right]^{\frac{1}{n+1}}, \qquad (5.44\text{b})$$

where, as before, the constants a and b are the limiting values of $a(X)$ and $b(X)$ as $X \to 1$. Substitution of the expansions (5.42) into the equation of state and viscosity law gives

$$\hat{H}_0 = \frac{1}{(\gamma-1)\hat{R}_0}, \qquad \hat{H}_1 = -\frac{\hat{R}_1}{(\gamma-1)\hat{R}_0^2}, \qquad \hat{\mu}_0 = \hat{H}_0^n. \qquad (5.45\text{a,b,c})$$

Therefore, from equations (5.44) and (5.45a,c), the leading-order terms in the expansions (5.42) for region I_α are a continuation into the interaction region of the solution in the upstream inner wall layer. Substitution of the expansions (5.42) with the scalings (5.30a), (5.30b) and (5.11a) for t', x' and y', respectively, into the Navier-Stokes equations gives

$$\hat{U}_0 \frac{\partial \hat{U}_1}{\partial x^*} + \hat{V}_1 \frac{d\hat{U}_0}{d\hat{Y}} = 0, \qquad \frac{\partial \hat{P}_1}{\partial \hat{Y}} = 0, \qquad (5.46\text{a,b})$$

and similarly the energy equation becomes

141

$$\hat{U}_0 \frac{\partial \hat{H}_1}{\partial x^*} + \hat{V}_1 \frac{\mathrm{d}\hat{H}_0}{\mathrm{d}\hat{Y}} = 0. \tag{5.47}$$

Therefore, the flow in region I_α is inviscid, and although the equations do not contain a time derivative, the boundary conditions (5.43) are time-dependent due to the unsteady displacement function $A^*(x^*,t^*)$ associated with the lower deck. The continuity equation becomes

$$\hat{U}_0 \frac{\partial \hat{R}_1}{\partial x^*} + \hat{R}_0 \frac{\partial \hat{U}_1}{\partial x^*} + \hat{V}_1 \frac{\mathrm{d}\hat{R}_0}{\mathrm{d}\hat{Y}} + \hat{R}_0 \frac{\partial \hat{V}_1}{\partial \hat{Y}} = 0. \tag{5.48}$$

Substitution of the expressions (5.45a,b) from the equation of state into the energy equation (5.47) produces the relation

$$\hat{U}_0 \frac{\partial \hat{R}_1}{\partial x^*} + \hat{V}_1 \frac{\mathrm{d}\hat{R}_0}{\mathrm{d}\hat{Y}} = 0, \tag{5.49}$$

from which it is seen that the continuity equation (5.48) is the same as that for the incompressible case, *i.e.*

$$\frac{\partial \hat{U}_1}{\partial x^*} + \frac{\partial \hat{V}_1}{\partial \hat{Y}} = 0. \tag{5.50}$$

The solution to equations (5.46), (5.47) and (5.50) which satisfies the matching conditions (5.43) is

$$\hat{U}_1 = A^*(x^*,t^*) \frac{\mathrm{d}\hat{U}_0}{\mathrm{d}\hat{Y}}, \quad \hat{V}_1 = -\frac{\partial A^*}{\partial x^*} \hat{U}_0(\hat{Y}), \quad \hat{H}_1 = A^*(x^*,t^*) \frac{\mathrm{d}\hat{H}_0}{\mathrm{d}\hat{Y}}, \quad \hat{P}_1 = p^*(x^*,t^*). \tag{5.51a,b,c,d}$$

These solutions for $\hat{U}_1$ and $\hat{V}_1$ were obtained from a simple integration of equation

(5.46a) with the continuity equation (5.50). The energy equation (5.47) was then integrated to obtain the solution for $\hat{H}_1$, and (5.51d) is a consequence of (5.46b). Observe from the expansions (5.42a,b) and the solution (5.51b) that to leading order the slope of the streamlines throughout the entire region I_α is

$$\frac{v'}{u'} = - Re_0^{-1/4} \frac{\partial A^*}{\partial x^*}, \tag{5.52}$$

which is the same as the slope of the streamlines at the outer edge of the viscous sublayer given in equation (5.39). In summary, region I_α is simply a continuation of the upstream inner wall layer through the interaction region and communicates changes in the displacement function $A^*(x^*,t^*)$ and pressure $p^*(x^*,t^*)$ between the viscous sublayer and the main deck. To consider the form of the solution in the main deck, it is useful to obtain the limiting solution at the top of region I_α. Taking the solution (5.44a,b) and (5.51a,b,c) as $\hat{Y} \to \infty$ and substituting into the expansions (5.42a,b,d) for u', v' and h' gives

$$u' \to U_\infty\, g_w\, a\; \hat{Y}^{\frac{1}{n+1}} + \cdots + U_\infty\, M_\infty^{1/2}\, g_w^{1/2}\, Re_0^{-1/8}\, A^*(x^*,t^*)\, \frac{a}{n+1}\; \hat{Y}^{-\frac{n}{n+1}} + \cdots, \tag{5.53a}$$

$$v' \to - U_\infty\, g_w\, Re_0^{-1/4}\, \frac{\partial A^*}{\partial x^*}\, a\; \hat{Y}^{\frac{1}{n+1}} + \cdots, \tag{5.53b}$$

$$h' \to U_\infty^2\, g_w\, b\; \hat{Y}^{\frac{1}{n+1}} + \cdots + U_\infty^2\, M_\infty^{1/2}\, g_w^{1/2}\, Re_0^{-1/8}\, A^*(x^*,t^*)\, \frac{b}{n+1}\; \hat{Y}^{-\frac{n}{n+1}} + \cdots, \tag{5.53c}$$

as $\hat{Y} \to \infty$.

143

5.2.6 The Main Deck

Next, the flow in region II, the main deck, is considered. It is found to be similar to region I_α in that it is a continuation of the upstream boundary layer β. In the main deck, the normal coordinate Y is the same as that in region β given by equation (5.4b), while the time scale and streamwise length scale are again the same as the rest of the interaction region and given by equations (5.30a,b). Relating the normal coordinates in regions α from equation (5.11a) and β from equation (5.4b) produces $\hat{Y} = g_w^{-(n+1)} Y$, and writing the form of the solution at the top of region I_α equation (5.53) in terms of Y gives the conditions

$$u' \to U_\infty a\, Y^{\frac{1}{n+1}} + U_\infty M_\infty^{1/2}\, g_w^{n+1/2}\, Re_0^{-1/8}\, A^*(x^*,t^*)\, \frac{a}{n+1}\, Y^{-\frac{n}{n+1}} + \cdots, \qquad (5.54a)$$

$$v' \to -U_\infty\, Re_0^{-1/4}\, \frac{\partial A^*}{\partial x^*}\, a\, Y^{\frac{1}{n+1}} + \cdots, \qquad (5.54b)$$

$$h' \to U_\infty^2 b\, Y^{\frac{1}{n+1}} + U_\infty^2 M_\infty^{1/2}\, g_w^{n+1/2}\, Re_0^{-1/8}\, A^*(x^*,t^*)\, \frac{b}{n+1}\, Y^{-\frac{n}{n+1}} + \cdots, \qquad (5.54c)$$

as $Y \to 0$. These matching conditions suggest the following expansions for the flow quantities in region II:

$$u' = U_\infty\, \tilde{U}_0(Y) + U_\infty M_\infty^{1/2}\, g_w^{n+1/2}\, Re_0^{-1/8}\, \tilde{U}_1(x^*,Y,t^*) + \cdots, \qquad (5.55a)$$

$$v' = U_\infty\, Re_0^{-1/4}\, \tilde{V}_1(x^*,Y,t^*) + \cdots, \qquad (5.55b)$$

$$p' = p_\infty + \rho_\infty\, U_\infty^2\, M_\infty^{-1}\, Re_0^{-1/4}\, \tilde{P}_1(x^*,Y,t^*) + \cdots, \qquad (5.55c)$$

$$h' = U_\infty^2\, \tilde{H}_0(Y) + U_\infty^2\, M_\infty^{1/2}\, g_w^{n+1/2}\, Re_0^{-1/8}\, \tilde{H}_1(x^*,Y,t^*) + \cdots, \qquad (5.55d)$$

144

$$\rho' = \rho_\infty M_\infty^{-2} \tilde{R}_0(Y) + \rho_\infty M_\infty^{-3/2} g_w^{n+1/2} Re_0^{-1/8} \tilde{R}_1(x^*,Y,t^*) + \cdots. \qquad (5.55e)$$

From a comparison of these expansions with the conditions (5.54), it is evident that matching to region I_α requires

$$\left. \begin{array}{l} \tilde{U}_0 \to a\, Y^{\frac{1}{n+1}} + \cdots, \quad \tilde{U}_1 \to A^*(x^*,t^*) \dfrac{a}{n+1} Y^{-\frac{n}{n+1}} + \cdots \\[2ex] \tilde{V}_1 \to -\dfrac{\partial A^*}{\partial x^*} a\, Y^{\frac{1}{n+1}} + \cdots \end{array} \right\} \quad \text{as} \quad Y \to 0. \qquad (5.56a,b,c)$$

The leading order terms $\tilde{U}_0$, $\tilde{H}_0$ and $\tilde{R}_0$ are obtained by matching as $x^* \to -\infty$ to the solution in the upstream boundary layer (see §5.2.1) as $X \to 1$ and must also satisfy the leading terms of (5.54) in order to match to region I_α below. Therefore, $\tilde{U}_0$, $\tilde{H}_0$ and $\tilde{R}_0$ are assumed known from the upstream solution. To determine the perturbation functions $\tilde{U}_1$, $\tilde{V}_1$, $\tilde{H}_1$ and $\tilde{R}_1$, the expansions (5.55) are substituted into the Navier-Stokes and energy equations from which it is found that

$$\tilde{R}_0\, \tilde{U}_0 \frac{\partial \tilde{U}_1}{\partial x^*} + \tilde{R}_0\, \tilde{V}_1 \frac{d\tilde{U}_0}{dY} = -S^* \frac{\partial \tilde{P}_1}{\partial x^*}, \qquad \frac{\partial \tilde{P}_1}{\partial Y} = 0, \qquad (5.57a,b)$$

$$\tilde{R}_0\, \tilde{U}_0 \frac{\partial \tilde{H}_1}{\partial x^*} + \tilde{R}_0\, \tilde{V}_1 \frac{d\tilde{H}_0}{dY} = S^* \tilde{U}_0 \frac{\partial \tilde{P}_1}{\partial x^*}, \qquad (5.58)$$

where a new dimensionless parameter $S^* = M_\infty^{1/2} g_w^{-(n+1/2)} Re_0^{-1/8}$ appears in front of the pressure gradient terms. In normal circumstances, the wall temperature is moderate and the temperature factor g_w is $O(1)$ and $S^* \ll 1$. However, for $g_w \ll 1$ and of the order given by equation (5.29) the wall is cold and S^* is $O(1)$. The latter case is the situation of interest here. From equation (5.57) it is observed that the flow in region II is also inviscid (just as in region I_α).

Substitution of the expansions (5.55) into the continuity equation produces

145

$$\tilde{U}_0 \frac{\partial \tilde{R}_1}{\partial x^*} + \tilde{R}_0 \frac{\partial \tilde{U}_1}{\partial x^*} + \tilde{V}_1 \frac{d\tilde{R}_0}{dY} + \tilde{R}_0 \frac{\partial \tilde{V}_1}{\partial Y} = 0, \tag{5.59}$$

and from the ideal gas equation of state it is easily shown that

$$\tilde{H}_0 = \frac{1}{(\gamma - 1)\,\tilde{R}_0}, \tag{5.60a}$$

$$\tilde{H}_1 = \frac{\gamma}{(\gamma - 1)\,\tilde{R}_0} S^* \tilde{P}_1 - \frac{\tilde{R}_1}{(\gamma - 1)\,\tilde{R}_0^2}. \tag{5.60b}$$

Substitution of equations (5.60) into the energy equation (5.58) then yields

$$\tilde{U}_0 \frac{\partial \tilde{R}_1}{\partial x^*} + \tilde{V}_1 \frac{d\tilde{R}_0}{dY} = S^* \tilde{R}_0 \tilde{U}_0 \frac{\partial \tilde{P}_1}{\partial x^*}, \tag{5.61}$$

which when introduced into the continuity equation (5.59) gives

$$\frac{\partial \tilde{U}_1}{\partial x^*} + \frac{\partial \tilde{V}_1}{\partial Y} = -S^* \tilde{U}_0 \frac{\partial \tilde{P}_1}{\partial x^*}. \tag{5.62}$$

Through substitution of $\partial \tilde{U}_1 / \partial x^*$ from equation (5.62) into the streamwise momentum equation (5.57a), a first-order equation for $\tilde{V}_1$ is obtained, namely

$$\frac{\partial \tilde{V}_1}{\partial Y} - \frac{1}{\tilde{U}_0} \frac{d\tilde{U}_0}{dY} \tilde{V}_1 = S^* \tilde{U}_0 \frac{\partial \tilde{P}_1}{\partial x^*} \left[\frac{1}{\tilde{R}_0 \tilde{U}_0^2} - 1 \right]. \tag{5.63}$$

Defining $M_0(Y)$ to be the local Mach number across the upstream boundary layer as $X \to 1$, it is readily determined that $M_0^2 = \tilde{R}_0 \tilde{U}_0^2$ to leading order. Therefore, the solution to equation (5.63) which satisfies the conditions (5.56a,c) as $Y \to 0$ is easily obtained and

$$\tilde{V_1} = \tilde{U_0}\left\{-\frac{\partial A^*}{\partial x^*} + S^*\frac{\partial p^*}{\partial x^*}\int_0^Y\left[\frac{1}{M_0^2} - 1\right]dY\right\}. \tag{5.64}$$

The solutions for the other perturbation variables may then be obtained using the result (5.64). From the expansions (5.55a,b) and evaluating (5.64) at the outer edge of region II, the slope of the streamlines at the outer edge of this region is found to be

$$\frac{v'}{u'} = Re_0^{-1/4}\left\{-\frac{\partial A^*}{\partial x^*} + S^*\mathcal{L}\frac{\partial p^*}{\partial x^*}\right\} \quad \text{for large } Y, \tag{5.65a}$$

where

$$\mathcal{L} = \int_0^{\delta_0}\left[\frac{1}{M_0^2} - 1\right]dY. \tag{5.65b}$$

This integral first appeared in a study by Pearson *et al.* (1958) and is sometimes referred to as the Pearson integral. Here, δ_0 is the thickness of the boundary layer just upstream of the interaction region. From a comparison with the result (5.39) in the viscous sublayer, it is evident that the first term on the right hand side of equation (5.65a) is due to the displacement effect of the viscous sublayer (region I), while the second term is the contribution due to the main deck (region II). Note that when $S^* \ll 1$, corresponding to the case for which there is no wall cooling, the contribution from the main deck is negligible and the problem reduces to the conventional triple-deck formulation. On the other hand, for $S^* \gg 1$ the displacement effect due to the main deck dominates that due to the viscous sublayer; this case has recently been considered by Kerimbekov, Ruban and Walker (1993) and Zhikharev (1993). In the current investigation the intermediate range is of interest corresponding to wall temperatures for which $S^* = O(1)$ and for which both regions I and II contribute to the displacement effect.

147

5.2.7 The Outer Inviscid Flow

The flow in the local interaction region III riding above the boundary layer consists of perturbations about the uniform external flow variables U_∞, p_∞, h_∞ and ρ_∞ and is associated with the displacement effect of the boundary layer within the interaction region. Again, the time scale and streamwise length scale are given by (5.30a,b), but the normal coordinate Y^* is defined by

$$y' = L\, M_\infty^{1/2}\, g_w^{n+1/2}\, Re_0^{-3/8}\, Y^*. \tag{5.66}$$

From equation (5.65a) it follows that the expansions of the dependent variables in region III have the form

$$u' = U_\infty + U_\infty\, M_\infty^{-1}\, Re_0^{-1/4}\, u_1(x^*,Y^*,t^*) + \cdots, \tag{5.67a}$$

$$v' = U_\infty\, Re_0^{-1/4}\, v_1(x^*,Y^*,t^*) + \cdots, \tag{5.67b}$$

$$p' = p_\infty + \rho_\infty\, U_\infty^2\, M_\infty^{-1}\, Re_0^{-1/4}\, p_1(x^*,Y^*,t^*) + \cdots, \tag{5.67c}$$

$$h' = h_\infty + U_\infty^2\, M_\infty^{-1}\, Re_0^{-1/4}\, h_1(x^*,Y^*,t^*) + \cdots, \tag{5.67d}$$

$$\rho' = \rho_\infty + \rho_\infty\, M_\infty\, Re_0^{-1/4}\, \rho_1(x^*,Y^*,t^*) + \cdots, \tag{5.67e}$$

and the matching condition to region II below is

$$v_1 \to -\frac{\partial A^*}{\partial x^*} + S^*\,£\,\frac{\partial p^*}{\partial x^*} \quad \text{as} \quad Y^* \to 0. \tag{5.68}$$

Substitution of the expansions (5.67) into the Navier-Stokes equations gives

148

$$\frac{\partial u_1}{\partial x^*} = -\frac{\partial p_1}{\partial x^*}, \qquad \frac{\partial v_1}{\partial x^*} = -\frac{\partial p_1}{\partial Y^*}, \qquad\qquad (5.69a,b)$$

and into the energy equation provides

$$\frac{\partial h_1}{\partial x^*} = \frac{\partial p_1}{\partial x^*}. \qquad\qquad (5.70)$$

The continuity equation becomes

$$\frac{\partial \rho_1}{\partial x^*} + \frac{\partial v_1}{\partial Y^*} = 0, \qquad\qquad (5.71)$$

and the ideal gas equation of state gives

$$h_1 = \frac{\gamma}{\gamma - 1}(p_1 - \rho_1). \qquad\qquad (5.72)$$

Integration of equations (5.69a) and (5.70) subject to the undisturbed flow conditions as $x^{*2} + Y^{*2} \to \infty$ gives the following relations for linearized compressible flow

$$u_1(x^*,Y^*,t^*) = -p_1(x^*,Y^*,t^*), \quad h_1(x^*,Y^*,t^*) = p_1(x^*,Y^*,t^*). \qquad (5.73a,b)$$

It follows from substitution of the result (5.73b) into the equation of state (5.72) that

$$p_1(x^*,Y^*,t^*) = \gamma \rho_1(x^*,Y^*,t^*), \qquad\qquad (5.74)$$

which when substituted into the continuity equation (5.71) and then combined with equation (5.69b) leads to the following wave equation for p_1

149

$$\frac{1}{\gamma}\frac{\partial^2 p_1}{\partial x^{*2}} - \frac{\partial^2 p_1}{\partial Y^{*2}} = 0. \tag{5.75}$$

Then from substitution of the condition (5.68) into equation (5.69b), it follows that

$$\frac{\partial p_1}{\partial Y^*} \rightarrow \frac{\partial^2 A^*}{\partial x^{*2}} - S^* \pounds \frac{\partial^2 p^*}{\partial x^{*2}} \quad \text{as} \quad Y^* \rightarrow 0, \tag{5.76}$$

in order to match to region II below. In general, solutions to equation (5.75) are of the form

$$p_1(x^*, Y^*, t^*) = f(x^* - \frac{Y^*}{\sqrt{\gamma}}) + g(x^* + \frac{Y^*}{\sqrt{\gamma}}), \tag{5.77}$$

but for flow from left to right in the upper half plane with the disturbances located at $Y^* = 0$, only right traveling waves are possible; thus, g must be equal to zero. The function f is determined from the condition (5.76) as $Y^* \rightarrow 0$ leading to the result

$$p^*(x^*, t^*) = p_1(x^*, 0, t^*) = -\frac{\partial A^*}{\partial x^*} + S^* \pounds \frac{\partial p^*}{\partial x^*}. \tag{5.78}$$

This equation is the interaction law coupling the pressure at the base of the outer inviscid region (which is imposed across the boundary layer) and the displacement effect of the viscous sublayer and main deck. Observe from equation (5.78) that when $\pounds > 0$, a pressure rise (*i.e.* $\partial p^*/\partial x^* > 0$) leads to an increase in the displacement thickness of region II just as for subsonic boundary-layer flows. In contrast, when $\pounds < 0$, a pressure rise produces a decrease in the contribution due to the main deck, just as for supersonic boundary layers. Therefore, when $\pounds > 0$ for the upstream boundary layer, the situation is referred to as subcritical, and when $\pounds < 0$, it is called supercritical.

150

5.2.8 General Interaction Formulation

In summary, the solution for the hypersonic boundary-layer flow over a cold surface defined by $y' = L\, M_\infty^{3/2}\, g_w^{n+1/2}\, Re_0^{-5/8}\, f^*(x^*, t^*)$ is determined from equations (5.35) in the viscous sublayer subject to the conditions (5.36)-(5.38) and the interaction condition (5.78). In order to scale out the constants λ and γ from these equations, it is convenient to apply the following transformations:

$$t^* = \lambda^{-3/2}\, t, \quad x^* = (\gamma - 1)^{1/2}\, \lambda^{-5/4}\, x, \quad y^* = (\gamma - 1)^{1/2}\, \lambda^{-3/4}\, (y + f), \quad (5.79\text{a,b,c})$$

$$u^* = (\gamma - 1)^{1/2}\, \lambda^{1/4}\, u, \quad v^* = (\gamma - 1)^{1/2}\, \lambda^{3/4}\left(v + \frac{\partial f}{\partial t} + u\, \frac{\partial f}{\partial x}\right), \quad (5.79\text{d,e})$$

$$p^* = \lambda^{1/2}\, p, \quad A^* = (\gamma - 1)^{1/2}\, \lambda^{-3/4}\, (A - f), \quad (5.79\text{f,g})$$

$$f^* = (\gamma - 1)^{1/2}\, \lambda^{-3/4}\, f, \quad S^* = (\gamma - 1)^{1/2}\, \lambda^{-5/4}\, S. \quad (5.79\text{h,i})$$

The scalings (5.79) also contain a Prandtl transposition, under which the boundary-layer equations are invariant, so that the wall conditions may be applied at $y = 0$. Applying the transformations (5.79), the interaction formulation in a general form becomes

$$\frac{\partial u}{\partial t} + u\, \frac{\partial u}{\partial x} + v\, \frac{\partial u}{\partial y} = -\frac{\partial p}{\partial x} + \frac{\partial^2 u}{\partial y^2}, \quad (5.80\text{a})$$

$$\frac{\partial u}{\partial x} + \frac{\partial v}{\partial y} = 0, \quad (5.80\text{b})$$

$$p = -\frac{\partial \dot{A}}{\partial x} + \frac{\partial f}{\partial x} + S\, \pounds\, \frac{\partial p}{\partial x}, \quad (5.80\text{c})$$

151

$$u = v = 0 \quad \text{at} \quad y = 0, \tag{5.80d}$$

$$u \to y + \cdots \quad \text{as} \quad x \to -\infty, \tag{5.80e}$$

$$u \to y + A(x,t) + \cdots \quad \text{as} \quad y \to \infty. \tag{5.80f}$$

This set of equations applies for hypersonic boundary-layer flows over cold walls encountering a small surface disturbance. The scaled equation of the surface is assumed to contain a small disturbance in the sense that $f(x,t)$ is $O(1)$ within the sublayer scalings (5.30). And by cold wall it is meant in the present context that $S = (\gamma - 1)^{-1/2} \lambda^{5/4} M_\infty^{1/2} g_w^{-(n + 1/2)} Re_0^{-1/8}$ is $O(1)$ where the temperature factor $g_w = h_w'/U_\infty^2 \ll 1$. Here, h_w' is the enthalpy at the wall. The behavior of the boundary layer within the interaction region is determined by the sign of $\pounds$, where

$$\pounds = \int_0^{\delta_0} \left[\frac{1}{M_0^2} - 1 \right] dY. \tag{5.81}$$

Here, δ_0 is the thickness of the boundary layer, and $M_0(Y)$ is the Mach number distribution across the boundary layer just upstream of the interaction. If the average Mach number is less than one, $\pounds > 0$ and a pressure rise leads to thickening of the main deck; this is called the subcritical case. On the other hand, if the average Mach number is greater than one, then $\pounds < 0$ and a pressure rise leads to a decrease in the thickness of the main deck (the supercritical case).

Note from the set of equations (5.80), that when $S \pounds = 0$, corresponding to moderate to high wall temperatures, the formulation is the same as the triple deck for supersonic flows developed by Stewartson and Williams (1969) and Neiland (1969). Numerical solutions for the supersonic triple deck have been obtained by Rizzetta, Burggraf and Jenson (1978), Ruban (1978) and Smith and Khorrami (1991) and these solutions will be considered further in chapter 6.

152

The theory just presented is based on the approach initiated by Neiland (1973) and differs in many respects from the recent study of Brown, Cheng and Lee (1990). While the two theories agree qualitatively on some of the effects of wall cooling on the hypersonic triple deck, it is not clear how (or if) many of the specific aspects of the two theories can be reconciled at present. As in the present approach, the theory of Brown *et al.* (1990) recognizes that there is a critical range of surface temperatures for which the contribution to the displacement thickness due to the main deck becomes an $O(1)$ effect when the wall is cooled. Brown *et al.* (1990) describe a critical temperature as T_w^* and found it to be small of $O(\chi^{1/(4n+2)})$ which agrees with the order of magnitude of g_w in the present theory (compare the result 5.29 with the definition 5.3 for χ). The range for which the wall temperature $T_w = O(T_w^*)$ is referred to as the transcritical case by Brown *et al.* (1990), and this range is the primary case of interest in the present investigation. The interaction law used by Brown *et al.* (1990) was $p = -\sigma(dA/dx + Vdp/dx)$, where the parameters σ and V depend upon the temperature regime. For their transcritical case, they specify that $\sigma = 1$ and $V = O(1)$ but then only show results for $V > 0$ which corresponds to the supercritical case ($\pounds < 0$) in the present theory. There is no mention of a case corresponding to subcritical boundary layers ($\pounds > 0$), and it is not clear whether $V < 0$ is permissible in their theory. Brown *et al.* (1990) also consider wall temperatures much greater than ($T_w \gg T_w^*$) and much less than ($T_w \ll T_w^*$) the critical value and refer to these temperature regimes as supercritical and subcritical, respectively. For supercritical wall temperatures, they take $\sigma = 1$ and $V \ll 1$, whereas for subcritical wall temperatures $V = 1$ and $\sigma \gg 1$. Their supercritical case, therefore, corresponds to the case without wall cooling ($S \pounds = 0$) considered here or, equivalently, the classical supersonic triple deck. Although the relationship is not clear, their subcritical case would apparently have some correlation to the strong wall cooling case considered by Kerimbekov, Ruban and Walker (1993). In addition to these superficial differences in terminology, there are some differences in the scalings of the triple-deck formulation itself. These discrepancies make comparison of the two theories difficult and preclude a clear reconciliation of the underlying

153

differences.

5.3 Compression Ramp Geometry

Although the triple-deck formulation articulated in §5.2.8 applies for general surface shapes $f(x,t)$ consistent with the lower-deck scalings (5.30b,c), attention will now be focussed on the compression ramp geometry. A compression ramp is defined by

$$f(x) = \begin{cases} 0, & x < 0 \\ \alpha x, x > 0 \end{cases}, \tag{5.82}$$

where α is the scaled ramp angle. From comparison of the streamwise and normal length scales (5.30b) and (5.30c) of the viscous sublayer, this represents a very small physical ramp angle which is $O(Re_0^{-1/4})$. While this geometry is very simple, the flow over a compression ramp exhibits boundary-layer separation at the corner for sufficiently high α which is characteristic of many viscous-inviscid interactive flows. Moreover, the compression ramp geometry has been considered extensively in the past. Rizzetta, Burggraf and Jenson (1978), Ruban (1978) and Smith and Khorrami (1991) considered the supersonic case, or equivalently the hypersonic case without wall cooling, for various α. In addition, Brown, Cheng and Lee (1990), Kerimbekov, Ruban and Walker (1993) and Zhikharev (1993) considered the case of hypersonic flow over a cold wall.

5.4 Viscous-Inviscid Singularities

Recently, two types of singularities have been identified as occurring in problems associated with supersonic ramp flows and hypersonic flows over strongly cooled compression ramps. These are discussed in the following two sections.

154

5.4.1 Large Ramp Angle Singularity

Many investigators have attempted to consider the nature of the transition from small-scale to large-scale separation in high Reynolds number flows. Such attempts have in general been unsuccessful because severe numerical difficulties are often encountered once a separated flow region begins to increase substantially in size. Smith (1988a) has observed that many interacting boundary-layer flow calculations exhibit increasing maximums in the pressure gradient and decreasing minimums in the wall shear at some point between separation and reattachment as the controlling parameter is increased. In the case of shock-induced boundary-layer separation, the controlling parameter is the strength of the shock; for surface humps, it is the hump height. This behavior may be observed in Rizzetta *et al.* (1978) and Ruban (1978) for the compression ramp, where the ramp angle α is the controlling parameter. Smith (1988a) developed a general theory for the reversed-flow singularity in viscous-inviscid interacting flows at high Reynolds number, and Smith and Khorrami (1991) compared the theoretical prediction with numerical results for supersonic flow over a ramp.

Referring to the value of the controlling parameter at which the singularity occurs as α_s and the streamwise location of the singularity as x_s, the general theory describes a singularity in which

$$\max\left(\frac{\mathrm{d}p}{\mathrm{d}x}\right) \to +\infty, \quad \min(\tau_w) \to -\infty \quad \text{as} \quad \alpha \to \alpha_s^-, \tag{5.83a,b}$$

where

$$\frac{\max(\mathrm{d}p/\mathrm{d}x)}{\left[\min(\tau_w)\right]^2} \to O(1). \tag{5.83c}$$

Here, p is the pressure, and τ_w is the wall shear. The flow in the immediate vicinity of the singularity develops on a short streamwise length scale $(x - x_s) = O(\hat{\Delta})$ and is

155

inviscid to leading order. The maximum in the pressure gradient and minimum in the wall shear have the following orders of magnitude

$$\max\!\left(\frac{\mathrm{d}p}{\mathrm{d}x}\right) \sim \hat{\Delta}^{-1}, \quad \min(\tau_w) \sim -\hat{\Delta}^{-1/2}, \tag{5.84a,b}$$

where $\hat{\Delta} \to 0^+$ as $\alpha \to \alpha_s^-$. For the case of the supersonic compression ramp, the streamwise length scale is

$$\hat{\Delta} = (\alpha_s - \alpha)^2. \tag{5.85}$$

The numerical results of Smith and Khorrami (1991) did not precisely pinpoint the value of α_s for the supersonic ramp, but they found it to be "somewhat below 9."

The implication of these results is that the interactive boundary-layer formulation fails for even moderate values of the controlling parameter. In order to relieve the reversed-flow singularity, it was suggested by Smith (1988a) that a short streamwise region forms locally about $x = x_s$. In this region the inviscid Euler equations would govern and normal pressure gradient effects become important and act to relieve the singularity. This stage would act on an $O(Re_0^{-5/8})$ streamwise length scale in the triple-deck case and on an $O(Re_0^{-1/2})$ length scale in the finite Reynolds number case.

5.4.2 Strong Wall Cooling Singularities in Hypersonic Flow

For the case of hypersonic flow over cooled walls (as formulated in §5.2), Kerimbekov, Ruban and Walker (1993) and Zhikharev (1993) considered the flow over a compression ramp for a situation where the wall was cooled to the point where $S\pounds$ became very large. Recall that as the wall is cooled, the contribution to the displacement effect due to the main deck increases relative to that due to the viscous

sublayer. When $S\pounds$ becomes very large, the contribution due to the viscous sublayer ultimately becomes too small to influence the leading-order pressure distribution in the external flow. Therefore, the interaction is an inviscid-inviscid one between the inviscid main deck and the inviscid outer flow. In order to investigate this case, a new dimensionless parameter is introduced; the Neiland number is defined by

$$N = \left[\frac{\lambda^5 S^{*4} |\pounds|^4}{(\gamma - 1)^2} \right]^{1/3} = [S|\pounds|]^{4/3}. \tag{5.86}$$

where $S = \lambda^{5/4} S^* / (\gamma - 1)^{1/2}$. The Neiland number N represents the ratio of the contributions to the displacement thickness due to the main deck and the viscous sublayer. Kerimbekov *et al.* (1993) and Zhikharev (1993), therefore, considered the case where $N \to \infty$. The formulation (5.80) may be recast such that the dependence on N is shown explicitly. To this end, the variables are scaled as follows

$$x = N^{3/4} \bar{x}, \quad y = N^{1/4} \bar{y}, \tag{5.87a,b}$$

$$u = N^{1/4} \bar{u}, \quad v = N^{-1/4} \bar{v}, \quad p = N^{1/2} \bar{p}, \tag{5.87c,d,e}$$

$$A = N^{1/4} \bar{A}, \quad f = N^{5/4} \bar{f}. \tag{5.87f,g}$$

Considering the case of steady flow, and defining the streamfunction by $\bar{u} = \partial \bar{\psi} / \partial \bar{y}$, $\bar{v} = -\partial \bar{\psi} / \partial \bar{x}$, the formulation in equations (5.80) becomes

$$\frac{\partial \bar{\psi}}{\partial \bar{y}} \frac{\partial^2 \bar{\psi}}{\partial \bar{x} \partial \bar{y}} - \frac{\partial \bar{\psi}}{\partial \bar{x}} \frac{\partial^2 \bar{\psi}}{\partial \bar{y}^2} = -\frac{\partial \bar{p}}{\partial \bar{x}} + \frac{\partial^3 \bar{\psi}}{\partial \bar{y}^3}, \tag{5.88a}$$

$$\bar{p} = -\frac{1}{N} \frac{\partial \bar{A}}{\partial \bar{x}} + \frac{\partial \bar{f}}{\partial \bar{x}} + \text{sgn}(\pounds) \frac{\partial \bar{p}}{\partial \bar{x}}, \tag{5.88b}$$

157

$$\overline{\psi} = \frac{\partial \overline{\psi}}{\partial \overline{y}} = 0 \quad \text{at} \quad \overline{y} = 0, \tag{5.88c}$$

$$\overline{\psi} \to \frac{1}{2}\, \overline{y}^2 + \cdots \quad \text{as} \quad \overline{x} \to -\infty, \tag{5.88d}$$

$$\overline{\psi} \to \frac{1}{2}\, \overline{y}^2 + A(\overline{x})\, \overline{y} + \cdots \quad \text{as} \quad \overline{y} \to \infty. \tag{5.88e}$$

The surface geometry is given by

$$\overline{f}(\overline{x}) = \begin{cases} 0, & \overline{x} < 0 \\ \overline{\alpha}\, \overline{x}, & \overline{x} > 0 \end{cases}, \tag{5.89a}$$

where the ramp angle is now defined by

$$\overline{\alpha} = N^{-1/2}\, \alpha. \tag{5.89b}$$

Now from the interaction law (5.88b), the effect of increasing the Neiland number is evident. As N becomes large, the first term in the interaction law, representing the contribution to the displacement thickness due to the viscous sublayer, becomes small.

Kerimbekov *et al.* (1993) considered the solutions to (5.88) with (5.89) for both the subcritical ($\pounds > 0$) and supercritical ($\pounds < 0$) wall cooling cases, while Zhikharev (1993) considered solutions for the subcritical case. The form of the interaction law (5.88b) suggests the following expansions for the streamfunction, pressure distribution and displacement function

$$\overline{\psi}(\overline{x}, \overline{y}) = \psi_0(\overline{x}, \overline{y}) + N^{-1}\, \psi_1(\overline{x}, \overline{y}) + \cdots, \tag{5.90a}$$

$$\overline{p}(\overline{x}) = p_0(\overline{x}) + N^{-1}\, p_1(\overline{x}) + \cdots, \tag{5.90b}$$

$$\bar{A}(\bar{x}) = A_0(\bar{x}) + N^{-1} A_1(\bar{x}) + \cdots. \tag{5.90c}$$

Substitution of the expansions (5.90b,c) into the interaction law (5.88b) gives the following expression for the leading-order pressure term

$$p_0 = \text{sgn}(\pounds) \frac{\partial p_0}{\partial \bar{x}} + \bar{\alpha} H(\bar{x}), \tag{5.91}$$

where $H(\bar{x})$ is the Heaviside unit step function. The solution of equation (5.91) for a supercritical boundary layer $(\pounds < 0)$ is

$$p_0 = \begin{cases} 0, & \bar{x} < 0 \\ \bar{\alpha}(1 - e^{-\bar{x}}), & \bar{x} > 0 \end{cases}, \tag{5.92}$$

while for a subcritical boundary layer $(\pounds > 0)$, the solution is

$$p_0 = \begin{cases} \bar{\alpha} e^{\bar{x}}, & \bar{x} < 0 \\ \bar{\alpha}, & \bar{x} > 0 \end{cases}. \tag{5.93}$$

Therefore, for the supercritical case (5.92) there are no disturbances upstream of $\bar{x} = 0$, and the pressure begins to increase at the corner toward $\bar{\alpha}$ as $\bar{x} \to \infty$. On the other hand, for the subcritical case (5.93), the pressure increases from zero far upstream to $\bar{\alpha}$ at the corner and is constant along the ramp. Substituting (5.90a,b) into the momentum equation (5.88a) in the viscous sublayer gives

$$\frac{\partial \psi_0}{\partial \bar{y}} \frac{\partial^2 \psi_0}{\partial \bar{x} \partial \bar{y}} - \frac{\partial \psi_0}{\partial \bar{x}} \frac{\partial^2 \psi_0}{\partial \bar{y}^2} = -\frac{\partial p_0}{\partial \bar{x}} + \frac{\partial^3 \psi_0}{\partial \bar{y}^3}, \tag{5.94a}$$

and the boundary conditions (5.88c,d,e) become

159

$$\psi_0 = \frac{\partial \psi_0}{\partial \bar{y}} = 0 \quad \text{at} \quad \bar{y} = 0, \tag{5.94b}$$

$$\psi_0 \to \frac{1}{2}\bar{y}^2 + \cdots \quad \text{as} \quad \bar{x} \to -\infty, \tag{5.94c}$$

$$\psi_0 \to \frac{1}{2}\bar{y}^2 + A_0(\bar{x})\bar{y} + \cdots \quad \text{as} \quad \bar{y} \to \infty. \tag{5.94d}$$

Observe that the problem (5.94) is simply a classical boundary-layer problem with a prescribed pressure gradient given by either equation (5.92) or equation (5.93). Therefore, the solution may be obtained using a conventional numerical procedure starting from the initial condition given by equation (5.94c) and marching downstream.

Such solutions were obtained by Kerimbekov *et al.* (1993) for the supercritical pressure distribution (5.92). The solution for increasing ramp angle $\bar{\alpha}$ was found to exhibit the phenomenon of marginal separation; there is a minimum in wall shear which decreases with increasing ramp angle until eventually a zero is reached at a critical ramp angle $\bar{\alpha}_0 = 0.7548$ at $\bar{x} = \bar{x}_0 = 0.5$. This type of behaviour also occurs in a boundary layer near the leading edge of thin airfoils at some critical angle of attack, and the marginal separation theory of Ruban (1981) for the airfoil at angle of attack shows that a singularity develops at the point of zero wall shear x_0 as this critical angle of attack is approached. The singularity that develops is weak in the sense that solutions of the boundary-layer equations may be obtained downstream of $\bar{x}_0$. A local interaction region develops near $\bar{x}_0$ in order to relieve the singularity as has been considered by Stewartson, Smith and Kaups (1982) and Ruban (1982). It is demonstrated by Kerimbekov *et al.* (1993) that this same marginal separation theory applies to the supercritical wall cooling case for large Neiland number.

For the subcritical wall cooling case, a solution to equation (5.94) subject to the pressure distribution (5.93) exhibits a Goldstein (1948) singularity at a point of zero wall shear for sufficiently high ramp angle $\bar{\alpha}$. As determined by Smith and Daniels (1981), this singularity can be removed by a series of regions which have successively

160

shorter streamwise length scales allowing for a smooth transition into the separated region downstream. Physically, this is described as a compensation regime in which the combination of the surface shape and the displacement thickness of the boundary layer cancel such that the streamlines at the outer edge of the boundary layer are not effected by the small surface feature. This is the case when the streamwise extent of the surface feature is much smaller than the length of the interaction region as is the case here for the local region about the point of zero wall shear within the larger interaction region. Kerimbekov *et al.* (1993) showed that the theory of Smith and Daniels (1981) applies to the subcritical wall cooling case for $N \gg 1$.

6. Hypersonic Boundary-Layer Solutions

6.1 Introduction

The hypersonic triple-deck formulation described in §5.2 applies to surfaces of general shape with length scales consistent with those of the viscous sublayer and for situations with and without wall cooling. In §6.2 a description will be given of the algorithm that was used here to solve the hypersonic triple-deck equations. It is based on an algorithm developed by Ruban (1978) to solve the classical supersonic triple deck, but it has been extended here in order to provide a general numerical procedure for two-dimensional unsteady hypersonic triple-deck flows with and without wall cooling. The triple-deck equations are first recast in terms of the shear stress as the principal dependent variable, as described in §6.2.1, in order to eliminate the need to explicitly compute the pressure distribution and the displacement function at each iteration during the course of the iterative scheme. In addition, an analytical transformation is applied for computational convenience to map the doubly infinite streamwise range to a finite domain and also to more accurately resolve the flow near the center of the domain; this is considered in §6.2.2. The numerical algorithm, described in §6.2.3, is very efficient and couples the interaction condition with the boundary-layer equations in the viscous sublayer in a unique manner. Before considering the numerical results obtained using this algorithm, the results of Tutty and Cowley (1986) will be discussed which suggest that instabilities are possible within triple-deck formulations. Therefore, a linear stability analysis of the hypersonic triple deck will be considered in §6.3 in order to determine the conditions for which an instability may possibly occur.

The compression ramp geometry has been studied extensively in the past and will be considered in detail here. Particular focus will be placed on investigating the effect of various levels of both subcritical and supercritical wall cooling on the steady

separation within the viscous sublayer over a range of ramp angles. Results for both the cold wall case and the non-cold wall case will be discussed in §6.4.

6.2 Solution Procedure for the Hypersonic Triple Deck

6.2.1 Shear Stress Formulation

It is convenient to reformulate the interaction problem (5.80) in terms of the scaled shear stress $\tau = \partial u / \partial y$. This procedure simplifies the formulation by allowing for the elimination of the pressure $p(x,t)$ and displacement function $A(x,t)$ from the streamwise momentum equation. First, define a streamfunction by

$$u = \frac{\partial \psi}{\partial y}, \quad v = -\frac{\partial \psi}{\partial x}. \tag{6.1a,b}$$

Differentiating the momentum equation (5.80a) with respect to y and using the continuity equation (5.80b) gives the equation for the shear stress

$$\frac{\partial \tau}{\partial t} + u \frac{\partial \tau}{\partial x} + v \frac{\partial \tau}{\partial y} = \frac{\partial^2 \tau}{\partial y^2}. \tag{6.2a}$$

An additional equation relating τ and ψ is obtained by differentiating (6.1a) with respect to y to give

$$\frac{\partial^2 \psi}{\partial y^2} = \tau. \tag{6.2b}$$

The conditions (5.80d,e,f) provide the following conditions on the streamfunction and shear stress:

$$\psi = \frac{\partial \psi}{\partial y} = 0 \quad \text{at} \quad y = 0, \tag{6.2c}$$

$$\tau \to 1 \quad \text{as} \quad x \to \pm\infty, \tag{6.2d}$$

$$\tau \to 1 \quad \text{as} \quad y \to \infty. \tag{6.2e}$$

Note that the condition in (6.2d) is also applied as $x \to +\infty$ because the interaction is assumed local; thus, downstream of the interaction region the flow returns to its upstream form. The initial flow distribution is taken to be that for a continuous flat plate in which case the initial condition is

$$\tau = 1 \quad \text{at} \quad t = 0, \tag{6.2f}$$

and the ramp geometry is assumed to be introduced abruptly at $t = 0$. The solution of equations (6.2) is then advanced forward in time with the expectation that, at least for some situations, the solution will evolve toward a steady state.

Next, consider the interaction condition (5.80c). From the matching condition (5.80f), the displacement function may be written as

$$A(x,t) = \lim_{y \to \infty} (u - y). \tag{6.3}$$

Differentiating the interaction law (5.80c) with respect to x and substituting (6.3) gives

$$\frac{\partial p}{\partial x} = -\frac{\partial^2}{\partial x^2}[\lim_{y \to \infty} (u - y)] + \frac{\partial^2 f}{\partial x^2} + S \, \pounds \, \frac{\partial^2 p}{\partial x^2}. \tag{6.4}$$

Observe from the momentum equation (5.80a) and the surface conditions (5.80d) that the pressure gradient is also related to the shear gradient at the surface by

164

$$\frac{\partial p}{\partial x} = \frac{\partial \tau}{\partial y}\bigg|_{y=0}, \tag{6.5}$$

and from the definition of τ that

$$u = \int_0^y \tau \, dy. \tag{6.6}$$

Substituting (6.5) and (6.6) into equation (6.4) gives the interaction law expressed solely in terms of gradients of the shear stress

$$\frac{\partial \tau}{\partial y}\bigg|_{y=0} = -\frac{\partial^2}{\partial x^2} \int_0^\infty (\tau - 1) \, dy + \frac{\partial^2 f}{\partial x^2} + S \pounds \frac{\partial}{\partial x}\left[\frac{\partial \tau}{\partial y}\bigg|_{y=0} \right]. \tag{6.7}$$

Therefore, the shear stress $\tau(x,y,t)$ is obtained from a solution to (6.2a) with the interaction law (6.7) and the conditions (6.2d,e,f). The streamfunction $\psi(x,y,t)$ is then determined from (6.2b,c) in order to provide the velocity coefficients in (6.2a).

6.2.2 Finite-Domain Transformation

Just as for the unsteady problem considered in part I, it is convenient to transform the region $(-\infty,0) \le (x,y) \le (+\infty,+\infty)$ into a finite rectangular domain. This is accomplished through the transformations

$$\hat{x} = \frac{2}{\pi} \arctan\left(\frac{x}{a}\right), \quad \hat{y} = \frac{2}{\pi} \arctan\left(\frac{y}{b}\right), \tag{6.8a,b}$$

so that the computational domain is transformed to $(-1,0) \le (\hat{x},\hat{y}) \le (+1,+1)$. The constants a and b are transformation parameters which determine the concentration of points in (x,y)-space; reducing a and b focuses more points near the ramp corner

165

at $x = 0$ and the surface at $y = 0$, respectively. The transformation (6.8a) also eliminates the need to truncate the domain at some finite value of x upstream and downstream of the disturbance as has been done in previous studies (see, for example, Rizzetta, Burggraf and Jenson, 1978 and Ruban, 1978). The transformation laws for (6.8) are

$$\frac{\partial}{\partial x} = \frac{\Gamma(\hat{x})}{a} \frac{\partial}{\partial \hat{x}}, \quad \frac{\partial^2}{\partial x^2} = \frac{\Gamma(\hat{x})}{a} \frac{\Gamma'(\hat{x})}{a} \frac{\partial}{\partial \hat{x}} + \frac{\Gamma^2(\hat{x})}{a^2} \frac{\partial^2}{\partial \hat{x}^2}, \qquad (6.9\text{a,b})$$

$$\frac{\partial}{\partial y} = \frac{\Gamma(\hat{y})}{b} \frac{\partial}{\partial \hat{y}}, \quad \frac{\partial^2}{\partial y^2} = \frac{\Gamma(\hat{y})}{b} \frac{\Gamma'(\hat{y})}{b} \frac{\partial}{\partial \hat{y}} + \frac{\Gamma^2(\hat{y})}{b^2} \frac{\partial^2}{\partial \hat{y}^2}, \qquad (6.9\text{c,d})$$

where

$$\Gamma(\zeta) = \frac{1}{\pi} [1 + \cos(\pi \zeta)]. \qquad (6.9\text{e})$$

Therefore, applying the transformation (6.8) to the momentum equation (6.2a) gives

$$\frac{\partial \tau}{\partial t} + \frac{\Gamma(\hat{x})}{a} u \frac{\partial \tau}{\partial \hat{x}} + \frac{\Gamma(\hat{y})}{b} v \frac{\partial \tau}{\partial \hat{y}} = \frac{\Gamma(\hat{y})}{b} \frac{\Gamma'(\hat{y})}{b} \frac{\partial \tau}{\partial \hat{y}} + \frac{\Gamma^2(\hat{y})}{b^2} \frac{\partial^2 \tau}{\partial \hat{y}^2}, \qquad (6.10\text{a})$$

and the boundary conditions (6.2d,e) become

$$\tau \rightarrow 1 \quad \text{as} \quad \hat{x} \rightarrow \pm 1, \qquad (6.10\text{b})$$

$$\tau \rightarrow 1 \quad \text{as} \quad \hat{y} \rightarrow 1. \qquad (6.10\text{c})$$

The interaction law (6.7) is now

166

$$\frac{\Gamma(0)}{b}\frac{\partial \tau}{\partial \hat{y}}\bigg|_{\hat{y}=0} = -\left[\frac{\Gamma(\hat{x})}{a}\frac{\Gamma'(\hat{x})}{a}\frac{\partial}{\partial \hat{x}} + \frac{\Gamma^2(\hat{x})}{a^2}\frac{\partial^2}{\partial \hat{x}^2}\right]b\int_0^1 \frac{\tau-1}{\Gamma(\hat{y})}\,d\hat{y}$$

$$+\frac{\partial^2 f}{\partial x^2} + S\, \pounds\, \frac{\Gamma(\hat{x})}{a}\frac{\partial}{\partial \hat{x}}\left[\frac{\Gamma(0)}{b}\frac{\partial \tau}{\partial \hat{y}}\bigg|_{\hat{y}=0}\right]. \tag{6.11}$$

Note that $f(x,t)$ is a known analytical function describing the surface shape; therefore, its second derivative is most conveniently left in terms of x. Equation (6.2b) and its boundary conditions (6.2c) now become

$$\frac{\Gamma(\hat{y})}{b}\frac{\partial}{\partial \hat{y}}\left[\frac{\Gamma(\hat{y})}{b}\frac{\partial \psi}{\partial \hat{y}}\right] = \tau, \tag{6.12a}$$

$$\psi\bigg|_{\hat{y}=0} = \frac{\Gamma(\hat{y})}{b}\frac{\partial \psi}{\partial \hat{y}}\bigg|_{\hat{y}=0} = 0, \tag{6.12b}$$

and equations (6.1) become

$$u = \frac{\Gamma(\hat{y})}{b}\frac{\partial \psi}{\partial \hat{y}}, \quad v = -\frac{\Gamma(\hat{x})}{a}\frac{\partial \psi}{\partial \hat{x}}. \tag{6.13a,b}$$

6.2.3 Numerical Methods

At each time step a solution to the momentum equation (6.10a) subject to the conditions (6.10b,c) and the interaction law (6.11) is required. Then for the updated $\tau(\hat{x},\hat{y},t)$ distribution, equation (6.12a) is integrated subject to conditions (6.12b) to obtain the streamfunction $\psi(\hat{x},\hat{y},t)$ from which the updated velocity components $u(\hat{x},\hat{y},t)$ and $v(\hat{x},\hat{y},t)$ are obtained from equations (6.13). The implicit algorithm described below combines the momentum equation and the interaction law in a unique manner such that no iteration is necessary between the boundary-layer solution and outer inviscid

167

solution at each time step. The algorithm was first developed by Ruban (1978) for the supersonic triple-deck formulation, and here it was extended to allow for cold wall effects in the hypersonic case. All spatial approximations are second-order accurate, while the algorithm is first-order accurate in time. Here, steady-state solutions were sought as the large time limit of an unsteady solution; therefore, the first-order temporal accuracy was of no consequence in terms of the final solution.

Although the $(\hat{x}, \hat{y})$ domain is finite, the streamwise velocity is of the form $u \sim y$ as $y \to \infty$, and it is necessary, therefore, to choose a finite value of y at which to truncate the vertical extent of the domain. Let this value be y_{max} with corresponding $\hat{y}_{max}$ from equation (6.8b). The region $(-1,0) \le (\hat{x}, \hat{y}) \le (+1, \hat{y}_{max})$ was then divided into $I-1$ and $J-1$ equal subintervals $\Delta \hat{x}$ and $\Delta \hat{y}$ in the $\hat{x}$ and $\hat{y}$ directions, respectively, and a uniform mesh was defined by $i = 1,...,I$ and $j = 1,...,J$. Quantities, such as $\tau(\hat{x}, \hat{y}, t)$, at the point $(\hat{x}_i, \hat{y}_j)$ are denoted by $\tau_{i,j}$ at the current time step where the solution is sought; the corresponding values at the previous time step where the solution is known are denoted by $\tau_{i,j}^*$. Approximating the normal derivatives by second-order central differences and the time derivative by a first-order backward difference, the difference equation derived from equation (6.10a) is

$$\frac{\tau_{i,j} - \tau_{i,j}^*}{\Delta t} + \frac{\Gamma(\hat{x}_i)}{a} \left(u^* \frac{\partial \tau^*}{\partial \hat{x}} \right)_{i,j} + \frac{\Gamma(\hat{y}_j)}{b} v_{i,j}^* \frac{\tau_{i,j+1} - \tau_{i,j-1}}{2 \Delta \hat{y}}$$
$$= \frac{\Gamma(\hat{y}_j)}{b} \frac{\Gamma'(\hat{y}_j)}{b} \frac{\tau_{i,j+1} - \tau_{i,j-1}}{2 \Delta \hat{y}} + \frac{\Gamma^2(\hat{y}_j)}{b^2} \frac{\tau_{i,j+1} - 2 \tau_{i,j} + \tau_{i,j-1}}{(\Delta \hat{y})^2}, \qquad (6.14)$$

where the streamwise convection term and the normal velocity are to be evaluated at the previous time step as shown; note that this latter approximation incurs an error $O(\Delta t)$. The streamwise convection term is approximated by a second-order accurate (in $\Delta \hat{x}$) backward difference in regions of positive streamwise velocity and forward difference in regions of negative velocity as follows

$$\left(u^* \frac{\partial \tau^*}{\partial \hat{x}}\right)_{i,j} = \begin{cases} u_{i,j}^* \dfrac{3\,\tau_{i,j}^* - 4\,\tau_{i-1,j}^* + \tau_{i-2,j}^*}{2\,\Delta\hat{x}}, & u_{i,j}^* \geq 0 \\[4mm] -u_{i,j}^* \dfrac{3\,\tau_{i,j}^* - 4\,\tau_{i+1,j}^* + \tau_{i+2,j}^*}{2\,\Delta\hat{x}}, & u_{i,j}^* < 0 \end{cases}, \tag{6.15}$$

and is evaluated at the previous time plane as indicated. Equation (6.14) leads to the following tridiagonal problem for $\tau_{i,j}$ at each $\hat{x}_i$, $i = 2,\dots,J-1$

$$c_j^- \, \tau_{i,j-1} + c_j \, \tau_{i,j} + c_j^+ \, \tau_{i,j+1} = d_j, \quad j = 2,\dots,J-1, \tag{6.16a}$$

where

$$c_j = -\frac{\Gamma^2(\hat{y}_j)}{b^2} \frac{2}{(\Delta\hat{y})^2} - \frac{1}{\Delta t}, \tag{6.16b}$$

$$c_j^- = \frac{\Gamma^2(\hat{y}_j)}{b^2} \frac{1}{(\Delta\hat{y})^2} - \frac{\Gamma(\hat{y}_j)}{b} \frac{\Gamma'(\hat{y}_j)}{b} \frac{1}{2\,\Delta\hat{y}} + \frac{\Gamma(\hat{y}_j)}{b} \frac{v_{i,j}^*}{2\,\Delta\hat{y}}, \tag{6.16c}$$

$$c_j^+ = \frac{\Gamma^2(\hat{y}_j)}{b^2} \frac{1}{(\Delta\hat{y})^2} + \frac{\Gamma(\hat{y}_j)}{b} \frac{\Gamma'(\hat{y}_j)}{b} \frac{1}{2\,\Delta\hat{y}} - \frac{\Gamma(\hat{y}_j)}{b} \frac{v_{i,j}^*}{2\,\Delta\hat{y}}, \tag{6.16d}$$

$$d_j = \frac{\Gamma(\hat{x}_i)}{a} \left(u^* \frac{\partial \tau^*}{\partial \hat{x}}\right)_{i,j} - \frac{\tau_{i,j}^*}{\Delta t}. \tag{6.16e}$$

Using pivotal condensation, a solution of the difference equations (6.16a) can be expressed as the recursive relation

$$\tau_{i,j} = R_j \, \tau_{i,j-1} + Q_j, \quad j = 2,\dots,J, \tag{6.17a}$$

where to satisfy the condition (6.10c), the coefficients at the boundary-layer edge

169

(defined by $j = J$) must satisfy

$$R_J = 0, \quad Q_J = 1, \qquad (6.17b)$$

and for $j = J-1,...,2$

$$R_j = -\frac{c_j^-}{c_j + c_j^+ R_{j+1}}, \quad Q_j = -\frac{c_j^+ Q_{j+1} - d_j}{c_j + c_j^+ R_{j+1}}. \qquad (6.17c)$$

Note that these relations are essentially an elimination procedure similar to the Thomas algorithm with equations (6.17b) and (6.17c) constituting the forward elimination in a recursive calculation to evaluate the coefficients R_j and Q_j starting at the boundary-layer edge and moving toward the wall. The back substitution portion of the algorithm in equation (6.17a) gives a recursive formula to evaluate the shear stress $\tau_{i,j}$ at the ith station starting from the wall and moving toward the boundary-layer edge. Because portions of the convective terms are evaluated at the previous time step, the difference equations are linear, and equation (6.17a) expresses $\tau_{i,j}$ in terms of the value at the mesh point immediately below, *i.e.* $\tau_{i,j-1}$. Using these relations the shear stress at any $\hat{y}_j$ for given $\hat{x}_i$ may conveniently be expressed in terms of the shear stress at the wall $\tau_{i,1}$, and it is easily shown that

$$\tau_{i,j} = C_{i,j} \tau_{i,1} + B_{i,j}, \quad j = 2,...,J, \qquad (6.18a)$$

where the arrays $C_{i,j}$ and $B_{i,j}$ are easily evaluated according to the recursion relations

$$C_{i,1} = 1, \quad B_{i,1} = 0, \qquad (6.18b)$$

$$C_{i,j} = R_j C_{i,j-1}, \quad B_{i,j} = R_j B_{i,j-1} + Q_j, \quad j = 2,...,J. \qquad (6.18c)$$

Therefore, the solution to the momentum equation for the shear stress distribution $\tau_{i,j}$

170

at the current time t may be evaluated from equation (6.18a) throughout the domain if the wall shear stress $\tau_{i,1}$ can be determined.

In order to calculate the wall shear stress, consider the interaction law (6.11). The integral in equation (6.11) may be approximated using the trapezoidal rule to give

$$b \int_0^{y_{max}} \frac{\tau - 1}{\Gamma(\hat{y})} \, d\hat{y} = \sum_{j=2}^{J} \frac{\Delta \hat{y}}{2} \left[\frac{b}{\Gamma(\hat{y}_j)} (\tau_{i,j} - 1) + \frac{b}{\Gamma(\hat{y}_{j-1})} (\tau_{i,j-1} - 1) \right]. \tag{6.19}$$

Substitution of equation (6.18a) into (6.19) gives an expression for the integral which, again, can be written in terms of the wall shear, and it is easily shown that

$$b \int_0^{y_{max}} \frac{\tau - 1}{\Gamma(\hat{y})} \, d\hat{y} = N_i \, \tau_{i,1} + M_i, \qquad \text{at } \hat{x} = \hat{x}_i, \tag{6.20a}$$

where the coefficients on the right side are given by

$$N_i = \sum_{j=2}^{J} \frac{\Delta \hat{y}}{2} \left[\frac{b}{\Gamma(\hat{y}_j)} C_{i,j} + \frac{b}{\Gamma(\hat{y}_{j-1})} C_{i,j-1} \right], \tag{6.20b}$$

$$M_i = \sum_{j=2}^{J} \frac{\Delta \hat{y}}{2} \left[\frac{b}{\Gamma(\hat{y}_j)} (B_{i,j} - 1) + \frac{b}{\Gamma(\hat{y}_{j-1})} (B_{i,j-1} - 1) \right]. \tag{6.20c}$$

Likewise, approximating $\partial \tau / \partial \hat{y}$ at $\hat{y} = 0$ in equation (6.11) by a second-order accurate forward difference, and substituting equation (6.18a) with (6.18b) produces the following expression for the shear stress gradient in terms of the wall shear stress

$$\left. \frac{\partial \tau}{\partial \hat{y}} \right|_{\hat{y}=0} = \frac{4 \, C_{i,2} - 3 - C_{i,3}}{2 \, \Delta \hat{y}} \tau_{i,1} + \frac{4 \, B_{i,2} - B_{i,3}}{2 \, \Delta \hat{y}} \qquad \text{at } \hat{x} = \hat{x}_i. \tag{6.21}$$

Equations (6.20a) and (6.21) express the relevant quantities in terms of the wall shear

stress distribution and coefficients, all of which are functions of $\hat{x}$. Therefore, substitution of (6.20a) and (6.21) into the interaction law (6.11) with second-order central difference approximations for the derivatives in $\hat{x}$ yields the following tridiagonal system for the wall shear stress:

$$\bar{c}_i^- \, \tau_{i-1,1} + \bar{c}_i \, \tau_{i,1} + \bar{c}_i^+ \, \tau_{i+1,1} = \bar{d}_i, \quad i = 2,\ldots,I-1, \tag{6.22a}$$

where

$$\bar{c}_i = \frac{\Gamma^2(\hat{x}_i)}{a^2} \frac{2\,N_i}{(\Delta\hat{x})^2} - \frac{\Gamma(0)}{b} \frac{4\,C_{i,2} - 3 - C_{i,3}}{2\,\Delta\hat{y}}, \tag{6.22b}$$

$$\bar{c}_i^- = -\frac{\Gamma^2(\hat{x}_i)}{a^2} \frac{N_{i-1}}{(\Delta\hat{x})^2} + \frac{\Gamma(\hat{x}_i)}{a} \frac{\Gamma'(\hat{x}_i)}{a} \frac{N_{i-1}}{2\,\Delta\hat{x}}$$
$$- S\,\pounds \, \frac{\Gamma(\hat{x}_i)}{a} \frac{\Gamma(0)}{b} \frac{1}{2\,\Delta\hat{x}} \frac{4\,C_{i-1,2} - 3 - C_{i-1,3}}{2\,\Delta\hat{y}}, \tag{6.22c}$$

$$\bar{c}_i^+ = -\frac{\Gamma^2(\hat{x}_i)}{a^2} \frac{N_{i+1}}{(\Delta\hat{x})^2} - \frac{\Gamma(\hat{x}_i)}{a} \frac{\Gamma'(\hat{x}_i)}{a} \frac{N_{i+1}}{2\,\Delta\hat{x}}$$
$$+ S\,\pounds \, \frac{\Gamma(\hat{x}_i)}{a} \frac{\Gamma(0)}{b} \frac{1}{2\,\Delta\hat{x}} \frac{4\,C_{i+1,2} - 3 - C_{i+1,3}}{2\,\Delta\hat{y}}, \tag{6.22d}$$

$$\bar{d}_i = \frac{\Gamma^2(\hat{x}_i)}{a^2} \frac{M_{i+1} - 2\,M_i + M_{i-1}}{(\Delta\hat{x})^2} + \frac{\Gamma(\hat{x}_i)}{a} \frac{\Gamma'(\hat{x}_i)}{a} \frac{M_{i+1} - M_{i-1}}{2\,\Delta\hat{x}} - \left.\frac{\partial^2 f}{\partial x^2}\right|_{x=x_i} + \frac{\Gamma(0)}{b} \frac{4\,B_{i,2} - B_{i,3}}{2\,\Delta\hat{y}}$$
$$- S\,\pounds \, \frac{\Gamma(\hat{x}_i)}{a} \frac{\Gamma(0)}{b} \frac{1}{2\,\Delta\hat{x}} \left[\frac{4\,B_{i+1,2} - B_{i+1,3}}{2\,\Delta\hat{y}} - \frac{4\,B_{i-1,2} - B_{i-1,3}}{2\,\Delta\hat{y}} \right]. \tag{6.22e}$$

In equation (6.22e) the second derivative of the surface contour $\partial^2 f/\partial x^2$ is assumed to be a known function of x. At any time step the coefficients in equations (6.17), (6.18) and (6.20) are evaluated first, and then the tridiagonal system (6.22) is solved for the wall shear $\tau_{i,1}$ using the Thomas algorithm subject to the boundary condition (6.10b),

172

or

$$\tau_{1,1} = \tau_{I,1} = 1. \tag{6.23}$$

The shear stress throughout the two-dimensional domain is then computed from equation (6.18) for $i = 2,...,I-1$ where again from equations (6.10b) at the streamwise boundaries of the domain

$$\tau_{1,j} = \tau_{I,j} = 1, \quad j = 2,...,J. \tag{6.24}$$

Next, the velocity components at the current time step are calculated by integrating equation (6.12) throughout the domain to obtain the streamfunction. This process requires two integrations for fixed $\hat{x}$ according to

$$\bar{u} = b \int_0^{\hat{y}} \frac{\tau}{\Gamma(\hat{y})} \, d\hat{y}, \quad \psi = b \int_0^{\hat{y}} \frac{\bar{u}}{\Gamma(\hat{y})} \, d\hat{y}, \tag{6.25a,b}$$

and these are carried out for each $\hat{x}_i$, $i = 1,...,I$ using the trapezoidal rule as follows

$$\bar{u}_{i,1} = 0, \quad \psi_{i,1} = 0, \tag{6.26a}$$

and for $j = 2,...,J$

$$\bar{u}_{i,j} = \bar{u}_{i,j-1} + \frac{\Delta\hat{y}}{2}\left[\frac{b}{\Gamma(\hat{y}_j)}\tau_{i,j} + \frac{b}{\Gamma(\hat{y}_{j-1})}\tau_{i,j-1}\right], \tag{6.26b}$$

$$\psi_{i,j} = \psi_{i,j-1} + \frac{\Delta\hat{y}}{2}\left[\frac{b}{\Gamma(\hat{y}_j)}\bar{u}_{i,j} + \frac{b}{\Gamma(\hat{y}_{j-1})}\bar{u}_{i,j-1}\right]. \tag{6.26c}$$

The next task is to evaluate the velocity components at the current time plane which will

173

be required for the next time step; these components are determined throughout the two-dimensional domain from equations (6.13) using central differences according to

$$u_{i,j} = \frac{\Gamma(\hat{y}_j)}{b} \frac{\psi_{i,j+1} - \psi_{i,j-1}}{2\,\Delta\hat{y}}, \tag{6.27a}$$

$$v_{i,j} = -\frac{\Gamma(\hat{x}_i)}{a} \frac{\psi_{i+1,j} - \psi_{i-1,j}}{2\,\Delta\hat{x}}. \tag{6.27b}$$

While determination of the pressure distribution is not necessary for continuation of the unsteady calculation, it is of physical interest and may be computed at any desired time from the shear stress at the wall as follows. Substitution of equation (6.3) with (6.6) into the interaction law (5.80c), and application of the transformation (6.8) gives

$$p = -\frac{\Gamma(\hat{x})}{a} \frac{\partial}{\partial\hat{x}} \left[b \int_0^{y_{max}} \frac{\tau - 1}{\Gamma(\hat{y})}\,d\hat{y} \right] + \frac{\partial f}{\partial x} + S\,£\,\frac{\Gamma(\hat{x})}{a} \frac{\partial p}{\partial\hat{x}}. \tag{6.28}$$

Using second-order central difference approximations for the $\hat{x}$ derivatives and substitution of (6.20a) for the integral yields the following tridiagonal system for the pressure distribution

$$\tilde{c}_i^- \, p_{i-1} + \tilde{c}_i \, p_i + \tilde{c}_i^+ \, p_{i+1} = \tilde{d}_i, \quad i = 2,\dots,I-1, \tag{6.29a}$$

where the coefficients are

$$\tilde{c}_i = -1, \tag{6.29b}$$

$$\tilde{c}_i^- = -S\,£\,\frac{\Gamma(\hat{x}_i)}{a} \frac{1}{2\,\Delta\hat{x}}, \tag{6.29c}$$

174

$$\tilde{c}_i^+ = S \, \pounds \, \frac{\Gamma(\hat{x}_i)}{a} \frac{1}{2 \, \Delta \hat{x}}, \tag{6.29d}$$

$$\tilde{d}_i = -\frac{\partial f}{\partial x} + \frac{\Gamma(\hat{x}_i)}{a} \frac{N_{i+1} \, \tau_{i+1,1} + M_{i+1} - N_{i-1} \, \tau_{i-1,1} - M_{i-1}}{2 \, \Delta \hat{x}}. \tag{6.29e}$$

The boundary conditions for a general surface shape $f(x,t)$ are

$$p_1 = \left. \frac{\partial f}{\partial x} \right|_{x \to -\infty}, \qquad p_I = \left. \frac{\partial f}{\partial x} \right|_{x \to +\infty}, \tag{6.30}$$

which for the compression ramp become

$$p_1 = 0, \qquad p_I = \alpha, \tag{6.31}$$

where α is the ramp angle. As before, the Thomas algorithm was used to solve the tridiagonal system (6.29) with the conditions (6.31) for the pressure distribution at each time step for which it was desired.

Finally, the stability of the numerical algorithm described above is considered. A standard von Neumann analysis of the linearized discretization of the momentum equation (6.14) is given in appendix D and leads to the Courant-Friedrichs-Lewy criterion, modified due to the finite-domain transformation (6.8), for stability of the numerical scheme, namely

$$\Delta t \le \frac{a}{\Gamma(\hat{x})} \frac{\Delta \hat{x}}{2 \, |u_{\max}|}. \tag{6.32}$$

From the definition (6.9e) of Γ, the maximum value of Γ is $2/\pi$ which occurs when $\hat{x} = 0$; therefore, the stability criterion may be written as

175

$$\Delta t \leq \frac{\pi \, a \, \Delta \hat{x}}{4 \, |u_{\max}|}. \tag{6.33}$$

Recall that $u \sim y + A$ for $y \to \infty$; therefore, the maximum streamwise velocity $u_{\max}$ is roughly equal to the normal coordinate $y_{\max}$ at which the domain is truncated. The stability condition (6.33), therefore, restricts the time step for a given choice of the mesh.

6.3 Stability Analysis

In addition to stability of the numerical algorithm, the work of Tutty and Cowley (1986), as well as the results for the first interactive stage of unsteady separation discussed in part I, suggest the possibility of an instability within the triple-deck formulation itself. Therefore, a linear stability analysis will be given in order to determine the criteria for a possible instability. The exact solution to the hypersonic triple-deck problem (5.80) is here denoted by subscript zero, and infinitesimal harmonic disturbances are introduced where $\varepsilon \ll 1$. As found in the previous studies, it is expected that an instability would be of the inviscid type with short wavelengths (high frequencies) compared with the interaction length and time scales; therefore, the wavenumber α is large. Introducing normal modes as in §3.5

$$u = u_0(x,y,t) + \varepsilon \, e^{i(\alpha x - \alpha c t)} \, u_1(x,y,t) + \cdots, \tag{6.34a}$$

$$v = v_0(x,y,t) + \varepsilon \, e^{i(\alpha x - \alpha c t)} \, \alpha \, v_1(x,y,t) + \cdots, \tag{6.34b}$$

$$p = p_0(x,t) + \varepsilon \, e^{i(\alpha x - \alpha c t)} \, p_1(x,t) + \cdots, \tag{6.34c}$$

$$A = A_0(x,t) + \varepsilon \, e^{i(\alpha x - \alpha c t)} \, A_1(x,t) + \cdots, \tag{6.34d}$$

176

where α is real, and $c = c_r + i c_i$ is the complex wavespeed. If $c_i > 0$, a small disturbance becomes unstable.

Substituting (6.34) into the momentum and continuity equations (5.80a,b), the $O(1)$ terms are satisfied by the exact solution, and the $O(\varepsilon\alpha)$ terms $(O(\varepsilon\alpha) > O(\varepsilon))$ give the long-wave Rayleigh equation, namely

$$i\,(u_0 - c)\,u_1 + v_1\,\frac{\partial u_0}{\partial y} = -\,i\,p_1, \qquad (6.35\text{a})$$

$$i\,u_1 + \frac{\partial v_1}{\partial y} = 0. \qquad (6.35\text{b})$$

Substituting equation (6.35b) into (6.35a) and rearranging yields the first-order linear equation for v_1

$$\frac{\partial v_1}{\partial y} - \frac{\partial u_0/\partial y}{u_0 - c}\,v_1 = \frac{i\,p_1}{u_0 - c}. \qquad (6.36)$$

This equation may be solved using the integrating factor $(u_0 - c)^{-1}$ to give

$$v_1 = (u_0 - c)\left\{-i\,p_1 \int_y^\infty \frac{dy}{(u_0 - c)^2} + g(x,t)\right\}. \qquad (6.37)$$

Differentiating with respect to y produces

$$\frac{\partial v_1}{\partial y} = \frac{\partial u_0}{\partial y}\left\{-i\,p_1 \int_y^\infty \frac{dy}{(u_0 - c)^2} + g(x,t)\right\} + \frac{i\,p_1}{u_0 - c}. \qquad (6.38)$$

Substitution of (6.34c,d) into the interaction condition (5.80c) and retaining $O(\varepsilon\alpha)$ terms requires that

177

$$A_1 - S\,£\,p_1 = 0. \tag{6.39}$$

Similarly, to satisfy condition (5.80d) for v requires

$$v_1 = 0 \quad \text{at} \quad y = 0, \tag{6.40}$$

and condition (5.80f) with continuity (6.35b) gives the condition

$$u_1 = -\frac{1}{i}\frac{\partial v_1}{\partial y} \to A_1 \quad \text{as} \quad y \to \infty. \tag{6.41}$$

Therefore, recalling that $u_0 \to \infty$ and $\partial u_0/\partial y \to 1$ as $y \to \infty$, the result (6.38) subject to the condition (6.41) yields

$$g(x,t) = -\,i\,A_1(x,t). \tag{6.42}$$

Thus, the solution (6.37) becomes

$$v_1 = -\,i\,(u_0 - c)\left\{ p_1 \int_y^\infty \frac{dy}{(u_0 - c)^2} + A_1 \right\}. \tag{6.43}$$

Applying the condition (6.40) to (6.43) gives

$$p_1 \int_0^\infty \frac{dy}{(u_0 - c)^2} = -\,A_1, \tag{6.44}$$

which from (6.39) becomes

$$\int_0^\infty \frac{dy}{(u_0 - c)^2} = -\,S\,£. \tag{6.45}$$

178

Because of the form (5.80f) of u_0 as $y \to \infty$, the eigenvalue relation (6.45) is rewritten in the form

$$\int_0^\infty \frac{1 - \partial u_0 / \partial y}{(u_0 - c)^2} \, dy - \frac{1}{c} = -S \, \pounds. \tag{6.46}$$

Application of the finite-domain transformation (6.8b) with the transformation law (6.9c) to this equation gives the eigenrelation

$$\int_0^1 \frac{\dfrac{b}{\Gamma(\hat{y})} - \dfrac{\partial u_0}{\partial \hat{y}}}{(u_0 - c)^2} \, d\hat{y} - \frac{1}{c} = -S \, \pounds, \tag{6.47}$$

where $\Gamma(\hat{y})$ is defined by (6.9e). Therefore, for a given velocity profile $u_0(\hat{y})$ and level of wall cooling $S \, \pounds$, the complex wavespeed c must be determined such that the eigenrelation (6.47) is satisfied. The flow is unstable to small disturbances if $c_i > 0$.

In order to gain additional physical insight into the flow conditions necessary for an instability, it is instructive to apply the steps of the proofs of Rayleigh's and Fjørtoft's classical theorems for inviscid flows (see, for example, Drazin and Reid, 1981) to the present case. Returning to the linear equation (6.36) for v_1, differentiating with respect to y and multiplying by the complex conjugate of v_1, denoted by v_1^*, gives

$$v_1^* \frac{\partial^2 v_1}{\partial y^2} - \frac{\partial^2 u_0}{\partial y^2} \frac{|v_1|^2}{u_0 - c} = 0, \tag{6.48}$$

where the fact that $v_1^* v_1 = |v_1|^2$ was used. Integrating equation (6.48) from 0 to y and evaluating the first term using integration by parts yields

179

$$\int_0^y \left\{ \left| \frac{\partial v_1}{\partial y} \right|^2 + \frac{\partial^2 u_0}{\partial y^2} \frac{|v_1|^2}{u_0 - c} \right\} dy = \left[v_1^* \frac{\partial v_1}{\partial y} \right]_0^y. \tag{6.49}$$

Taking $y \to \infty$ and evaluating the right hand side of (6.49) using the boundary conditions (6.40) and (6.41) with the interaction condition (6.39) leads to

$$\int_0^\infty \left\{ \left| \frac{\partial v_1}{\partial y} \right|^2 + \frac{\partial^2 u_0}{\partial y^2} \frac{|v_1|^2}{u_0 - c} \right\} dy = -i \, v_1^* \, S \, \pounds \, p_1. \tag{6.50}$$

But from the solution (6.43) for v_1, equation (6.39) and the condition $u_0 \to y + A_0 + \cdots$ as $y \to \infty$

$$v_1 \to -i \, (y + A_0 - c) \, S \, \pounds \, p_1 \quad \text{as} \quad y \to \infty. \tag{6.51}$$

Taking the complex conjugate of (6.51) and substituting for v_1^* in equation (6.50) gives

$$\int_0^\infty \left\{ \left| \frac{\partial v_1}{\partial y} \right|^2 + \frac{\partial^2 u_0}{\partial y^2} \frac{|v_1|^2}{u_0 - c} \right\} dy = (y + A_0 - c^*) \, (S \, \pounds)^2 \, |p_1|^2. \tag{6.52}$$

Recognizing that $(u_0 - c)^{-1} = (u_0 - c)^* [(u_0 - c) (u_0 - c)^*]^{-1} = (u_0 - c^*) |u_0 - c|^{-2}$ and rearranging, equation (6.52) becomes

$$\int_0^\infty \left\{ \left| \frac{\partial v_1}{\partial y} \right|^2 - (S \, \pounds)^2 |p_1|^2 + \frac{\partial^2 u_0}{\partial y^2} \frac{u_0 - c^*}{|u_0 - c|^2} |v_1|^2 \right\} dy = (A_0 - c^*) \, (S \, \pounds)^2 \, |p_1|^2. \tag{6.53}$$

Taking the imaginary part of this equation yields

180

$$\int_0^\infty \frac{\partial^2 u_0}{\partial y^2} \frac{|v_1|^2}{|u_0 - c|^2} \, dy = (S \, \pounds)^2 |p_1|^2, \tag{6.54}$$

and when $S \, \pounds = 0$, therefore, $\partial^2 u_0/\partial y^2$ must change sign somewhere in the interval $0 < y < \infty$ in order for the flow to become unstable. In other words, the velocity profile $u_0(y)$ must have an inflection point. This is Rayleigh's theorem for instabilities in inviscid flows. On the other hand, when $S \, \pounds \neq 0$, an instability can only occur if $\partial^2 u_0/\partial y^2 > 0$ for at least part of the interval $0 < y < \infty$. This condition replaces Rayleigh's theorem when the cold wall case is considered. Now taking the real part of equation (6.53) produces

$$\int_0^\infty \left\{ \left|\frac{\partial v_1}{\partial y}\right|^2 - (S \, \pounds)^2 |p_1|^2 + \frac{\partial^2 u_0}{\partial y^2} \frac{u_0 - c_r}{|u_0 - c|^2} |v_1|^2 \right\} dy = (A_0 - c_r)(S \, \pounds)^2 |p_1|^2. \tag{6.55}$$

For the case without wall cooling ($S \, \pounds = 0$), in which an inflection point is a necessary condition, $u_0(y_{ip})$ is defined to be the velocity at the inflection point y_{ip}, and the expression

$$[c_r - u_0(y_{ip})] \int_0^\infty \frac{\partial^2 u_0}{\partial y^2} \frac{|v_1|^2}{|u_0 - c|^2} \, dy = 0 \tag{6.56}$$

is added to the left hand side of (6.55) to obtain

$$\int_0^\infty \frac{\partial^2 u_0}{\partial y^2} \frac{u_0 - u_0(y_{ip})}{|u_0 - c|^2} |v_1|^2 \, dy = - \int_0^\infty \left|\frac{\partial v_1}{\partial y}\right|^2 dy. \tag{6.57}$$

Therefore, Fjørtoft's theorem for inviscid flows is reproduced when $S \, \pounds = 0$ which states that a necessary condition for instability is that

181

$$\frac{\partial^2 u_0}{\partial y^2} \left[u_0(y) - u_0(y_{ip}) \right] < 0 \qquad\qquad (6.58)$$

somewhere in the flow field where y_{ip} is the location of the inflection point. Unfortunately, a generalization of Fjørtoft's theorem is not evident from (6.55) for flows involving wall cooling ($S \, \pounds \neq 0$). In summary, in order for an instability to occur in the hypersonic triple-deck formulation without wall cooling, Rayleigh's and Fjørtoft's criteria must be met. And for the cold wall case, $\partial^2 u_0/\partial y^2 > 0$ must be true across at least part of the viscous sublayer. Note that these conditions are necessary, but not sufficient, for the occurrence of an instability, while the condition (6.46) (or (6.47)) is both necessary and sufficient.

6.4 Calculated Results

In this section detailed numerical solutions of the hypersonic triple deck as formulated in §6.2 will be considered. For the reasons discussed in §5.3, the compression ramp geometry has been considered here. However, a slight modification to the surface geometry was made. Observe from equation (6.22) of the numerical algorithm that the surface shape $f(x,t)$ enters the algorithm as a second-derivative with respect to x. But when the slope of $f(x,t)$ is discontinuous, as for the true compression ramp (5.82), the second-derivative of $f(x,t)$ contains a delta function, and this necessitates special treatment at the corner (see Rizzetta *et al.*, 1978 and Brown *et al.*, 1990). In order to keep the present algorithm general for various surface shapes $f(x,t)$, the corner was rounded slightly so that $\partial^2 f/\partial x^2$ was a smooth function everywhere. Here, the surface shape was defined by

$$f(x) = \frac{1}{2}\, \alpha \left[x + \sqrt{x^2 + r^2} \,\right], \qquad\qquad (6.48)$$

where α is the scaled downstream ramp angle. Here, r is called the rounding

parameter, and the surface collapses to the sharp compression ramp as $r \to 0$. All results shown are for $r = 0.5$, although calculations were also carried out for other values. This value was found to eliminate the difficulties at the corner while minimizing the effect on the overall results. Generally, the value of r has a significant influence on the ramp angle at which separation first occurs; however, once separation occurs the flow development is essentially similar for all small values of r.

As discussed in §6.2, a finite value of y_{max} must be chosen at which to terminate the vertical extent of the computational domain. Numerical experimentation revealed that the solution was surprisingly insensitive to the value of y_{max}. For example, for a scaled ramp angle of $\alpha = 2.5$, there was no noticeable change in solutions having $y_{max} \geq 10$. However, due to the transformation (6.8b) used for the y coordinate, there is little advantage in minimizing y_{max} as was necessary in previous studies (see, for example, Rizzetta *et al.*, 1978). Therefore, $y_{max} = 50$ was used throughout, and the transformed $\hat{y}$ coordinate was discretized by defining a uniform mesh over the range $0 \leq \hat{y} \leq \hat{y}_{max}$ where $\hat{y}_{max}$ is related to y_{max} by equation (6.8b). Note, however, that the choice of y_{max} does effect the maximum time step which may be used as specified by the numerical stability criterion (6.33).

Here, steady-state solutions for various parameters were sought as the large time limit of unsteady calculations. The initial condition was taken to be that for a flat plate $(\alpha = 0)$ in which case $u = y$. Then at $t = 0$ the ramp angle was impulsively adjusted to its final value, and the computation marched forward in time until a steady state was reached. The unsteady numerical calculation was terminated at some large time at which $\partial \tau / \partial t$, computed using a first-order backward difference, was below a given tolerance value at each mesh point along the wall where the shear stress undergoes the most change. This tolerance was less than 5×10^{-4} in all cases. For example, this tolerance was achieved for $\alpha = 3.5$ at approximately $t = 180$ and at earlier times for smaller α.

6.4.1 No Wall Cooling: $S\,£ = 0$

Recall from §5.2.8 that the hypersonic triple-deck formulation with $S\,£ = 0$ reduces to that for a supersonic external flow. Therefore, the results shown here apply equivalently to flows with supersonic mainstreams and hypersonic flows in regions of weak global interaction ($\chi \ll 1$) and high wall temperatures ($g_w^{n+1/2} \gg M_\infty^{1/2} Re_0^{-1/8}$). This case was considered initially in the present investigation in order to verify the algorithm through comparison with previously published results since the supersonic flow over a compression ramp on triple-deck scales has been considered by Rizzetta, Burggraf and Jenson (1978), Ruban (1978) and Smith and Khorrami (1991). In doing so, however, a new phenomenon was observed in large ramp-angle flows which has not previously been documented.

The flow for small ramp angles was considered by Rizzetta *et al.* (1978) and has been repeated here. The pressure and wall shear distributions for a range of small ramp angles are shown in figure 6.1a and figure 6.1b, respectively. Calculations were carried out for a number of mesh sizes, and the results shown are believed to be grid independent. In this and subsequent figures, the finest mesh sizes used are shown in the captions along with the stretching factors a and b in the transformation (6.8); note that smaller values of a and b mean that in physical space progressively more mesh points are packed near the corner and wall, respectively. The pressure tends to zero as $x \rightarrow -\infty$ and tends to the reduced ramp angle α as $x \rightarrow \infty$. Likewise, the scaled wall shear tends to one as $|x| \rightarrow \infty$. Reversed flow occurs adjacent to the surface when the wall shear becomes negative, and Rizzetta *et al.*(1978) found that this first occurs for $\alpha = 1.57$. In the present results, incipient separation first occurs at a slightly higher ramp angle, $\alpha = 1.9$ to two significant figures, and this is due to the rounding of the corner in the present calculations. As the ramp angle is increased, the recirculating-flow region grows in extent, and a constant pressure plateau forms in the pressure distribution in the center of this region. Streamlines are shown for several cases involving separation ($\alpha = 2.0$, 2.5, 3.0 and 3.5) in figures 6.2, 6.3, 6.4 and 6.5

184
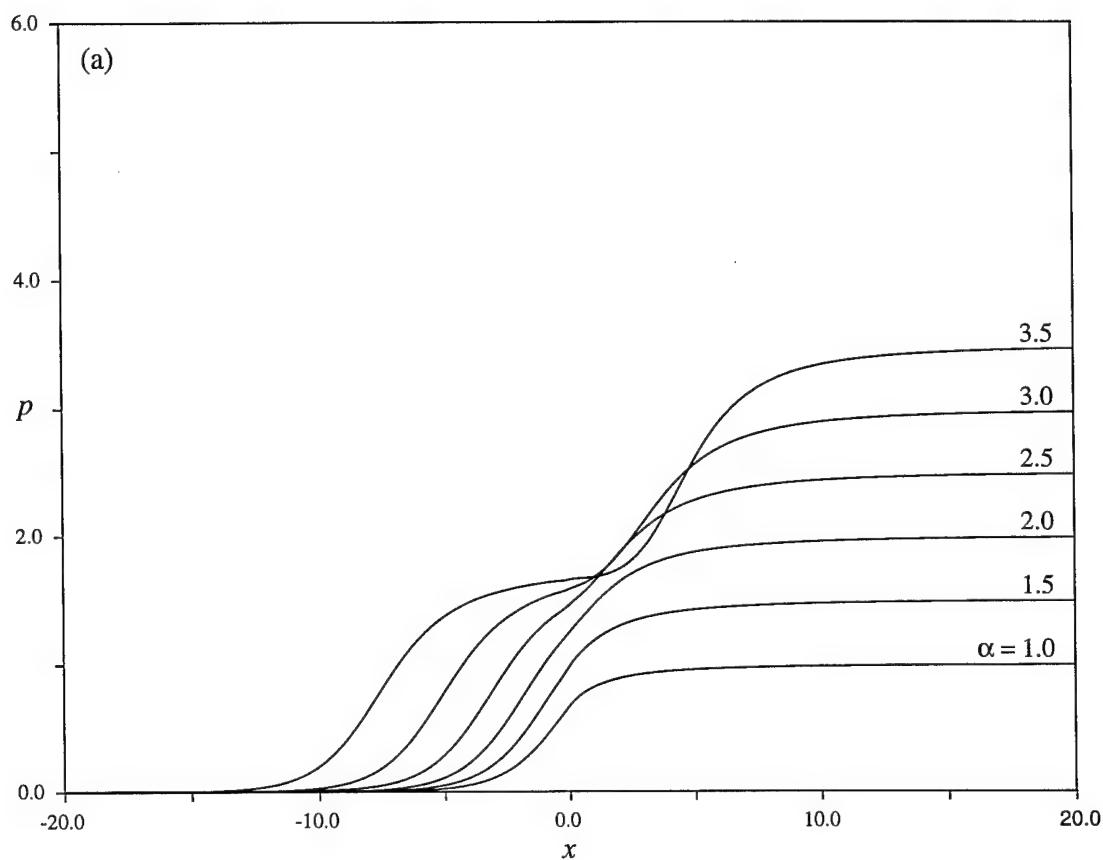
(a) Pressure p.

Figure 6.1 - Numerical solutions for various small ramp angles α:
$I = 101$, $J = 51$ and $a = b = 5.0$ for $\alpha = 1.0$, 1.5;
$I = 201$, $J = 101$ and $a = b = 5.0$ for $\alpha = 2.0$, 2.5, 3.0,
3.5.
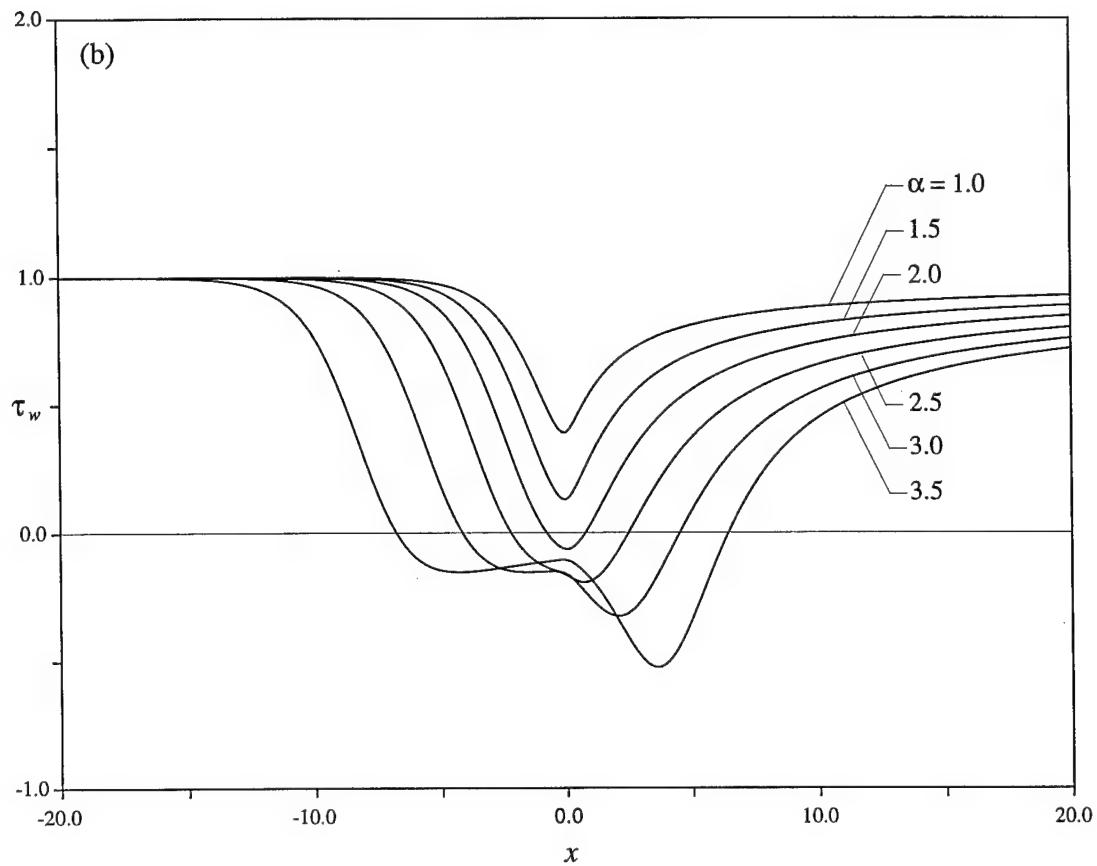
(b) Wall shear stress τ_w.

Figure 6.1 - Continued.

186
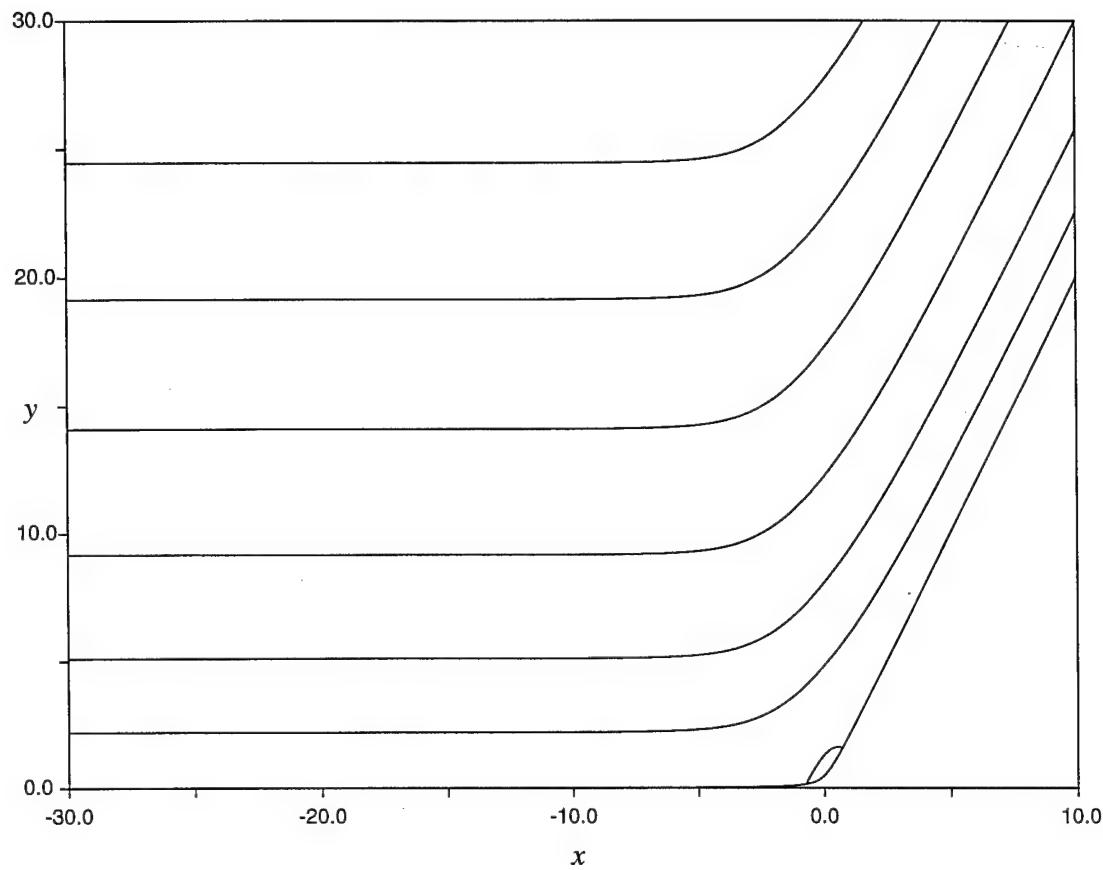
Figure 6.2 - Streamlines for $\alpha = 2.0$ with $I = 201$, $J = 101$
and $a = b = 5.0$.

187
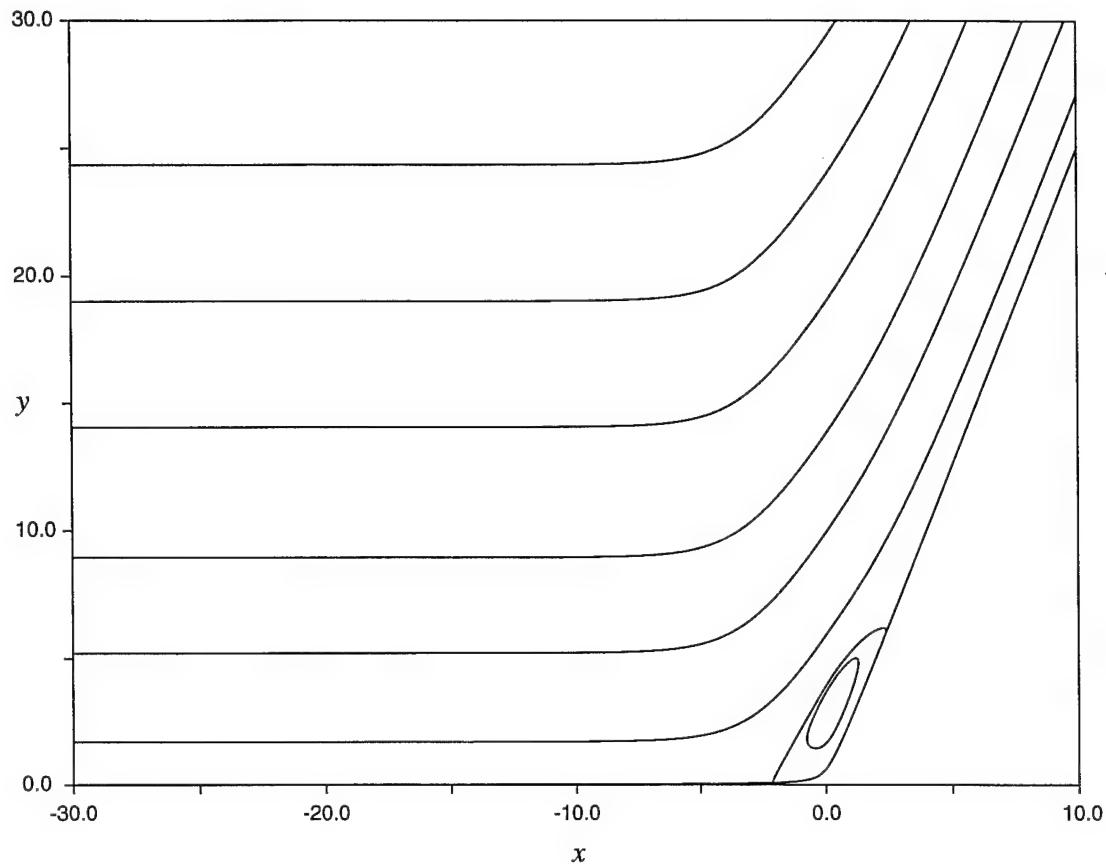
Figure 6.3 - Streamlines for $\alpha = 2.5$ with $I = 201$, $J = 101$
and $a = b = 5.0$.

188
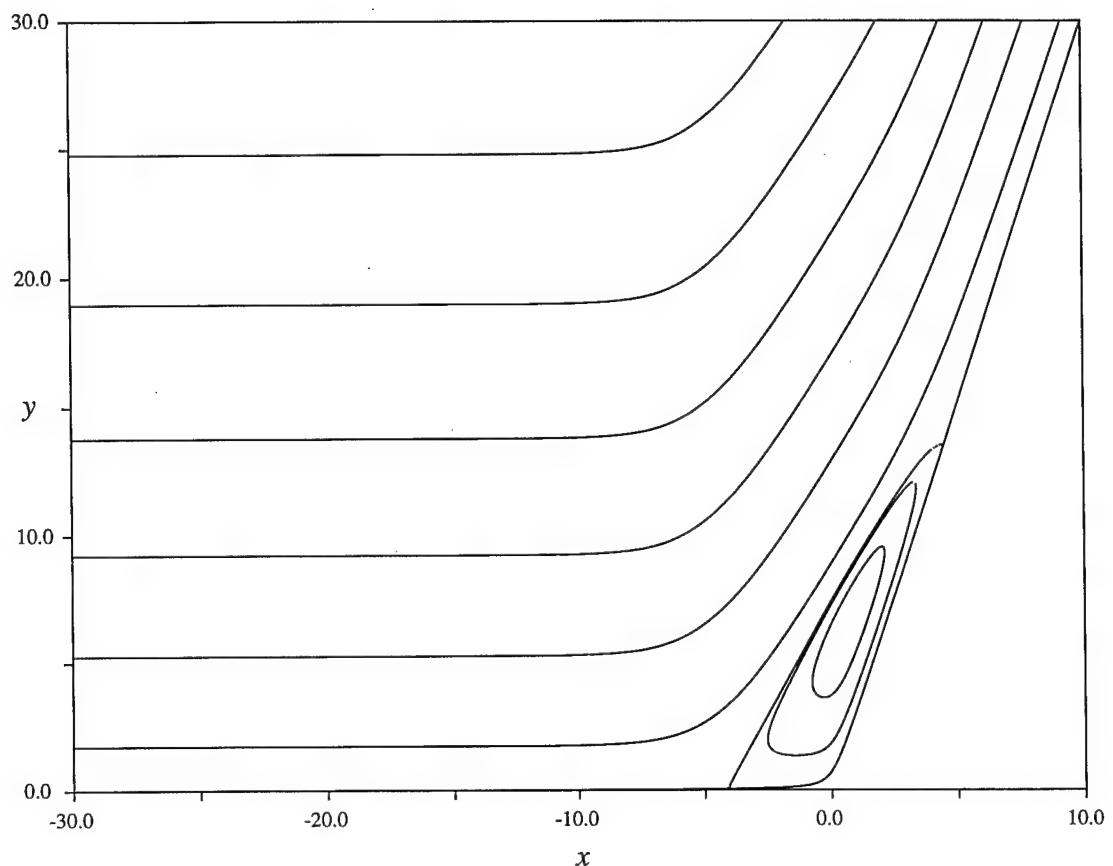
Figure 6.4 - Streamlines for $\alpha = 3.0$ with $I = 201$, $J = 101$
and $a = b = 5.0$.

189
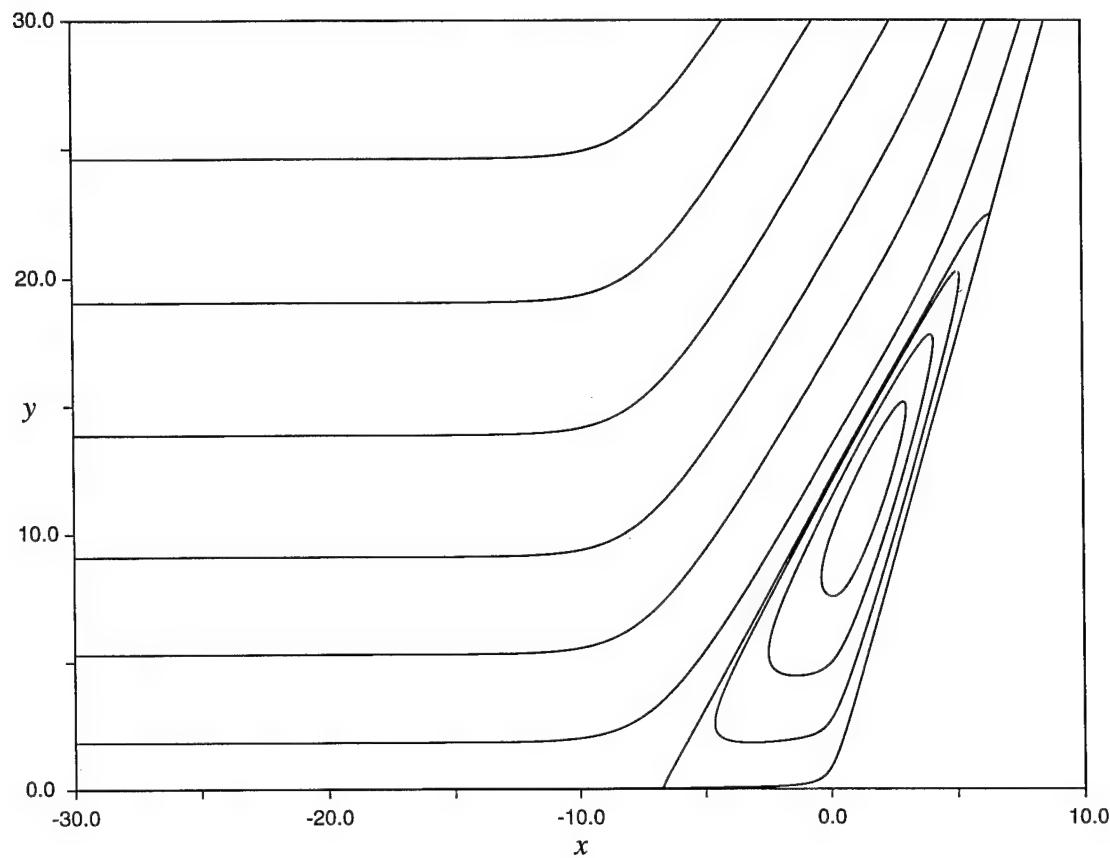
Figure 6.5 - Streamlines for $\alpha = 3.5$ with $I = 201$, $J = 101$
and $a = b = 5.0$.

190

illustrating the growth in the region of recirculation with increasing ramp angle. Note that the separation point moves progressively upstream with increasing α, but that the reversed-flow region expands more rapidly downstream.

The present results for small ramp angles are in good agreement with the results obtained in previous investigations. They compare well with the results of Rizzetta *et al.* (1978) for $\alpha \leq 2.5$, but for larger ramp angles, the current results reveal a reversed-flow region having smaller streamwise and normal extent than that observed by Rizzetta *et al.* (1978), and the present results are in better agreement with the results of Ruban (1978) for $\alpha = 3.0$ and Smith and Khorrami (1991) for $\alpha = 3.5$. Rizzetta *et al.* (1978) also showed that the triple-deck solutions agree well with the experimental results of Lewis, Kubota and Lees (1968) and with finite Reynolds number interacting boundary-layer theory (see also Burggraf *et al.*, 1979).

For cases involving separation, the rise in pressure and the drop in wall shear from their upstream values each have invariant shape, with origin at the separation point where $\tau_w = 0$, as the ramp angle is increased. This corresponds to the free interaction considered experimentally by Chapman, Kuehn and Larsen (1957) and theoretically by Stewartson and Williams (1969). Increasing the strength of the disturbance, in this case the compression ramp, beyond a certain level does not change the flow approaching the reversed-flow region except to shift the separation point upstream. This was clearly illustrated in the numerical solutions obtained by Ruban (1978) who plotted the results for several cases involving separation with origin at the separation point.

The steady solutions obtained by Smith and Khorrami (1991) for larger ramp angles ($\alpha \geq 3.5$) reveal a continuation of the trends observed at lower ramp angles. As observed in figure 6.1b, the minimum in wall shear drops below zero with increasing ramp angle, and eventually the wall shear at the corner ($x = 0$) begins to rise as the ramp angle is increased above $\alpha = 3.0$ apparently anticipating secondary separation at the corner. Indeed, the numerical results of Smith and Khorrami show secondary

191

separation ($\tau_w > 0$) at the corner for $\alpha \geq 4.5$ and a corresponding drop in pressure just downstream of the pressure plateau prior to a subsequent rise to the downstream ramp pressure. As the ramp angle is increased further, there is a pronounced decrease in the wall shear minimum and increase in the pressure gradient maximum just upstream of the reattachment point. Smith and Khorrami (1991) showed that in the steady solution, the wall shear and pressure gradient become singular at some large α. The form of this singularity was determined by Smith (1988a) and is described in §5.4.1.

The present results, however, suggest that the unsteady flow becomes unstable for large ramp angles in the form of a stationary wave packet at ramp angles well below the larger angles considered by Smith and Khorrami (1991). Recall from §6.3 that Rayleigh's and Fjørtoft's theorems are necessary conditions for an instability to occur in the case without wall cooling. These criteria are satisfied when a velocity profile develops an inflection point such that the curvature of the velocity profile $\partial^2 u/\partial y^2$ is negative below the inflection point and positive above it. It was found that to two significant figures the flow is free of inflectional velocity profiles for $\alpha \leq 3.8$, but that inflection points first form for $\alpha = 3.9$ near the surface in velocity profiles immediately downstream of the corner. This critical value was determined by evaluating $\partial^2 u/\partial y^2$, using a second-order central difference, from the steady solutions for various ramp angles. As the ramp angle is increased (ramp angles up to $\alpha = 5.0$ were considered here), the inflection point subsequently moves away from the surface, and there is an expanding streamwise range near $\hat{x} = 0$ over which inflectional profiles appear. Using sufficiently refined grids, the numerical solutions did indeed become unstable for $\alpha \geq 3.9$ at the streamwise location where the velocity profiles are inflectional. Velocity profiles are shown at the corner ($x = 0$) for three different ramp angles ($\alpha = 3.5$, 3.9 and 4.5) in figure 6.6. Here, coarse meshes ($I = 101, J = 51$) were used for $\alpha = 3.9$ and 4.5 in order to suppress the instability. The velocity profile for $\alpha = 3.5$ shows that reversed flow can occur in the corner of the compression ramp without the appearance of inflection points. This is in contrast to the hump geometries considered by Kazakov (1985), Duck (1985) and Tutty and Cowley (1986). In these

192
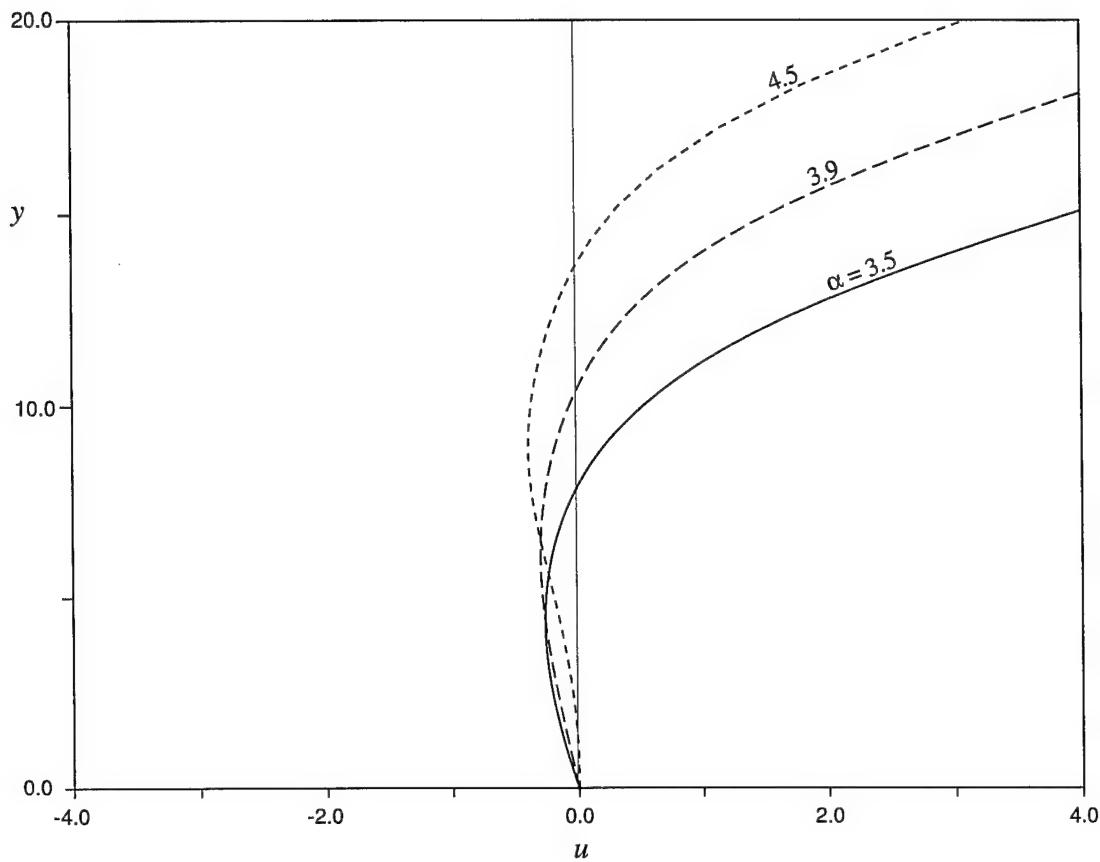
Figure 6.6 - Streamwise velocity profiles at $x = 0$ for $\alpha = 3.5$ (————),
$\alpha = 3.9$ (– – – – –) and $\alpha = 4.5$ (----------).

studies triple-deck solutions were found (using various interaction conditions) for the flow over smooth humps of various heights for which separation occurs on the downstream side of the hump for large enough hump heights. In their results, however, inflection points were found to appear in velocity profiles for hump heights smaller than that necessary for reversed flow. Observe from figure 6.6 that as the ramp angle is increased, the magnitude of the reversed-flow velocity adjacent to the surface decreases, and the lower portion of the velocity profile straightens out prior to formation of an inflection point. For $\alpha = 3.9$ the inflection point near $y = 0$ (from evaluation of $\partial^2 u/\partial y^2$) is not detectable graphically, while for $\alpha = 4.5$ the inflection point has moved away from the surface and is clearly visible.

In order to further verify the existence of the instability, attempts were made to compute the eigenrelation (6.47) using the same algorithm as in part I (see appendix C). It proved difficult, however, to find $O(1)$ values of the complex wavespeed c which were clearly unstable for the ramp angles considered. In order to test the algorithm used for evaluating the integral in (6.47), the flow over the hump considered by Tutty and Cowley (1986) was recomputed, and the stability criterion (6.47) was evaluated in order to attempt to reproduce their results using the present code. The surface geometry was defined by

$$f(x) = h\, e^{-10\,x^2},\qquad\qquad (6.49)$$

and the flow was computed as for the compression ramp keeping in mind, however, that the solutions of Tutty and Cowley (1986) were obtained using the interaction condition $A = 0$ rather than the supersonic interaction condition ($p = -\partial A/\partial x$) used here. They show, for example, results for Re(c) and Im(c) for a hump of height $h = 2$ (see their figure 2a) where c was found from evaluation of the instability criterion (6.47) for velocity profiles over a range of x using a secant method. For this case Re(c) and Im(c) are $O(1)$, and their results were reproduced using the present codes. However,

for smaller hump heights close to the critical value at which Tutty and Cowley (1986) found the flow to become unstable, it proved difficult to precisely determine c. In these cases $\text{Im}(c)$ is smaller and the streamwise range of unstable profiles is much shorter. Therefore, it is believed that in the case of the compression ramp the $\text{Im}(c)$, and thus the growth rate, is small for the ramp angles considered here and is therefore difficult to determine from integration of equation (6.47). A contributing factor may also be the difference in the normal location of the inflection point in velocity profiles from the compression ramp and hump geometries as discussed above.

The instability is manifest in the form of a stationary wave packet which develops in the unsteady solution. An example is shown in figures 6.7 and 6.8 where a and b have been increased to 10.0 in order to insure that the time step is sufficiently small to avoid instability of the numerical algorithm according to equation (6.33). Figure 6.7 shows the pressure and wall shear distributions after the instability has developed for a case with $\alpha = 4.0$, and figure 6.8 shows the temporal development of the wave packet for the same case. For $\alpha \geq 3.9$ the general form of the wave packet and its streamwise location remain the same, and the results shown are representative of those for other ramp angles. The effect of mesh size on the instability is similar to that observed in part I for the first interactive stage. Sufficient resolution is required in order to reveal the instability in the numerical calculations. This is apparently why the instability has not been observed in previous investigations that computed the unsteady flow over compression ramps. Even in the present study, where the transformations (6.8) were used to concentrate grid points near the corner, no instability was observed in the numerical solutions for $3.9 \leq \alpha \leq 5.0$ where $I = 101$ and $J = 51$. In these cases the results were in good agreement with those of Smith and Khorrami (1991). As the mesh was reduced, smaller wavelength, faster growing unstable modes were admitted, and the small numerical errors introduced in the calculation were magnified causing the instability to form. For even finer meshes, the instability occurred at earlier times and evolved more rapidly due to the faster growth rates. For example, the case shown in figures 6.7 and 6.8 computed with $I = 301$ and $J = 151$ became unstable at
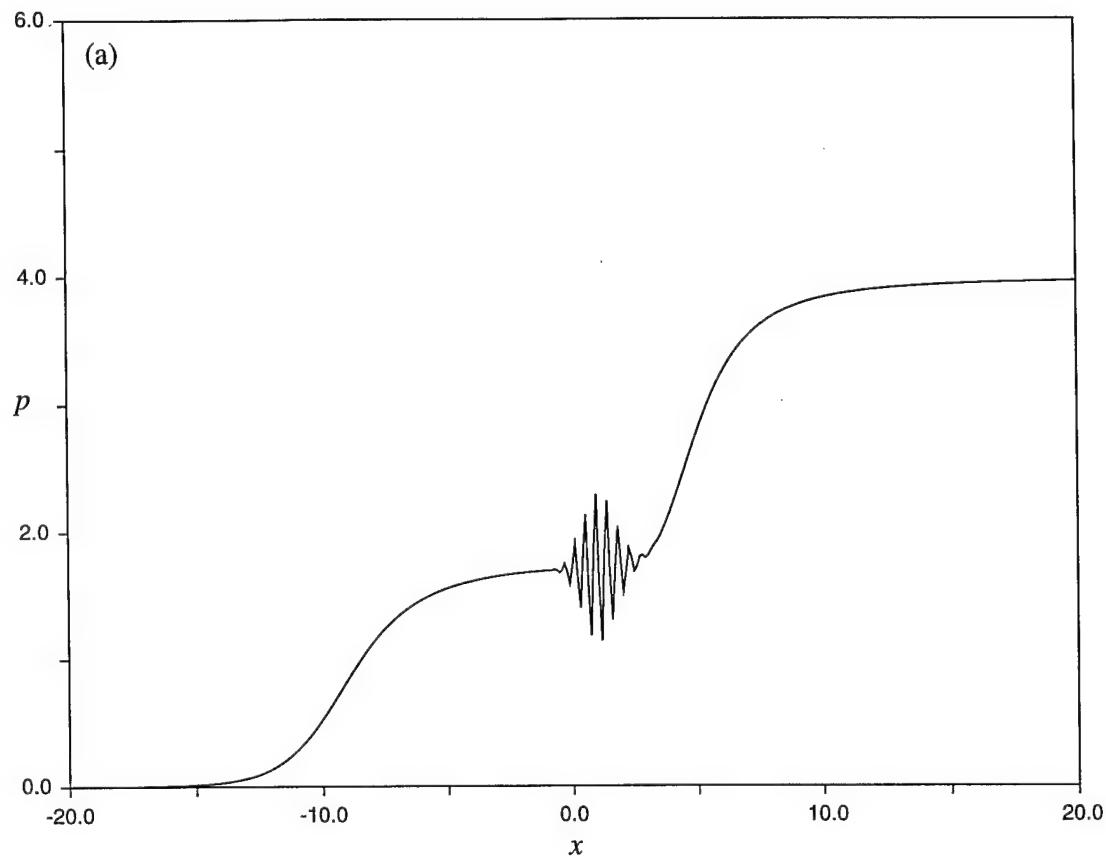
(a) Pressure p.

Figure 6.7 - Stationary wave packet for $\alpha = 4.0$ at $t = 85.0$ with $I = 301$, $J = 151$ and $a = b = 10.0$.
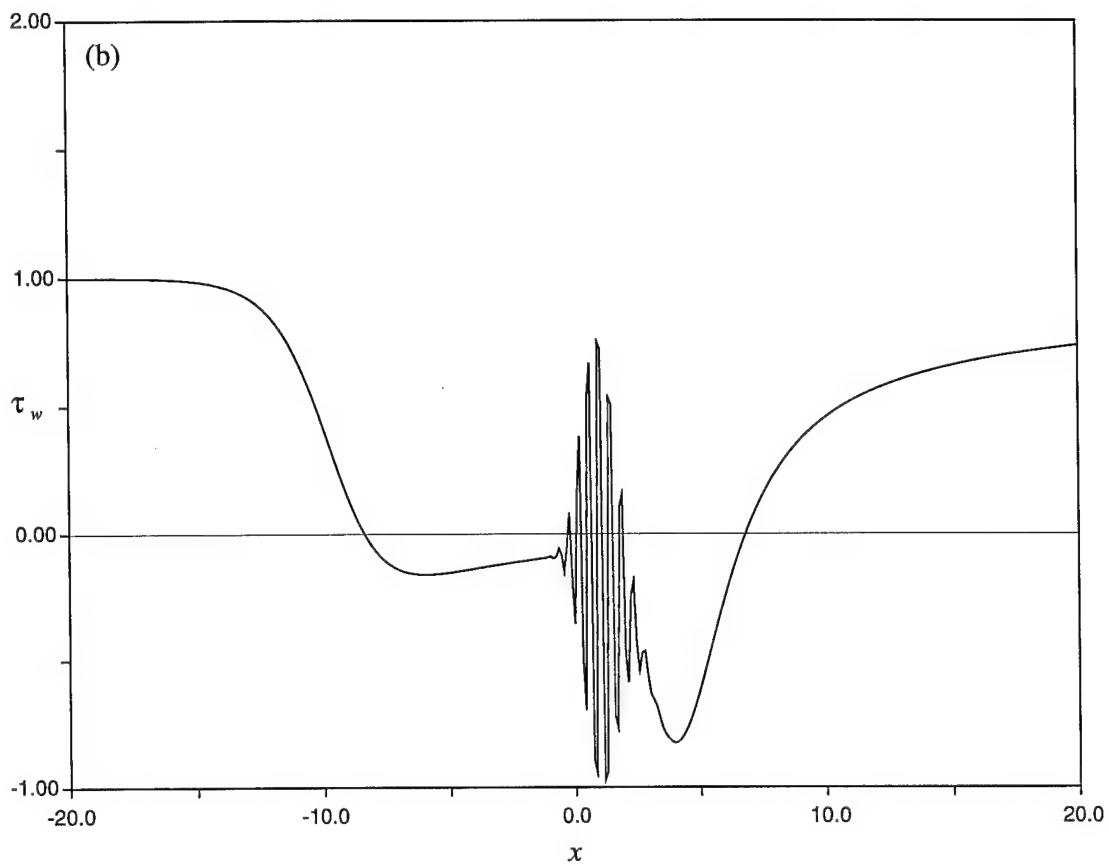
(b) Wall shear stress τ_w.

Figure 6.7 - Continued.
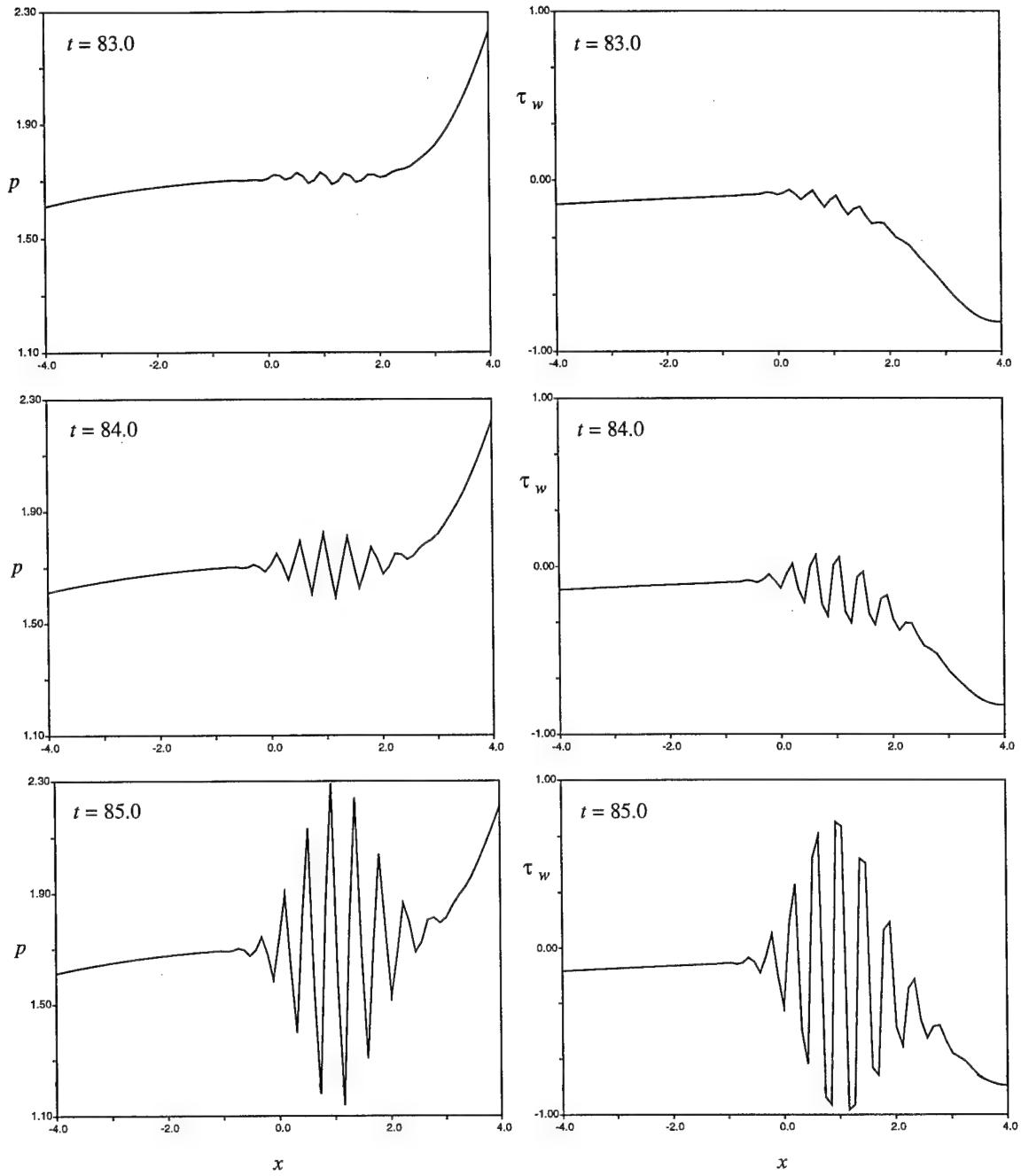
Figure 6.8 - Temporal development of wave packet in pressure p and wall shear stress τ_w (same case as in figure 6.7).

198

approximately $t = 85$, while the same case computed with $I = 201$ and $J = 101$ became unstable at about $t = 128$. The oscillations in figures 6.7 and 6.8 are basically point to point, and finer meshes produce smaller scale oscillations. In addition, reductions in time step were found to delay, but not eliminate, the onset of the instability. Although changes in the spatial mesh and time step alter the time at which the instability forms, they do not alter the streamwise extent and shape of the envelope surrounding the wave packet.

While similar instabilities have been observed in previous studies of triple-deck flows, this appears to be the first case known in which the instability was exhibited in the form of a stationary wave packet. The flow over a hump on the triple-deck scales was considered by Kazakov (1985) and Tutty and Cowley (1986) and was found to become unstable as well. In particular, both studies demonstrated that a wave packet forms downstream of a hump having sufficient height. In these cases, however, the wave packet convected downstream after formation; therefore, it is referred to as a convective instability (Drazin and Reid, 1981). The instability in that case was hypothesized by Tutty and Cowley (1986) to be responsible for the periodic eddy splitting observed downstream of the hump. One qualitative difference between the flow over a hump and the flow over a compression ramp is the normal location of the inflection point in the velocity profiles. As mentioned briefly above, the inflection point forms away from the surface in the flow over a hump, while for the compression ramp, the inflection point first forms near the surface. Whereas the inflection point is always located within the reversed-flow region in the case of a compression ramp (see figure 6.6), it is always located in a region of positive velocity in the case of a hump. More study is required in order to determine if this is an important feature distinguishing stationary and convective instabilities. The evolution of an instability for flow over an unsteady hump, again on triple-deck scales, has also been considered by Duck (1985) and Tutty and Cowley (1986). In both studies, the generation of wave packet type instabilities convecting downstream from the hump was attributed to a

high-frequency inviscid instability.

The generation and evolution of convective wave packets has been considered in several studies. Gaster and Grant (1975) studied experimentally the evolution of three-dimensional wave packets generated by an acoustic pulse within the boundary layer on a flat plate. It was shown that the three-dimensional wave packet initially grows in amplitude and expands with a smooth envelope. But as it convects downstream, non-linear effects distort and alter the smooth peaks. This was also demonstrated in the theoretical study by Ryzhov (1990). This study, as well as the work of Ruban (1988), investigated the evolution of wave packets in the framework of triple-deck theory. Additional studies (see, for example, Gaster, 1982, Jiang, 1991 and the references therein) have sought to develop theoretical models which describe the evolution of wave packets during their linear stage of development. Whereas classical stability theory only considers the stability of particular modes, these theoretical models take into account modes having a broad range of frequencies which describes the formation of wave packets. It is believed that wave packets are a precursor to the formation of turbulent spots in the transition process from laminar to turbulent flow.

6.4.2 Wall Cooling: $S \, \pounds \neq 0$

Next, the effects of wall cooling on the results discussed in the previous section were considered. In particular, the effects of wall cooling on separation and stability characteristics were of interest. Recall from §5.2 that in the present context, the term cold wall means that the wall cooling parameter $S = (\gamma - 1)^{-1/2} \lambda^{5/4} M_{\infty}^{1/2} g_w^{-(n + 1/2)} Re_0^{-1/8}$ is $O(1)$ where the wall temperature factor g_w is small. As g_w is increased, S becomes small, and the limiting case ($S = 0$) is the non-cold wall case which was considered in the previous section and which is equivalent to the classical supersonic triple deck. In that case the displacement effect of the viscous sublayer dominates over that of the main deck. On the other hand, as g_w is reduced below the critical range where S is $O(1)$, S becomes large, and the displacement effect of the main deck dominates over

200

that of the viscous sublayer. This is referred to as the strong wall cooling case and was considered by Kerimbekov, Ruban and Walker (1993) and Zhikharev (1993).

In addition to the magnitude of S, the hypersonic boundary layer with wall cooling is characterized by the sign of $\pounds$ where $\pounds$ is given by equation (5.81). When the average Mach number across the boundary layer just upstream of the interaction region is less than one, $\pounds$ is positive; this is called the subcritical case. When the average Mach number is greater than one, $\pounds$ is negative, and the boundary layer is called supercritical. For hypersonic flows, which have large mainstream Mach numbers, the supercritical case is expected to be more common in practice. Indeed, it can be shown that when viscosity depends linearly on temperature ($n = 1$), the Blasius boundary layer on a flat plate is supercritical for gases having specific heat ratio $\gamma < 2.37$ and subcritical for gases with $\gamma > 2.37$ (Zhikharev, 1993, private communications). Therefore, the boundary-layer flow of common gases, such as air, would be supercritical in most situations. However, subcritical boundary layers may occur for specialized gases or situations such as those involving dissociation or ionization. An interesting possibility arises when the average Mach number across the boundary layer is one ($\pounds = 0$) in which case the effects of wall cooling are negated (for $S = O(1)$).

Here, the wall cooling case for which $S\pounds = O(1)$ is of interest where the contributions of the viscous sublayer and main deck to the displacement thickness are of the same order; results were obtained for both subcritical and supercritical cases. Unless stated otherwise, all results shown in the remainder of this chapter were obtained on a mesh defined by $I = 201$, $J = 101$ and $a = b = 10.0$ except for cases with $\alpha = 1.0$ where the mesh was defined by $I = 101$, $J = 51$ and $a = b = 5.0$. A comprehensive set of numerical results with various levels of wall cooling for a series of ramp angles is shown in figures 6.9 through 6.17. Figures 6.9, 6.10, 6.11, 6.12 and 6.13 show pressure and wall shear distributions for a range of both subcritical and supercritical $S\pounds$ for $\alpha = 1.0$, 2.0, 3.0, 4.0 and 5.0, respectively. Note that for $\alpha \geq 2.0$, some cases have been omitted; these are cases for which the solutions became unstable
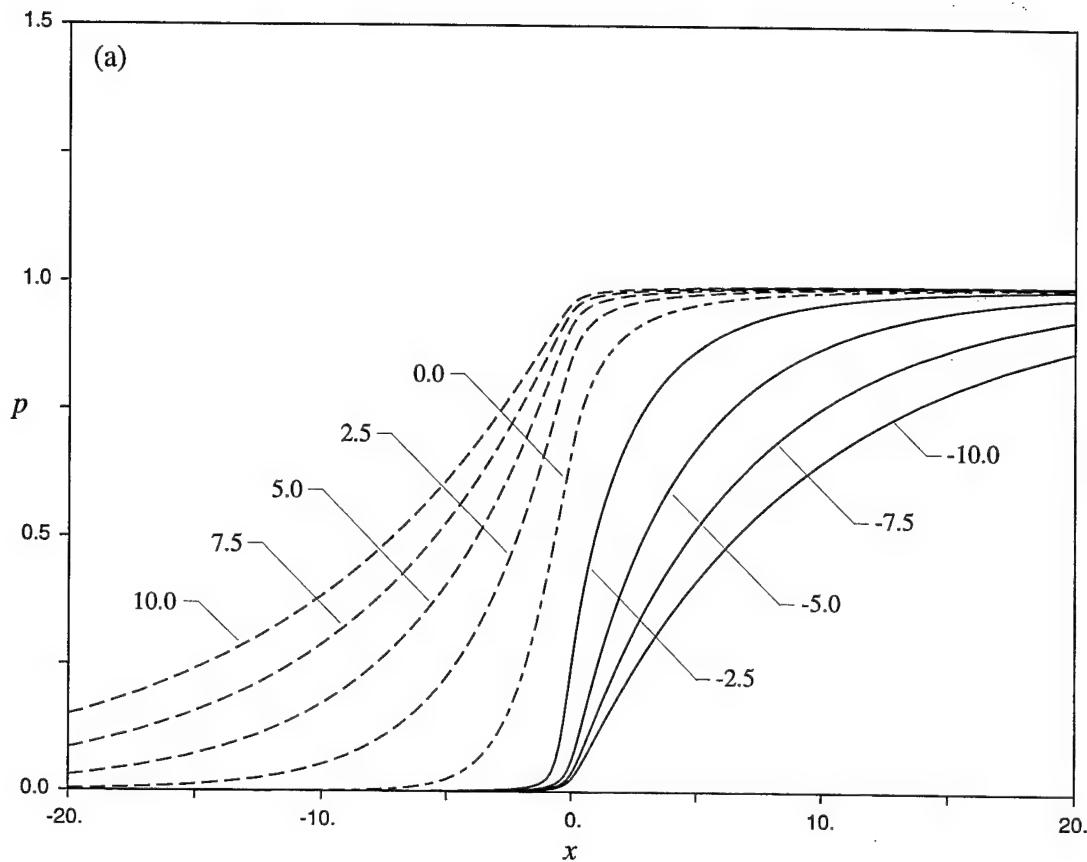
(a) Pressure p.

Figure 6.9 - Numerical solutions for $\alpha = 1.0$ with various levels of wall
cooling; $S \pounds = -10.0,...,10.0$ in increments of 2.5: no wall
cooling (– - – - – - –), subcritical boundary layer (– – – – –)
and supercritical boundary layer (————).
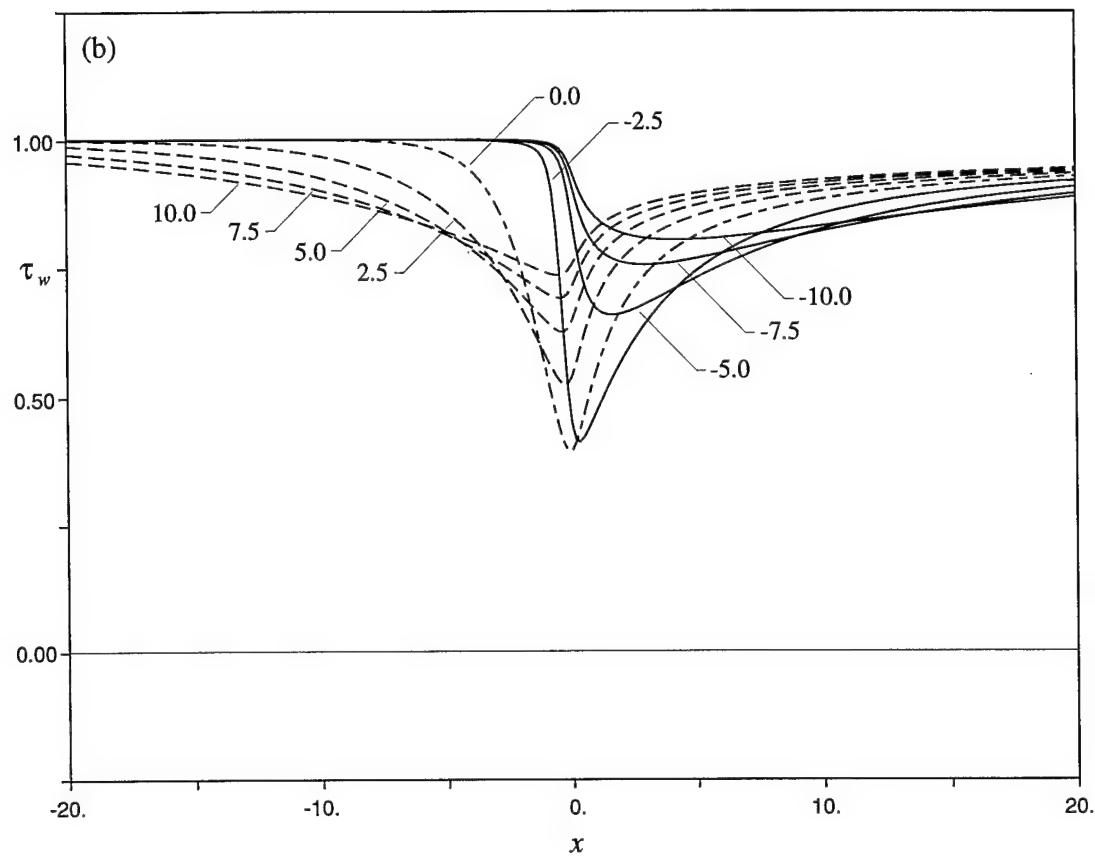
(b) Wall shear stress τ_w.

Figure 6.9 - Continued.
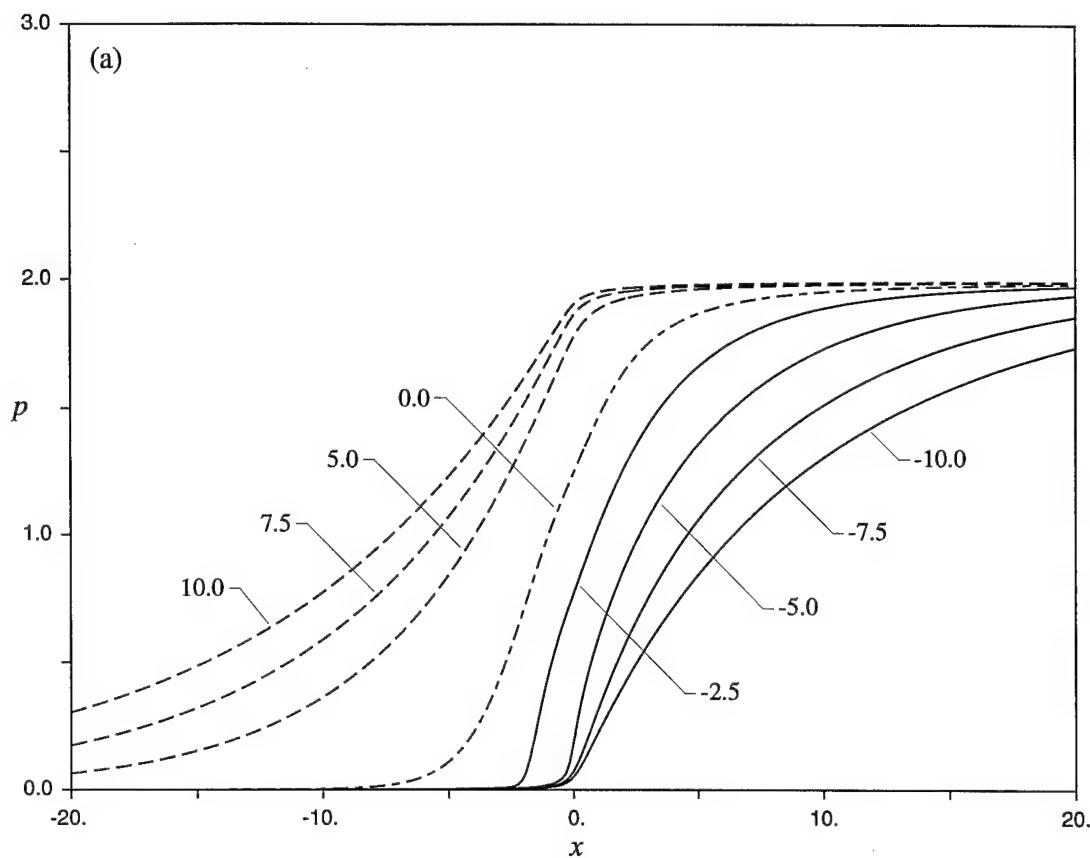
(a) Pressure p.

Figure 6.10 - Numerical solutions for $\alpha = 2.0$ with various levels of wall cooling; $S\,\pounds = -10.0,...,\,10.0$ in increments of 2.5 (case not shown was unstable): no wall cooling (– – – – – –), subcritical boundary layer (– – – – –) and supercritical boundary layer (————).
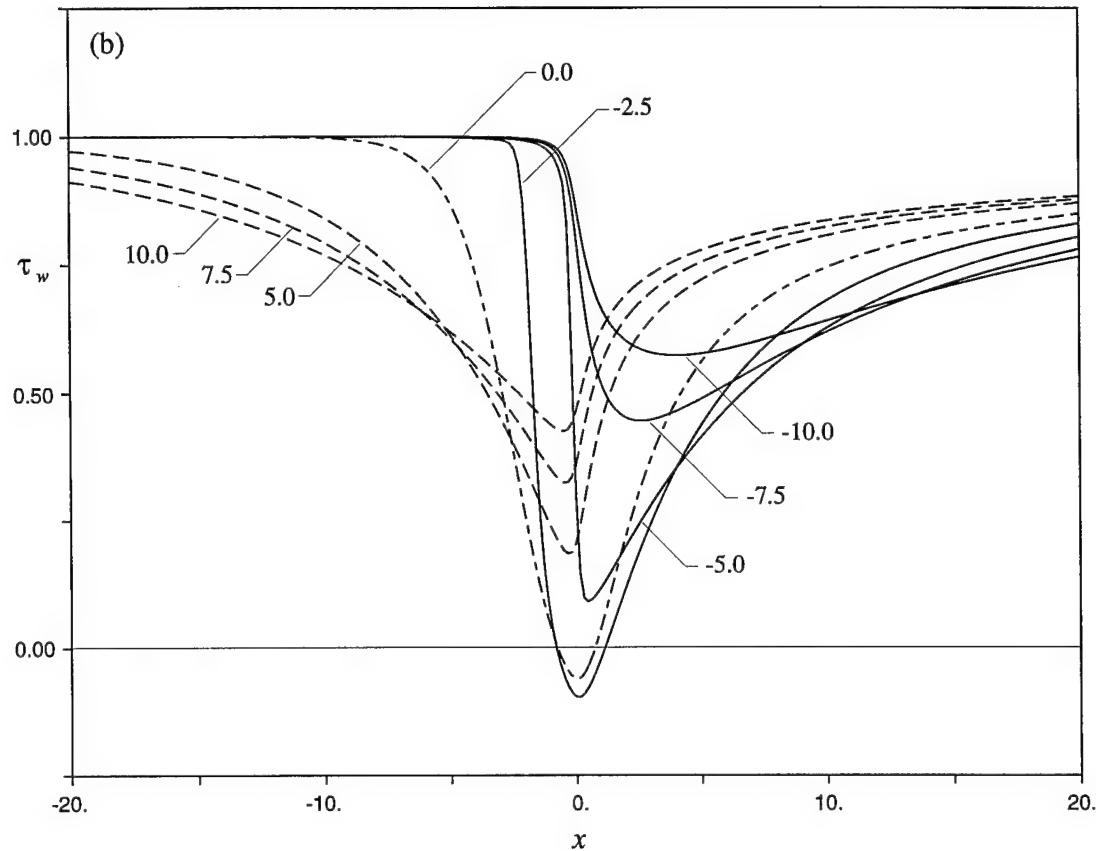
(b) Wall shear stress τ_w.

Figure 6.10 - Continued.
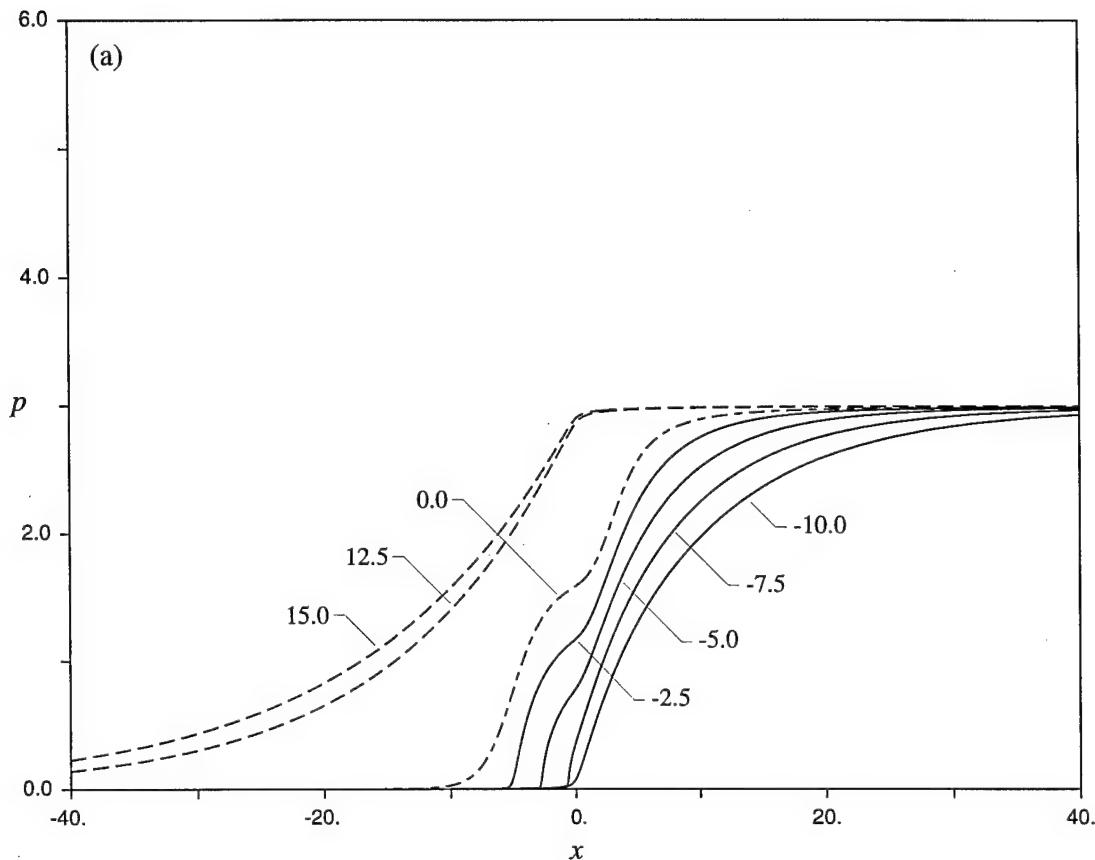
(a) Pressure p.

Figure 6.11 - Numerical solutions for $\alpha = 3.0$ with various levels of wall cooling; $S \pounds = -10.0,..., 15.0$ in increments of 2.5 (cases not shown were unstable): no wall cooling (– - – - –), subcritical boundary layer (– – – – –) and supercritical boundary layer (————).
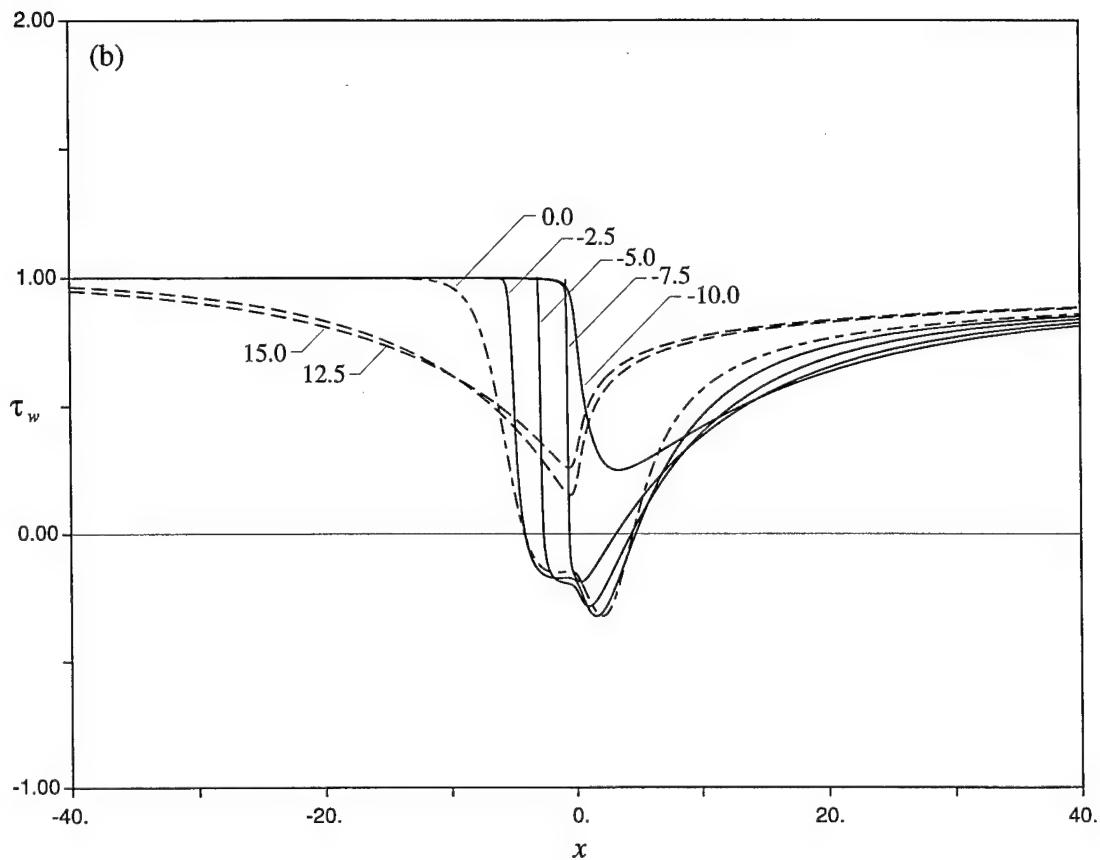
(b) Wall shear stress τ_w.

Figure 6.11 - Continued.
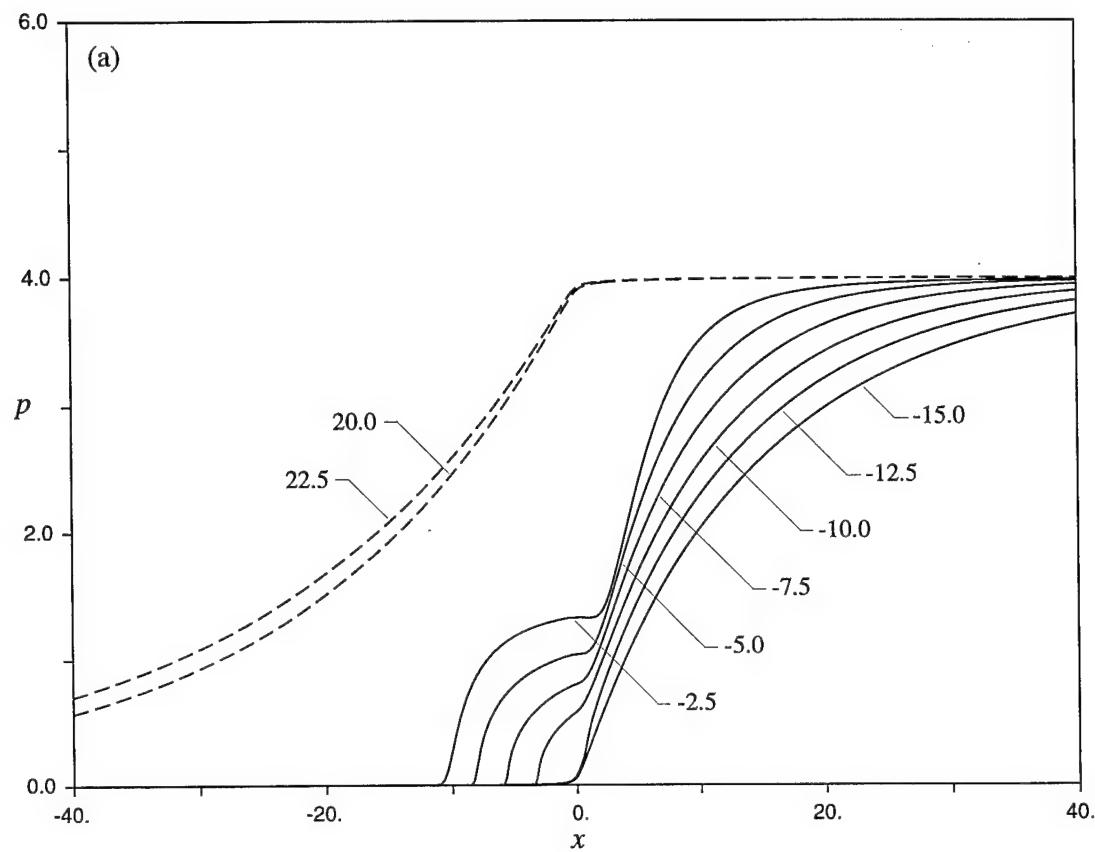
(a) Pressure p.

Figure 6.12 - Numerical solutions for $\alpha = 4.0$ with various levels of wall
cooling; $S\pounds = -15.0,...,22.5$ in increments of 2.5 (cases not
shown were unstable): subcritical boundary layer ($-----$)
and supercritical boundary layer (———).

208
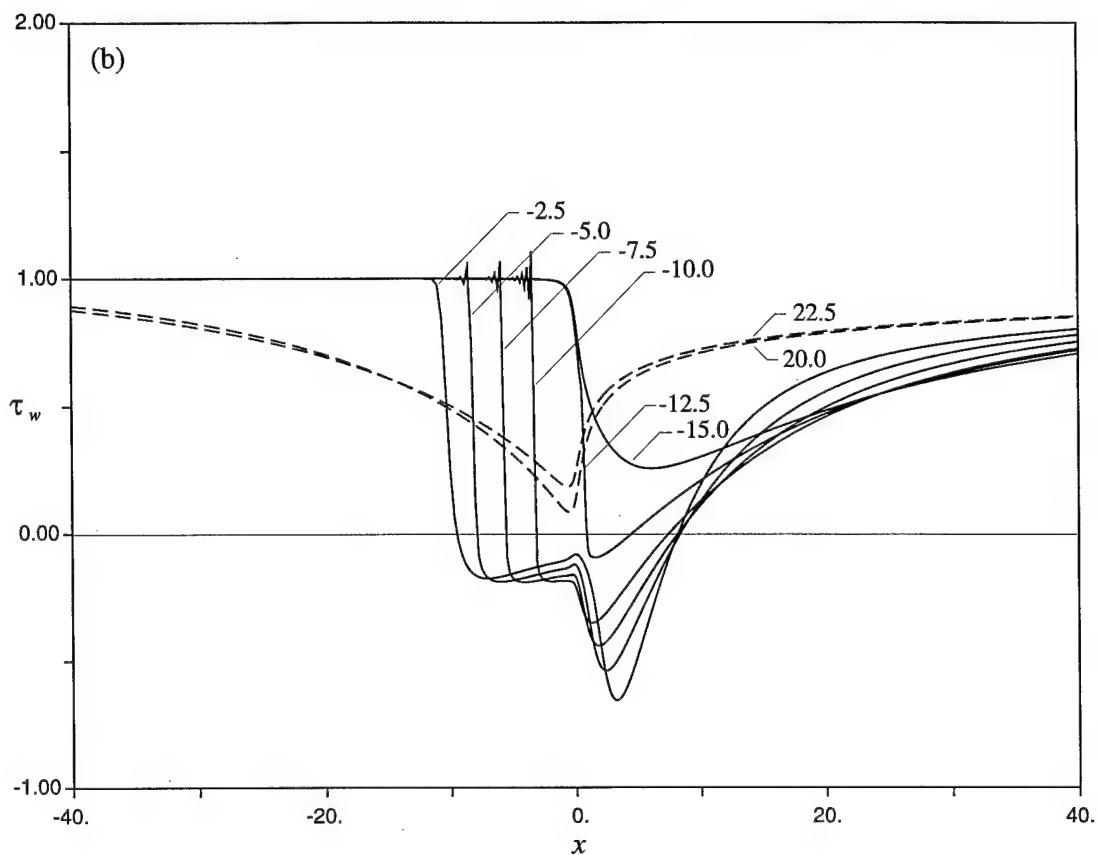
(b) Wall shear stress τ_w.

Figure 6.12 - Continued.

209
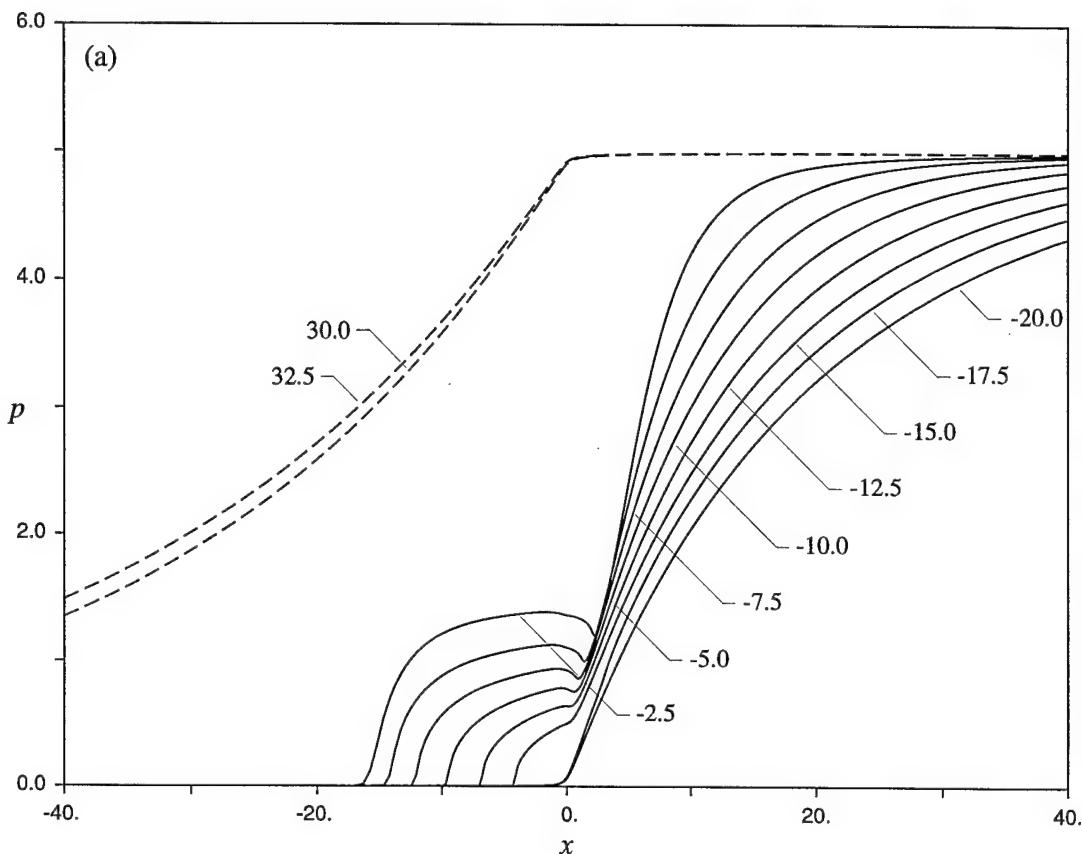
(a) Pressure p.

Figure 6.13 - Numerical solutions for $\alpha = 5.0$ with various levels of wall cooling; $S\,\pounds = -20.0,..., 32.5$ in increments of 2.5 (cases not shown were unstable): subcritical boundary layer ($-----$) and supercritical boundary layer (———).

210
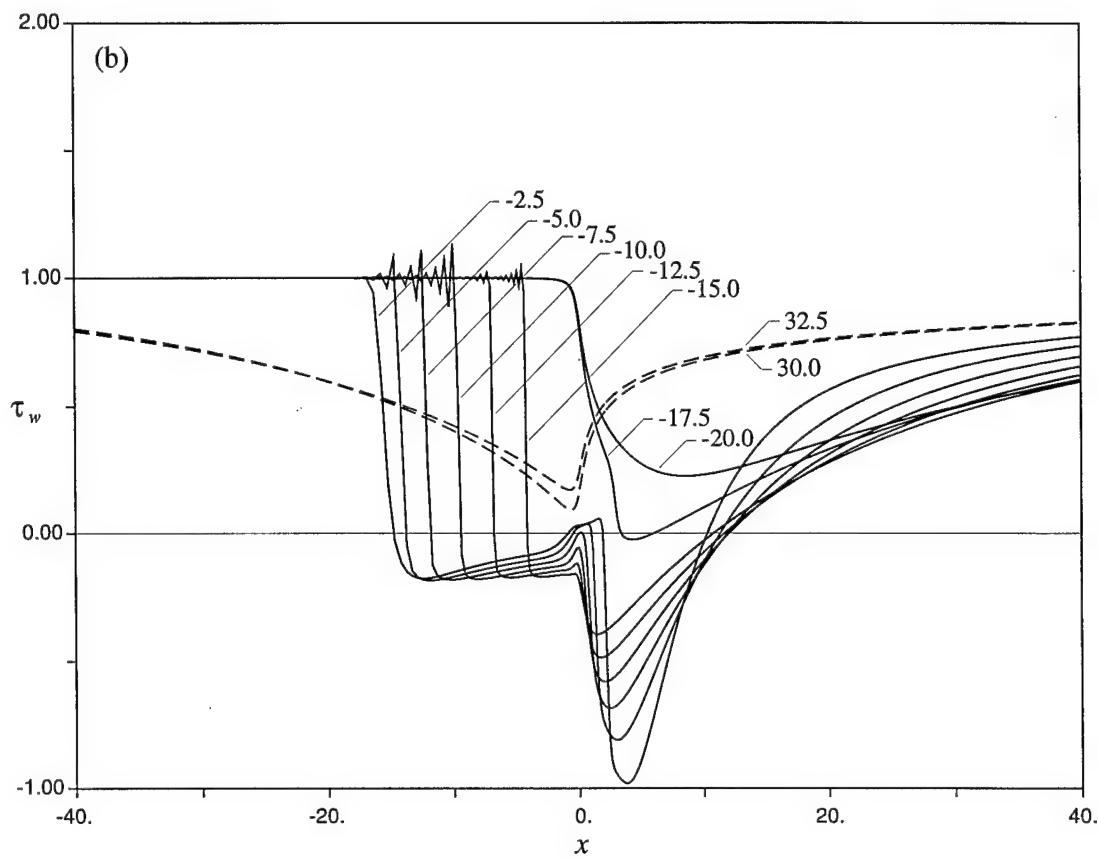
(b) Wall shear stress τ_w.

Figure 6.13 - Continued.

211
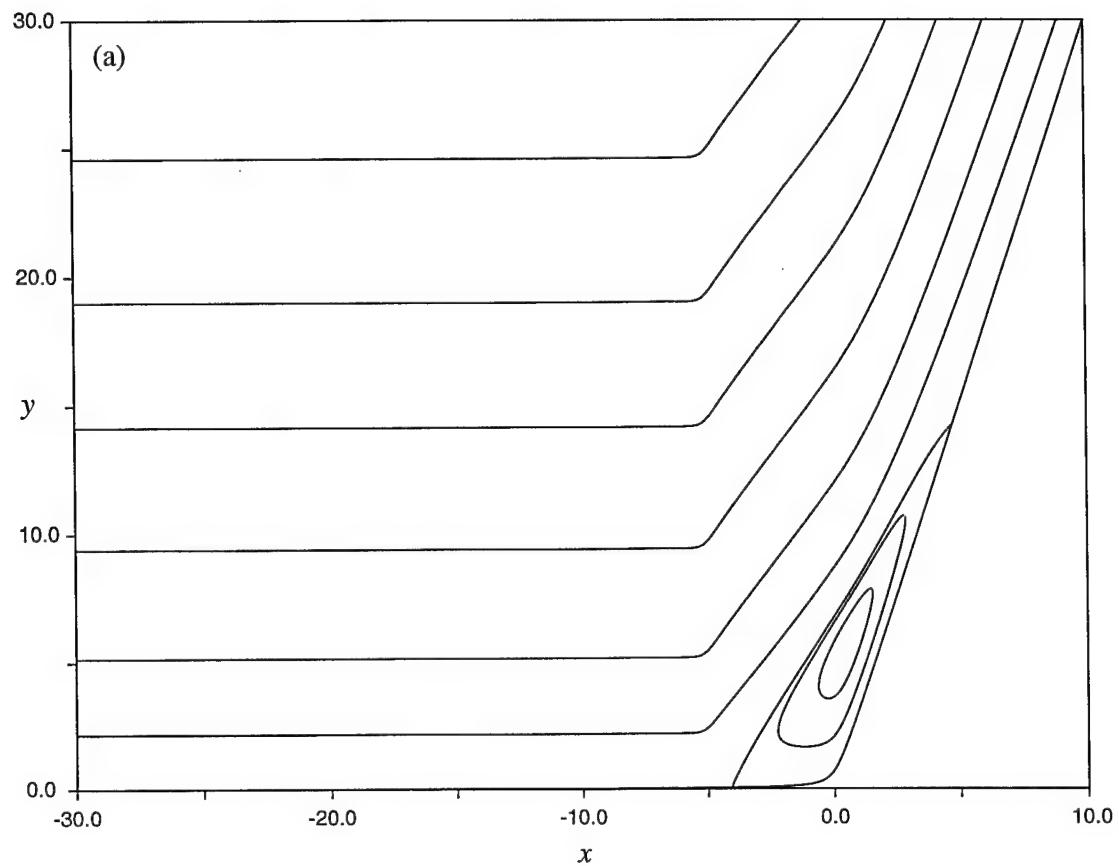
(a) $S\,\pounds = -2.5$.

Figure 6.14 - Streamlines for $\alpha = 3.0$.
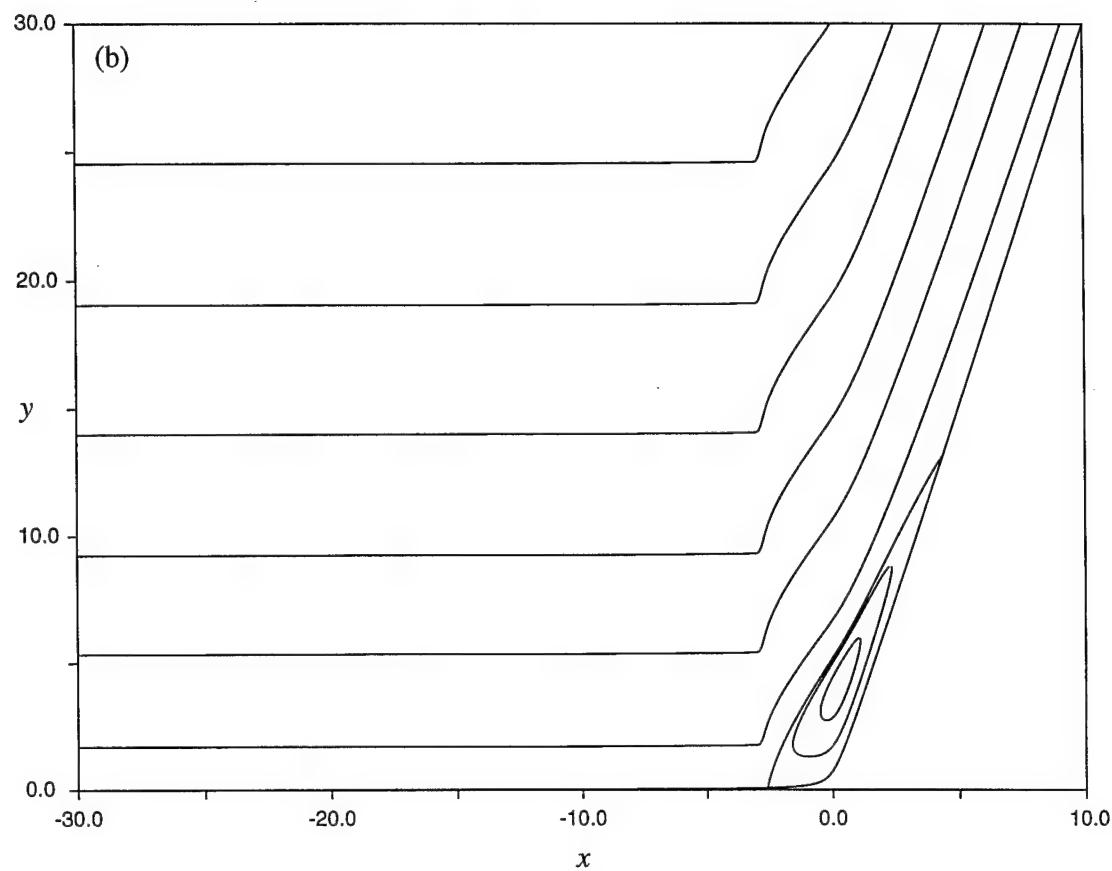
(b) $S \pounds = -5.0$.

Figure 6.14 - Continued.

213
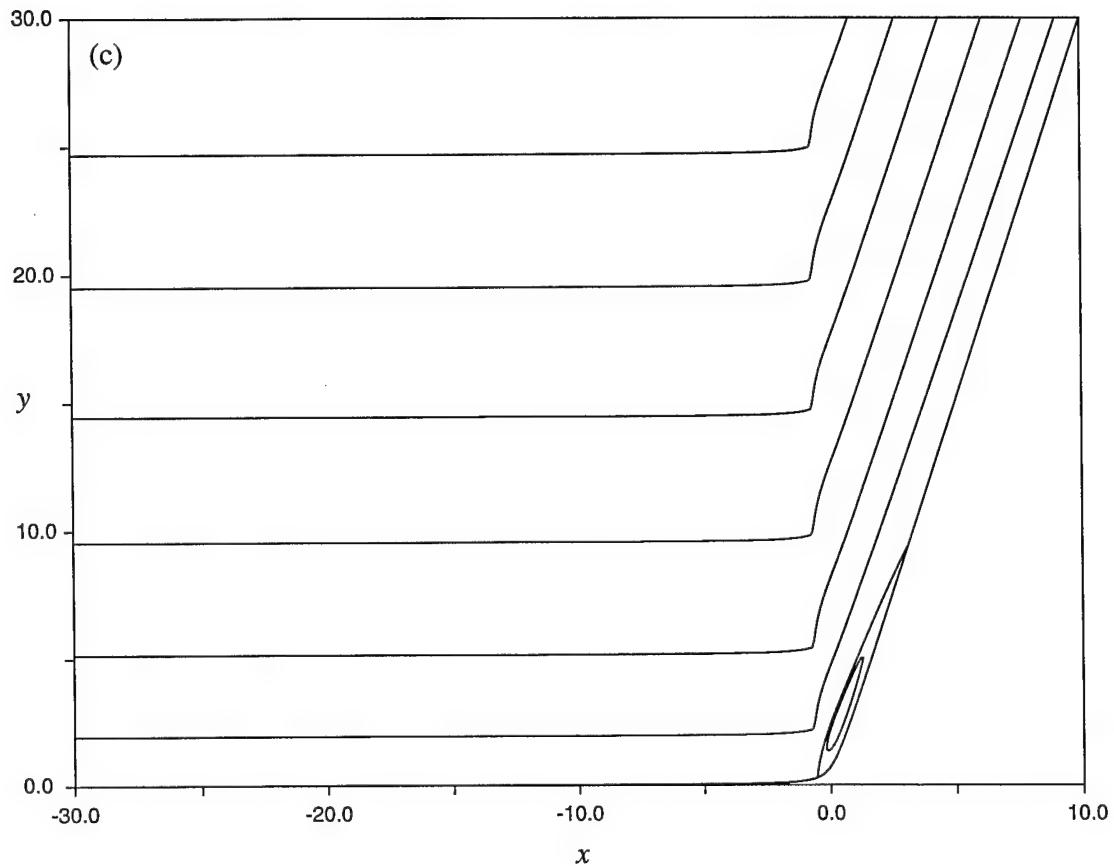
(c) $S \pounds = -7.5$.

Figure 6.14 - Continued.
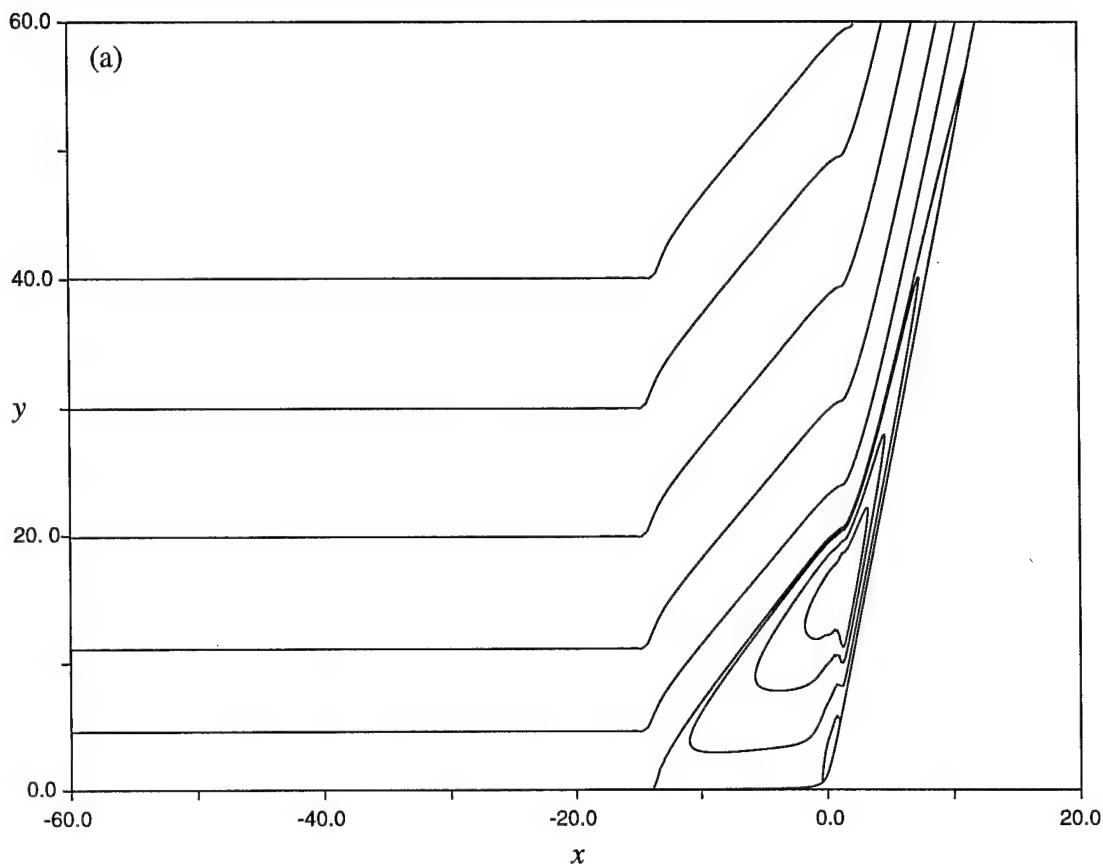
(a) $S \pounds = -5.0$.

Figure 6.15 - Streamlines for $\alpha = 5.0$.
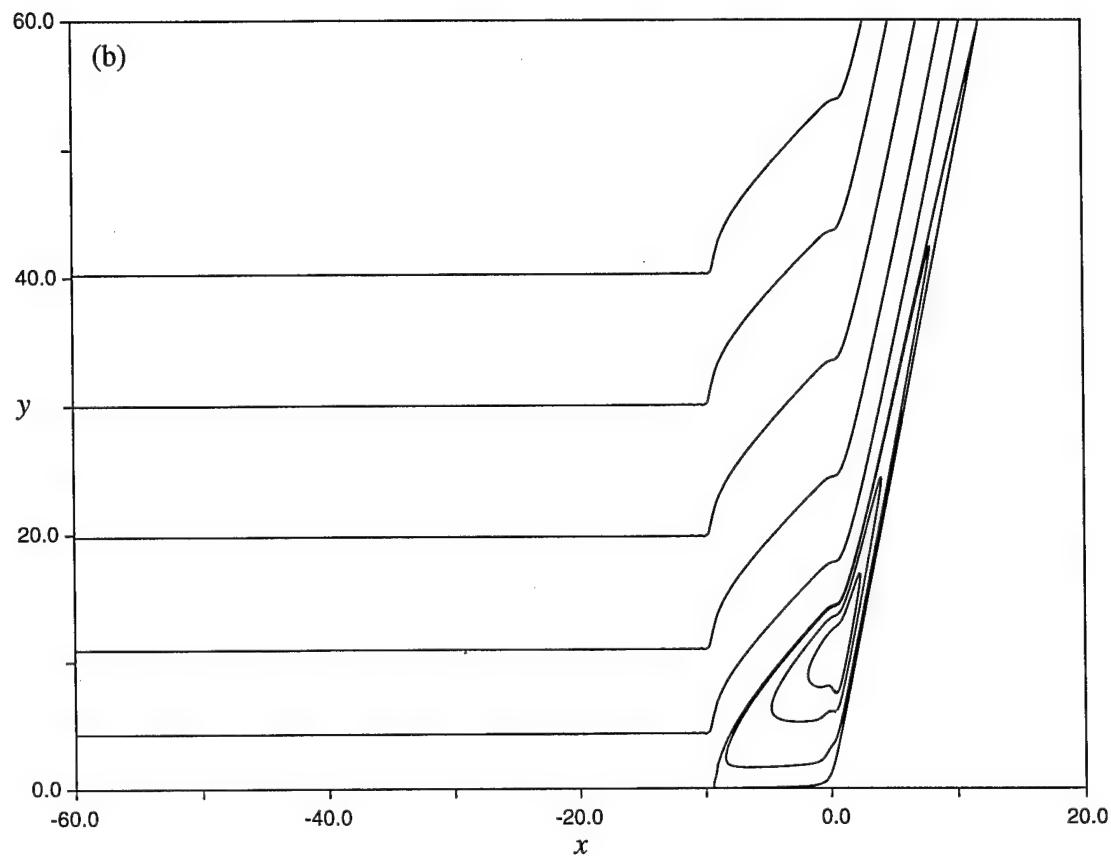
(b) $S \pounds = -10.0$.

Figure 6.15 - Continued.
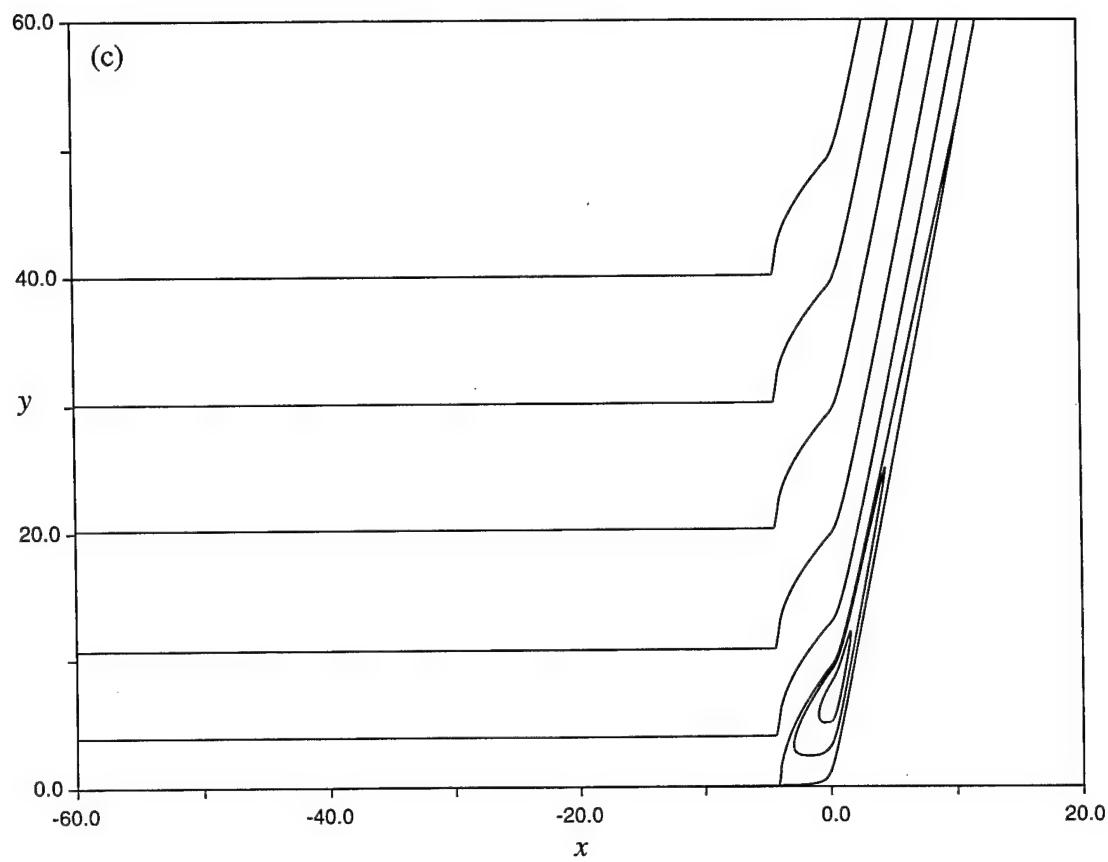
(c) $S \pounds = -15.0$.

Figure 6.15 - Continued.

217
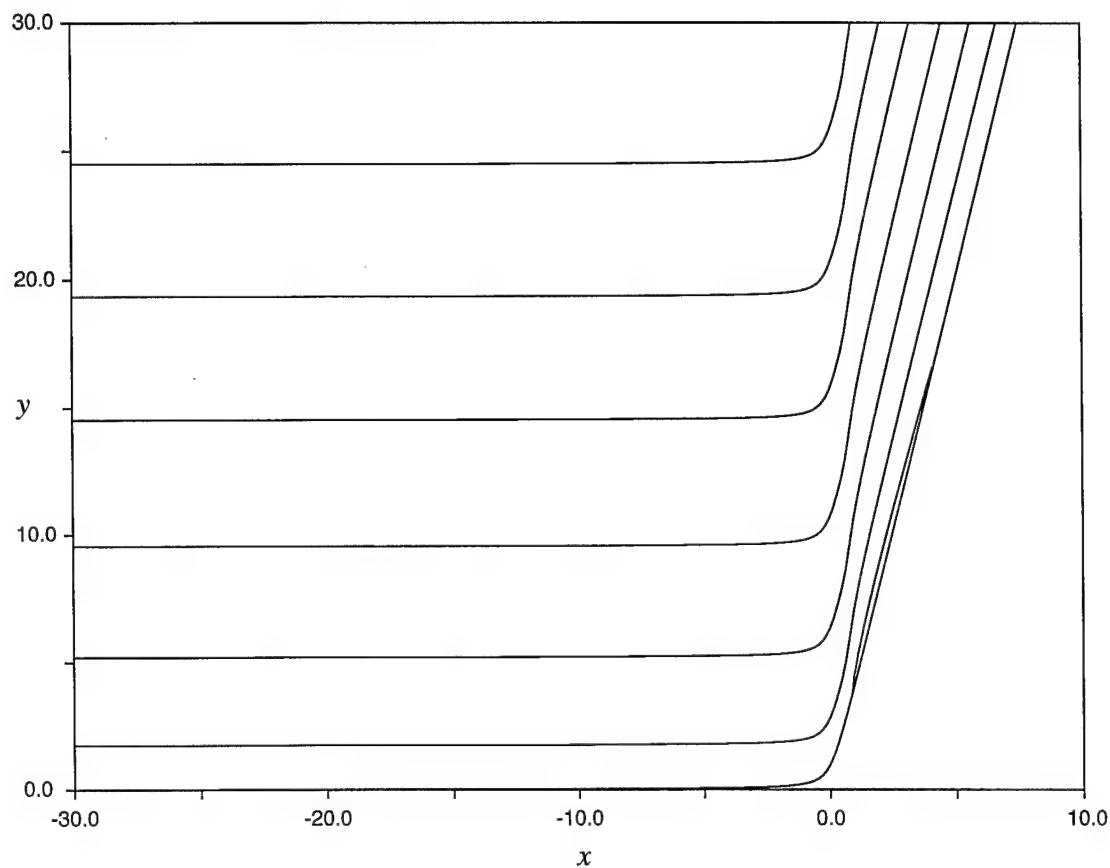
Figure 6.16 - Streamlines for $\alpha = 4.0$ and $S \, \pounds = -12.5$.
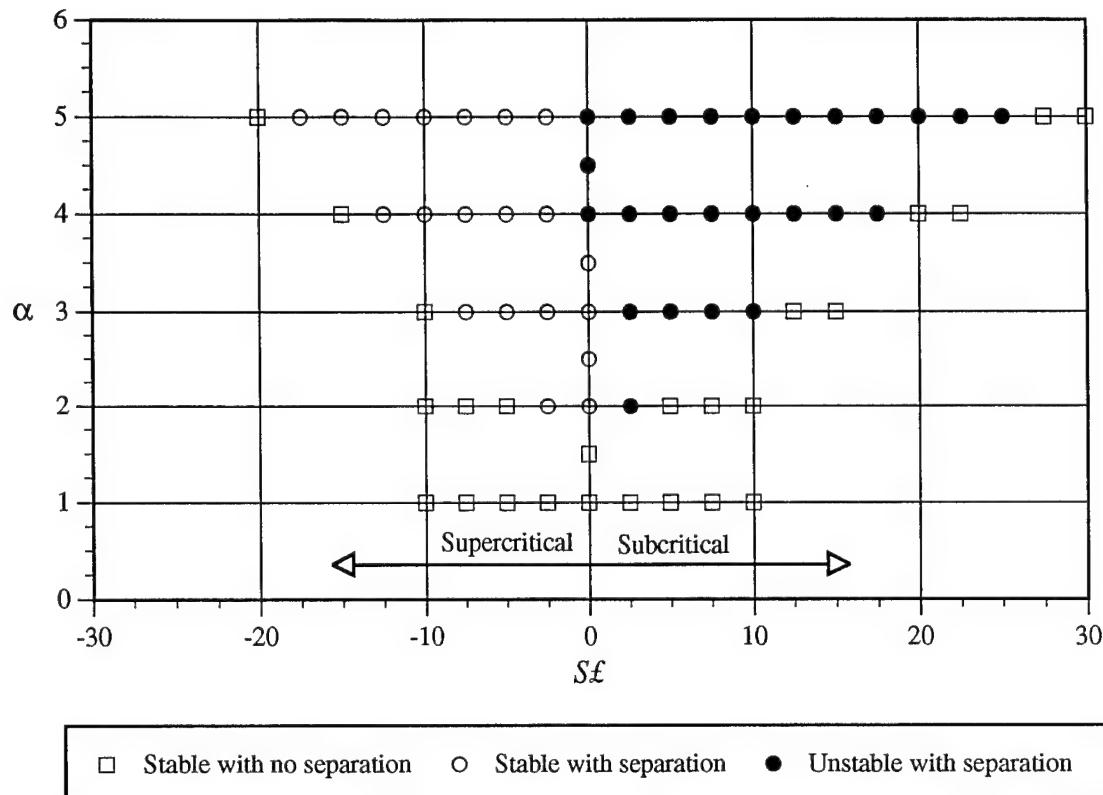
Figure 6.17 - Summary of separation and stability characteristics for flows computed with various ramp angles α and levels of wall cooling $S\text{\pounds}$.

in the form of stationary wave packets near the corner as described in the previous section. Streamlines are shown for ramp angles $\alpha = 3.0$ and 5.0 in figures 6.14 and 6.15, respectively, for a series of wall cooling cases in the supercritical regime involving separation. In addition, streamlines for a particular case with $\alpha = 4.0$ and $S \pounds = -12.5$ are shown in figure 6.16. The separation and stability characteristics of all the solutions represented in the above mentioned figures are summarized in figure 6.17. The features of these results will be discussed subsequently.

The most obvious effect of wall cooling exhibited in the pressure and wall shear distributions for all ramp angles shown (see figures 6.9 through 6.13) is the limiting of upstream or downstream influence as the wall is cooled. In the case of subcritical boundary layers, increased wall cooling reduces the downstream extent of influence of the compression ramp. In the pressure distributions, this is observed as an abrupt decrease in the distance downstream of the corner at which the pressure reaches its downstream value. Similarly, the wall shear tends more rapidly to its downstream value as the wall is cooled. In addition, increasing the wall cooling in the subcritical case results in a significant increase in the upstream influence of the ramp which is observed as a much slower decay of the pressure and wall shear to their upstream values. In the case of supercritical boundary layers, just the opposite behavior is observed. As the wall is cooled, the upstream influence of the ramp is reduced dramatically, and the point at which the pressure and wall shear begin to rise and fall, respectively, from their upstream values moves downstream into the corner. Likewise, the decay of the pressure and wall shear distributions to their downstream values occurs over a longer streamwise distance as the wall cooling is increased. This reduction in upstream influence as the wall is cooled in the supercritical case has been observed experimentally by Lewis, Kubota and Lees (1968). In the extreme case of very large $|S\pounds|$, Kerimbekov *et al.* (1993) show that there are no disturbances upstream of the corner due to the ramp in the supercritical case and none downstream of the corner for subcritical flow. In cases for which no separation occurs (see figures

220

6.9b and 6.10b), the wall shear reveals an additional feature. For subcritical boundary layers, increases in wall cooling dramatically increase the magnitude of the minimum in the wall shear and shift it upstream slightly. While there is also an increase in the magnitude of the wall shear minimum as the wall is cooled in the case of supercritical boundary layers, the minimum is shifted downstream instead.

Wall cooling was found to have an even more pronounced effect on cases involving separation. Although stability characteristics will be discussed later, it is pertinent at this stage to point out that in every case where the flow was subcritical and separation occurred, the numerical solution became unstable in the form of a stationary wave packet near the corner as described in §6.4.1. This is reflected in figures 6.10b, 6.11b, 6.12b and 6.13b where τ_w is positive for all x in every case involving subcritical flow in which a stable solution was obtained. In contrast, many cases involving separation in supercritical flows were found to remain stable; for these cases wall cooling was found to have a significant effect upon the flow. From the wall shear distributions (figures 6.10b, 6.11b, 6.12b and 6.13b), it is observed that separation persists for even relatively large values of wall cooling, and the drop in wall shear from its upstream value to zero at separation steepens and occurs over a much shorter streamwise distance as the wall cooling is increased. In fact, this is believed to be the cause of the oscillations in wall shear observed in the numerical solutions immediately upstream of the separation point for large ramp angles (see figures 6.12b and 6.13b). This behavior is not believed to be due to an instability because of the streamwise locations where it occurs (well upstream of the corner) and the fact that the amplitude of the oscillations do not continue to grow with time (results shown are steady solutions). Rather, the oscillations are believed to be a numerical consequence of the apparent development of a jump discontinuity in the slope of the wall shear distribution at the upstream limit of influence of the compressive disturbance. Reductions in the mesh result in smaller scale oscillations. As the wall cooling is increased further, there is a dramatic decrease in the streamwise extent of the recirculating-flow region just prior to its elimination.

The effects of wall cooling in the supercritical regime on the recirculating region itself are displayed in the results for pressure and wall shear in figures 6.10 through 6.13 and the streamline plots shown in figures 6.14 through 6.16. The primary features observed are a downstream shift in the point of separation and an overall reduction in the streamwise and normal extents of the recirculating-flow region. Indeed, for all ramp angles (for which solutions were obtained) where separation occurs in the non-cold wall case ($\alpha = 2.0$, 3.0, 4.0 and 5.0), separation was ultimately eliminated by sufficient wall cooling. Figures 6.12a and 6.13a also show that increased wall cooling decreases the value of the pressure plateau in the region of recirculating flow. Comparison of figure 6.14 for $\alpha = 3.0$ with figure 6.4 for the non-cold wall case shows the effects of wall cooling on the streamlines. Whereas the flow without wall cooling passes smoothly over the recirculating-flow region, the flow with wall cooling experiences an increasingly abrupt change in direction just upstream of separation as the wall cooling is increased until separation is completely suppressed at which point the streamlines become smooth. This is also shown in the streamline plots of figure 6.15 for a series of cases with $\alpha = 5.0$. In addition, figure 6.15 shows that for high ramp angles, there is a dramatic thinning of the recirculation zone downstream of the corner when the wall is cooled but with little change in the streamwise location of reattachment. Note that figure 6.15a shows the streamlines for a case involving secondary separation at the corner in which a small recirculating flow region forms within the primary reversed-flow region. Observe that the streamlines in the primary recirculating-flow region rise abruptly as they pass over the secondary separation. This secondary separation is eliminated as the wall cooling is increased in the same way that the primary reversed-flow region vanishes. Figure 6.16 shows the streamlines for an example with $\alpha = 4.0$ and $S\pounds = -12.5$ in which the separation point is located on the ramp downstream of the corner. For this case, the recirculating flow is completely contained on the ramp showing dramatically the effect of the limiting of upstream influence which results for wall cooling of supercritical boundary layers as described by Kerimbekov *et al.* (1993). Many other cases were found to have separation

occurring downstream of the corner, but as observed in figure 6.16, the recirculating flow region is very thin and becomes difficult to see in the streamlines as the wall cooling is increased.

The separation and stability characteristics of all the cases shown in this and the previous section are summarized in figure 6.17. The non-cold wall results of §6.4.1 are shown along the line $S\pounds = 0$, and wall cooling cases in the supercritical and subcritical regimes are shown for $S\pounds < 0$ and $S\pounds > 0$, respectively. Recall from §6.4.1 that separation occurs in cases without wall cooling for $\alpha \geq 1.9$ and becomes unstable for $\alpha \geq 3.9$. Observe from figure 6.17 that as the ramp angle is increased, there is a larger range of $S\pounds$ (both subcritical and supercritical) for which separation occurs. But for both subcritical and supercritical boundary layers, separation is eliminated with sufficient wall cooling (at least for $\alpha \leq 5.0$). However, supercritical wall cooling is more effective in suppressing separation. For example, for $\alpha = 5.0$ separation is eliminated for $S\pounds \leq -20.0$ in the supercritical regime but for $S\pounds \geq 27.5$ in the subcritical regime.

While the effects of wall cooling on separation increase gradually with $S\pounds$, the effect on stability is more dramatic. Wall cooling of supercritical boundary layers has a strong stabilizing effect, while that of subcritical boundary layers has a strong destabilizing effect. From figure 6.17 it can be seen that all supercritical cases computed remained stable, while all subcritical cases involving separation became unstable and those where separation did not occur remained stable. The stabilizing effect of wall cooling on supercritical boundary layers in two-dimensional flow has been observed experimentally by Lewis *et al.* (1968) who considered the supersonic flow over compression ramps, and the same effect is also discussed in the review by Stetson and Kimmel (1992) of the stability characteristics of hypersonic boundary layers. Note that in the majority of investigations of hypersonic boundary-layer flows, there is no recognition of the two flow regimes, but the bulk of the cases considered are likely to be supercritical for the reasons discussed above.

Next, it is of interest to verify the scalings (5.87) for the strong wall cooling

223

case considered by Kerimbekov *et al.* (1993). This has been done through comparison of the results obtained here for $|S\pounds|$ large, but $O(1)$, with some of the results of Kerimbekov *et al.* (1993) discussed in §5.4.2 for the strong wall cooling case. Recall from equations (5.87a), (5.87e) and (5.89b) that the strong wall cooling variables $\bar{x}$, $\bar{p}$ and $\bar{\alpha}$ of Kerimbekov *et al.* (1993) are related to the current variables by $\bar{x} = N^{-3/4} x$, $\bar{p} = N^{-1/2} p$ and $\bar{\alpha} = N^{-1/2} \alpha$, respectively. For $N = [S|\pounds|]^{4/3} \gg 1$, the leading-order pressure distribution for the compression ramp is given by equation (5.92) for supercritical boundary layers and by equation (5.93) for subcritical ones. In order to compare the numerical results obtained here with these analytical results, the computed pressure distributions for $\alpha = 1.0$, 2.0, 3.0, 4.0 and 5.0 for both the subcritical and supercritical cases were replotted in terms of the scaled variables and compared with the analytical results. Note that the scales on $\bar{p}$ and $\bar{\alpha}$ are the same; therefore, the pressure distributions defined by equations (5.92) and (5.93) are the same in terms of p and α. For each ramp angle, the subcritical and supercritical case computed with the largest level of wall cooling (see figure 6.17) was scaled in terms of $\bar{x}$ and compared to the analytical results for pressure given by equations (5.92) and (5.93), respectively. The wall cooling parameters used for each ramp angle are shown in table 6.1, and the comparisons are shown in figure 6.18a for the subcritical regime and figure 6.18b for the supercritical regime. Observe that the agreement is very good even for the relatively small values of $|S\pounds|$ used in the numerical calculations. Note that the small discrepancies near $\bar{x} = 0$ are due to the slight rounding of the corner used in the numerical calculations.

In addition to the above comparisons of the pressure distributions, a series of calculations were carried out in order to determine the incipient separation characteristics as $|S\pounds|$ is increased for the supercritical case. This was done by determining the ramp angle α_0 and streamwise location x_0 at which separation first appears for various levels of wall cooling. For each value of $-S\pounds$ in increments of 5.0, a series of calculations were carried out with increasing values of the ramp angle α until a small separation bubble formed on the surface. This ramp angle α_0 and the

Ramp Angle α	Subcritical $S\pounds$	Supercritical $S\pounds$
1.0	10.0	−10.0
2.0	10.0	−10.0
3.0	15.0	−10.0
4.0	22.5	−15.0
5.0	30.0	−20.0

Table 6.1 - Wall cooling values $S\pounds$ used with the subcritical and supercritical regimes for each ramp angle α in the numerical calculations for comparison in figure 6.18 with the strong wall cooling results.
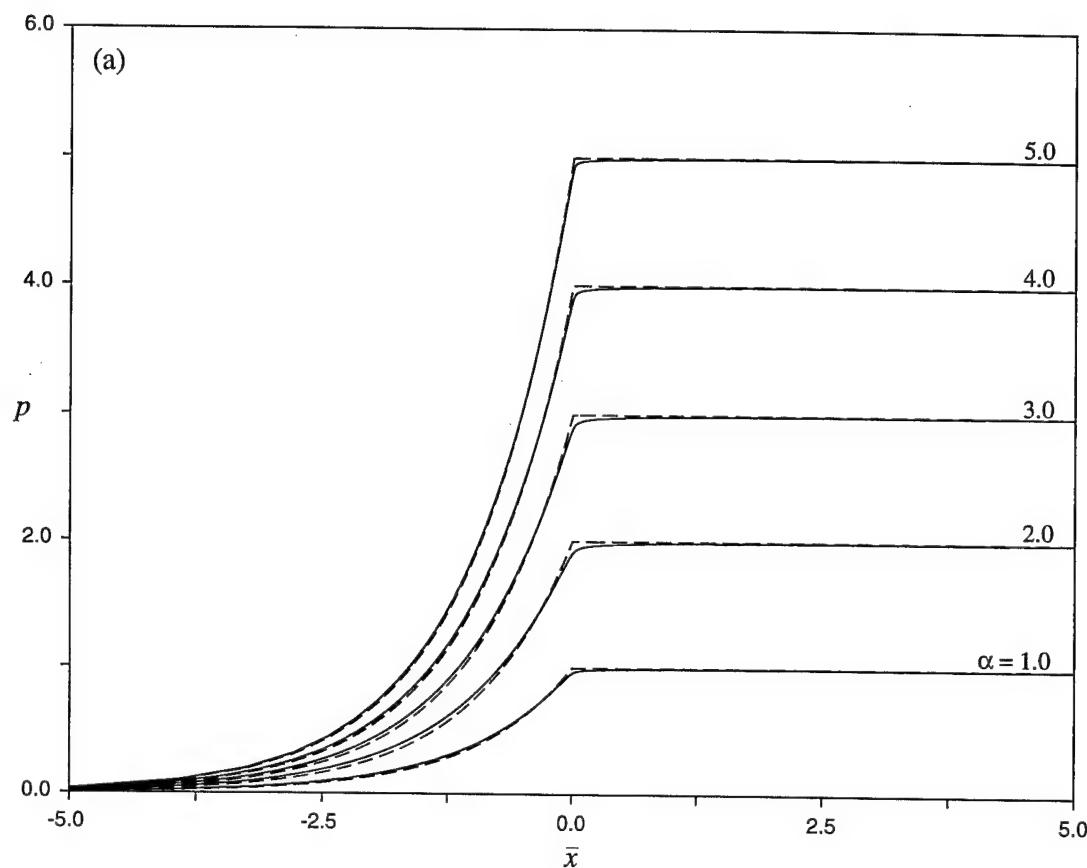
(a) Subcritical boundary layer.

Figure 6.18 - Comparison of pressure distributions from numerical results
(———) for cases given in table 6.1 with analytical results
(---------) for strong wall cooling case.

226
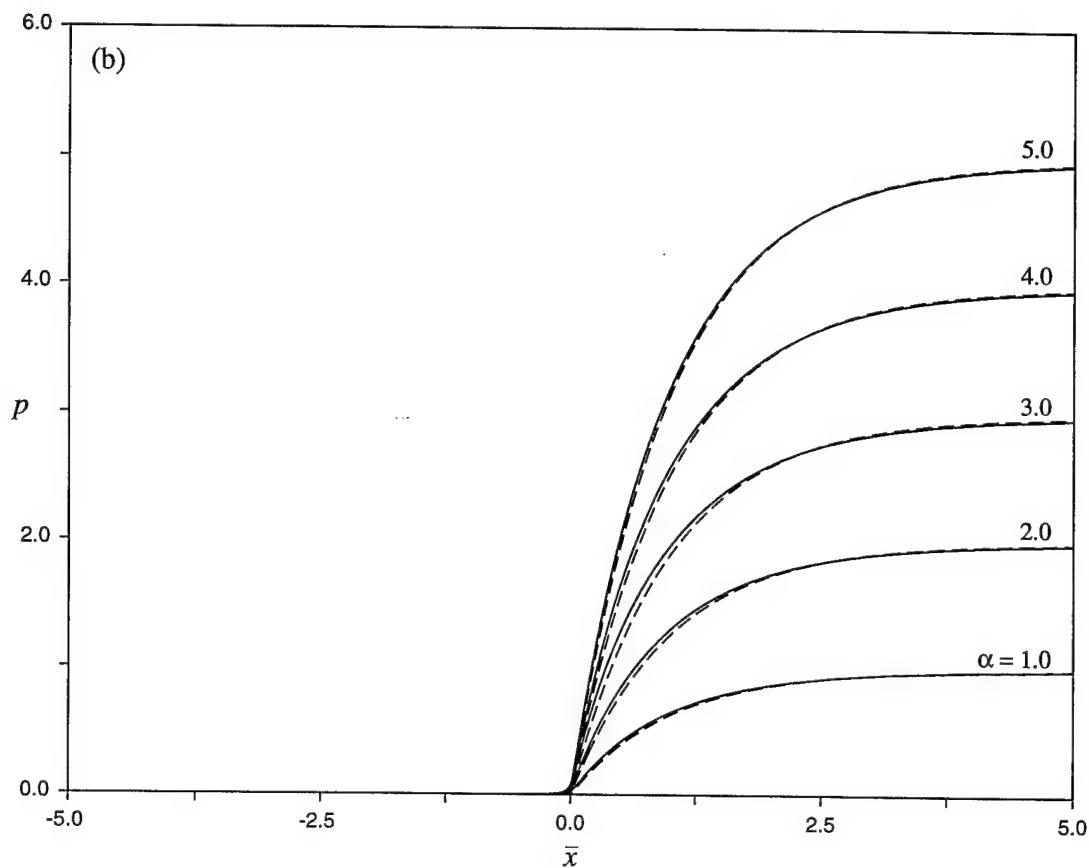
(b) Supercritical boundary layer.

Figure 6.18 - Continued.

227

streamwise location x_0 at which it occurs for each value of $-S\pounds$ is shown in figure 6.19. These results were obtained on meshes defined by $I = 201$, $J = 101$, $a = b = 10.0$ for $|S\pounds| \leq 30.0$ and $a = b = 20.0$ for $|S\pounds| \geq 35.0$. An expanded mesh was used for higher levels of wall cooling because as $-S\pounds$ is increased, separation moves downstream and greater resolution is necessary away from the corner. As the degree of wall cooling is increased, figure 6.19 shows that the critical ramp angle required for separation increases. In addition, the streamwise location where separation appears moves well downstream of the corner as predicted by Kerimbekov *et al.* (1993). This procedure was terminated at $S\pounds = -45.0$ because as separation moves downstream of the corner for increased wall cooling, it becomes increasingly difficult to obtain accurate numerical solutions using the present algorithm which packs points near the corner at the expense of resolution upstream and downstream. It is likely that this procedure could be carried out for larger levels of wall cooling if a transformation similar to equation (6.8a) was used but with an adjustable value of the streamwise location of grid packing.

Recall from §5.4.2 that the results of Kerimbekov *et al.* (1993) show that for $N \gg 1$, the critical ramp angle and the location at which separation first occurs in terms of the scaled variables (5.87) with (5.89) are $\bar{\alpha}_0 = 0.7548$ and $\bar{x}_0 = 0.5$, respectively. In order to confirm these values, the incipient separation results shown in figure 6.19 are shown in figure 6.20 in terms of the scaled variables $\bar{\alpha}$ and $\bar{x}$. Again, accurate results for larger values of $-S\pounds$ could not be obtained with the algorithm used here. It is evident from figure 6.20b that the results for x_0 when $S\pounds = -45.0$ are questionable. However, as $|S\pounds|$ increases, it does appear that the numerical results for $\bar{\alpha}_0$ and $\bar{x}_0$ are tending to the critical values for large N determined by Kerimbekov *et al.* (1993). Therefore, the present numerical investigation appears to confirm the scalings (5.87) for the strong wall cooling case. Particularly strong evidence of this is given by the comparisons of the pressure distributions obtained numerically and analytically shown in figures 6.18a and 6.18b.

Observe from the numerical results discussed in this section that one of the
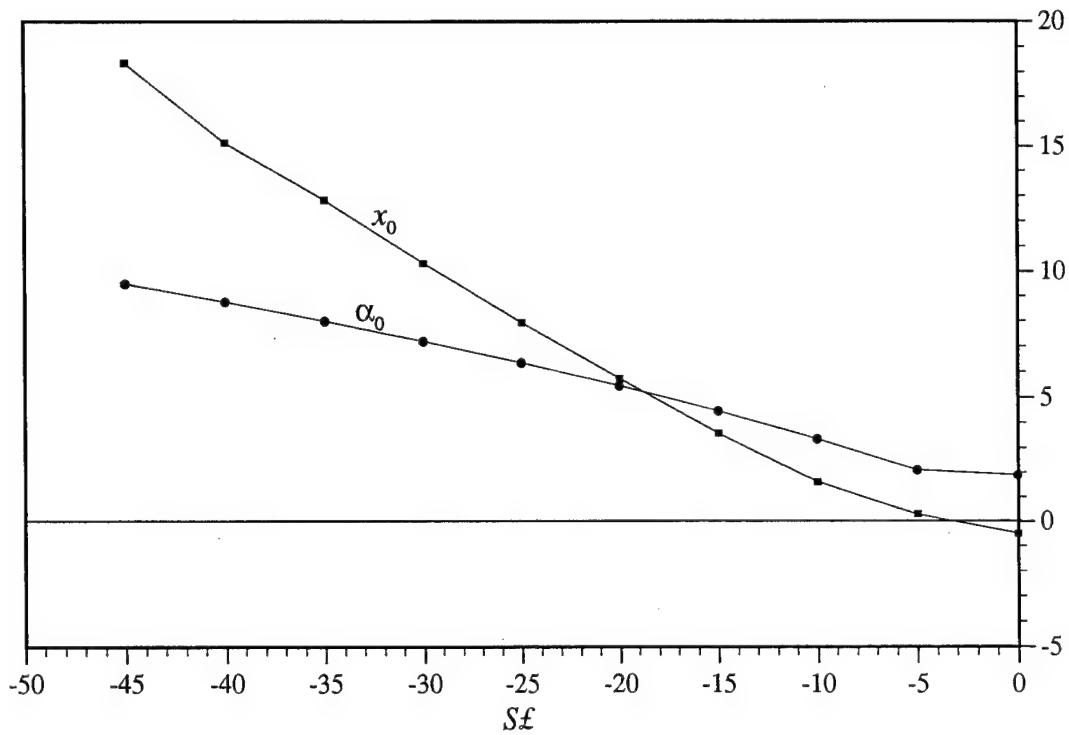
Figure 6.19 - Critical ramp angle α_0 at which incipient separation of a supercritical boundary layer occurs for various values of wall cooling and the streamwise location x_0 where it appears.
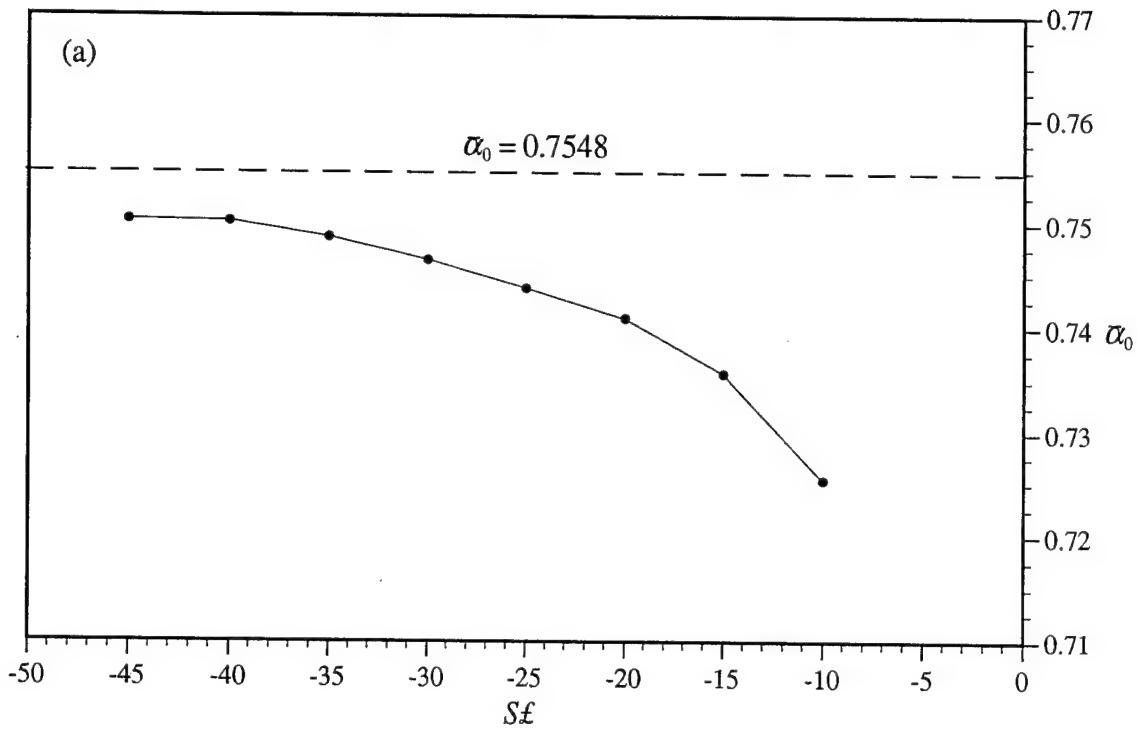
(a) Critical ramp angle α_0 at which separation first occurs.

Figure 6.20 - Incipient separation results from figure 6.19 shown in terms
of strong wall cooling variables with critical values from
Kerimbekov *et al.* (1993) shown for comparison.
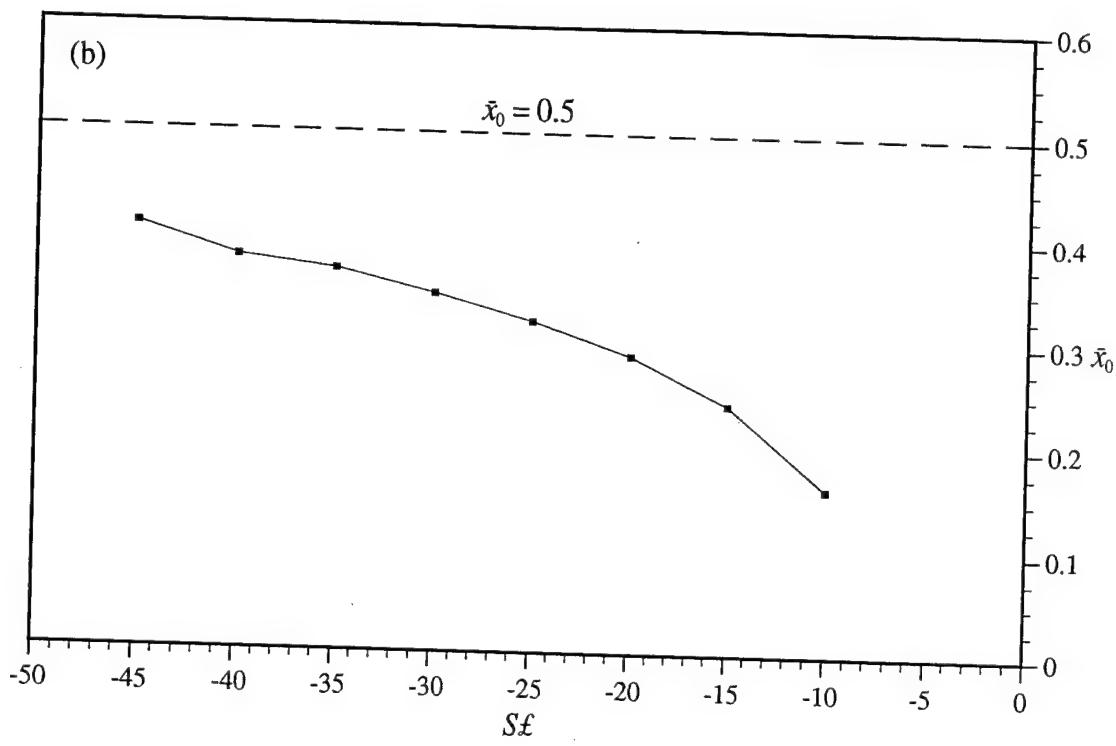
(b) Streamwise location $\bar{x}_0$ where incipient separation appears.

Figure 6.20 - Continued.

primary effects of wall cooling is a dramatic increase in the streamwise scale of the interaction region (relative to the scaled triple-deck variables) as the wall is cooled (N increased). This is reflected in the streamwise scale (5.87a), where $x = N^{3/4} \bar{x}$, for the strong wall cooling case considered by Kerimbekov *et al.* (1993). This is in contrast to the strong wall cooling case considered by Brown *et al.* (1990) (referred to there as the subcritical case). Their streamwise variable, here denoted by $\tilde{x}$, is related to the triple-deck variables used here by $x = N^{-9/4} \tilde{x}$. Therefore, as N becomes large, their interaction region becomes significantly smaller than that considered here, and separation must then be confined to a small region centered at the corner. This is in clear conflict with the present results, however, where separation is found to move upstream or downstream away from the corner as the wall is cooled. Therefore, the present results for hypersonic flow over cold walls raises some questions with regard to the subcritical case considered by Brown *et al.* (1990).

7. Conclusions

A general algorithm has been implemented for calculation of the hypersonic triple-deck on a cold wall. While the algorithm applies for general surface shapes on the triple-deck scale; here, it has been used to compute the flow over the compression ramp geometry with various reduced ramp angles α and levels of wall cooling $S\pounds$. The steady-state solutions were calculated as the large-time limit of unsteady calculations.

Due to the occurrence of instabilities in previous investigations of interactive flow (see Tutty and Cowley, 1986 and part I of the present study) a linear stability analysis was performed for the hypersonic triple deck on a cold wall. It was shown that for the non-cold wall case, Rayleigh's and Fjørtoft's criteria are necessary conditions for an instability. Simply stated, these criteria require the formation of an inflection point in a velocity profile such that the curvature is negative below the inflection point and positive above it. For the cold wall case, however, no analogous conditions could be determined which were particularly useful in identifying an instability. In addition, a stability condition was determined which provides a necessary and sufficient criterion for the occurrence of an instability for cases both with and without wall cooling. This condition, however, was difficult to accurately evaluate numerically for the flow over the compression ramp.

Numerical solutions were first determined for various ramp angles without wall cooling ($S\pounds = 0$). This case also corresponds to the triple deck with a supersonic external flow. The results for small ramp angles ($\alpha \leq 3.5$) were in good agreement with previous studies by Rizzetta, Burggraf and Jenson (1978), Ruban (1978) and Smith and Khorrami (1991). As was shown by these studies, the flow for ramp angles above a critical value separates from the wall in the corner; in the present investigation, where the corner was rounded slightly, this occurred for $\alpha \geq 1.9$. As the ramp angle is increased, the streamwise and normal extent of the recirculating-flow

region grows substantially, and the pressure distribution develops a pressure plateau. As the ramp angle is increased further, it was found in the present study that a high-frequency instability develops in the numerical solution in the form of a stationary wave packet near the corner. This was found to occur for $\alpha \geq 3.9$ when sufficiently refined grids were used. Just as in part I, this instability has high frequencies and short wavelengths, and for this reason it is highly mesh dependent. As the mesh is reduced, smaller wavelength, faster growing modes are manifest in the calculation, and the instability appears earlier in the unsteady calculation and grows more rapidly. While the specific form of the instability and the time at which it appears is highly mesh dependent, the bounding envelope of the wave packet maintains the same shape and streamwise extent regardless of the mesh used. In addition, the wave packet remains largely the same for all ramp angles considered in which the flow becomes unstable. The existence of the instability in the numerical calculations without wall cooling is consistent with Rayleigh's and Fjørtoft's criteria. For $\alpha \leq 3.8$ the flow was found to contain no inflection points in the velocity profiles, and the numerical solutions remained stable. Inflectional profiles which satisfied Fjørtoft's criterion were found for $\alpha \geq 3.9$, and it was these cases for which the numerical solution became unstable.

Wall cooling was found to have a significant effect upon both the separation and stability characteristics of the flow. Numerical solutions were obtained for various ramp angles and a range of wall cooling values for both subcritical and supercritical boundary layers. The most prominent effect of wall cooling was found to be on the stability of the flow. Wall cooling of subcritical boundary layers has a strong destabilizing effect, while that for supercritical flows has a strong stabilizing effect. In fact, every case considered involving supercritical boundary layers for the ramp angles investigated (up to $\alpha = 5.0$) remained stable. On the other hand, every case computed with subcritical flow which involved separation became unstable while those without separation remained stable.

The location and extent of the recirculating flow is also affected significantly by wall cooling. It was shown that sufficient wall cooling of both subcritical and

234

supercritical boundary layers is capable of eliminating separation altogether. For the supercritical cases, increasing the level of wall cooling reduces the size of the recirculating-flow region and shifts the separation point downstream. This is a consequence of the overall effect of wall cooling in reducing the upstream influence in supercritical flows. Conversely, wall cooling of subcritical flows reduces the downstream influence. This trend continues until, in the limit of large Neiland number N, no disturbances associated with the ramp are permitted upstream of the corner for supercritical flow or downstream of the corner for subcritical flow (see §5.4.2).

Finally, the present algorithm was used to verify the scalings for the strong wall cooling case considered by Kerimbekov, Ruban and Walker (1993) which is characterized by large N. This has been done in two ways. First, the pressure distributions obtained numerically for large but finite $|S \pounds|$ were compared with the analytical results obtained in the limit of large N for the leading-order pressure in both the subcritical and supercritical cases. The agreement was good for a range of ramp angles even for relatively small $|S \pounds|$. The second comparison was made with the incipient separation results of Kerimbekov *et al.* (1993) obtained for the supercritical case in the limit of large N. They found that in terms of the strong wall cooling variables, incipient separation occurs at the critical ramp angle $\bar{\alpha}_0 = 0.7548$ at a streamwise location $\bar{x}_0 = 0.5$. In order to compare with these results, the ramp angle and streamwise location of incipient separation were determined numerically for increasing values of $-S \pounds$ (supercritical flow). As $-S \pounds$ is increased, it was shown that the ramp angle at which incipient separation occurs also increases, and the separation point moves well downstream of the corner. When scaled according to the strong wall cooling variables, these results did tend toward the critical values determined by Kerimbekov *et al.* (1993) as $-S \pounds$ increased. Therefore, it was demonstrated that the streamwise extent of the interaction region expands (relative to the triple-deck variables) as the wall is cooled, and it does so with the scalings given by Kerimbekov *et al.* (1993).

235

References

Abramowitz, M. and Stegun, I.A. (1964) *Handbook of Mathematical Functions*, US Government Printing Office, Washington, DC.

Acarlar, M.S. and Smith, C.R. (1987a) "A Study of Hairpin Vortices in a Laminar Boundary Layer. Part 1. Hairpin Vortices Generated by Hemisphere Protuberances" *J. Fluid Mech.* **175**, pp. 1-41.

Acarlar, M.S. and Smith, C.R. (1987b) "A Study of Hairpin Vortices in a Laminar Boundary Layer. Part 2. Hairpin Vortices Generated by Fluid Injection" *J. Fluid Mech.* **175**, pp. 43-83.

Ackeret, J., Feldmann, F. and Rott, N. (1947) "Investigations of Compression Shocks and Boundary Layers in Gases Moving at High Speed" Translated in *Nat. Adv. Comm. Aeronaut. Tech. Memo.* No. 1113 from *E.T.H. Zurich* No. 10 (1946).

Adamson, T.C. Jr. and Messiter, A.F. (1980) "Analysis of Two-Dimensional Interactions Between Shock Waves and Boundary Layers" *Ann. Rev. Fluid Mech.* **12**, pp. 103-138.

Anderson, J.D. Jr. (1989) Hypersonic and High Temperature Gas Dynamics McGraw Hill, New York.

Baker, C.J. (1979) "The Laminar Horseshoe Vortex" *J. Fluid Mech.* **95**, pp. 347-367.

Bar-Lev, M. and Yang, H.T. (1975) "Initial Flow Field over an Impulsively Started Circular Cylinder" *J. Fluid Mech.* **72**, pp. 625-647.

Bodonyi, R.J. and Duck, P.W. (1988) "A Numerical Method for Treating Strongly Interactive Three-Dimensional Viscous-Inviscid Flows" *Computers & Fluids* **16**, pp. 279-290.

Bouard, R. and Coutanceau, M. (1980) "The Early Stage of Development of the Wake Behind an Impulsively Started Cylinder for $40 < Re < 10^4$" *J. Fluid Mech.* **101**, pp. 583-607.

Brotherton-Ratcliffe, R.V. and Smith, F.T. (1987) "Complete Breakdown of an Unsteady Interacting Boundary Layer (over a Surface Distortion or on a Liquid Layer)" *Mathematika* **34**, pp. 86-100.

Brown, S.N., Cheng, H.K. and Lee, C.J. (1990) "Inviscid-Viscous Interaction on Triple-Deck Scales in a Hypersonic Flow with Strong Wall Cooling" *J. Fluid Mech.* **220**, pp. 309-337.

Brown, S.N., Cheng, H.K. and Smith, F.T. (1988) "Nonlinear Instabilities and Break-Up of Separated Flow" *J. Fluid Mech.* **193**, pp. 191-216.

Brown, S.N., Stewartson, K. and Williams, P.G. (1975) "Hypersonic Self-Induced Separation" *Phys. Fluids* **18**, pp. 633-639.

Burggraf, O.R., Rizzetta, D., Werle, M.J. and Vatsa,V.N. (1979) "Effect of Reynolds Number on Laminar Separation of a Supersonic Stream" *AIAA J.* **17**, pp. 336-343.

Cebeci, T. (1979) "The Laminar Boundary Layer on a Circular Cylinder Started Impulsively from Rest" *J. Comp. Phys.* **31**, pp. 153-172.

Cebeci, T. (1982) "Unsteady Separation" In *Numerical and Physical Aspects of Aerodynamic Flows* (ed. T. Cebeci), pp. 265-277. Springer.

Cebeci, T. (1986) "Unsteady Boundary Layers with an Intelligent Numerical Scheme" *J. Fluid Mech.* **163**, pp. 129-140.

Chapman, D.R., Kuehn, D.M. and Larson, H.K. (1957) "Investigation of Separated Flows in Supersonic and Subsonic Streams with Emphasis on the Effect of Transition" *NACA Tech. Note* No. 3869, pp. 419-460.

Cheng, H.K. (1993) "Perspectives on Hypersonic Viscous Flow Research" *Ann. Rev. Fluid Mech.* **25**, pp. 455-484.

Chu, C.C. and Falco, R.E. (1988) "Vortex Ring/Viscous Wall Layer Interaction Model of the Turbulence Production Process Near Walls" *Exp. Fluids* **6**, pp. 305.

Chuang, F.S. and Conlisk, A.T. (1989) "Effect of Interaction on the Boundary Layer Induced by a Convected Rectilinear Vortex" *J. Fluid Mech.* **200**, pp. 337-365.

Collins, W.M. and Dennis, S.C.R. (1973) "Flow Past an Impulsively Started Circular Cylinder" *J. Fluid Mech.* **60**, pp. 105-127.

Cowley, S.J. (1983) " Computer Extension and Analytic Continuation of Blasius'
        Expansion for Impulsive Flow Past a Circular Cylinder" *J. Fluid Mech.* **135**,
        pp. 389-405.

Cowley, S.J., Hocking, L.M. and Tutty, O.R. (1985) "The Stability of Solutions of the
        Classical Unsteady Boundary-Layer Equations" *Phys. Fluids* **28**, pp. 441-
        443.

Cowley, S.J., Van Dommelen, L.L. and Lam, S.T. (1990) "On the Use of Lagrangian
        Variables in Descriptions of Unsteady Boundary-Layer Separation" *Phil.
        Trans. R. Soc. Lond. A* **333**, pp. 343-378.

Degani, A.T. and Walker, J.D.A. (1994) "Unsteady Separation Past Moving Surfaces"
        (to appear)

Dennis, S.C.R. (1972) "The Motion of a Viscous Fluid Past an Impulsively Started
        Semi-Infinite Flat Plate" *Inst. Maths. Applics.* **10**, pp. 105-117.

Doligalski, T.L., Smith, C.R. and Walker, J.D.A. (1994) "Vortex Interactions with
        Walls" *Ann. Rev. Fluid Mech.* (to appear).

Doligalski , T.L. and Walker, J.D.A. (1984) "The Boundary Layer Induced by a
        Convected Two-Dimensional Vortex" *J. Fluid Mech.* **139**, pp. 1-28.

Drazin, P.G. and Reid, W.H. (1981) Hydrodynamic Stability Cambridge University
        Press.

Duck, P.W. (1985) "Laminar Flow over Unsteady Humps: the Formation of Waves"
        J. Fluid Mech. **160**, pp. 465-498.

Duck, P.W. and Burggraf, O.R. (1986) "Spectral Solutions for Three-Dimensional
        Triple-Deck Flow Over Surface Topography" *J. Fluid Mech.* **162**, pp. 1-22.

Ece, M.C., Walker, J.D.A. and Doligalski, T.L. (1984) "The Boundary Layer on an
        Impulsively Started Rotating and Translating Cylinder" *Phys. Fluids* **27**,
        pp.1077-1089.

Elliott, J.W., Cowley, S.J. and Smith, F.T. (1983) "Breakdown of Boundary Layers:
        (i) on Moving Surfaces; (ii) in Semi-Similar Unsteady Flow; (iii) in Fully
        Unsteady Flow" *Geophys. Astrophys. Fluid Dynamics* **25**, pp. 77-138.

238

Elliott, J.W. and Smith, F.T. (1987) "Dynamic Stall Due to Unsteady Marginal Separation" *J. Fluid Mech.* **179**, pp. 489-512.

Ersoy, S. and Walker, J.D.A. (1985) "Viscous Flow Induced by Counterrotating Vortices" *Phys. Fluids* **28**, pp. 2687-2698.

Ersoy, S. and Walker, J.D.A. (1986) "Flow Induced at a Wall by a Vortex Pair" *AIAA J.* **24**, pp. 1597-1605.

Ersoy, S. and Walker, J.D.A. (1987) "The Boundary Layer Due to a Three-Dimensional Vortex Loop" *J. Fluid Mech.* **185**, pp. 569-598.

Falco, R.E. (1991) "A Coherent Structure Model of the Turbulent Boundary Layer and its Ability to Predict Reynolds Number Dependence" *Phil. Trans. Roy. Soc. Lond. A* **336**, pp. 103-130.

Fletcher, C.A.J. (1991) Computational Techniques for Fluid Dynamics 1 - Fundamentals and General Techniques Springer-Verlag.

Fornberg, B (1985) "Steady Viscous Flow Past a Circular Cylinder up to Reynolds Number 600" *J. Comput. Phys.* **61**, pp. 297-320.

Gaster, M. (1982) "Estimates of the Errors Incurred in Various Asymptotic Representations of Wave Packets" *J. Fluid Mech.* **121**, pp. 365-377.

Gaster, M. and Grant, I. (1975) "An Experimental Investigation of the Formation and Development of a Wave Packet in a Laminar Boundary Layer" *Proc. R. Soc. Lond. A* **347**, pp. 253-269.

Goldstein, S. (1930) "Concerning Some Solutions of the Boundary-Layer Equations in Hydrodynamics" *Proc. Camb. Phil. Soc.* **26**, pp. 1-30.

Goldstein, S. (1948) "On Laminar Boundary-Layer Flow Near a Point of Separation" *Q. J. Mech. App. Maths.* **1**, pp. 43-69.

Grass, A.J., Stuart, R.J., Mansour-Tehrani, M. (1991) "Vortical Structures and Coherent Motion in Turbulent Flow over Smooth and Rough Boundaries" *Phil. Trans. Roy. Soc. Lond. A* **336**, pp. 35-66.

Harvey, J.K. and Perry, F.J. (1971) "Flowfield Produced by Trailing Vortices in the Vicinity of the Ground" *AIAA J.* **9**, pp. 1659-1660.

Head, M.R. and Bandyopadhyay, P. (1981) "New Aspects of Turbulent Boundary Layer Structure" *J. Fluid Mech.* **107**, pp. 297-338.

Henkes, R.A.W.M. and Veldman, A.E.P. (1987) "On the Breakdown of the Steady and Unsteady Interacting Boundary-Layer Description" *J. Fluid Mech.* **179**, pp. 513-529.

Hon, T.L. and Walker, J.D.A. (1987) "An Analysis of the Motion and Effects of Hairpin Vortices" Rep. FM-11, Department of Mechanical Engineering and Mechanics, Lehigh University.

Hon, T.L. and Walker, J.D.A. (1988) "Evolution of Hairpin Vortices in a Shear Flow" NASA Technical Memorandum 100858 ICOMP-88-9.

Hon, T.L. and Walker, J.D.A. (1991) "Evolution of Hairpin Vortices in a Shear Flow" *Computs. and Fluids* **20**, pp. 343-358.

Howarth, L. (1938) "On the Solution of the Laminar-Boundary Equations" *Proc. Roy. Soc. Lond. A* **164**, pp. 547-579.

Hoyle, J.M., Smith, F.T. and Walker, J.D.A. (1991) "On Sublayer Eruption and Vortex Formation" *Comput. Phys. Commun.* **65**, pp. 151-157.

Ingham, D.B. (1984) "Unsteady Separation" *J. Comput. Phys.* **53**, pp. 90-99.

Inoue, O. (1981) "MRS Criterion for Flow Separation over Moving Walls" *AIAA J.* **19**, pp. 1108-1111.

Jenson, R. (1977) "Numerical Solution of Weakly Separated Supersonic Flows at High Reynolds Number" Ph.D. Dissertation, The Ohio State University.

Jiang, F. (1991) "Asymptotic Evaluation of Three-Dimensional Wave Packets in Parallel Flows" *J. Fluid Mech.* **226**, pp. 573-590.

Jobe, C.E. and Burggraf, O.R. (1974) "The Numerical Solution of the Asymptotic Equations of Trailing Edge Flow" *Proc. R. Soc. Lond. A.* **340**, pp. 91-111.

Kazakov, V.A. (1985) "Strongly Implicit Alternately-Triangular Method for Solving Problems of Asymptotic Boundary-Layer Theory" *U.S.S.R. Comput. Maths. Math. Phys.* **25**, pp. 68-73.

240

Kerimbekov, R.M., Ruban, A.I. and Walker, J.D.A. (1993) "Hypersonic Boundary-Layer Separation on a Cold Wall" (to be published).

Kogan, M.N. (1973) "Molecular Gas Dynamics" *Ann. Rev. Fluid Mech.* **5**, pp. 383-404.

Krasny, R. (1986) "A Study of Singularity Formation in a Vortex Sheet by the Point-Vortex Approximation" *J. Fluid Mech.* **167**, pp. 65-93.

Kwon, O.K. and Pletcher, R.H. (1979) "Prediction of Incompressible Separated Boundary Layers Including Viscous-Inviscid Interaction" *J. Fluids Eng.* **101**, pp. 466-472.

Lagerstrom, P.A. (1975) "Solutions of the Navier-Stokes Equation at Large Reynolds Number" *SIAM J. Appl. Math.* **28**, No. 1, pp. 202-214.

Lewis, J.E., Kubota, T. and Lees, L. (1968) "Experimental Investigation of Supersonic Laminar, Two-Dimensional Boundary-Layer Separation in a Compression Corner with and without Cooling" *AIAA J.* **6**, pp. 7-14.

Liepmann, H.W. (1946) "The Interaction Between Boundary Layers and Shock Waves in Transonic Flow" *J. Aeronaut. Sci.* **13**, pp. 623-637.

Lighthill, M.J. (1953a) "On Boundary Layers and Upstream Influence. I. A Comparison between Subsonic and Supersonic Flows" *Proc. Roy. Soc. Lond. A* **217**, No. 1131, pp. 344-357.

Lighthill, M.J. (1953b) "On Boundary Layers and Upstream Influence. II. Supersonic Flows without Separation" *Proc. Roy. Soc. Lond. A* **217**, pp. 478-507.

Matarrese, M.D., Messiter, A.F. and Adamson, T.C., Jr. (1990) "Control of Hypersonic Aerodynamic Forces with Surface Blowing" *AIAA J.* **29**, pp. 2094-2104.

McCroskey, W.J. (1982) "Unsteady Airfoils" *Ann. Rev. Fluid Mech.* **14**, pp. 285-311.

Messiter, A.F. (1970) "Boundary-Layer Flow Near the Trailing Edge of a Flat Plate" *SIAM J. Appl. Math.* **18**, No. 1, pp. 241-257.

Messiter, A.F. (1979) "Boundary Layer Separation" *Proc. 8th U.S. Natl. Congr. Appl. Mech.*, pp. 157-179; Western Periodicals, North Hollywood, California.

Messiter, A.F. (1983) "Boundary-Layer Interaction Theory" *Trans. ASME, J. Appl. Mech.* **50**, No. 4, pp. 1104-1113.

Messiter, A.F., Matarrese, M.D. and Adamson, T.C., Jr. (1991) "Strip Blowing From a Wedge at Hypersonic Speeds" *AIAA Paper No.* 91-0032.

Mikhailov, V.V., Neiland, V. Ya. and Sychev, V.V. (1971) "The Theory of Viscous Hypersonic Flow" *Ann. Rev. Fluid Mech.* pp. 371-396.

Moore, F.K. (1958) "On the Separation of the Unsteady Laminar Boundary Layer" In *Boundary-Layer Research* (ed. H.G. Gortler), pp. 296-310. Springer.

Neiland, V.Ya. (1969) "On the Theory of Laminar Bounary-Layer Separation in Supersonic Flow" *Izv. Akad. Nauk SSSR, MZhG,* No. 4, pp. 53-57.

Neiland, V.Ya. (1973) "Peculiarities of Boundary-Layer Separation on a Cooled Body and its Interaction with a Hypersonic Flow" *Izv. Akad. Nauk SSSR, MZhG,* No. 6, pp. 99-109.

Neiland, V.Ya. (1974) "Asymptotic Problems of the Viscous Supersonic Flow Theory" *TsAGI Trans.*, No. 1529.

Neiland, V.Ya. (1981) "Asymptotic Theory for Separation and Interaction of a Boundary Layer with Supersonic Gas Flow" *Advances in Mechanics* **4**, No. 2, pp. 3-62.

Neiland, V.Ya. and Sokolov, L.A. (1975) "On the Asymptotic Theory of Incipient Separation in Compression Ramp Hypersonic Flow on Cooled Body for a Weak Hypersonic Interaction Regime" *Uchen. Zap. TsAGI* **6**, No. 3, pp. 25-34.

Pearson, H. Holiday, J.B. and Smith, S.F. (1958) "A Theory of the Cylindrical Ejection Supersonic Propelling Nozzle" *J. Aeronaut. Soc.* **62**, pp. 756-761.

Peridier, V.J., Smith, F.T. and Walker, J.D.A. (1988) "Methods for the Calculation of Unsteady Separation" AIAA Paper No. 88-0604, presented at the 26th Aerospace Sciences Meeting, Reno, Nevada, January 11-14, 1988.

Peridier, V.J., Smith, F.T. and Walker, J.D.A. (1991a) "Vortex-Induced Boundary-Layer Separation. Part 1. The Unsteady Limit Problem Re $\rightarrow \infty$" *J. Fluid Mech.* **232**, pp. 99-131.

Peridier, V.J., Smith, F.T. and Walker, J.D.A. (1991b) "Vortex-Induced Boundary-Layer Separation. Part 2. Unsteady Interacting Boundary-Layer Theory" *J. Fluid Mech.* **232**, pp. 133-165.

Peridier, V.J. and Walker, J.D.A. (1989) "Vortex-Induced Boundary-Layer Separation" Rep. FM-13. Department of Mechanical Engineering and Mechanics, Lehigh University.

Prandtl, L. (1905) "Motion of Fluids with Very Little Viscosity" *Proc. 3rd Inter. Cong. of Math.*, Heidelberg, 1904, pp. 484-491. Translated in *NACA Tech. Memo.* No. 452 (1928).

Press, W.H., Flannery, B.P., Teukolsky, S.A. and Vetterling, W.T. (1989) <u>Numericial Recipes, The Art of Scientific Computing</u> Cambridge University Press.

Proudman, I. and Johnson, K. (1962) "Boundary-Layer Growth Near a Rear Stagnation Point" *J. Fluid Mech.* **12**, pp. 161-168.

Riley, N. (1975) "Unsteady Laminar Boundary Layers" *SIAM Rev.* **17**, pp. 274-297.

Riley, N. and Vasantha, R. (1989) "Unsteady High-Reynolds-Number Flows" *J. Fluid Mech.* **205**, pp. 243-262.

Rizzetta, D.P. (1976) "Asymptotic Solution for Two-Dimensional Viscous Supersonic and Hypersonic Flows Past Compression and Expansion Corners" Ph.D. Dissertation, The Ohio State University.

Rizzetta, D.P., Burggraf, O.R. and Jenson, R. (1978) "Triple-Deck Solutions for Viscous Supersonic and Hypersonic Flow Past Corners" *J. Fluid Mech.* **89**, pp. 535-552.

Rott, N. (1956) "Unsteady Viscous Flow in the Vicinity of a Stagnation Point" *Q. Appl. Maths.* **13**, pp. 444-451.

Robinson, S.K. (1991) "Coherent Motions in theTurbulent Boundary Layer" *Ann. Rev. Fluid Mech.* **23**, pp. 601-639.